

Studying Transiting Exoplanets with NGTS and TESS

by

Edward Michael Bryant

Thesis

Submitted to the University of Warwick

for the degree of

Doctor of Philosophy in Physics

Department of Physics

June 2022

Contents

List of Tables	v
List of Figures	vi
Acknowledgments	ix
Declarations	x
Abstract	xi
Abbreviations	xii
Chapter 1 Introduction	1
1.1 Exoplanets	1
1.2 Discovery Methods	4
1.2.1 Transiting Exoplanets	4
1.2.2 Radial Velocity	12
1.2.3 Astrometry	13
1.2.4 Microlensing	16
1.2.5 Direct Imaging	16
1.3 Transit Surveys	19
1.3.1 WASP	20
1.3.2 HATNet	20
1.3.3 HATSouth	21
1.3.4 Kepler	21
1.3.5 K2	22
1.4 The Next Generation Transit Survey (NGTS)	22
1.4.1 The NGTS Facility	23

1.4.2	NGTS Operations	23
1.4.3	NGTS Data Reduction	25
1.4.4	Light curve analysis and transit search	27
1.4.5	False Positives and Exoplanet Confirmation	29
1.4.6	NGTS Survey Highlights	31
1.5	Transiting Exoplanet Survey Satellite (<i>TESS</i>)	33
1.6	NGTS in the Era of <i>TESS</i>	37
1.7	Exoplanet Occurrence Rates	38
1.7.1	Current Overview	38
1.8	Thesis Outline	41
Chapter 2 NGTS-12b: A sub-Saturn mass transiting exoplanet in a 7.53 day orbit		43
2.1	Introduction	44
2.2	Observations	45
2.2.1	NGTS Photometry	45
2.2.2	<i>TESS</i> Photometry	45
2.2.3	CORALIE Spectroscopy	50
2.2.4	HARPS Spectroscopy	50
2.2.5	FEROS Spectroscopy	50
2.3	Analysis	51
2.3.1	Stellar Properties	51
2.3.2	Global Modelling	52
2.3.3	Dilution of the <i>TESS</i> transits	55
2.4	Discussion	56
2.5	Conclusions	64
Chapter 3 Simultaneous <i>TESS</i> and NGTS Observations of WASP-166b		65
3.1	Introduction	66
3.2	Observations	67
3.2.1	NGTS Photometry	67
3.2.2	<i>TESS</i> Photometry	69
3.3	Analysis	71
3.3.1	NGTS Noise Properties	71
3.3.2	Fitting Individual NGTS Light Curves	76
3.3.3	Fitting Combined Light Curve	80
3.3.4	Fitting <i>TESS</i> Data	81

3.3.5	NGTS and <i>TESS</i> Comparison	81
3.4	Discussion	83
3.5	Conclusion	84
Chapter 4 A transit timing variation observed for the long-period extremely low-density exoplanet HIP-41378 f		86
4.1	Introduction	87
4.2	Photometric Observations	89
4.2.1	NGTS	89
4.2.2	SPECULOOS	89
4.2.3	Asiago Telescope	90
4.2.4	Photometric Transit Detection	90
4.2.5	Additional Ground Based Photometry	91
4.3	Analysis	91
4.4	TTV Analysis	92
4.5	Conclusions	94
Chapter 5 Revisiting WASP-47 with ESPRESSO and TESS		97
5.1	Introduction	98
5.2	Observations	99
5.2.1	ESPRESSO	99
5.2.2	K2	102
5.2.3	<i>TESS</i>	103
5.3	Analysis	104
5.3.1	Transit Analysis	104
5.3.2	Radial Velocity Analysis	107
5.3.3	Stellar Rotation Analysis	108
5.3.4	Stellar Activity Analysis	114
5.3.5	Gaussian Process Analysis	114
5.3.6	Final Combined Model	119
5.3.7	Transit Timing Analysis	121
5.4	Discussions	123
5.5	Conclusions	128
Chapter 6 Transit search for gas giant planets orbiting low-mass stars		131
6.1	Introduction	132
6.2	Low-Mass Star Sample	135

6.3	Transit Search	141
6.4	False Positive Identification	141
6.4.1	Secondary Eclipse Events	142
6.4.2	Odd-Even Depth Differences	142
6.4.3	Sector Depth Differences	144
6.4.4	Transit Phased Variability	144
6.4.5	Lomb-Scargle Analysis	146
6.4.6	Light curve symmetry	148
6.4.7	Excess standard deviation scatter metric	148
6.4.8	Depth metric	148
6.5	Transit Fitting and Planet Candidates	149
6.6	Blend Scenario Checks	150
6.7	Giant Planet Candidates	151
6.8	ESPRESSO Radial Velocity Monitoring	161
6.9	Injection and Recovery Tests	161
6.10	Conclusions and Future Outlook	164
Chapter 7 Conclusions		165
7.1	The role of ground-based photometry in the <i>TESS</i> Era	165
7.1.1	NGTS Wide-Field Transit Observations	165
7.1.2	NGTS Multi-Telescope Observations	166
7.1.3	The long-period planet HIP-41378 f	167
7.1.4	Future Outlook	168
7.2	Exoplanet Populations	169
7.2.1	WASP-47	170
7.2.2	Giant planets orbiting low-mass stars	170
7.2.3	Future Outlook	171
7.3	The Future of Exoplanet Discovery	172

List of Tables

2.1	NGTS and <i>TESS</i> photometry for NGTS-12	46
2.2	Stellar Properties for NGTS-12	47
2.3	Radial Velocities for NGTS-12	51
2.4	Fitted parameters for NGTS-12 b	61
2.5	Derived parameters for NGTS-12 b	62
3.1	Stellar Properties for WASP-166	68
3.2	NGTS photometry of WASP-166	71
3.3	Planetary System properties for WASP-166	85
4.1	Confidence intervals for the predictions of $T_{C,4}$ and $T_{C,5}$	95
5.1	Key Stellar Properties for WASP-47	101
5.2	Derived parameters for WASP-47 b and e	117
5.3	Derived parameters for the WASP-47 c and d	118
5.4	Additional parameters from the WASP-47 radial velocity modelling	120
5.5	<i>TESS</i> mid-transit times for WASP-47 b	121
6.1	Parameter priors used in the transit fitting	149
6.2	Stellar magnitudes for our giant planet candidates	155
6.3	Stellar parameters the host stars of our giant planet candidates	156
6.4	Planetary parameters for eight of our giant planet candidates	158
6.5	Planetary parameters for the remaining six giant planet candidates	159
6.6	Available follow-up data for our giant planet candidates	160
7.1	Summary of the NGTS follow-up light curves contributed to published exoplanet discoveries.	167

List of Figures

1.1	Discovery data for 51 Pegasi b and PSR 1257+12 b and c	2
1.2	Cumulative number of exoplanet detections	3
1.3	Idealised transit geometry and light curve	5
1.4	Orbital geometry of a transiting exoplanet	6
1.5	Hubble Space Telescope transits of HD 209458 b	9
1.6	Transit timing variations for Kepler-9 b and c	11
1.7	An example exoplanet radial velocity curve	12
1.8	Mass and radius vs period distributions for known exoplanets	14
1.9	Minimum mass plotted against year discovered for radial velocity discoveries	15
1.10	Astrometric and spectroscopic orbits of ϵ Eridani b	15
1.11	Microlensing detection of the planet OGLE-2019-BLG-0960 Lb	17
1.12	Direct images of the HR 8799 planets	18
1.13	Protoplanetary disk images from the DSHARP survey	19
1.14	NGTS telescopes	22
1.15	NGTS survey field image	24
1.16	Example of a BLS detection of an exoplanet orbiting TIC-382602147	28
1.17	Eclipsing binary false positive identified by a secondary eclipse	29
1.18	Eclipsing binary false positive identified by odd-even depth difference	30
1.19	Transit depths of exoplanets discovered by ground based transit surveys	32
1.20	Illustration of the Transiting Exoplanet Survey Satellite	33
1.21	<i>TESS</i> Cycle 1 observation schedule	34
1.22	Comparison of NGTS and <i>TESS</i> images	35
1.23	HARPS survey planetary populations	38
1.24	Giant planet occurrence as a function of stellar mass	39
1.25	Occurrence rates of giant planets from <i>Kepler</i>	40
1.26	Planetary occurrence rates as a function of radius and period	40

2.1	NGTS and <i>TESS</i> light curves of NGTS-12	48
2.2	<i>TESS</i> Full-Frame Image cutout for NGTS-12	49
2.3	HARPS and FEROS radial velocities for NGTS-12	53
2.4	Phase-folded NGTS and <i>TESS</i> transit light curves for NGTS-12 b	54
2.5	Irradiating stellar flux as a function of planetary mass	57
2.6	Bulk densities of known exoplanets as a function of incident stellar flux	58
2.7	Transmission Spectroscopy Metric vs orbital period for known exoplanets	59
2.8	Orbital period vs transit depth for planets discovered by ground-based transit surveys	60
3.1	Individual NGTS telescope light curves for a WASP-166 b transit	70
3.2	NGTS photometric precision as a function of timescale	73
3.3	Correlation between the flux from each pair of NGTS telescopes	74
3.4	NGTS photometric precision as a function of the number of telescopes used	75
3.5	Variation of NGTS flux RMS during a night	77
3.6	Parameter posterior distributions for T_C and R_p/R_*	79
3.7	NGTS and <i>TESS</i> light curves of a transit of WASP-166 b	80
3.8	Comparison of NGTS and <i>TESS</i> posterior distributions	82
4.1	Time-series photometry for HIP-41378	88
4.2	Transit times for HIP-41378 f	93
5.1	Orbital configuration of the inner WASP-47 planetary system	100
5.2	<i>TESS</i> 20 second cadence photometry for WASP-47	103
5.3	Phase-folded <i>TESS</i> photometry for the WASP-47 planets	105
5.4	<i>TESS</i> transit times for WASP-47 b	106
5.5	K2 Campaign 3 photometry for WASP-47	110
5.6	Lomb-Scargle periodograms for ESPRESSO data of WASP-47	112
5.7	Contrast of the ESPRESSO CCFs of WASP-47 as a function of the FWHM	113
5.8	ESPRESSO time series data for WASP-47	115
5.9	Phase-folded RVs for the WASP-47 planets	122
5.10	Transit timing variations for WASP-47 b	123
5.11	Mass-radius diagram for low-mass exoplanets	124
5.12	Bulk planet density as a function of stellar irradiation for low-mass exoplanets	125
5.13	Transmission Spectroscopy metric as a function of orbital period for known exoplanets	126
5.14	Planet bulk density as a function of stellar metallicity	129

6.1	Radius of known transiting giant planets as a function of host star mass	134
6.2	Photometric precision plotted against apparent magnitude for <i>TESS</i> low-mass stars	136
6.3	Histograms of <i>TESS</i> low-mass star sample	137
6.4	<i>Gaia</i> colour-magnitude diagram	139
6.5	The BLS periodogram of TIC-335590096 plotted as an example. The red dashed line shows the level of the $SDE = 8$ threshold for this candidate, and the detected period of 1.523 d is clearly visible.	140
6.6	Example of eclipsing binaries identified by a secondary eclipse	142
6.7	Example of eclipsing binary identified by odd-even depth difference	143
6.8	Example of a nearby eclipsing binary identified through a sector depth difference	145
6.9	Examples of variable stars identified by the vetting checks	147
6.10	Flow chart of the steps of the planet search pipeline	152
6.11	Giant planet candidate transit light curves	153
6.12	Giant planet candidates compared to known transiting gas giant exoplanets . . .	154
6.13	Comparison of giant planet candidates to the low-mass star <i>Gaia</i> colour-magnitude distribution	157
6.14	ESPRESSO radial velocities for our giant planet candidates	162

Acknowledgments

First and foremost I would like to thank my supervisor Dan Bayliss for your guidance, support, and enthusiasm throughout my PhD. Without you I would not have become the scientist I am today.

Thanks to everyone in the Warwick Astro group – students and staff – for making this department such an enjoyable place to work for the past 3 and a half years. I won't try to name you all as there are so many of you, and I'm bound to forget someone. Thank you for the pub trips, game nights, movie nights, and lunchtime conversations I will not forget in a hurry (for better or worse).

I would also like to thank my parents for their support of this adventure and their understanding of my putting off getting a proper job for so long.

Finally, a huge thank you to Kate. For always being so interested to hear about my work. For constantly reminding me how cool what I do is, especially when I occasionally have forgot. And especially for your support over these past few months.

Declarations

I declare that this thesis is my own work except where explicitly stated otherwise. This thesis has not been submitted to this or any other academic institution for any other degree or qualification. A large amount of the research presented in this thesis has been published in peer reviewed journals. In particular:

- **Chapter 2** : This chapter is a reproduction of Bryant et al. (2020a);
- **Chapter 3** : This chapter is a reproduction of Bryant et al. (2020b);
- **Chapter 4** : This chapter is a reproduction of Bryant et al. (2021);
- **Chapter 5** : This chapter is a reproduction of Bryant and Bayliss (2022) .

The exact contributions to these works by collaborators are declared at the start of each chapter.

Abstract

Studying exoplanets enables us to better understand our place in the Universe. Transiting exoplanets, where the planet passes in front of its host star, provide us with a great wealth of information on the properties of the planet. In this thesis, I use high precision photometry from the Next Generation Transit Survey (NGTS) and the Transiting Exoplanet Survey Satellite (*TESS*) to discover and characterise transiting exoplanets. I also include spectroscopic observations to monitor the radial velocity of the host stars in order to measure the planet mass.

I present the discovery of NGTS-12 b, a $1.05 R_J$ transiting exoplanet orbiting a $V = 12.38$ mag star with a period of 7.53 days. Using spectroscopic observations from HARPS, I measured the mass of the planet as being $0.21 M_J$.

I present a novel observing method that involves the use of multiple NGTS telescopes to simultaneously observe the same star. I tested this method on the bright ($V = 9.35$ mag) exoplanet hosting star WASP-166 achieving a photometric precision of 152 ppm per half hour. This is some of the highest photometric precision data for ground-based observations of bright stars, opening up multiple avenues for new NGTS science. Using this technique I was able to observe a transit of the 542 day period exoplanet HIP-41378 f. These observations revealed the presence of transit timing variations for this planet.

Planet formation is generally well understood, however there are a number of planetary systems which challenge the current theories. One such system is the WASP-47 system, which contains a hot Jupiter with a close orbiting inner super-Earth companion. I present new spectroscopic observations obtained with ESPRESSO and analysis to improve our understanding of the properties of the WASP-47 planets. This analysis included the use of a Gaussian Process to model a stellar activity signal present in the radial velocity data. The Gaussian Process was motivated by measurements of the rotation period of the host star. The results of my analysis have begun to reveal the presence of a potential new population of exoplanets, one which if better studied might shed more light on how this remarkable system formed.

Finally, I present a study of the occurrence rates of transiting gas giant exoplanets with low-mass stellar hosts. These occurrence rates are currently not well constrained and so the results of this project will be of great importance for understanding the formation mechanisms of giant planets. This search has yielded fourteen giant planet candidates from a sample of 91,306 low-mass stars, and radial velocity monitoring with ESPRESSO is underway to confirm the candidates. These candidates will form the basis of a calculation of the occurrence rates for these systems, which will be performed over the coming months.

Abbreviations

BIC Bayesian Information Criterion	RMS Root Mean Square
BLS Box-fitting Least Squares	RV Radial Velocity
CCD Charge Coupled Device	TESS Transiting Exoplanet Survey Satellite
CCF Cross-Correlation Function	TFOP TESS Follow-up Observing Program
ESO European Southern Observatory	TIC TESS Input Catalogue
ESPRESSO Echelle SPectrograph for Rocky Exoplanets and Stable Spectroscopic Observations	TOI TESS Object of Interest
FFI Full-Frame Image	TTV Transit Timing Variation
GP Gaussian Process	VLT Very Large Telescope
HARPS High Accuracy Radial velocity Planet Searcher	WASP Wide Angle Search for Planets
JWST James Webb Space Telescope	R_{\oplus} Earth Radius : 6,378 km
K2 Kepler 2nd mission	M_{\oplus} Earth Mass : 5.972×10^{24} kg
MCMC Markov Chain Monte Carlo	R_J Jupiter Radius : 71,492 km
NGTS Next Generation Transit Survey	M_J Jupiter Mass : 1.898×10^{27} kg
PSF Point Spread Function	R_{\odot} Solar Radius : 695,700 km
	M_{\odot} Solar Mass : 1.988×10^{30} kg
	au Astronomical Unit : 1.496×10^{11} m

Chapter 1

Introduction

1.1 Exoplanets

The discovery of planets began in the ancient civilisations. There is evidence that the ancient Babylonians knew of the existence of the five planets closest to Earth – Mercury, Venus, Mars, Jupiter, Saturn (Sachs, 1974) – which are bright enough to be seen with the naked eye. The discovery of the remaining Solar System planets had to wait until the invention of the telescope. Uranus was initially observed in 1781 by William Herschel (Pasachoff and Olson, 2011), although it was initially classified as a comet. Neptune was first observed in 1846 by Galle (Galle, 1846), who used calculations performed by Le Verrier to locate the planet in the sky. Throughout history philosophers have debated whether the Solar System stands alone in the Universe or whether there exist planets orbiting stars other than the Sun.

These distant worlds are called “exoplanets”. The International Astronomical Union (IAU) recently provided a working definition for exoplanets as objects with masses below the limiting mass for the thermonuclear fusion of deuterium ($\approx 13 M_J$) (Lecavelier des Etangs and Lissauer, 2022). Exoplanets must also orbit a star, brown dwarf, or stellar remnant. Objects which are more massive but are not sufficiently massive to trigger nuclear fusion in the core are known as brown dwarfs. While the mass of $13 M_J$ is often adopted as the boundary between planets and brown dwarfs, the exact differentiation between these two classes of objects is still unclear. The IAU working definition also stipulates that any exoplanet must have a mass ratio with the central object below $M/M_{\text{central}} \lesssim 1/25$. The minimum mass limit for an exoplanet is the same as for a Solar System planet, namely that any (exo)planet must have sufficient mass that it assumes a (nearly round) hydrostatic equilibrium shape under its self-gravity.

Despite all this debate and wonder, it was not until the 20th century that a concrete method of detecting these planets was proposed (Struve, 1952). It took astronomers a further 40 years

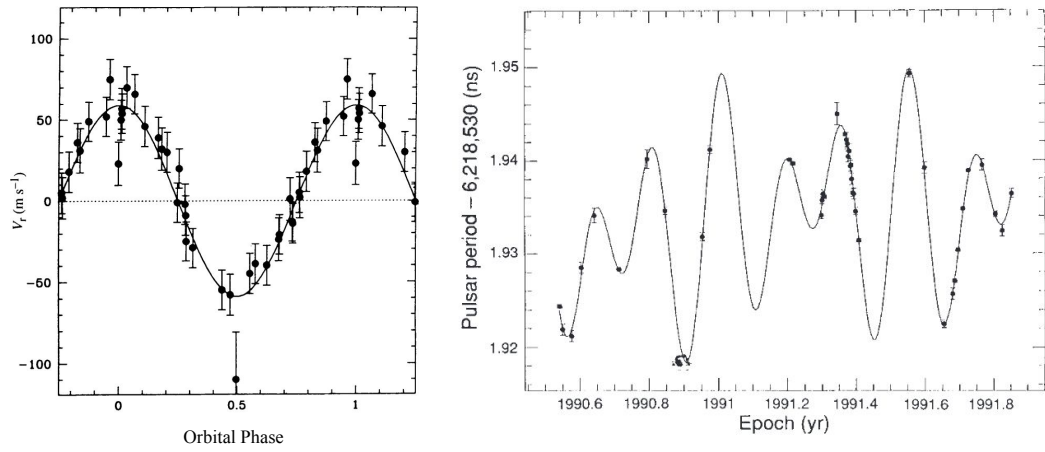


Figure 1.1: Discovery data for 51 Pegasi b and PSR 1257+12 b and c. **Left:** Phase folded radial velocities of the star 51 Pegasi showing clearly the variation due to the 4.23 d orbit of 51 Pegasi b. Plot from Mayor and Queloz (1995). **Right:** Variations in the period of the pulsar PSR 1257+12 due to the motion of the two planets orbiting the pulsar. Plot from Wolszczan and Frail (1992).

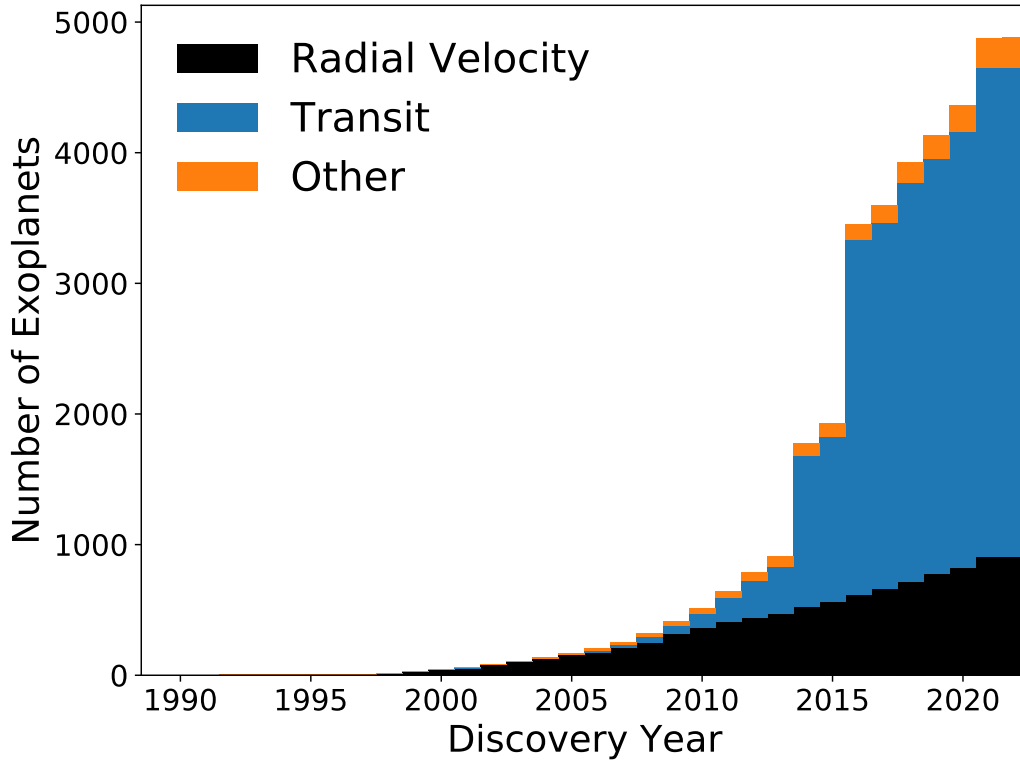


Figure 1.2: Cumulative number of exoplanet detections by year, colour coded by the detection method. The sharp rises in 2014 and 2016 are from statistically validated exoplanets from the *Kepler* mission (Rowe et al., 2014; Morton et al., 2016). Data accessed from NASA Exoplanet Archive on 2022 February 01.

before the first exoplanet discovery was reported in 1992 (PSR 1257+12 b and c; Wolszczan and Frail, 1992). These first planets were orbiting a pulsar and were revealed by a quasiperiodic variability observed in the arrival times of the pulsar pulses (see right-hand panel of Figure 1.1). This variation in the arrival times was deduced as being a result of the orbital motion of two planets around the pulsar. A few years later, the first exoplanet orbiting a main-sequence star, 51 Pegasi b, was detected. This exoplanet has a minimum mass of $0.47 \pm 0.02 M_J$ and orbits its host star in just 4.23 d (Mayor and Queloz, 1995). The presence of this planet was revealed by the resultant sinusoidal variation in the radial velocity of the host star (see left-hand panel of Figure 1.1 for the data and Section 1.2.2 for more details on this method).

1.2 Discovery Methods

Since this initial discovery, the field of exoplanet detection has exploded, with 4,884¹ planets being discovered over the past 27 years through the use of a number of different detection methods (see Figure 1.2). The two methods that have dominated exoplanet science are the transit (Winn, 2010) and radial velocity (Lovis and Fischer, 2010) methods. I will now present and discuss these two main methods, as well as other methods through which exoplanets have been detected.

1.2.1 Transiting Exoplanets

Transits arise as a result of the exoplanet passing through the line-of-sight from the observer to the host star and thereby passing across, or transiting, the main stellar disc. The transit of the planet causes the apparent brightness of the host star to decrease.

The first ever known transiting exoplanet was the hot Jupiter HD 209458 b. The presence of this planet was revealed with radial velocity measurements from the Keck/HIRES spectrograph (Henry et al., 2000). Henry et al. (2000) also reported photometric data which showed a clear dip around the expected transit time, indicating that the planet transited its host star. The first full transits of this planet, which allowed for the planet radius and orbital inclination to be precisely determined, were obtained shortly after (Charbonneau et al., 2000).

It was not until a few years after the detection of HD 209458 b that the first planet was discovered through observations of its transit events by the OGLE facility (Udalski et al., 1992; Konacki et al., 2003). Over the past 20 years, a total of 3,750 exoplanets have been discovered using the transit method, often by transit surveys, such as WASP (Pollacco et al., 2006), *Kepler* (Borucki et al., 2010), or NGTS (Wheatley et al., 2018). However, of these 3,750 exoplanets, only 894 have a well measured mass, often obtained through radial velocity measurements (see Section 1.2.2). The others have been statistically validated (e.g. Morton et al., 2016) but are too faint to be amenable to radial velocity follow-up.

Transit Light Curves

The transit method relies on detecting the decrease in the apparent brightness of a star that is caused by an exoplanet moving across the main disc of the star, as viewed by an observer. We can use various features of the resultant stellar light curve to learn a substantial amount of information about the physical properties of the planet and the orbital configuration of the system. We can also use transit light curves to learn about the host star.

¹Data accessed from the NASA Exoplanet Archive on 2022 February 01.

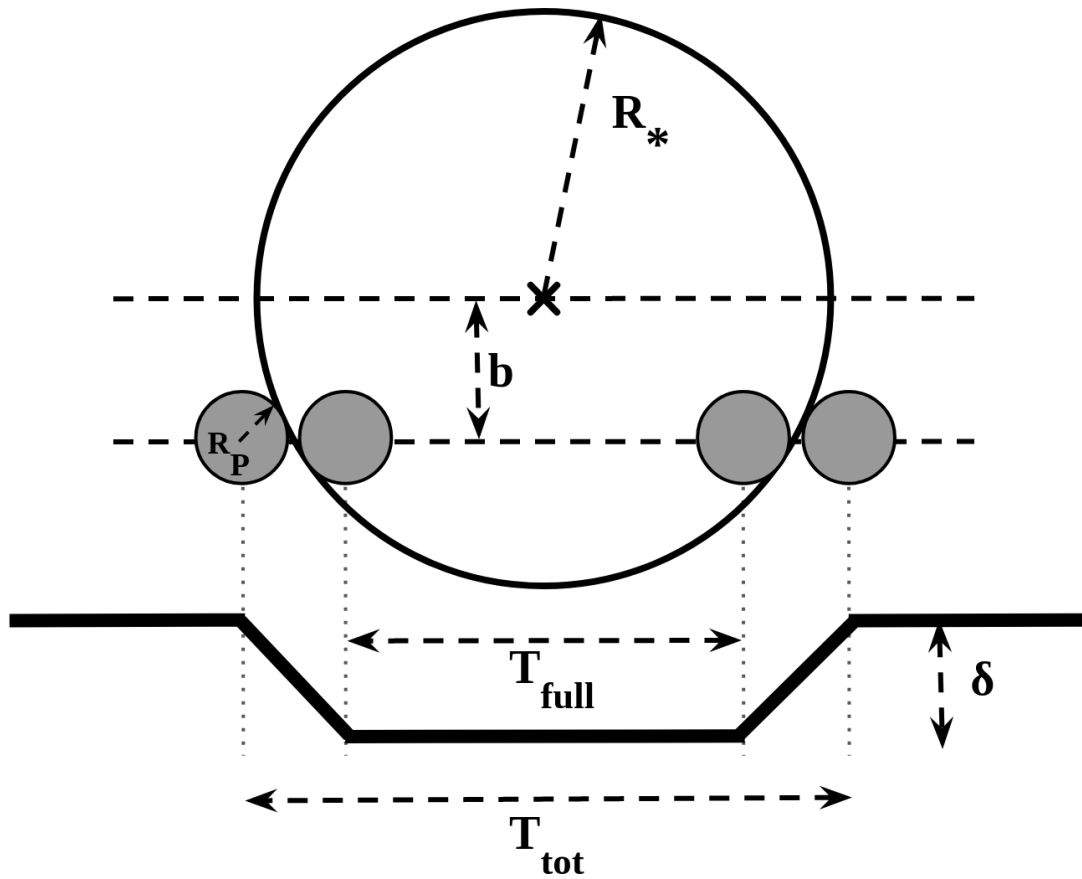


Figure 1.3: Idealised transit geometry and resultant light curve. Adapted from Figure 2 of Winn (2010). The large circle is the stellar disc and the small circle is the transiting planet. The bold line gives the transit light curve shape. R_P is the planet radius and R_* is the stellar radius. b is the impact parameter (Equation 1.3) and δ is the transit depth (Equation 1.1). T_{tot} is the total transit duration and T_{full} is the *full* transit duration (Equations 1.5 and 1.6).

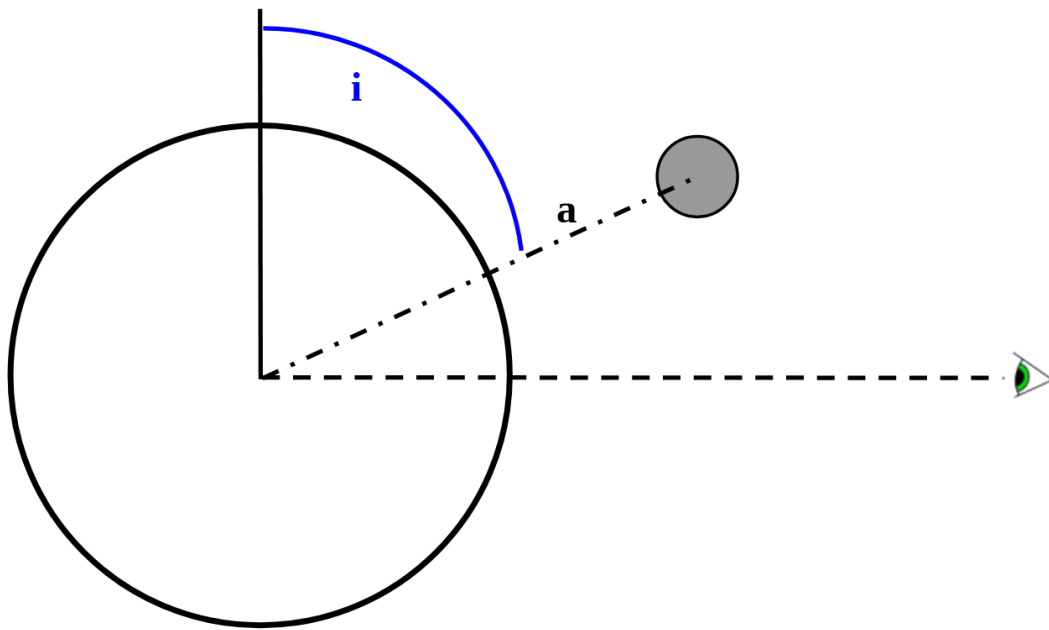


Figure 1.4: Schematic showing some of the key features of the orbital geometry of a transiting exoplanet. The large circle is the star and the small circle is the transiting planet. i is the orbital inclination and a is the semi-major axis of the orbit. The eye is the position of the observer.

The first feature of interest is the temporal spacing between subsequent transit events. This spacing tells us the orbital period of the exoplanet. Often for transit surveys, three separate transits are needed as a minimum to derive a unique orbital period for a planet. This is especially the case for long period planets or datasets with large gaps.

The next key feature is the depth of the transit events, δ (see Figure 1.3). The decrease in flux, ΔF relative to the baseline out-of-transit flux level, F_0 , gives us the radius of the planet, R_P , relative to the stellar radius, R_* . These values are all linked by the following equation:

$$\frac{\Delta F}{F_0} \equiv \delta = \left(\frac{R_P}{R_*} \right)^2. \quad (1.1)$$

The radius of the host star can be obtained through a number of methods (e.g. SED modelling; spectral analysis; isochrone fitting) and with this we can determine the physical radius of a transiting exoplanet. For a host star with a radius of $1 R_\odot$, an exoplanet with $R_P = 1 R_J$ gives a transit depth of 1%, and an exoplanet with $R_P = 1 R_\oplus$ gives an even shallower transit of just 0.008% depth.

In addition to the need to measure such small deviations in the flux of a star, this method is limited by the fact that the orbit of the planet must be precisely aligned in order for the transit to occur. The orbital inclination of the planet, i , defined such that $i = 90^\circ$ for a edge-on orbit and $i = 0^\circ$ for a face-on orbit (see Figure 1.4), must be greater than a critical value i_{crit} which is given by

$$\cos(i_{\text{crit}}) = \frac{R_P + R_*}{a}, \quad (1.2)$$

where a is the semi-major axis of the planet's orbit. Based on this requirement, we can also estimate a geometric probability that a randomly orientated exoplanet system will be observed to transit its host star. As an example, for a distant observer on a random planet, the Earth would have a 0.47% chance of transiting. Jupiter would have an even smaller probability of 0.099%. In terms of exoplanet observations, a $1 R_J$ planet on a 4 d orbit around a $1 R_\odot$ host star has a geometric transit probability of approximately 10%.

Related to the geometry of the exoplanetary system, we now define a further quantity: the impact parameter, b . This value is given by the equation (Winn, 2010)

$$b = \frac{a \cos i}{R_*} \left(\frac{1 - e^2}{1 + e \sin \omega} \right), \quad (1.3)$$

where e is the eccentricity of the planet's orbit ($e = 0$ for a circular orbit) and ω is the longitude of periastron for the orbit. The impact parameter relates to the latitude of the stellar disk that is occulted by the planet, with $b = 0$ being an equatorial transit and $b = 1 + R_P/R_*$ for a fully

grazing eclipse (see Figure 1.3).

Along with the depth, δ , two further measurable characteristics of a transit light curve, from which we can derive the geometry of the system, are the total transit duration, T_{tot} , and the *full* transit duration, T_{full} , (see Figure 1.3). With these three values, all of which can be directly measured from a transit light curve, we can derive the following dimensionless planetary system parameters (Winn, 2010):

$$\frac{R_P}{R_*} = \sqrt{\delta} \quad (1.4)$$

$$b^2 = \frac{(1 - \sqrt{\delta})^2 - (T_{\text{full}}/T_{\text{tot}})^2(1 + \sqrt{\delta})^2}{1 - (T_{\text{full}}/T_{\text{tot}})^2} \quad (1.5)$$

$$\frac{R_*}{a} = \frac{\pi}{2\delta^{1/4}} \frac{\sqrt{T_{\text{tot}}^2 - T_{\text{full}}^2}}{P} \left(\frac{1 + e \sin \omega}{\sqrt{1 - e^2}} \right). \quad (1.6)$$

With these relations and the stellar radius, we can then derive values for the planet radius and semi-major axis of the orbit. The third of these quantities, R_*/a , is especially interesting, as from Kepler's third law we can derive the relation

$$\rho_* = \frac{3\pi}{GP^2} \left(\frac{a}{R_*} \right)^3 \quad (1.7)$$

where ρ_* is the stellar density, in the limit that $(R_P/R_*)^3 \ll 1$, which is very often the case for transiting planets. Consequentially, from direct transit observable quantities, not only can we derive planet and orbital parameters, but can also gain information on the host star itself. This is useful in transit surveys for assessing whether a given transit signal is likely to be a true planet transit on the target star, by comparing the measured ρ_* to the expected value from prior knowledge of the star's characteristics. It can also be useful for providing an independent measurement of the stellar parameters. It is important to note here that as the a/R_* parameter is influenced by the orbital eccentricity, knowledge of the eccentricity is required to ensure accuracy of this ρ_* measurement.

The orbital eccentricity is hard to derive from transit photometry alone. For highly eccentric cases, slight differences arise between the durations of the transit ingress and egress. However, in most cases this effect is too small to reliably measure. If the stellar density of the host star is well constrained, then from the transit duration and orbital period it is possible to interrogate whether a circular orbit is physically reasonable. In this case though, there is still a strong degeneracy between e and ω , and so deriving a unique eccentricity remains difficult. For transiting planets, typically the orbital eccentricity cannot be derived from the transit light curve

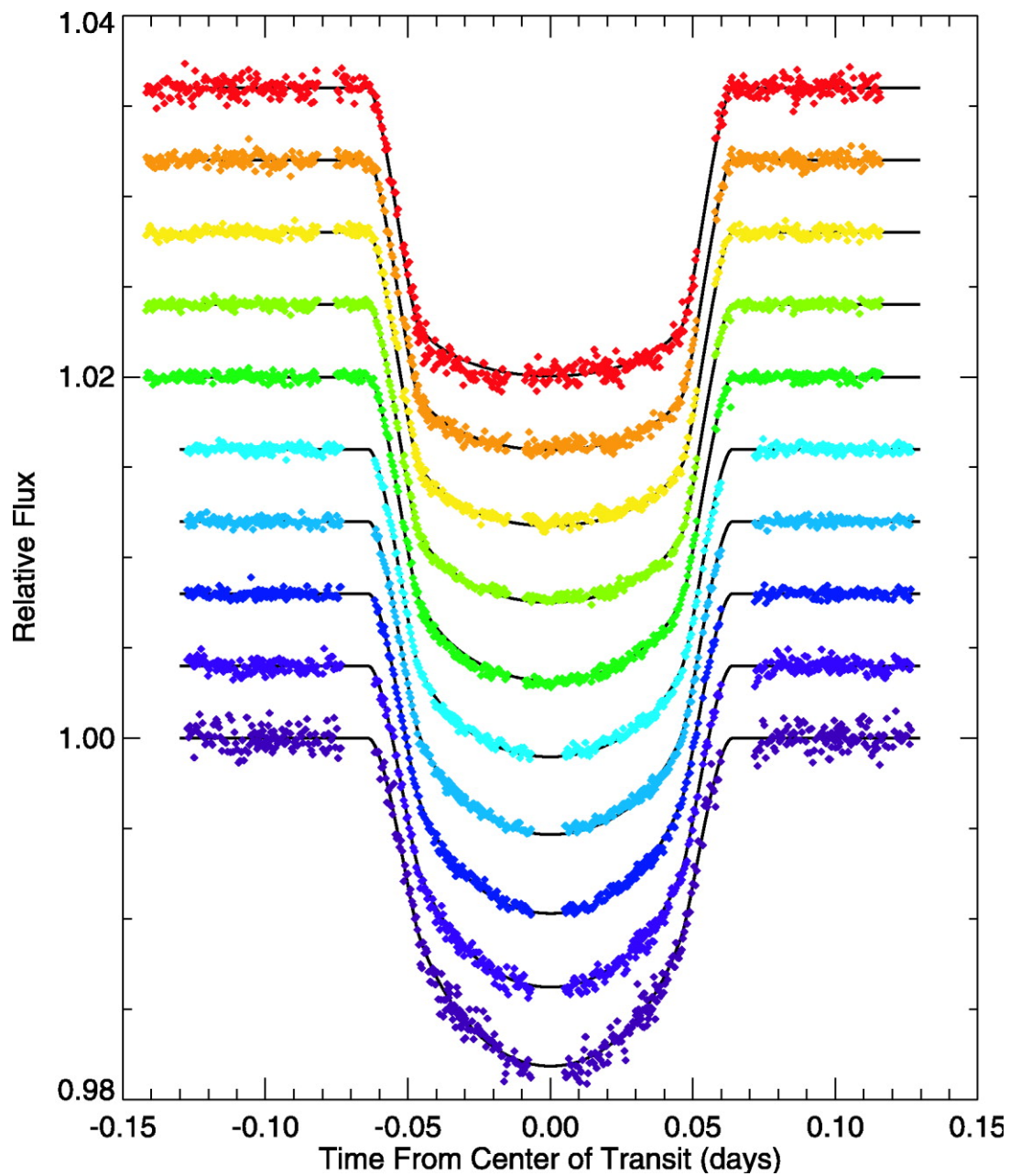


Figure 1.5: Transits of HD 209458 b observed with the Hubble Space Telescope in different wavelength bandpasses ranging from 300–350 nm (bottom) to 920–1000 nm (top). The varying effect on the transit shape of limb darkening with the wavelength of the observations is clearly demonstrated. Plot from Knutson et al. (2007).

alone and further observations, often radial velocity measurements, are required.

Limb-Darkening

The transit shape shown in Figure 1.3 is a simplified approximation. This very flat transit shape is what would be observed if the host star was uniformly bright across the entire stellar disk. In reality this is not the case, and stars are instead brighter in the centre of the stellar disk and fainter towards the edges, or limbs. This phenomenon is known as limb-darkening, and it is important to account for this when modelling transits, else there is a risk of biasing the R_P measurement (Espinoza and Jordán, 2015). The effect this has on the shape of a transit light curve, as well as the dependence of the effect on the wavelength of the observations, are demonstrated beautifully by transit observations of HD 209458 b taken with the Hubble Space Telescope (see Figure 1.5 and Knutson et al., 2007).

To model the limb-darkening of stars during transit fitting, parametric laws are often adopted to describe the change in intensity across the stellar disc. The coefficients for these laws depend on the host star and can be obtained through a number of ways. The first is to use existing knowledge of the host star and stellar models to predict them (e.g. Claret and Bloemen, 2011; Parviainen and Aigrain, 2015). The second relies on a parameterisation derived by Kipping (2013a). This parameterisation ensures the computed limb-darkening law is physically realistic while not requiring any prior knowledge of the host star.

Transit Timing Variations

In some cases, the orbits of planets are not strictly periodic. This results in variations in the temporal separation between subsequent transits, called transit timing variations (TTVs; see Figure 1.6 for an example). These TTVs arise in multi-planetary systems, particularly those in which the planets reside in a first-order mean motion resonance. This is where the ratio of the orbital periods of a pair of exoplanets is of the form $j:j+1$ (e.g. 1:2; 2:3, ...). In these cases, gravitational interactions between the planets can perturb the orbits, giving rise to TTVs. These systems are particularly interesting, as through monitoring these TTVs it is possible to determine the masses of the planets (e.g. K2-19; Barros et al. 2015 and K2-24; Petigura et al. 2018). Thus, in certain cases, it is possible to obtain from transit light curves estimates for the mass and radius of an exoplanet, relative to the mass and radius of the host star. Combined with knowledge of the stellar mass and radius, the absolute mass and radius of the exoplanet, and therefore its bulk density, can be determined. Additional observations, often radial velocity monitoring, are usually required to obtain density measurements. These density measurements can provide initial insights into the possible composition of an exoplanet.

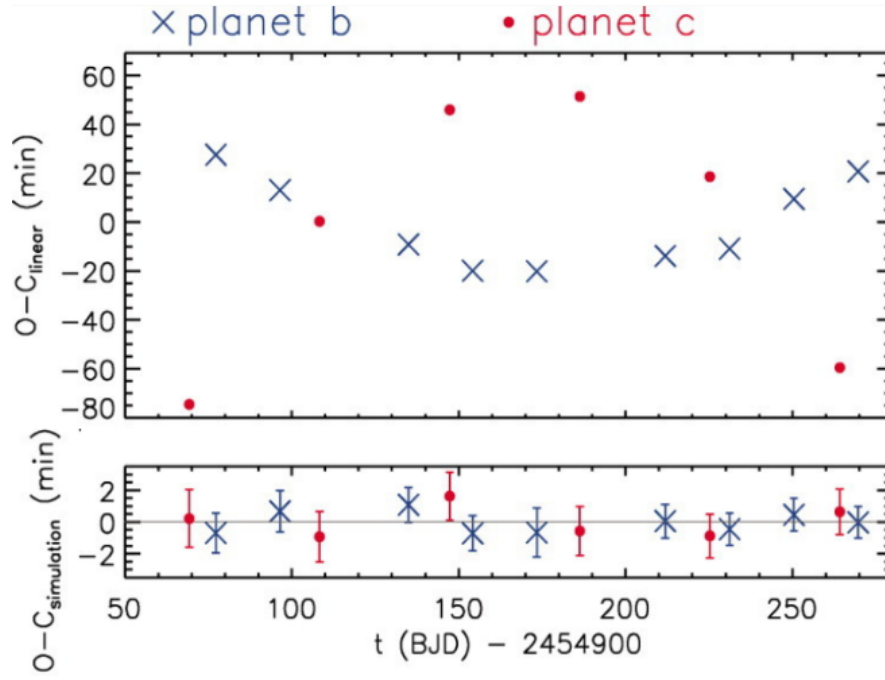


Figure 1.6: Transit timing variations for Kepler-9 b and c. The main panel shows the deviations of the measured transit times from a linear orbital period and the bottom panel shows the residuals to a dynamical fit to the TTVs for the system. Plot adapted from Figure 3 of Holman et al. (2010).

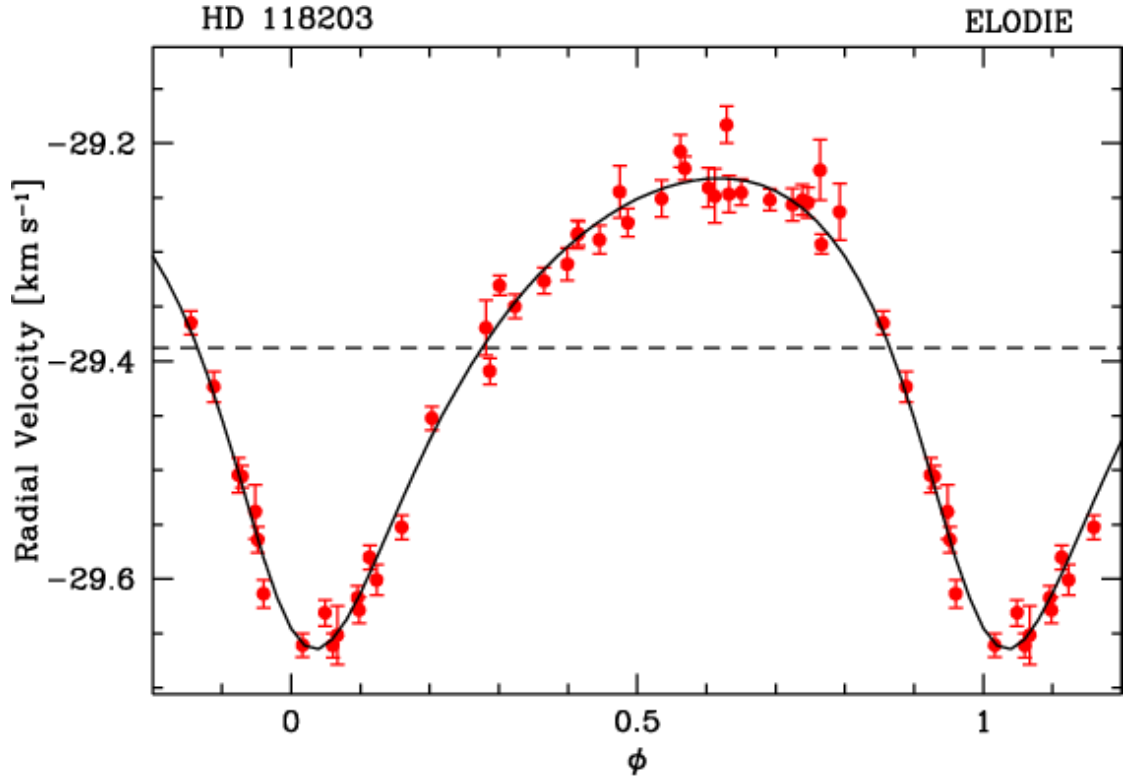


Figure 1.7: An example radial velocity curve for the exoplanet HD 118203 b (da Silva et al., 2006). The data have been phase-folded using the orbital period of the planet. Note the non-sinusoidal shape of the radial velocity variation, which is a result of the eccentricity of the planet's orbit of 0.309 ± 0.014 .

1.2.2 Radial Velocity

As a planet orbits the star, both planet and star are orbiting around the position of the centre-of-mass of the star-planet system. The motion of the planet along its orbit thus causes the star to "wobble", which is observed as a variation in the speed of the star's motion along the line-of-sight from observer to star, known as the star's radial velocity. Through exploitation of the Doppler effect we can measure this radial velocity variation by measuring the wavelengths at which various absorption lines in the stellar spectrum are observed. By monitoring the radial velocity of a star over multiple epochs, we can observe a variation due to the orbit of the planet (see Figure 1.7 for an example).

The period and amplitude of this variation can be determined. The period of the variation is equal to the orbital period of the planet. The mass of the planet, M_P , can be determined from the semi-amplitude of the radial velocity variation, K , using the following equation (from e.g.

Perryman, 2018)

$$K = \left(\frac{2\pi G}{P} \right)^{1/3} \frac{M_P \sin i}{(M_* + M_P)^{2/3}} \frac{1}{(1 - e^2)^{1/2}}. \quad (1.8)$$

As can be seen from Equation 1.8, the semi-amplitude of the radial velocity signal is greater for more massive planets and shorter orbital periods. This makes this detection method sensitive to giant planets and planets on short orbital periods < 100 d (e.g. Figure 1.8).

This was the method which yielded the detection of 51 Pegasi b in 1995 (Mayor and Queloz, 1995), the discovery which kick-started the exoplanet revolution. This method also dominated the first decade of exoplanet discovery. Since the initial discovery of 51 Pegasi b, a total of 904 exoplanets have been discovered using the radial velocity method. As can be seen from Figure 1.8, these radial velocity exoplanets span a wide range of masses and periods, but are limited to shorter orbital periods for lower mass planets. As can also be seen from the upper panel of Figure 1.8, only a very small handful of planets detected through the radial velocity method have measured radii. The large majority of mass measurements for transiting exoplanets with a measured mass were obtained using radial velocity monitoring.

As can be seen from Figure 1.9, technological advancements in spectrographs over the past two decades have allowed the radial velocity technique to be used to discover lower mass exoplanets. The next stage in this progression is to develop facilities with the capabilities of detecting an Earth twin: a $1 M_\oplus$ exoplanet on a one year orbit around a $1 M_\odot$ star (see Crass et al., 2021, for details). Such a planet would result in a radial velocity semi-amplitude of 0.089 m s^{-1} , for an inclination of 90° and a circular orbit.

1.2.3 Astrometry

The astrometric method arises from the same root as the radial velocity method in that it exploits the reflex motion of a star due to the orbit of the exoplanet. Here, the visual motion of the star on the sky due to the orbit of the planet is measured and tracked (see e.g. Quirrenbach, 2010). This makes astrometry sensitive to large planets in face-on inclined orbits with wide orbital separations, making it a complementary method to radial velocity detections. To date, just one planetary companion has been discovered using astrometry: a Saturn-like exoplanet orbiting the M9 dwarf star TVLM 513-46546 (Curiel et al., 2020). A second sub-stellar object has been discovered (Sahlmann et al., 2013), but with an estimated mass of $28 \pm 2 M_J$ the companion is a brown dwarf and not a planet. However, roughly 21,000 new exoplanets are predicted to be discovered by astrometric measurements from the nominal *Gaia* mission (Perryman et al., 2014). This yield is predicted to increase to 70,000 planets for a 10 year *Gaia* mission (Perryman et al., 2014). Moreover, astrometric measurements have been used to great success to constrain the

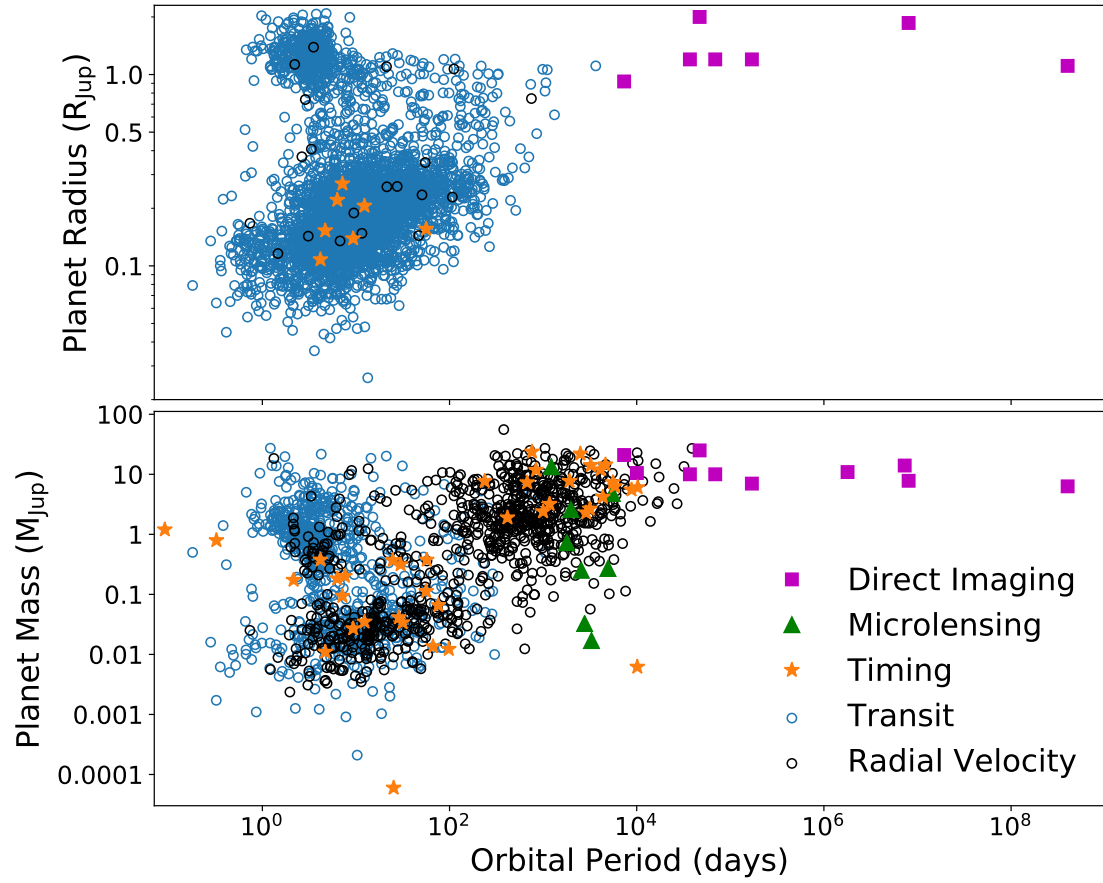


Figure 1.8: Distribution of mass and radius of known exoplanets with their orbital periods. The markers represent the different discovery methods used for each planet. The data were accessed from the NASA Exoplanet Archive on 2022 February 01.

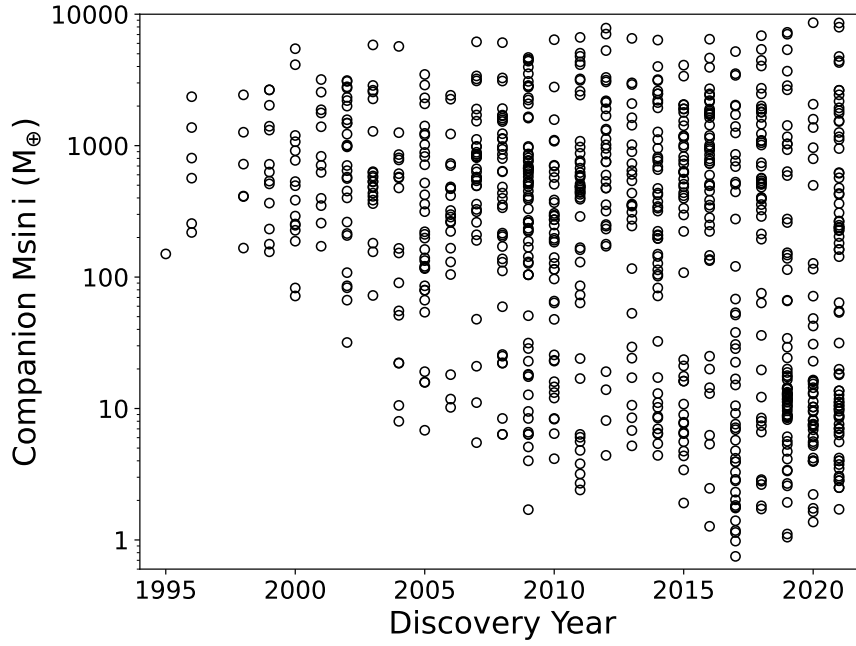


Figure 1.9: Minimum mass of exoplanets and brown dwarfs plotted by year discovered for radial velocity discoveries. Data accessed from NASA Exoplanet Archive on 2022 February 01.

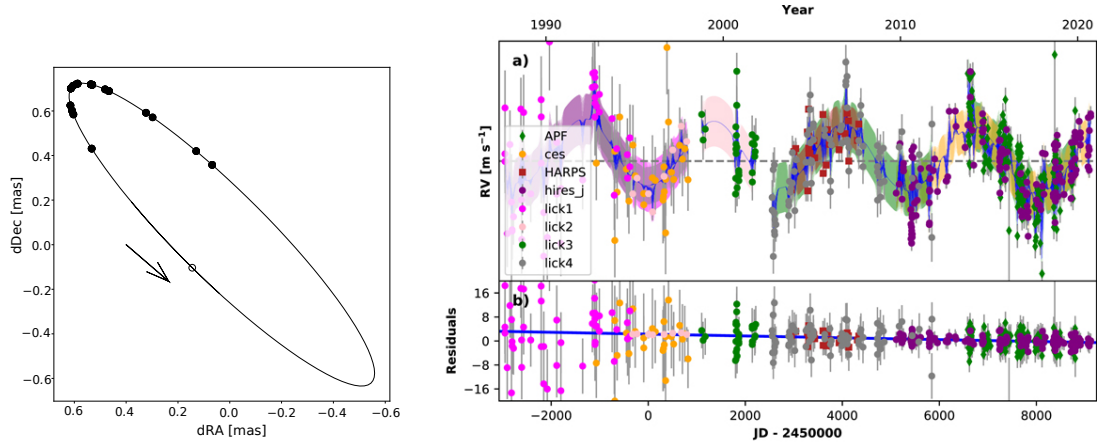


Figure 1.10: Astrometric (left) and radial-velocity (right) orbits of ϵ Eridani b. In the left panel, the filled circles are from Hipparcos measurements and the open circle is the *Gaia* DR2 measurement. The combination of these two datasets can be used to constrain the true mass of the planet without the need for transits. The plots are from Llop-Sayson et al. (2021).

orbital inclinations of non-transiting planets detected through radial velocity measurements. The combination of astrometry and radial velocity datasets provide strong constraints on the orbital inclination of a perturbing exoplanet, which enables the mass of the exoplanet to be robustly determined (e.g. Gliese 876 b (Benedict et al., 2002) and ϵ Eridani b (Benedict et al., 2006; Llop-Sayson et al., 2021) and see Figure 1.10).

1.2.4 Microlensing

The microlensing method exploits the result of general relativity that massive bodies bend light around them (Einstein, 1936). A single massive body passing in front of a distant source can amplify the intensity of the light from this source that is received by an observer (Schneider et al., 1992). If the lens is a planet hosting star, then the planet can cause there to be a second lensing peak in the brightness of the source (e.g. Figure 1.11 and Paczynski, 1996). Bond et al. (2004) reported the first microlensing exoplanet discovery, and to date 124 planets have been detected using this method, including multi-planet systems (e.g. Gaudi et al., 2008).

1.2.5 Direct Imaging

The methods discussed so far all rely on revealing the presence of a planet through the effect it has on other celestial bodies, including its host star or other planets in the same system. However, it is possible, under certain conditions, to directly detect the light from an exoplanet (e.g. Lagrange, 2014). To do this, a large angular separation between planet and host star is preferable to ensure the light from the host star does not engulf the light from the planet. This results in direct imaging being sensitive to planets on very wide orbits around nearby stars. A coronagraph is often used to block out as much of the stellar light as possible. It is also preferable that the exoplanet is hot enough to be sufficiently luminous. This makes direct imaging more sensitive to young planets which have not had time yet to cool. The first exoplanet to be discovered through direct imaging was a giant planet orbiting the brown dwarf 2MASSWJ 1207334-393254 in the TW Hydrae association (Chauvin et al., 2004) and since then a total of 55 planets have been discovered through direct imaging, including the four-planet HR 8799 system (Figure 1.12; Marois et al., 2008, 2010). This small number of directly imaged planets is primarily a result of the low occurrence rates of the giant planets on wide orbits (> 10 au) to which direct imaging is sensitive (e.g. Bowler, 2016).

As well as imaging exoplanets directly themselves, images of protoplanetary disks can be used to reveal the presence of young and forming exoplanets. Imaging of protoplanetary disks has revealed a wide range of features of these disks, such as rings and gaps (e.g. Andrews et al., 2018, and Figure 1.13). It has been suggested that these gaps are likely due to planets

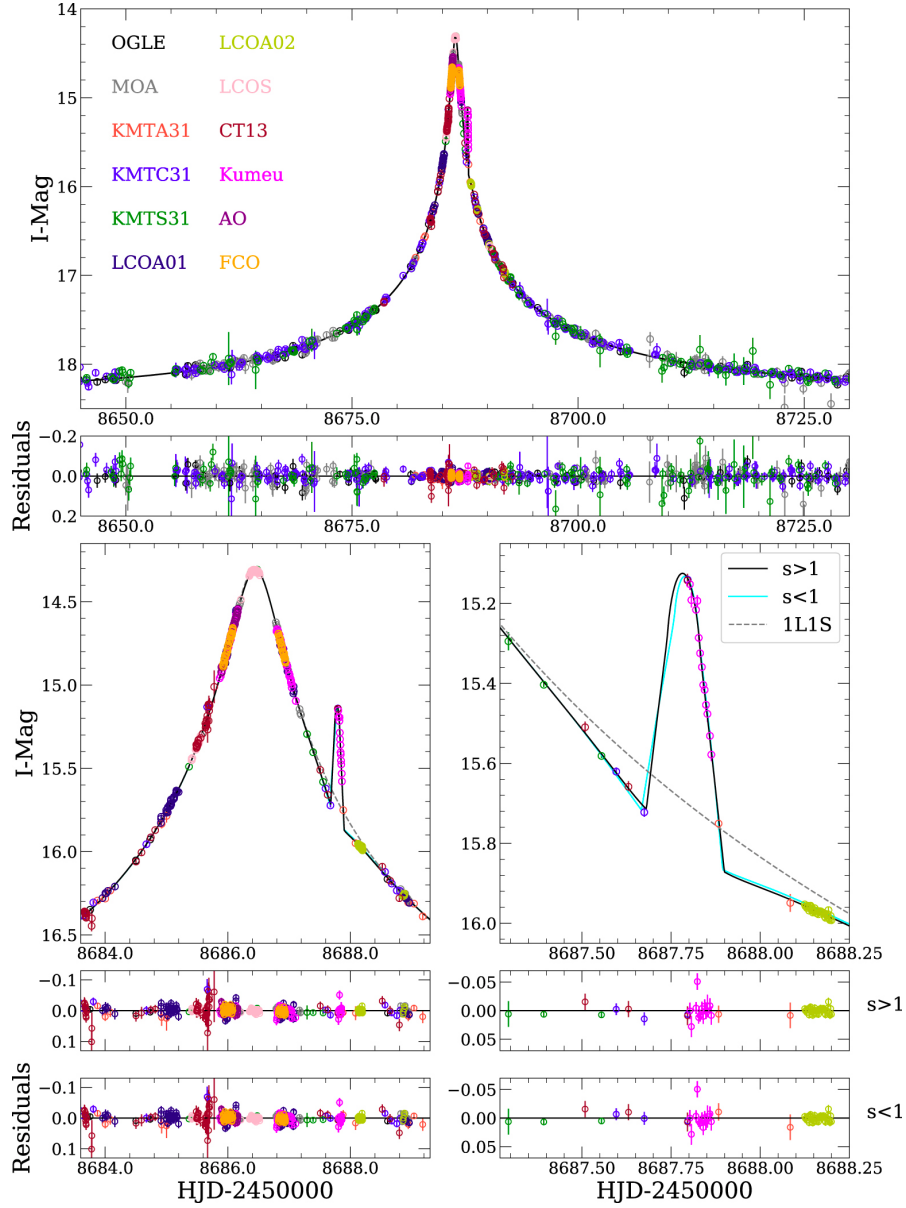


Figure 1.11: Microlensing detection of the planet OGLE-2019-BLG-0960 Lb. The main brightness spike shown in the top panel is the amplification of the distant source due to the passing host star, and the secondary spike seen in the bottom panels is due to the planet. Plot from Yee et al. (2021).

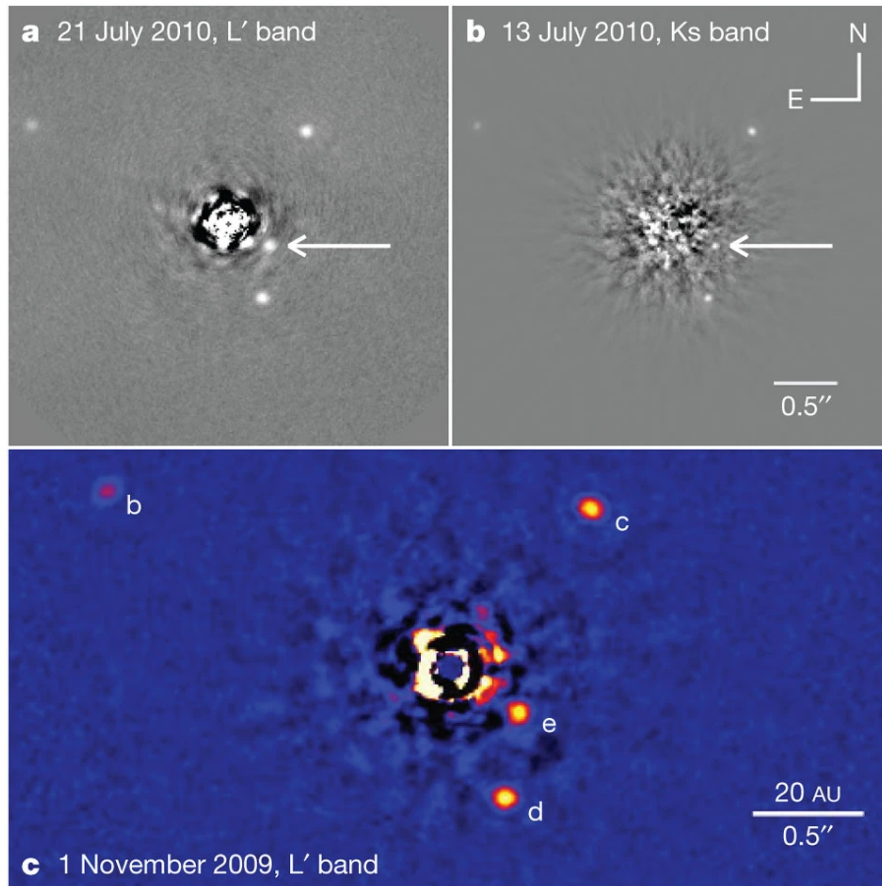


Figure 1.12: Direct images of the four planets in the HR 8799 planetary system. Plot from Marois et al. (2010). The planets b, c, d, and e are labelled on the bottom panel.

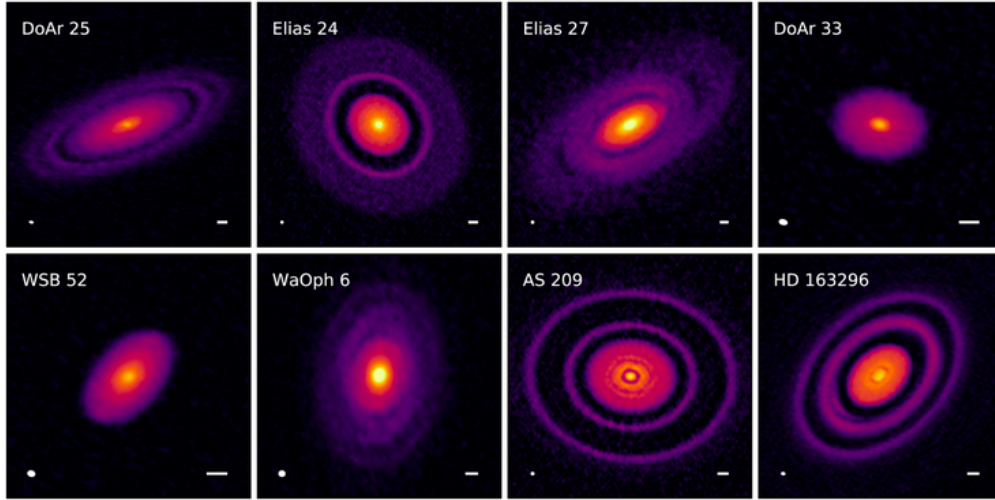


Figure 1.13: Examples of protoplanetary disks with gaps, arms, and other structures from the DSHARP survey. The data for this survey were obtained using the Atacama Large Millimeter Array (ALMA) and the plot is from Andrews et al. (2018).

forming in the disk (Dipierro et al., 2015), however the exact cause of the gaps, or even the relation between the gap and planet parameters remains unclear. To date, there have been a few promising detections of young planets embedded with disks, which have been corroborated by independent observations. Additional gas and dust kinematic measurements have been able to confirm the presence of a giant planet residing in the gap in the disk around the star HD 97048 (Pinte et al., 2019). Two planets interior to the disk around the star PDS 70 have been also been confirmed through direct imaging observations (Keppler et al., 2018; Haffert et al., 2019).

1.3 Transit Surveys

Due to the requirement that the orbital inclination be very close to edge-on for transits to occur, a given exoplanet has a fairly low probability to transit its host star. These probabilities range from $\approx 25\%$ for a $1 R_J$ planet in a 1 d orbit, to $\approx 5\%$ for a 10 d orbit. Combining these geometric probabilities with the estimated occurrence for planets at these short periods, which range from 0.015% for planets in 1 d orbits to 0.18% for planets in a 10 d orbit (Fressin et al., 2013), results in a very small probability that a given star will host an observable transiting planet. These probabilities are always under 0.02% for hot Jupiters, and often $< 0.01\%$.

Therefore, in order to discover a transiting exoplanet, roughly 10,000–20,000 stars need to be monitored per detection. In order to yield a good number of exoplanet detections, hundreds of thousands, and even millions of stars must be observed. These huge numbers can be achieved

through wide-field transit surveys. Transit surveys are designed to monitor hundreds of thousands of stars over a timescale of multiple months each. In this section I will briefly detail a few key historic transit surveys.

1.3.1 WASP

The Wide Angle Search for Planets (WASP; Pollacco et al., 2006) was one of the first large scale transiting exoplanet survey missions and achieved first light in 2003. It consisted of two observatories, one at La Roque de los Muchachos Observatory in La Palma which surveyed the Northern hemisphere, and the other at the South African Astronomical Observatory (SAAO) which surveyed the south. With eight cameras at each site, the full WASP mission had an instantaneous field-of-view of 482 square-degrees. The WASP mission primarily discovered Jupiter sized exoplanets orbiting solar-like main sequence stars, and was capable of detecting transiting exoplanets with transit depths as low as 0.4 % (e.g. WASP-150 b Cooke et al., 2020).

WASP targeted bright stars with magnitudes in the range $9 \leq V \leq 13$ mag, detecting exoplanets that are amenable to both radial velocity mass measurement as well as further follow-up observations, including measurement spin-orbit misalignment through the Rossiter-McLaughlin effect (e.g. Rubenzahl et al., 2021) or atmospheric characterisation through transmission spectroscopy (e.g. Wilson et al., 2020). To date WASP has discovered 176 transiting exoplanets. Five of these planets have giant planet companions on wide orbits which have been revealed by radial velocity monitoring. These wide orbit giant planets are: WASP-8 c (Knutson et al., 2014), WASP-41 c and WASP-47 c (Neveu-VanMalle et al., 2016), WASP-107 c (Piaulet et al., 2021), and WASP-148 c (Hébrard et al., 2020). In the WASP-47 system two additional transiting planets were discovered by the K2 mission (Becker et al., 2015, and see Chapter 5 for a further study of the masses of these planets). The presence of outer companions to the planets WASP-18 b and WASP-126 b has also been claimed from the reported presence of transit timing variations seen in the *TESS* data for these two planets (Pearson, 2019).

1.3.2 HATNet

The Hungarian-made Automated Telescope Network (HATNet; Bakos et al., 2004; Bakos, 2018) was another wide-field transit survey which also saw first light in 2003. HATNet consisted of seven 11 cm telescopes, with five at the Fred Lawrence Whipple Observatory in Arizona, USA and two at the Mauna Kea Observatory in Hawaii, USA.

HATNet targeted stars in a similar magnitude range to the WASP mission, yielding the detection of Jupiter-sized planets orbiting host stars with magnitudes $9 \leq V \leq 14$ mag. In total, HATNet has discovered 67 transiting exoplanets at the time of writing. In four of these systems,

an additional giant planet on a wide orbit has been discovered through long term radial velocity monitoring. These giant planets are: HAT-P-11 c (Yee et al., 2018), HAT-P-13 c (Winn et al., 2010), HAT-P-17 c (Fulton et al., 2013), and HAT-P-44 c (Sarkis et al., 2018).

1.3.3 HATSouth

The Hungarian-made Automated Telescope Network-South (HATSouth; Bakos et al., 2013) consists of six telescope systems across three countries in the southern hemisphere: Chile, Namibia, and Australia. There are two stations at each location, each consisting of four 18 cm optical telescopes. HATSouth saw first light in 2009.

The exoplanets discovered by HATSouth are again all giant planets, with HATSouth targeting slightly fainter stars than HATNet or WASP, yielding primarily discoveries around $12 \leq V \leq 14$ mag stars. However, HATSouth also targeted M-dwarf stars, discovering four giant planets orbiting stars with $T_{\text{eff}} \leq 4000$ K – HATS-6 b (Hartman et al., 2015), HATS-71 b (Bakos et al., 2020), HATS-74 A b and HATS-75 b (Jordán et al., 2022).

1.3.4 Kepler

The primary aim of the *Kepler* mission, which was launched in March 2009, was to determine the occurrence rate of Earth-sized planets that orbit Sun-like stars in the habitable zone (Borucki et al., 2010). To achieve this, the *Kepler* space telescope was designed in such a way as to ensure that the precision achieved was sufficient for the detection of a $1 R_{\oplus}$ planet transiting a $1 R_{\odot}$ star ($\delta = 84$ ppm). The telescope also observed the same patch of the sky constantly across the 4 year mission duration. Using this precision-focused design and observing strategy, *Kepler* was capable of detecting almost every exoplanet transiting the approximately 150,000 target stars it observed (out of a total of roughly 500,000 in the field-of-view; Batalha et al. 2010) with an orbital period of 1 year or less (a minimum of three transits were required for a confident detection).

The *Kepler* space telescope yielded the detection of 2,709 exoplanets. However, due to the faintness of the host stars and the low masses of the exoplanets, a large majority of these host stars are not within reach of current radial velocity spectrographs. In fact only 276 of these detections have had either a mass measurement or an upper limit placed on the mass. The remaining detections have been validated as high probability planet candidates (see e.g. Morton et al., 2016). Using these statistical validation methods, the *Kepler* results have been used to derive robust occurrence rates for exoplanets of all sizes orbiting Sun-like (FGK-spectral type) stars (e.g. Fressin et al., 2013; Hsu et al., 2019).



Figure 1.14: The NGTS telescopes in the enclosure at Paranal. Ten of the twelve can be seen, with the other two located behind the camera. This photo was taken by Dan Bayliss, and obtained through private communication.

1.3.5 K2

Following the failure of two of the reaction wheels on the *Kepler* satellite, the telescope could no longer operate under the initial observing strategy. It was thus re-purposed into the K2 mission (Howell et al., 2014). The new observing strategy was to monitor stars along the ecliptic plane, observing each field for roughly 80 d at a time. The target selection was also updated for the K2 mission. K2 focused on observing host stars which would result in exoplanet detections amenable to further follow-up observations. These included stars of lower masses and brighter magnitudes than the *Kepler* targets, allowing for the discovery and mass measurement of small, rocky planets. A further 477 exoplanets were discovered by the K2 mission, of which 89 have had at least an upper limit placed on their mass.

1.4 The Next Generation Transit Survey (NGTS)

The first generation of ground-based transit surveys, such as WASP and HATSouth, were limited to discovering mainly hot Jupiter planets. The Next Generation Transit Survey (NGTS; Wheatley et al., 2018) was designed to build upon the successes of earlier missions to achieve greater precision from the ground than before, thereby pushing the capabilities to the detection of smaller exoplanets. In this section I will introduce the NGTS facility and observing strategies. I will also use NGTS as an example to present and detail the methodologies behind performing an exoplanet transit survey.

1.4.1 The NGTS Facility

The NGTS facility consists of twelve independently operated robotic telescopes, each with 20 cm diameter apertures and a total instantaneous field-of-view of 96 square-degrees situated at the ESO Paranal Observatory in Chile (see Figure 1.14). The design of the telescopes, combined with the excellent observing conditions at Paranal allow NGTS to achieve 0.1% precision over a 1 hour timescale for stars with magnitudes $I \leq 13$ mag.

The NGTS telescopes are fitted with a custom filter, observing in the 520–890 nm wavelength range. This observing bandpass increases the precision achieved for red stars, making NGTS sensitive to the detection of Neptune-sized exoplanets orbiting Sun-like stars and super-Earth sized exoplanets orbiting M-dwarf stars. The 890 nm limit at the red end was selected to avoid the strong water absorption bands at 900 nm. Observing at these wavelengths would result in highly varying levels of atmospheric extension due to varying atmospheric water vapour concentration levels. The telescope tubes themselves are made using carbon fibre as this material does not undergo significant contraction or expansion with temperature fluctuations. The focus of the NGTS telescopes is therefore resistant to temperature changes and stable throughout the night, thereby helping to avoid large correlated noise trends due to changes in the point-spread-function (PSF) of the stars during the night. The CCDs (Charge Coupled Devices) used by the NGTS cameras are deep depleted and back-illuminated, providing excellent sensitivity and efficiency for red optical wavelengths. These red-sensitive CCDs further improve the photometric precision achieved for red stars.

1.4.2 NGTS Operations

The primary science goal of NGTS was to perform a transit survey of the southern sky, with the aim of detecting super-Earth and Neptune sized exoplanets. Each telescope has a field-of-view of 8 square-degrees. During NGTS survey operations, the survey fields were selected and allocated such that in general each telescope observed two fields per night. The result of this was that 192 square-degrees of the sky was monitored for exoplanet transits on a given night. An example NGTS survey image is shown in Figure 1.15. Across a full NGTS observing season, a survey field would receive around 500 hours of observations across a baseline of 250 d.

The NGTS survey field selection was performed against various criteria, including the density of stars and fraction of dwarf stars in the field, and the presence of any particularly bright objects. These criteria maximised the number of stars in the field suitable for exoplanet transit searches. The NGTS survey fields tended to lie at separations of greater than 20° from the Galactic plane. The high density of stars close to the Galactic plane complicates transit searches as stars are often blended with other stars in the image. The NGTS pixel scale is $4.97''/\text{pix}$. Fields



Figure 1.15: Raw NGTS image taken on the night of 2018-02-05 of the survey field centred on $RA = 11^{\text{h}}46^{\text{m}}09^{\text{s}}$ and $Dec = -36^{\circ}33'45''$ from which NGTS-12 b was discovered.

close to the ecliptic plane are also more adversely affected by the presence of the Moon increasing the sky background level of the images, resulting in a lower photometric precision. Due to this, fields within 30° of the ecliptic were generally avoided by NGTS. These various considerations resulted in a general NGTS survey field containing $\leq 15,000$ stars with magnitudes $I \leq 16$ mag, of which $\geq 70\%$ are dwarf stars suitable for transiting planet detection.

A final piece of the puzzle for achieving the high precisions required by NGTS for the detection of small transiting exoplanets is the cutting-edge autoguiding software implemented. This autoguiding is performed using the DONUTS algorithm (McCormac et al., 2013). This algorithm uses a master reference image of the field to re-centre the field in real time during the night. The same reference image is used for every observation of a given field, resulting in exquisite sub-pixel level guiding across multiple nights. In an early test observation, the RMS offset between frames of a star was just 0.04 pixels across 11 nights. This excellent autoguiding improves the photometric precision by minimising the noise in the light curves due to sensitivity differences between neighbouring CCD pixels.

1.4.3 NGTS Data Reduction

The reduction of the NGTS survey images is performed using a custom-built pipeline. This pipeline consists of the following steps:

1. The target star catalogue for each field is generated.
2. Each image is calibrated using bias frames and flat fields.
3. An astrometric solution is obtained for each image.
4. Photometric measurements are performed for each star in the field catalogue.

I will now discuss each of these steps in more detail.

Stellar Catalogue Generation

Source detections are performed for each NGTS field to generate catalogues of stars from which to extract photometric measurements. This source extraction is performed using `IMCORE`, which is a component of the `CASUTOOLS` software package (Irwin et al., 2004). A stacked master image of each field is produced for this source extraction. Each master field image is also solved astrometrically. Generating custom stellar catalogues is particularly important for NGTS observations, as without this step there is a risk of placing apertures for high proper motion stars in the wrong locations on the image. These high proper motion stars are predominantly

M-dwarfs. These are a target of particular interest for NGTS, as they are optimal targets for the detection of small exoplanets.

The NGTS source catalogues are limited to magnitudes $I < 16$ mag. Each source is then cross-matched with numerous all-sky catalogues. As well as matching on astrometric sky position, limits on colour are also imposed in order to avoid spuriously matching an NGTS source to the incorrect all-sky source.

Recent years saw the release of version 8 of the *TESS* Input Catalog (TIC; Stassun et al., 2019) which incorporates magnitude, colour, and parallax measurements from *Gaia* DR2 (Gaia Collaboration, 2018). Thanks to the TIC up-to-date positions and properties are available for ≈ 1.7 billion stars across the sky. Therefore, for the most recent NGTS data reduction pipeline run, this custom source catalogue generation was replaced in favour of a target selection driven by the parameters available from the TIC. This allowed for greater confidence that the target stars were dwarf stars amenable to transit searches, not evolved giant stars. It also allowed for targeted searches for specific classes of stars which are in general too faint for the usual source extraction, but still of great scientific interest, such as white dwarf stars.

Image Calibration

For photometric observations there are a number of calibration steps which are performed to improve the quality of the images and remove instrumental artifacts. There are three main calibrations which are often performed (Davenhall et al., 2001).

The first of these is to correct for the CCD bias. This bias is a constant electronic offset which is added to the CCD counts by the camera. This can be corrected using bias frames, which are zero-second exposures that reveal what the level of the bias is, and how it varies across the detector. The NGTS reduction pipeline does not use bias frames, but instead corrects for the bias using an overscan region. These are two strips on either side of the CCD which are not illuminated during observations, and so keep a real-time measurement of the CCD bias level. These strips are the two vertical black bars visible in Figure 1.15. The overscan value is subtracted from the pixel count values in each NGTS image.

The next effect that needs calibrating is the dark current, which arises thermally within the detector. The effect of the dark current on the image is estimated by taking exposures with the telescope shutter closed. These exposures are known as dark frames. NGTS obtains multiple bias frames for each camera, which are combined into a single master dark frame. This master dark is then used to correct each image taken with the corresponding camera.

The final main calibration performed is flat-fielding. This is where a uniformly illuminated region is observed with the telescope, often the twilight sky at dawn and dusk. These

flat-fields reveal imperfections variations in sensitivity from the telescope and detector. These include sensitivity differences between pixels and the presence of small amounts of dust on the CCD or telescope filter. As with the dark frames, multiple flat fields are obtained for each camera and combined into a master flat-field, which is then used for the image calibration.

Astrometry

Every NGTS science image is solved astrometrically in the World Coordinate System (WCS). This allows for precise photometric aperture placement for each star in the target catalogues. Despite the sub-pixel level autoguiding of the NGTS telescopes, provided by the DONUTS algorithm, this additional step is nevertheless required for optimal aperture placement and photometric results. Across a night, differential atmospheric refraction results in stretching of the field-of-view of a telescope at lower observing altitudes. This results in movement of stars in the outer regions of an NGTS image by ≈ 0.75 pixels between elevations of 30° and 90° during a night.

Photometry

The CASUTOOLS software is used again by the NGTS pipeline to perform the simple aperture photometry measurements. Photometric apertures with a radius of 3 pixels are used for every target star and are placed using the WCS astrometric solutions obtained for each image. The pixels in each image store the electron counts measured by the CCDs during each exposure, and the total count from the pixels within the aperture is recorded as the photometric measurement for each image. An interpolation is performed on a 64×64 pixel grid surrounding each star to determine the sky background level at the position of each star.

1.4.4 Light curve analysis and transit search

In order to prepare the photometric light curves for the planet search, systematic signals in the data must be identified and removed. This is performed for NGTS light curves using a number of detrending algorithms. The first is an implementation of the SysREM algorithm (Tamuz et al., 2005), which identifies and removes any signal which is common to multiple stars. The SysREM algorithm is sensitive to removing signals even in the case where the amplitude varies for different stars, but the periodicity and phase are shared.

There are some further signals which remain in the light curves that are not fully removed by SysREM. These can be either additional systematics or real stellar variability signals. While the latter of these two signal types is not necessarily noise, such variability does make the detection of transiting exoplanets much more difficult. The additional systematic signals often correlate with the Moon phase and arise from an imperfect sky background subtraction coupled

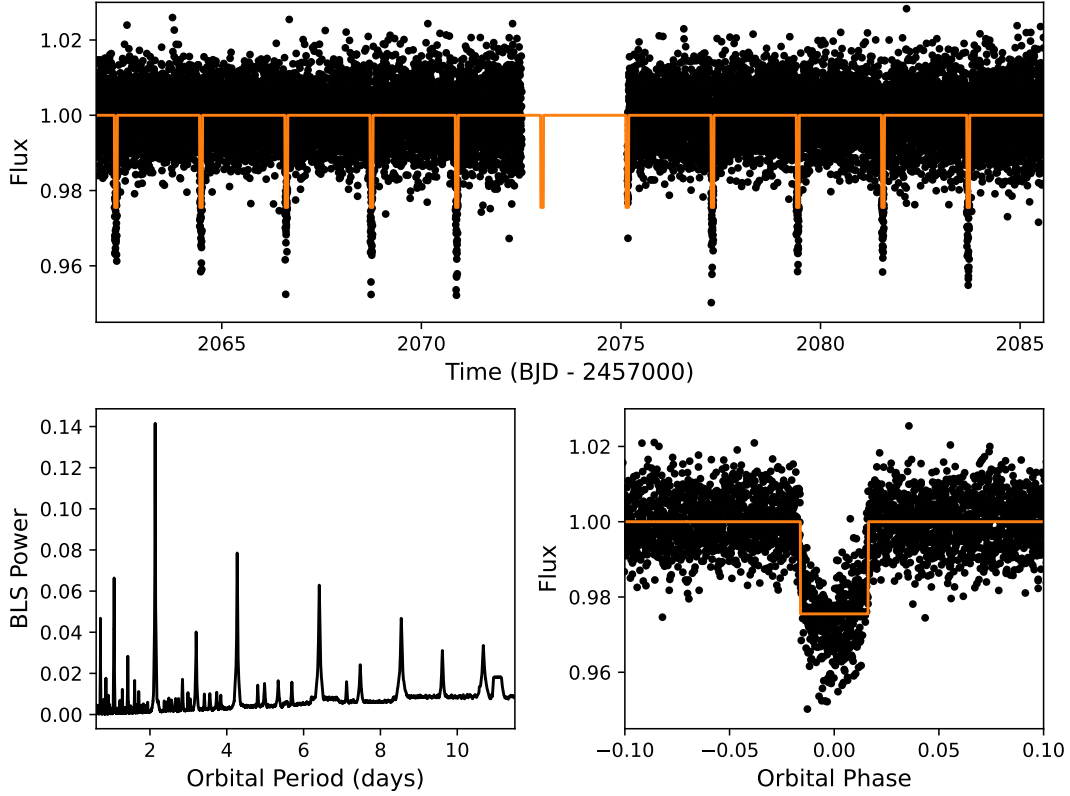


Figure 1.16: An example of the Box-fitting Least Squares (BLS) detection of a transiting planet orbiting the star TIC-382602147. **Top:** The *TESS* sector 28 light curve for this object with the best BLS model shown in orange. **Bottom Left:** The BLS periodogram for this light curve, clearly displaying the most likely orbital period at 2.135 d. **Bottom Right:** The light curve and model phase-folded on the best period and zoomed around the transit event. The box shape of the model is clearly demonstrated.

with the sky background level varying with the phase of the Moon. After identifying these additional signals, they are analysed to determine whether a sinusoidal or transit-like shape is a better explanation of the periodic variability. If the signal is determined to be non-transit-like, a floating mean - in phase - is used to remove the signal from the data.

The detrended light curves are then searched for periodic transit-like signals. This search is performed using the Box-fitting Least Squares algorithm (BLS; Kovács et al., 2002), which is a common choice of algorithm for transiting planet searches. The BLS algorithm fits a periodic box-shaped transit signal to the light curve, and trials different box widths and depths across a range of periods. At each trial period, the merit-of-fit value for the best fitting box shape is recorded, and used to construct a periodogram. Significant peaks in these periodograms point

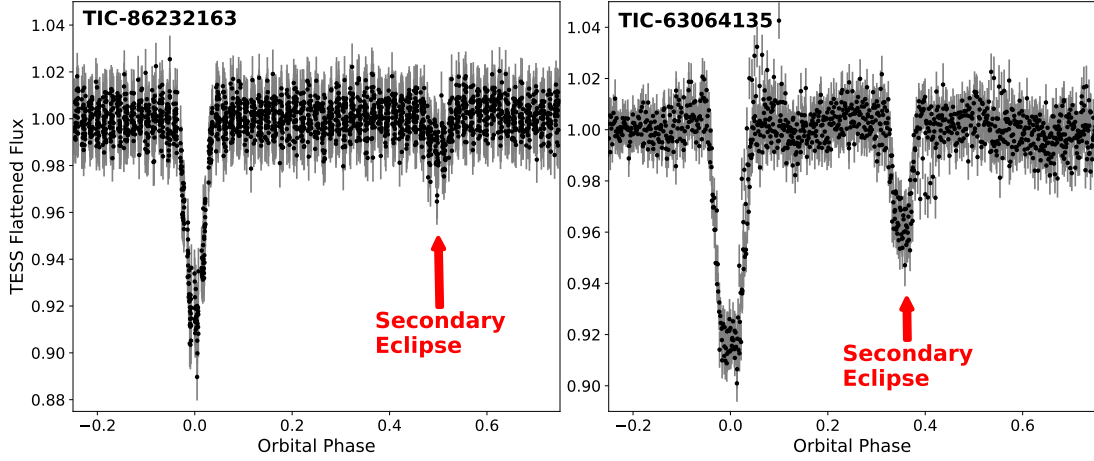


Figure 1.17: Two examples of transit search false positives identified as eclipsing binaries through the presence of a secondary eclipse.

towards the presence of transiting planets at these orbital periods. Figure 1.16 demonstrates the BLS model and periodogram for the star TIC-382602147.

1.4.5 False Positives and Exoplanet Confirmation

The BLS algorithm is very successful at recovering transiting planets. However it is equally successful at finding a wide array of astrophysical false positives. These false positive scenarios must be ruled out for a transit candidate to be confirmed. To do this, we must first understand what false positives are possible and how they can be identified from transit survey light curves and additional follow-up observations.

One of the main astrophysical false positives which contaminates transit planet searches are eclipsing binary star systems (Almenara et al., 2009; Santerne et al., 2012). These eclipsing binaries are systems consisting of two stars which are orbiting and eclipsing each other, resulting in eclipse signals which can mimic exoplanet transit light curves. Fortunately, there are a few ways to identify these eclipsing binaries.

The first of these is the presence of a secondary eclipse in the light curve. For an eclipsing binary system consisting of two stars of different sizes and brightness, the two sets of eclipses will be of different depths (see Figure 1.17). If the two stars in the binary are similar enough in size then the primary and secondary eclipses will be of similar depths. In these cases, if the secondary eclipse occurs at phase 0.5, then the BLS algorithm can obtain half the true period as its result, placing both eclipses at phase 0. This results in what is known as an odd-even depth difference, as the primary eclipses occur at the even epochs (0, 2, 4, ...) and the secondary

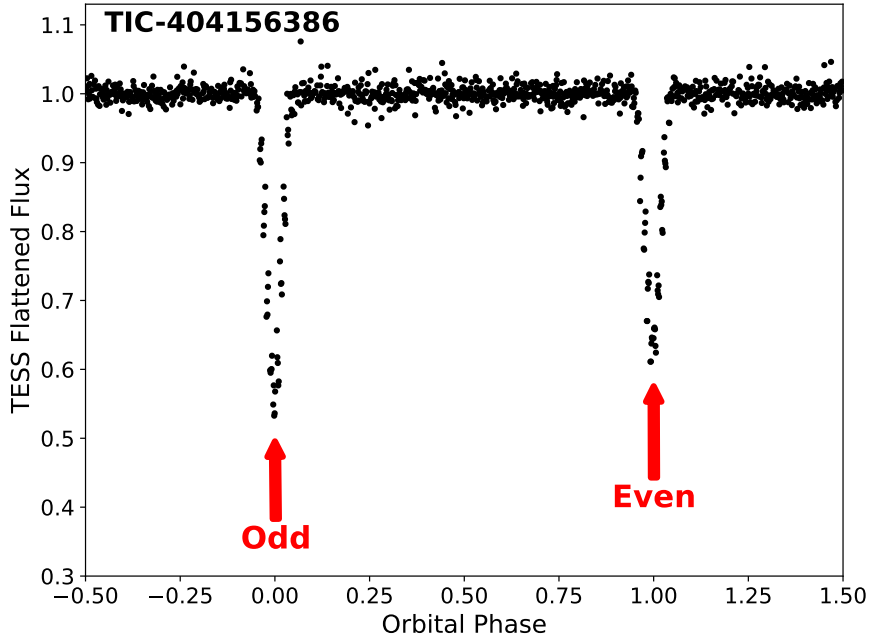


Figure 1.18: Example of an object identified as an eclipsing binary through the presence of an odd-even depth difference.

eclipses, which are a different depth, occur at the odd epochs (1, 3, 5, ...). Comparing the depth of the odd eclipses with that of the even eclipses can reveal these eclipsing binary false positives. See Figure 1.18 for an example. Tidal interactions between a close orbiting binary star pair can lead to the stars becoming ellipsoidal. This distortion of the stars results in the apparent brightness of the system being at a maximum midway between eclipses, and minimum around the times of eclipse, resulting in a variability signal in phase with the eclipses. Identifying the presence of this phased variability enables the identification of false positives.

These signs that the BLS detection is not a planet but instead an eclipsing binary can be readily identified through manual human inspection of the light curves. A further cause of false positives are variable stars. These stars can result in BLS detections despite exhibiting neither transits nor eclipses, but are fairly simple to identify through human inspection of the light curves.

While human vetting has been the most widely used method of identifying false positives from the light curves, in recent years, machine learning algorithms have been employed to replace it (e.g. Armstrong et al., 2021). These improve upon human vetting in speed and efficiency and are especially useful for vetting shallow transit signals and determining whether they are likely to be real or spurious. These shallow signals, which often are low signal-to-noise, are those

produced by the super-Earth and Neptune planets for which NGTS hunts. Recently, a machine vetting method that utilises a convolutional neural network was applied to NGTS data to aid the recovery of these shallow transits from small planets (Chaushev et al., 2019).

While a large number of false positives can be identified from the transit survey light curve alone, there are a few more which require further follow-up observations to identify. The first of these are background eclipsing binaries (BEBs). This is where a chance alignment occurs between a foreground target star and an eclipsing binary directly behind the target star along the same line of sight. The stellar eclipses from the BEB contaminate the target star light curve, mimicking transit events. While an exoplanet transit has the same approximately the same depth when viewed in different wavelength ranges, the eclipses of a BEB do not if the stars in the binary are sufficiently different in temperature to the foreground star (O'Donovan et al., 2006). Therefore, obtaining observations of the transit events in multiple different colours allows for the identification of background eclipsing binaries (e.g. Colón et al., 2012).

For a candidate transiting planet which does not exhibit any of the signs discussed above, the final step in the confirmation process is to measure the mass of the transiting companion. The most widely used method for this is radial velocity monitoring. This monitoring can also reveal the candidate to be a false positive, and so is often crucial for confirming the planetary nature of the companion. Eclipses of a larger star by a smaller and cooler star (such as an M-Dwarf) or indeed of any star by a brown dwarf, can mimic the transit light curve of a Jupiter-sized planet. Often the only way to conclusively identify these false positives is through radial velocity observations. These objects are significantly more massive than Jupiter-sized planets and so result in radial velocity variations with much larger semi-amplitudes (see Equation 1.8). Therefore, often just a small number of radial velocity observations are required to determine whether the mass of the companion is too high for the companion to be an exoplanet.

1.4.6 NGTS Survey Highlights

One of the main discoveries from the NGTS survey is NGTS-4b (West et al., 2019), a $3.18 \pm 0.26 R_{\oplus}$ exoplanet in a 1.34 d orbit. NGTS-4b has the lowest transit depth of any exoplanet discovered by a ground-based transit survey (Figure 1.19). This discovery highlighted the ability of NGTS to detect exoplanets which were undetectable by previous surveys. NGTS also discovered the giant planet NGTS-1b that is orbiting an M-dwarf star (Bayliss et al., 2018). Only a handful of such systems are currently known. These systems challenge current theories of planet formation (e.g. Laughlin et al., 2004) and through their discovery we can better understand how planets form. In total, NGTS has discovered 17 exoplanets and two transiting brown dwarfs, as well as a host of low-mass eclipsing binary systems. I present the discovery of one of these

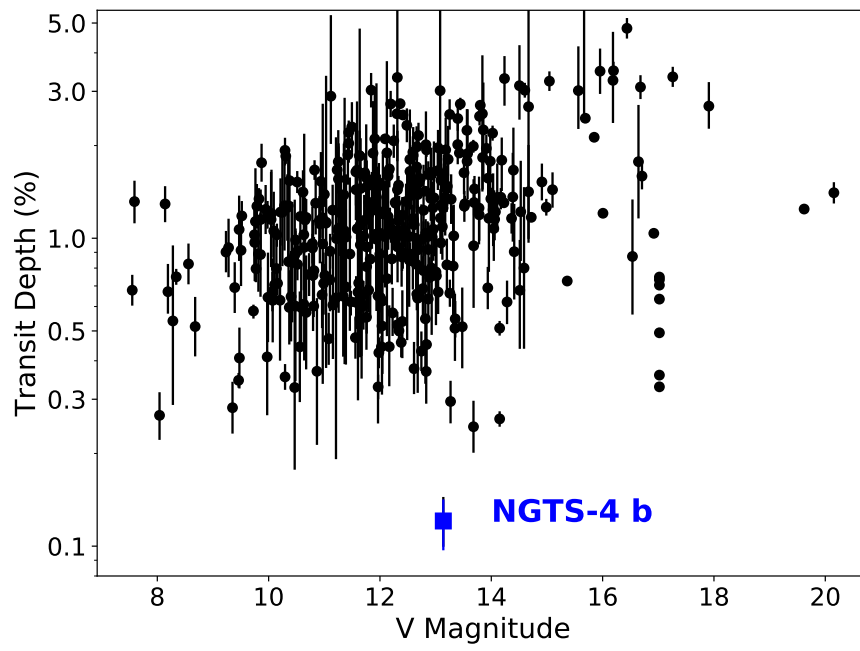


Figure 1.19: Transit depths of transiting exoplanets discovered by ground based transit surveys. Data from NASA Exoplanet Archive, accessed 2022 February 23. The blue square highlights NGTS-4 b (West et al., 2019).

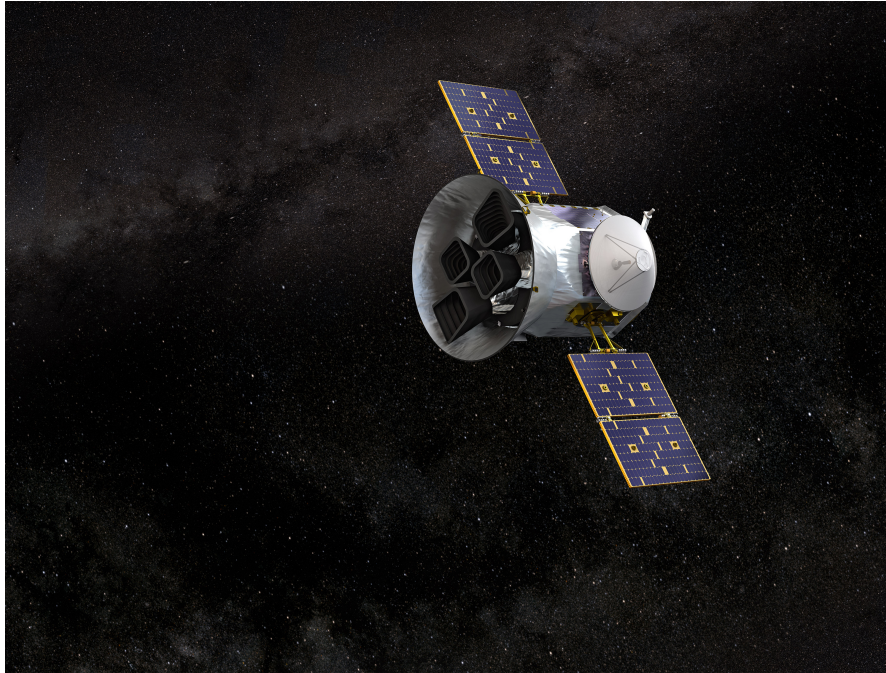


Figure 1.20: Artist illustration of NASA's Transiting Exoplanet Survey Satellite: *TESS*. Credits: NASA's Goddard Space Flight Center

exoplanets, NGTS-12 b, in Chapter 2.

1.5 Transiting Exoplanet Survey Satellite (*TESS*)

While the *Kepler* mission revealed that there is an abundance of planets with radii between that of Earth and Neptune in the Galaxy, most of the *Kepler* discoveries were around host stars which are too faint for radial velocity mass measurements of the planets. Therefore, while it was known that these planets exist, detailed information about their bulk densities and atmospheric compositions is unavailable for the majority of these planets. The NASA Transiting Exoplanet Survey Satellite (*TESS*; Ricker et al., 2015, and see Figure 1.20) mission was designed to allow these questions to be answered. *TESS* has been surveying the whole sky for transiting exoplanets since 2018.

The *TESS* satellite and observing strategy have been designed specifically for the detection of low-radius exoplanets ($R_p \leq 4.0 R_\oplus$) orbiting host stars which are bright enough for detailed study of the exoplanets, through both radial velocity mass measurement and atmospheric characterisation observations. The *TESS* facility consists of four 10 cm diameter telescopes. This aperture size was selected to ensure that the precision required for the detection of super-Earths

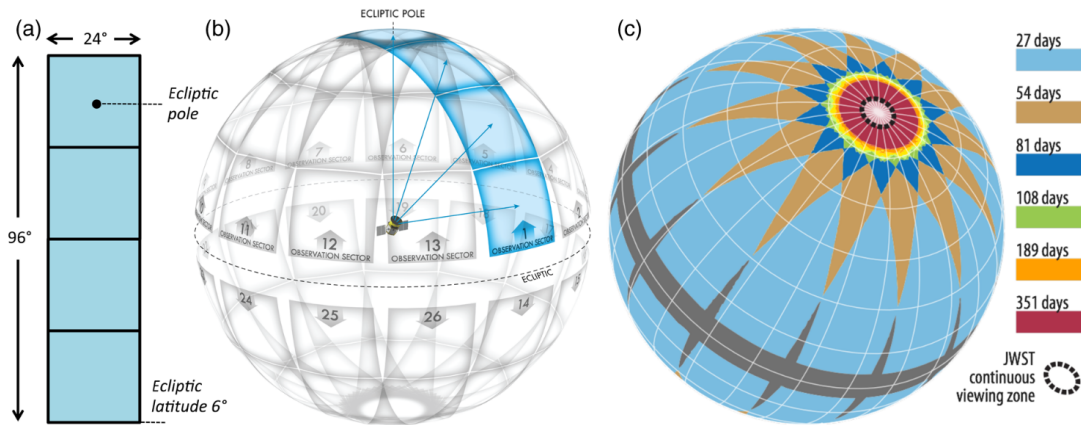


Figure 1.21: Plot demonstrating the instantaneous field-of-view of the *TESS* cameras and how the observing sectors map onto the sky. The observation durations shown on the right (panel c) are accurate for the primary mission. Plot from (Ricker et al., 2015).

was possible (Ricker et al., 2015). The observing bandpass of the *TESS* telescopes spans the wavelength range 600–1000 nm, representing a union of the more common R_C , I_C , and z bands. This enhanced sensitivity was selected to improve the precision obtained for cool, red stars. These stars are smaller than Solar-type stars, and so the small planets *TESS* is hunting are more easily detectable around them. To date² *TESS* observations have resulted in the discovery of 197 exoplanets, of which 124 have $R_P \leq 4.0 R_\oplus$.

TESS observes in sectors, in which a given set of four fields are observed for ≈ 27.4 d. Each of the four cameras has a $24^\circ \times 24^\circ$ field-of-view, resulting in an instantaneous field-of-view of the whole facility of 2304 square-degrees. These sectors are made up of two continuous observation orbits of ≈ 13.7 d with a gap in the observations between these two orbits during which the data are downloaded to Earth. The telescope then rotates its view to observe four new fields. In this observing strategy, near to a whole hemisphere on the sky is observed in 13 sectors, which corresponds to 26 orbits or just under one year. The *TESS* observing sector coverage is shown in Figure 1.21. In order to achieve this incredibly wide field-of-view, the *TESS* cameras have a large pixel scale of $21''/\text{pix}$. This is more than a factor of four larger than the NGTS pixel scale ($4.97''/\text{pix}$). A comparison of NGTS and *TESS* images is provided in Figure 1.22. This large pixel scale makes the *TESS* images particularly susceptible to blending from nearby stars. With the knowledge of all surrounding stars from *Gaia* DR2, the effect of these nearby stars to dilute transit events on the target star is corrected during the reduction pipeline. However, nearby eclipsing binary systems contaminating the target pixels and imprinting their signal into the target

²Data from NASA Exoplanet Archive, accessed 2022 February 23

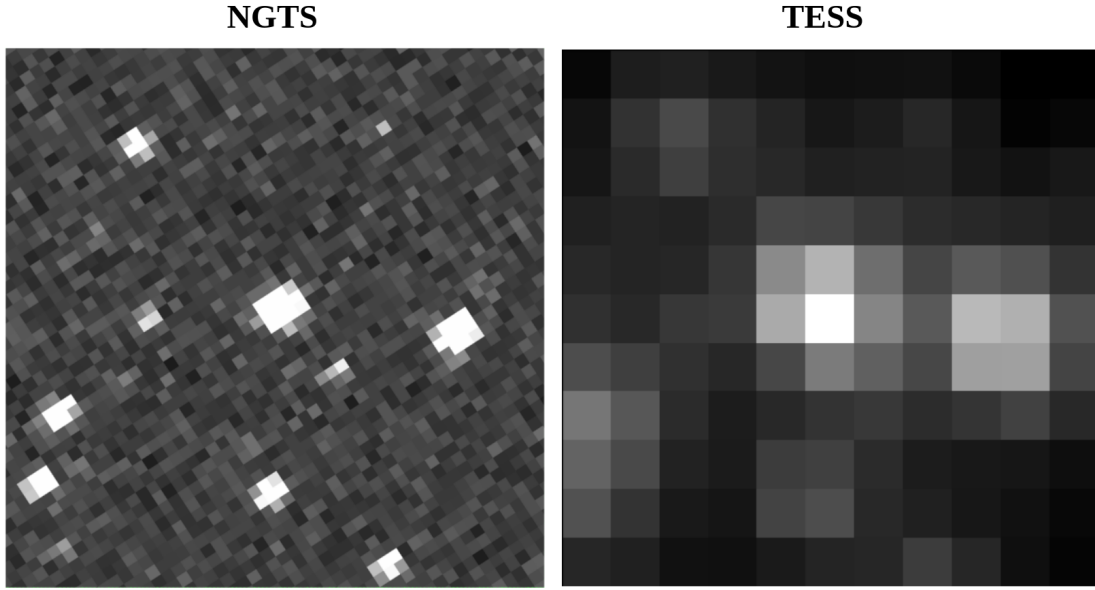


Figure 1.22: A comparison of the NGTS and *TESS* images nearby NGTS-12 b. These two images cover the same 231×231 arcsecond area of the sky. The difference in the pixel scales of the two instruments can be clearly seen – *TESS* = $21''/\text{pixel}$; NGTS = $4.97''/\text{pixel}$.

star light curve cannot be so easily corrected. To account for this, follow-up photometry from ground-based facilities with much finer pixel scales is vital for confirming the candidate transit events as occurring on target or identifying them as nearby eclipsing binaries.

The choice of sector length was partially driven by the desire to discover transiting planets with orbital periods up to 10 d. However, this means that *TESS* is not sensitive to planets orbiting in the habitable zones around Sun-like stars. Some overlap between subsequent sectors does exist, especially around the ecliptic poles, and this results in a subset of stars being monitored for significantly longer than the nominal ≈ 27.4 d. The habitable zones around low-mass stars (e.g., M-dwarfs) are much closer to the star (Kasting et al., 1993). As an example, a planet orbiting around an M0 star ($T_{\text{eff}} = 3800$ K) with a period in the range 25–75 d will receive a bolometric insolation within a factor of two of that received by Earth. Therefore, *TESS* is sensitive to the discovery of planets orbiting in the habitable zones around M-dwarf stars close to the ecliptic poles (e.g. TOI-700 d; Gilbert et al., 2020; Rodriguez et al., 2020). The ecliptic poles were chosen as the regions of longest continuous observation as they are also the regions which have the most continuous observability with the recently launched James Webb Space Telescope (*JWST*).

During each *TESS* observing sector $\approx 20,000$ stars are observed at 2 minute cadence.

These high cadence targets are selected using the priority metric (Kunimoto et al., 2022)

$$\frac{\sqrt{N_S}}{\sigma_{1\text{ hr}} R_*^{3/2}}, \quad (1.9)$$

where N_S is the number of sectors in which a star is observed, $\sigma_{1\text{ hr}}$ is the expected noise on a 1 hour timescale and R_* is the stellar radius. This metric prioritises stars amenable to the detection of small planets, providing the main dataset for achieving the primary science goals of the *TESS* mission. The data reduction and light curve production for these 2 minute cadence light curves is performed by the *TESS* Science Processing Operations Centre (SPOC; Jenkins et al., 2016). Additionally to these 2 minute cadence observations, the *TESS* Full-Frame-Images (FFIs) for each CCD and camera are downloaded. The cadence of these FFI observations was 30 minutes in the primary mission (Year 1 and 2), increasing to 10 minutes in the extended mission. Multiple ensemble sets of light curves have been produced from these FFIs using well-tested pipelines (e.g., *TESS*-SPOC (Caldwell et al., 2020); QLP (Huang et al., 2020a)) providing the community with access to high quality, high precision light curves of stars across the whole sky. These all-sky light curve sets enable the undertaking of exoplanet population studies, from which we can better understand planet formation and evolution. I present one search study and the preliminary results from it in Chapter 6.

The primary aim of *TESS* is to discover small exoplanets amenable to follow-up, however the *TESS* telescope cannot perform this follow-up itself. A global network has been set up in order to achieve the necessary follow-up observations for these targets. This network is the *TESS* Follow-up Observing Program (TFOP; Collins et al., 2018a). TFOP is split into five separate Sub Groups (SGs), each dedicated to a separate class of follow-up. SG1 provides ground-based photometry to confirm *TESS* transit candidates and confirm the transit signal as occurring on the target or to identify a nearby star as being the true host. This is of particular importance for *TESS* due to the large pixel scale resulting in substantial blending in the *TESS* images. SG2 obtains reconnaissance spectroscopy to identify clear binary star systems and SG3 obtains high-resolution imaging to identify nearby blended sources. These first three groups in general aim to identify which candidates are likely transiting planets and which are false positives. The final two then further characterise the candidates which pass the first three groups. SG4 is the group dedicated to obtaining the precision radial-velocity monitoring required to confirm the planetary nature of the candidates and measure their masses. Finally, SG5 obtains space-based photometry to improve the orbital ephemerides and radii of the planets and to search for and monitor TTVs.

1.6 NGTS in the Era of *TESS*

With the *TESS* mission now dominating the field of transiting exoplanet discovery across the whole sky, in recent years the observing strategy of NGTS has pivoted away from the primary transit survey to focus on three new main science goals. These new science programs provide synergy with the *TESS* mission, as well as targeting particular exoplanets out of the reach of *TESS*.

The first of these focuses on the detection of long-period exoplanets. The targets for this program come from the *TESS* space telescope and are objects which only transit once or twice in the *TESS* observations (see e.g. Cooke et al., 2018, 2019). The single transit long-period planet candidates are then monitored continuously with NGTS in order to detect more transits and determine the orbital periods. Through these observations, this program has yielded the discovery of the 35.46 d period planet NGTS-11 b (Gill et al., 2020b), as well as a number of longer period low-mass eclipsing binary systems (e.g. Gill et al., 2020a). Planets displaying two transits in the *TESS* data separated by a large gap in observations can have a true period at any discrete divisor of the total time between the two transits. These period “aliases” are then targeted with NGTS in an attempt to recover the true orbital period (Cooke et al., 2021).

The second of these programs centres around the study of young stars (< 1 Gyr) often found in open stellar clusters. Stars in these regions of the sky are too tightly packed for reliable photometric observations with *TESS*. The large pixel scale of the *TESS* cameras results in extreme levels of blending and contamination for stars in stellar clusters. The young stars within these clusters are particularly interesting as through studying them we can learn about how planets evolve (e.g. Gillen et al., 2020). By discovering and studying young planets we can also learn about the mechanisms which govern how these planets and their orbits evolve, such as orbital migration and the loss of planetary atmospheres.

The final main program focuses on high precision follow-up photometric observations of bright ($V \lesssim 11$ mag) exoplanet host stars. The targets for this program are often candidates discovered from *TESS* data. These observations are often performed using a novel multi-telescope observing method (see Chapter 3; Bryant et al., 2020b). The aim of these observations is primarily the confirmation of exoplanet candidates, such as TOI-849 b (Armstrong et al., 2020) or TOI-201 b (Hobson et al., 2021). Further observations are carried out for the detection and monitoring of transit timing variations in multi-planet systems; see Kaye et al. (2022) or Chapter 4 for examples.

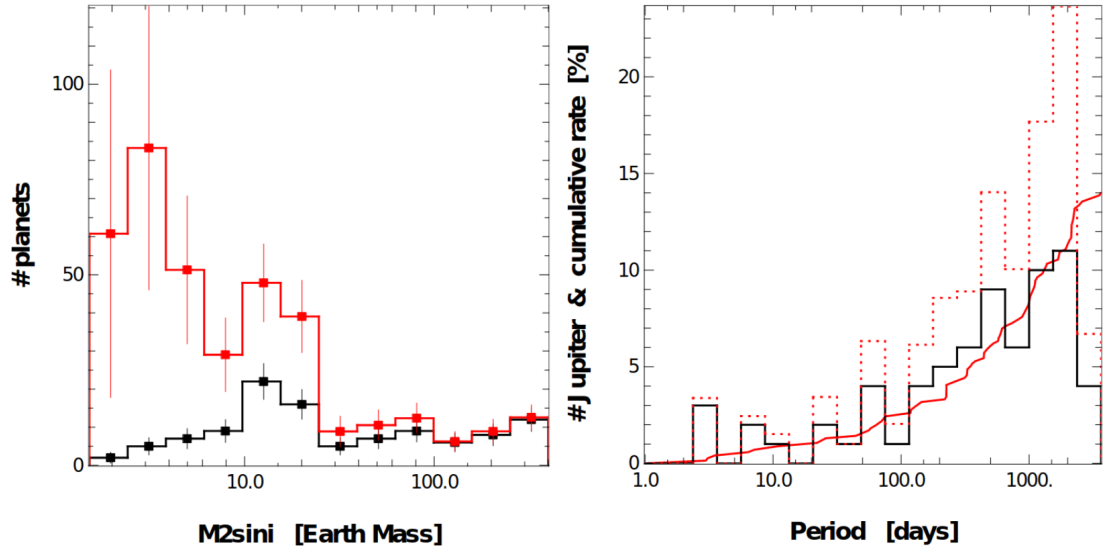


Figure 1.23: Planetary populations obtained from an 8 year survey with the HARPS spectrograph (Mayor et al., 2011). **Left:** This panel displays the number of planets of different masses detected by the HARPS survey. The black histogram shows the true number detected, and the red histogram includes a correction for the detection bias and limits of the survey. **Right:** This panel shows the number of planets with $M_P \sin i > 50 M_{\oplus}$ detected as a function of the planetary orbital period. Again, the black line gives the number of planets detected and the red includes the detection bias corrections. Both plots are from Mayor et al. (2011).

1.7 Exoplanet Occurrence Rates

1.7.1 Current Overview

As the known population of exoplanets grew, it became possible to use this population to begin to study features and characteristics of planets in the Galaxy. Through these population features, we are able to probe some of the implications for planetary formation and evolution to work out how these features are formed. A key aspect of the exoplanet population is the occurrence rate of exoplanets for different planetary and stellar sizes.

Our initial knowledge of the exoplanet populations came from radial velocity surveys during the early 21st century. One such survey was carried out across an eight year time frame using the HARPS spectrograph (Mayor et al., 2011), and a few key results are shown in Figure 1.23. This study found that giant planets are significantly less common than lower mass planets, with the exoplanet frequencies found decreasing drastically for $M_P \gtrsim 40 M_{\oplus}$. Focusing solely on giant planets, Mayor et al. (2011) found that these planets are more common on longer period orbits. A second study was carried out by Johnson et al. (2010) using results from

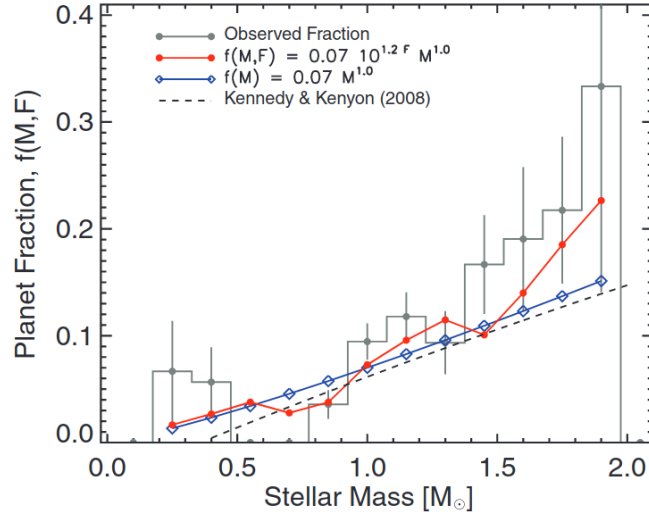


Figure 1.24: Occurrence rates for giant planets as a function of stellar mass, as derived from the results from the radial velocity California Planet Survey. The red and blue lines give trend fits to the derived occurrence rates and the dashed line gives a theoretical prediction. The plot is from Johnson et al. (2010).

the California Planet Survey. This study focused solely on the frequency of giant planets, and they found a monotonic increase in the planet occurrence rate with the stellar mass of the host (Figure 1.24).

Following the early results from radial velocity studies came the revolutionary *Kepler* telescope. With the primary aim of the *Kepler* mission (Borucki et al., 2010) being to study exoplanet populations, the mission yielded excellent results for giant planet occurrence rates. An early set of *Kepler* results was presented by Fressin et al. (2013), and can be seen in Figure 1.25. Fressin et al. (2013) found that across all spectral types the frequency of giant planets is $5.24 \pm 0.55\%$. That is, there are 0.0524 giant planets per star on average across the sky. As with the radial velocity results, the distribution of giant planets was found to not be constant with stellar mass. However, Fressin et al. (2013) did not find simply a monotonic increase as found by Johnson et al. (2010), but they found the distribution to peak at $6.1 \pm 0.9\%$ for G and K spectral type stars, falling to $4.3 \pm 1.0\%$ and $3.6 \pm 1.7\%$ for F and M spectral type stars respectively. In a more recent study, Hsu et al. (2019) combined the full *Kepler* DR25 dataset with stellar parameters from *Gaia* DR2 to improve upon these occurrence rates. Their results are summarised in Figure 1.26, and as with previous studies they find giant planets to be both less common than their lower mass counterparts and more common on wider orbits.

However, *Kepler* was unable to yield robust occurrence rates for giant planets orbiting

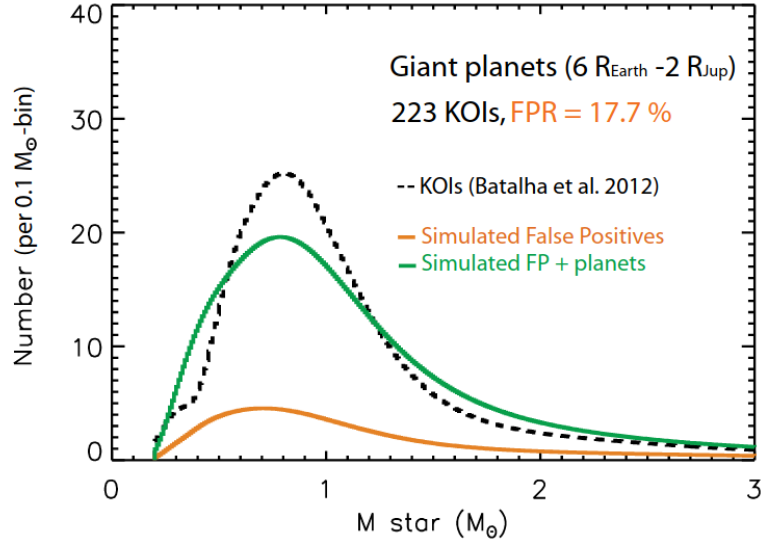


Figure 1.25: Occurrence rates for giant planets. The dashed line gives the real distribution of *Kepler* candidates and the green solid line represents the simulated populations of giant planets and false positives. The plot is from Fressin et al. (2013).

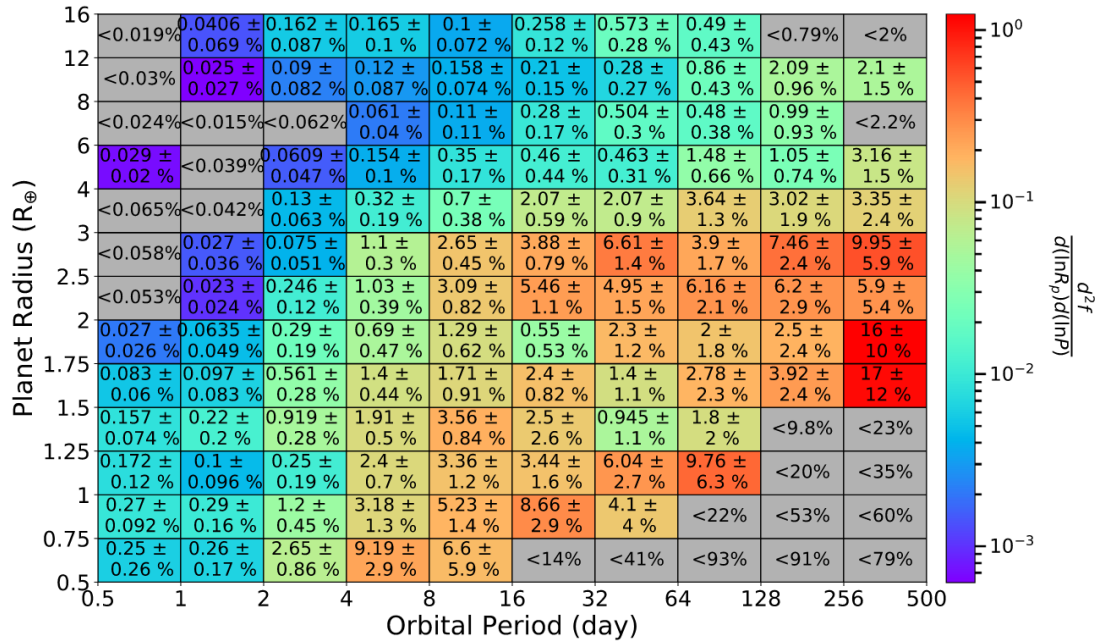


Figure 1.26: Grid highlighting the derived occurrence rates from Hsu et al. (2019) as a function of both planetary radius and orbital period. Plot from Hsu et al. (2019).

low-mass stars ($M_* \leq 0.7 M_\odot$). This is largely due to a lack of low-mass stars being targeted by the *Kepler* mission. Deriving giant planet frequencies for these lower-mass host stars is of particular importance for studying planet formation. The core-accretion theory of planet formation has been shown theoretically to result in a lack of giant planets orbiting M-dwarf stars (Laughlin et al., 2004). It was demonstrated that giant planets do not readily form around these low-mass stars as a result of the lower surface density of solids in the protoplanetary disk and the increased Keplerian timescales for bodies in orbit around these stars. These two factors compounded make it much harder to build up the protoplanetary core required for runaway gas accretion before the protoplanetary disk dissipates (after about 10 Myr). Recently, planet population synthesis experiments have also predicted a decrease in the occurrence rates of giant planets from a level similar to FGK stars for $0.7 M_\odot$ hosts down to zero for $0.3 M_\odot$ hosts (Burn et al., 2021).

With discoveries of hot Jupiters hosted by M-dwarf stars over the past few years (e.g. NGTS-1b (Bayliss et al., 2018); HATS-71b (Bakos et al., 2020)) it is clear that giant planets can form around low-mass stars, but with only a small number known to date, a robust occurrence rate is yet to be determined. Attempts have been made to do this. The Pan Planets survey (Obermeier et al., 2016) tried to answer this question by surveying roughly 60,000 M-dwarf stars with a brightness limit $i \leq 18$ mag but could only place an upper limit of the giant planet occurrence rate. More importantly, they could not conclude whether this occurrence rate differed significantly from that for FGK type host stars. Sabotta et al. (2021) used radial velocity data from CARMENES to derive planetary occurrence rates for M-dwarf host stars, however this effort suffered from a lack of stars and again could only place an upper limit on the giant planet occurrence rate. Obtaining a robust measurement of the giant planet occurrence rate for low-mass stars is crucial for fully understanding how planets form. More details on this are presented in Chapter 6 where I also present a systematic search for these systems in the *TESS* data.

1.8 Thesis Outline

This thesis contains research I have performed to observationally study transiting exoplanets. Chapter 2 presents the discovery and characterisation of the sub-Saturn mass exoplanet NGTS-12 b. In Chapter 3 I present a novel NGTS multi-telescope observing method and my work characterising and demonstrating the performance of this technique. In Chapter 4 I present the results of observations I performed with this method of a transit of the 542 d period planet HIP-41378 f, as well as some brief transit timing variation analysis for the system. A study into the multi-planet system WASP-47 using data from the ESPRESSO spectrograph and the *TESS* mission is presented in Chapter 5. The final science chapter, Chapter 6, presents a systematic search I have performed for gas giants transiting low-mass stars in the the *TESS* data. I finally

present my conclusions and future outlook in Chapter 7.

Chapter 2

NGTS-12b: A sub-Saturn mass transiting exoplanet in a 7.53 day orbit

Note

This chapter is a reproduction of the paper “*NGTS-12b: A sub-Saturn mass transiting exoplanet in a 7.53 day orbit*” (Bryant et al., 2020a) published in Monthly Notices of the Royal Astronomical Society in December 2020. The majority of the analysis and writing of the paper was performed by me. This paper also included external contributions, primarily in the form of observational data, and also some small parts of the analysis. Specifically, these co-author contributions are for Sections 2.2.2, 2.2.3, 2.2.4, 2.2.5, and 2.3.1. Parts of these sections were written by co-authors.

Abstract

We report the discovery of the transiting exoplanet NGTS-12b by the Next Generation Transit Survey (NGTS). The host star, NGTS-12, is a $V = 12.38$ mag star with an effective temperature of $T_{\text{eff}} = 5690 \pm 130$ K. NGTS-12b orbits with a period of $P = 7.53$ d, making it the longest period planet discovered to date by the main NGTS survey. We verify the NGTS transit signal with data extracted from the *TESS* Full-Frame Images, and combining the photometry with radial velocity measurements from HARPS and FEROS we determine NGTS-12b to have a mass of $0.208 \pm 0.022 M_J$ and a radius of $1.048 \pm 0.032 R_J$. NGTS-12b sits on the edge of the Neptunian desert when we take the stellar properties into account, highlighting the importance of considering both the planet and star when studying the desert. The long period of NGTS-12b combined with its low density of just $0.223 \pm 0.029 \text{ g cm}^{-3}$ make it an attractive target for atmo-

spheric characterization through transmission spectroscopy with a Transmission Spectroscopy Metric of 89.4.

2.1 Introduction

Detecting exoplanets via transits has proved to be a very successful path for discovering other worlds. The process began with discoveries from the deep OGLE (Udalski et al., 1992) survey (e.g. Konacki et al., 2003; Bouchy et al., 2004). Soon discoveries were being made via purpose built wide-field survey cameras such as WASP (Pollacco et al., 2006), HATNet (Bakos et al., 2004), and KELT (Pepper et al., 2007). Following these successes, space-based missions, primarily *CoRoT* (Baglin et al., 2006) and *Kepler* (Borucki et al., 2010), delivered high-precision photometry which allowed for the discovery of smaller-radius planets. Currently the *TESS* mission (Ricker et al., 2015) is combining the advantages of wide field cameras and space-based photometric precision to uncover transiting exoplanets orbiting bright stars over almost the entire sky.

The Next Generation Transit Survey (NGTS; Wheatley et al., 2018) is a ground-based exoplanet hunting facility which is situated at ESO’s Paranal Observatory in Chile. It consists of twelve fully robotic telescopes each with a 20 cm photometric aperture and a wide field-of-view of 8 deg^2 . By combining the excellent observing conditions at Paranal Observatory with back-illuminated CCD cameras and sub-pixel level autoguiding (McCormac et al., 2013) on ultra-stable mounts, NGTS can achieve a higher photometric precision than previous ground-based facilities. This was demonstrated with the discovery of NGTS-4b (West et al., 2019), a Neptune-sized exoplanet with a transit depth of just 0.13%. NGTS provides a useful complement to the *TESS* survey, with a higher spatial resolution, a more flexible observing schedule, and better photometric precision for stars with $T \geq 13 \text{ mag}$.

The majority of discoveries from ground-based transit surveys to date are exoplanets with periods shorter than 5 d. This bias towards short period planets is a combination of the geometric probability of transit and the difficulty of conducting long duration photometric campaigns. NGTS is able to mitigate this difficulty in two ways. Firstly, we can conduct longer monitoring campaigns due to the excellent site conditions at Paranal Observatory. Secondly, with higher photometric precision, the signal-to-noise of each individual transit is higher, and so fewer transits are required to build up the same total signal-to-noise.

In this chapter we report the discovery of NGTS-12b; a $0.208 \pm 0.022 M_J$, $1.048 \pm 0.032 R_J$ transiting exoplanet with a period of 7.53 d. NGTS-12b is the longest period planet discovered to date from the main NGTS survey. In Section 2.2 we detail the photometric and spectroscopic observations obtained of NGTS-12. In Section 2.3 we perform a global analysis of the data to

determine the stellar and planetary properties of the system. We discuss our results in Section 2.4 and finally present our conclusions in Section 2.5.

2.2 Observations

NGTS-12 is a $T = 11.6$ mag star in the southern hemisphere (RA=11^h44^m59^s986, Dec=−35°38′26″0267) which was monitored as part of the NGTS survey. In this section we set out the photometric and spectroscopic observations of NGTS-12 that led to the discovery of the exoplanet NGTS-12b.

2.2.1 NGTS Photometry

NGTS-12 was observed using a single NGTS telescope between 2017 December 10 and 2018 August 4. During this period a total of 250,503 images were taken with an exposure time of 10 seconds. Image reduction and photometry was performed using the *CASUTOOLS*¹ photometry package as detailed in Wheatley et al. (2018) and Section 1.4.3. The detrending of the light curve was performed using an implementation of the *SysREM* algorithm (Tamuz et al., 2005) to remove signals which are exhibited by multiple stars across the field. The full NGTS survey light curve is shown in Figure 2.1, and the photometry is provided in Table 2.1.

The NGTS-12 light curve was searched for periodic, transit-like signals using *ORION*, a custom implementation of the Box-fitting Least Squares algorithm (BLS; Kovács et al., 2002). A strong peak in the BLS periodogram was detected at 7.53 d. Folding the NGTS photometry on this period revealed a clear transit signal with a depth of 0.55% and a duration of 5.85 ± 0.073 hours.

In *Gaia* DR2 (Gaia Collaboration, 2018) there are no other stars within the photometric aperture radius (15'') of NGTS-12. The parallax and photometric measurements from *Gaia* DR2 (listed in Table 2.2) also rule out the possibility that NGTS-12 is a giant star. The light curve for NGTS-12 shows no evidence of a secondary eclipse, odd-even differences in the transit depths, or out-of-transit variability. A convolutional neural network implemented for NGTS data (Chaushev et al., 2019) reported a probability of > 0.99 for the transit signal being planetary in nature. We therefore concluded that NGTS-12b was a strong transiting exoplanet candidate, and initiated spectroscopic follow-up detailed in Sections 2.2.3 to 2.2.5.

2.2.2 TESS Photometry

One year after the NGTS monitoring set out in Section 2.2.1, NGTS-12 was also observed during Sector 10 (Camera 2; CCD 4) of the *TESS* mission (Ricker et al., 2015) between 2019 March

¹<http://casu.ast.cam.ac.uk/surveys-projects/software-release>

Table 2.1: NGTS and *TESS* photometry for NGTS-12. The full table is available in a machine-readable format from the online journal publication of this study (Bryant et al., 2020a). A portion is shown here for guidance.

Time (BJD-2450000)	Flux (normalised)	Flux error	Instrument	Exp. Time (s)
8097.82554	1.0092	0.0056	NGTS	10
8097.82569	0.9879	0.0055	NGTS	10
8097.82584	0.9899	0.0055	NGTS	10
8097.82599	0.9969	0.0055	NGTS	10
8097.82614	0.9918	0.0055	NGTS	10
8097.82628	1.0120	0.0055	NGTS	10
8097.82643	0.9885	0.0055	NGTS	10
8097.82658	1.0046	0.0055	NGTS	10
8097.82673	1.0085	0.0055	NGTS	10
8097.82689	0.9945	0.0055	NGTS	10
...
8572.01562	1.0005	0.0008	<i>TESS</i>	1800
8572.03644	0.9996	0.0008	<i>TESS</i>	1800
8572.05731	0.9991	0.0008	<i>TESS</i>	1800
8572.07812	1.0000	0.0008	<i>TESS</i>	1800
8572.09894	1.0004	0.0008	<i>TESS</i>	1800
8572.11981	1.0008	0.0008	<i>TESS</i>	1800
8572.14062	0.9988	0.0008	<i>TESS</i>	1800
8572.16144	0.9992	0.0008	<i>TESS</i>	1800
8572.18231	1.0001	0.0008	<i>TESS</i>	1800
8572.20312	1.0002	0.0008	<i>TESS</i>	1800
...

Table 2.2: Stellar Properties for NGTS-12

Property	Value	Source
Identifiers		
NGTS-12		
TIC-157230659		
<i>Gaia</i> DR2 3464620139089832960		
2MASS J11450000-3538261		
Astrometric Properties		
RA	11 ^h 44 ^m 59 ^s .986	<i>Gaia</i> DR2
Dec	−35°38′26″.0267	<i>Gaia</i> DR2
μ_{RA} (mas y ^{−1})	−18.4141 ± 0.0441	<i>Gaia</i> DR2
μ_{Dec} (mas y ^{−1})	7.3178 ± 0.0320	<i>Gaia</i> DR2
Parallax (mas)	2.212 ± 0.038	<i>Gaia</i> DR2
Photometric Properties		
NGTS (mag)	11.83 ± 0.01	This work
<i>TESS</i> (mag)	11.6634 ± 0.006	TIC8
<i>V</i> (mag)	12.382 ± 0.046	APASS
<i>B</i> (mag)	12.974 ± 0.051	APASS
<i>Gaia G</i> (mag)	12.1279 ± 0.0002	<i>Gaia</i> DR2
<i>Gaia G</i> _{Bp} (mag)	12.4947 ± 0.0008	<i>Gaia</i> DR2
<i>Gaia G</i> _{Rp} (mag)	11.6071 ± 0.0012	<i>Gaia</i> DR2
<i>J</i> (mag)	10.992 ± 0.026	2MASS
<i>H</i> (mag)	10.692 ± 0.024	2MASS
<i>K</i> (mag)	10.588 ± 0.021	2MASS
<i>W1</i> (mag)	10.555 ± 0.023	WISE
<i>W2</i> (mag)	10.597 ± 0.020	WISE
Derived Properties		
T_{eff} (K)	5690 ± 130	Sec. 2.3.1
[Fe/H]	−0.03 ± 0.11	Sec. 2.3.1
$v \sin i$ (km s ^{−1})	< 0.5	Sec. 2.3.1
Γ_{RV} (m s ^{−1})	−12595.6 ± 1.4	Sec. 2.3.2
log <i>g</i>	4.045 ± 0.038	Sec. 2.3.1
M_* (M _⊙)	1.021 ^{+0.056} _{−0.049}	Sec. 2.3.1
R_* (R _⊙)	1.589 ± 0.040	Sec. 2.3.1
ρ_* (g cm ^{−3})	0.359 ± 0.039	Sec. 2.3.1
Age (Gyr)	9.4 ± 1.5	Sec. 2.3.1
Distance (pc)	452.0 ± 7.6	Sec. 2.3.1
2MASS (Skrutskie et al., 2006);		
APASS (Henden and Munari, 2014); WISE (Wright et al., 2010);		
<i>Gaia</i> DR2 (Gaia Collaboration, 2018); TIC8 (Stassun et al., 2019)		

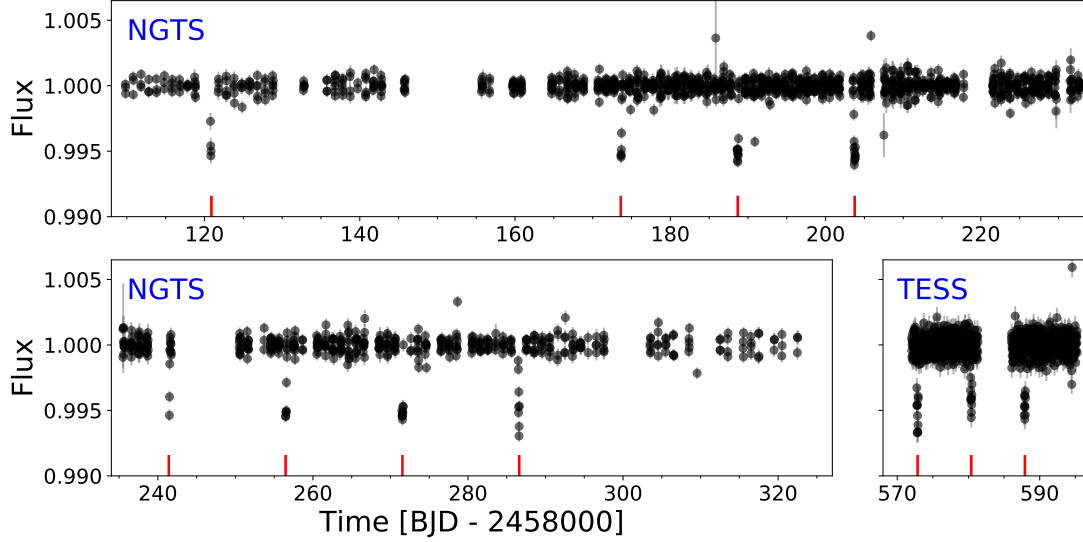


Figure 2.1: Full NGTS and *TESS* light curves for NGTS-12. The red vertical lines give the positions of the observed transits of NGTS-12b. A total of 8 transit events are recorded in the NGTS data, and 3 in the *TESS* data. The NGTS data have been binned to 30 minutes and flattened in a similar manner to the *TESS* data for visual comparison with the 30 minute cadence *TESS* data.

28 and 2019 April 21. NGTS-12 was not selected for 2-minute *TESS* photometry. We therefore created a light curve via aperture photometry of the *TESS* 30-minute cadence Full-Frame Images (FFIs) following the method set out in Gill et al. (2020b). Postage stamps of 15×15 pixels were downloaded for all Sector 10 *TESS* FFIs. We determined a threshold for target pixels and for background pixels based on an iterative sigma-clipping to determine the median and standard deviation of the background pixels. To exclude the neighbouring $T = 12.0$ mag star (TIC-157230670, $76''$ to the north-west, see Figure 2.2) as much as possible, we only include pixels in our final aperture for which neighbouring pixels closer to the centre of our target show a higher illumination. Otherwise we assume the pixel is influenced in majority by another source. For the final pixel mask of NGTS-12, 10 pixels over a threshold of 168 electrons/second were selected (see Figure 2.2). To remove the systematic trends from the *TESS* light curve, we mask out the transits, and then fit a spline with nodes spaced by 10 hours, interpolating across the positions of the transits.

The *TESS* photometry for NGTS-12 is shown in Figure 2.1, and clearly shows three transit events with depths, durations, and epochs consistent with the NGTS data. Again we see no evidence of secondary eclipses, odd-even differences in the transit depths, or out-of-transit variability. The *TESS* photometry is provided in Table 2.1.

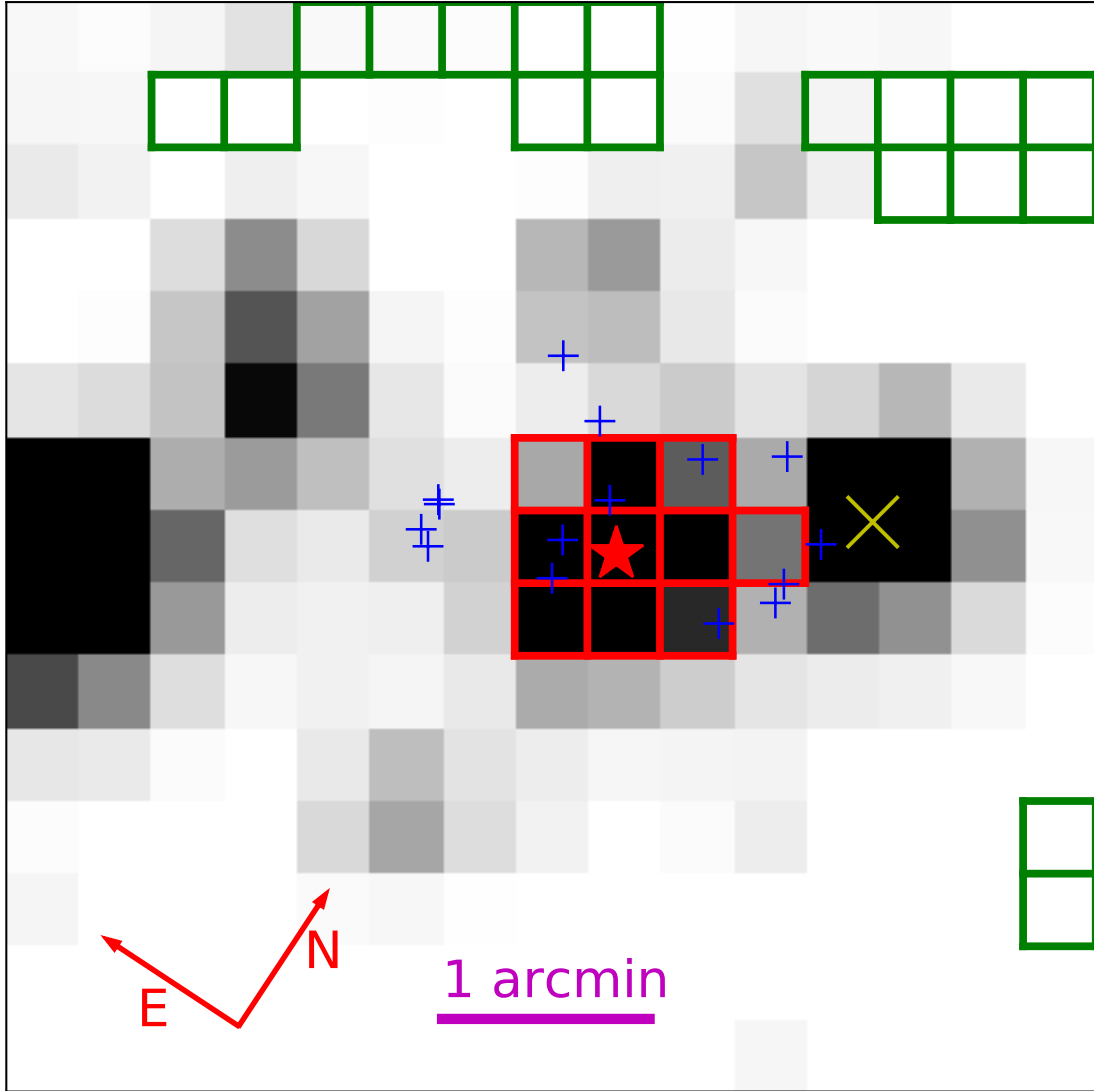


Figure 2.2: *TESS* Full-Frame Image cutout (15×15 pixels) in the region of NGTS-12 from which the *TESS* light curve was generated. The red boxes indicate the target pixel aperture mask used to extract the photometry and the green boxes denote the pixels used to determine the sky background. The red star indicates the position of NGTS-12, the yellow cross gives the location of TIC-157230670. The blue pluses denote the positions of faint neighbouring stars ($T > 15.5$ mag) detected in *Gaia* DR2 within $1'$ of NGTS-12, used for the dilution estimation (Section 2.3.3).

2.2.3 CORALIE Spectroscopy

Two reconnaissance spectra were obtained for NGTS-12 using the CORALIE spectrograph (Queloz et al., 2001) mounted on the Swiss-1.2 m Leonard Euler telescope, located at the ESO La Silla Observatory, Chile. An exposure time of 2,700 seconds was used for both observations. The spectra were reduced using the standard CORALIE data reduction pipeline. The radial velocities (RVs) were extracted via cross-correlation with a G2 binary mask and are given in Table 2.3. The RV measurements obtained from these spectra were useful in ruling out stellar mass companions. However, the mean uncertainty of the two RVs from these spectra is 34 m s^{-1} , which is roughly 1.5 times the RV semi-amplitude for NGTS-12b. As such, the CORALIE measurements do not have the precision to help constrain the planetary parameters, and so we do not include them in the global modelling detailed in Section 2.3.2.

2.2.4 HARPS Spectroscopy

We obtained multi-epoch spectroscopy for NGTS-12 with the HARPS spectrograph (Mayor et al., 2003). NGTS-12 was observed eight times with HARPS between the dates of 2019 December 28 and 2020 February 11 under programme ID 0104.C-0588 (PI Bouchy). The HARPS spectrograph is mounted on the ESO 3.6 m telescope at the La Silla Observatory, Chile. The spectra were reduced using the standard HARPS data reduction pipeline and RVs were extracted via cross correlation with a G2 binary mask. The full RV time series of eight measurements is given in Table 2.3. For all the HARPS observations an exposure time of 1,800 seconds was used. The typical RV uncertainty is 4 m s^{-1} . We plot the phase-folded RV measurements in Figure 2.3, which clearly shows an RV variation in-phase with the photometric period determined in Section 2.2.1. The RV semi-amplitude of $K = 20 \text{ m s}^{-1}$ is consistent with a transiting planet orbiting NGTS-12.

We also extract the bisector spans of the HARPS cross correlation functions. We investigate the correlation between the RV measurements and the bisector spans and find a Pearson-R correlation coefficient of -0.21, indicating no strong correlation (see Figure 2.3).

2.2.5 FEROS Spectroscopy

We obtained two further spectroscopic observations of NGTS-12 with the FEROS spectrograph (Kaufer et al., 1999) on UT 2020 January 1 and 3, using an exposure time of 1,200 seconds. The FEROS spectrograph is mounted on the MPG/ESO-2.2 m telescope at the La Silla Observatory, Chile. We reduced these spectra using the CERES pipeline (Brahm et al., 2017). CERES also calculates RVs by cross-correlating the reduced spectra with a G2 binary mask and then

Table 2.3: Radial Velocities for NGTS-12

BJD	RV (km s ⁻¹)	RV err (km s ⁻¹)	Instrument	Exp. Time (s)
2458826.809493	-12.61315	0.03399	CORALIE	2700
2458830.809847	-12.65738	0.03343	CORALIE	2700
2458845.783261	-12.61483	0.00835	HARPS	1800
2458846.773136	-12.61613	0.00370	HARPS	1800
2458847.794460	-12.59168	0.00295	HARPS	1800
2458849.81984	-12.5808	0.0103	FEROS	1200
2458851.80857	-12.6002	0.0096	FEROS	1200
2458869.833151	-12.60787	0.00410	HARPS	1800
2458871.854470	-12.58030	0.00357	HARPS	1800
2458887.816510	-12.57215	0.00409	HARPS	1800
2458889.835373	-12.60464	0.00453	HARPS	1800
2458890.765724	-12.61451	0.00600	HARPS	1800

fitting a double Gaussian model to the cross-correlation function in order to account for possible moonlight contamination. We note that the G2 mask used by the CERES pipeline is the same mask used to extract the CORALIE and HARPS RVs. The resulting RVs are listed in Table 2.3 and shown in Figure 2.3.

2.3 Analysis

Using the observations presented in Section 2.2, along with stellar properties from a variety of astronomical surveys, we modelled the NGTS-12b system. We set out that analysis in this section.

2.3.1 Stellar Properties

We determined stellar atmospheric parameters of NGTS-12 using isochrone fitting with the *ISOCHRONES* Python module (Morton, 2015). We obtained priors for T_{eff} , $[\text{Fe}/\text{H}]$, $\log g$ by spectral matching from the 1D stacked HARPS spectra (see Section 2.2.4), using a custom wavelet analysis algorithm (Gill et al., 2018) as well as *SPECMATCH-EMP* (Yee et al., 2017). We took priors for these parameters that encompassed both spectral matching methods, and the resulting Gaussian priors were $T_{\text{eff}} = 5649 \pm 153$ K, $[\text{Fe}/\text{H}] = -0.045 \pm 0.15$, and $\log g = 3.95 \pm 0.5$. For additional priors, we used the parallax, G_{Bp} magnitude, and G_{Rp} magnitude from *Gaia* DR2 (Gaia Collaboration, 2018) as listed in Table 2.2.

We selected the MIST stellar models (Choi et al., 2016; Dotter, 2016) to use for the

isochrone fitting within the `ISOCHRONES` module. The derived stellar parameters from this modelling are given in Table 2.2. From this analysis, we found NGTS-12 to be a slightly evolved G-type star with a mass and radius of $M_* = 1.021^{+0.056}_{-0.049} M_\odot$ and $R_* = 1.589 \pm 0.040 R_\odot$.

Using the wavelet analysis, we derived a rotational velocity of $v \sin i < 0.5 \text{ km s}^{-1}$. We also check for evidence of rotational modulation in the NGTS photometry by applying a Lomb-Scargle algorithm (Lomb, 1976; Scargle, 1982) to the NGTS photometric residuals. No significant rotation modulation was detected, indicating that NGTS-12 has a low degree of stellar activity. This is consistent with the low rotational velocity ($< 0.5 \text{ km s}^{-1}$) and the age of NGTS-12 derived from the `ISOCHRONES` fit ($9.4 \pm 1.5 \text{ Gyr}$).

2.3.2 Global Modelling

We used the `EXOPLANET` Python package (Foreman-Mackey et al., 2021) to simultaneously model the photometric and spectroscopic data. `EXOPLANET` is a Python toolkit which uses Hamiltonian Monte Carlo methods implemented through `PYMC3` (Salvatier et al., 2016) to probabilistically model transit and radial velocity time series data for exoplanet systems. At each step in the sampling, we determined the Keplerian orbit of the planet around NGTS-12, and used this orbit to compute the model the light curve (via `STARRY`; Luger et al., 2019) and the radial velocity.

We fitted for the following planetary system parameters: time of transit centre, T_C , the orbital period, P , the planet-to-star radius ratio, R_P/R_* , $\ln K$ (where K is the RV semi-amplitude), and the impact parameter, b . We constrained these parameters using the priors given in Table 2.4. The stellar density, ρ_* , was also included as a free parameter, and was constrained using the value derived in Section 2.3.1. This was done to ensure physically realistic orbital parameters were derived. In addition, we fitted for the limb-darkening coefficients for both NGTS and *TESS*. We used a quadratic limb-darkening model and sampled the parameters using the efficient parameterisation of Kipping (2013a). We also fitted for the mean out-of-transit flux levels in the NGTS and *TESS* light curves, $F_{0,\text{NGTS}}$ and $F_{0,\text{TESS}}$, as well as the systemic radial velocity of NGTS-12, Γ_{RV} , and the systematic instrumental radial velocity offset between HARPS and FEROS, ΔRV_{FEROS} . From an initial modelling run, we found the formal NGTS photometric uncertainties to be slightly underestimated, so we also included an additional error scaling term, σ_{NGTS} , which was added in quadrature to the formal NGTS photometry uncertainties.

Since *Gaia* DR2 shows no stars within the NGTS photometric radius of NGTS-12, we conclude that the NGTS survey photometry is undiluted. However from a visual inspection of the data it is evident that the *TESS* transits are slightly shallower depth compared with the transits in the NGTS data. This is a result of the larger pixel scale of *TESS*, meaning that the *TESS* photometry is diluted by nearby stars, especially TIC-157230670 (see Figure 2.2). We therefore

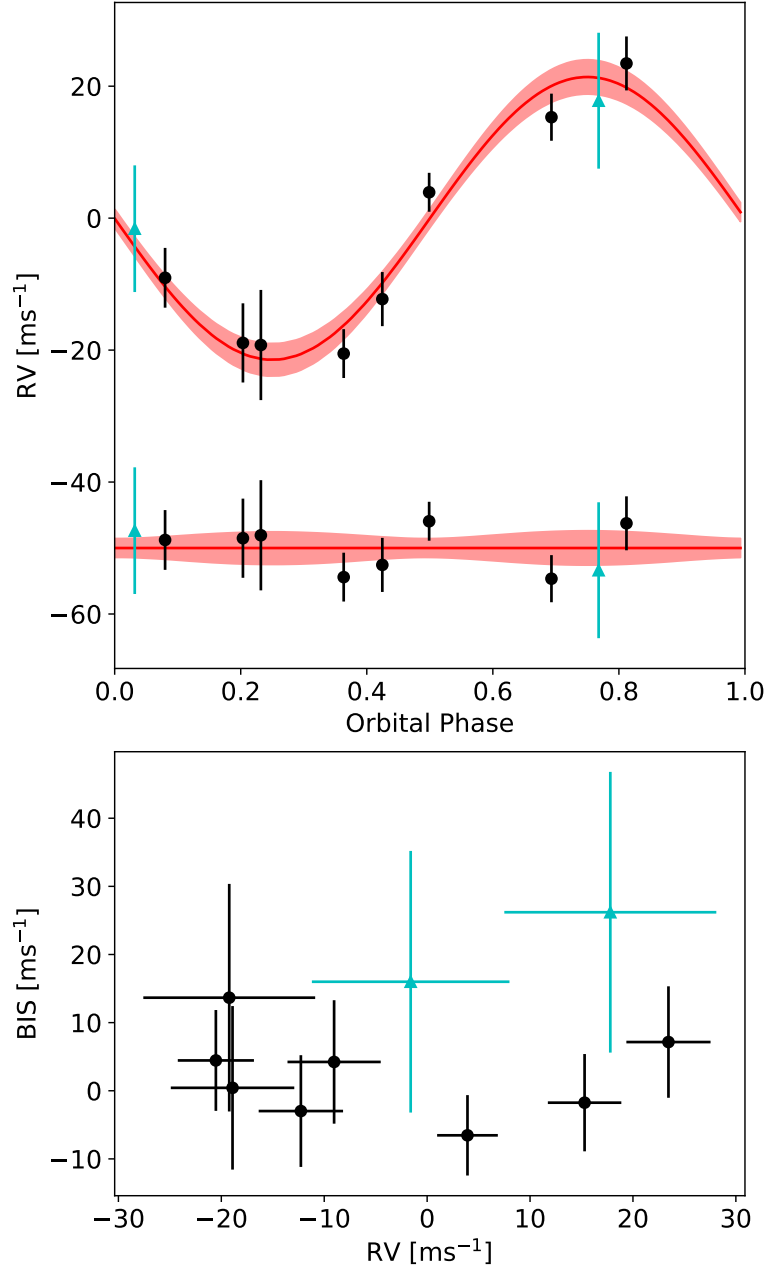


Figure 2.3: **Top:** Phase folded radial velocities of NGTS-12 from HARPS (black circles) and FEROS (blue triangles). The systemic γ_{RV} has been removed from the measurements and the FEROS points have had the RV offset applied. The red line gives the median RV model derived in Section 2.3.2, with the 1σ tolerance on this model given by the red shading. As with Figure 2.4, the residuals are plotted offset below the RV curve. **Bottom:** Bisector spans for the HARPS and FEROS CCFs. The errorbars on the bisector spans are taken as twice the RV error for a given data point.

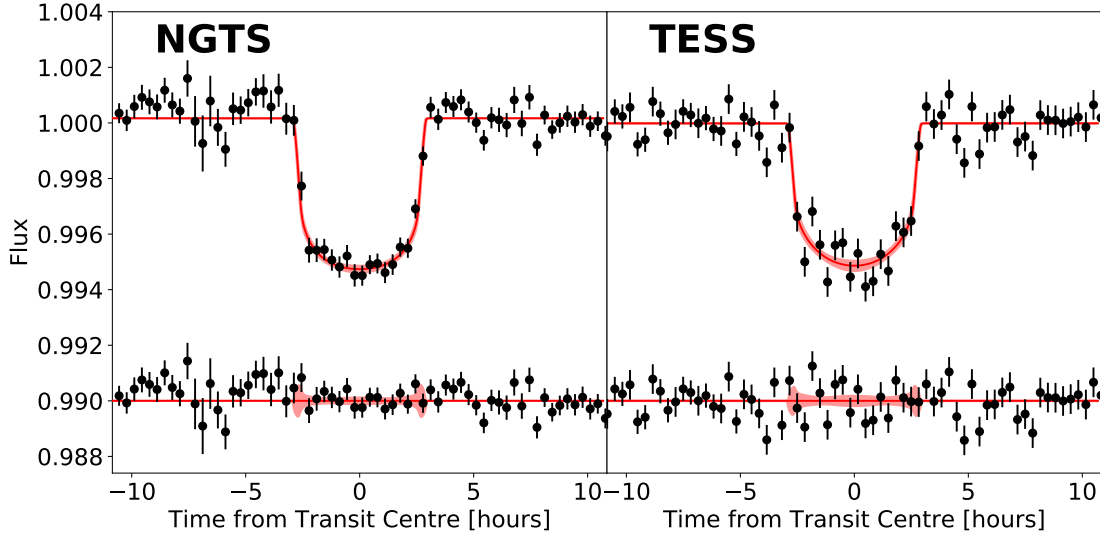


Figure 2.4: Phase-folded NGTS and *TESS* light curves for NGTS-12, with the models derived in Section 2.3.2 plotted. The solid red lines give the median models and the shaded bands give the 1σ uncertainties. The residuals are plotted below the light curves in both panels. For both datasets, the flux plotted has been binned to 20 minutes in phase. The *TESS* transit depth is slightly shallower due to blending in the *TESS* photometry as discussed in Section 2.3.3.

include a dilution factor, D , for the *TESS* photometry, given by

$$D = F_{\text{cont}}/F_{\text{target}}, \quad (2.1)$$

where F_{target} and F_{cont} are the flux contributions within the *TESS* photometric aperture from the target (NGTS-12) and contaminating stars respectively.

For the sampling we ran 10 chains for 4,000 steps each to tune the sampler, followed by a further 7,500 steps to sample the posterior distributions. The starting points for the chains were selected from the results of a least squares minimization prior to the sampling. We determined the Gelman-Rubin statistic (\hat{R} ; Gelman and Rubin, 1992) for each chain. For all chains, we found $\hat{R} \ll 1.01$, indicating that all the chains had converged, and were well-mixed. The resulting spectroscopic and photometric models are plotted in Figures 2.3 and 2.4 respectively. We note that the varying levels of photometric scatter in the NGTS light curve in Figure 2.4 are due to the non-uniform sampling of phase space in the NGTS photometry. This is because the orbital period is both long and close to a half-integer day. The median values from the posterior distributions of the fitted parameters are given in Table 2.4, along with the 1σ parameter uncertainties. These uncertainties are derived from the 16th and 84th percentile values of the posterior distributions.

The median derived parameter values and uncertainties are given in Table 2.5.

We ran two models; the first with a fixed circular orbit, and the second with the orbital eccentricity, e , and the argument of periastron, ω , allowed to freely vary. For the free eccentricity model, we constrained e with the beta distribution prior parameterisation from Kipping (2013b, 2014). From this second model, we derived a value of the eccentricity of $0.01^{+0.03}_{-0.01}$ with a 95% confidence upper limit of 0.08. Comparing the resultant maximum log-likelihoods ($\ln \mathcal{L}$) from the two fits, we find that allowing e to freely vary results in a slightly higher $\ln \mathcal{L}$. To determine whether this slight increase in $\ln \mathcal{L}$ warrants the inclusion of two additional free parameters to the model, we compare the Bayesian Information Criterion (BIC) for the two models. The BIC is given by

$$\text{BIC} = k \ln n - 2 \ln \mathcal{L}, \quad (2.2)$$

where k is the number of free parameters in the model, and n is the number of data points. A higher BIC denotes evidence against a given model. Comparing the BIC for the full global models, we find $\Delta \text{BIC} = \text{BIC}_{\text{ecc}} - \text{BIC}_{\text{circ}} = 19.56$. This is strong evidence in favour of the circular orbit model. Comparing the BIC for just the radial velocity data for the two models, we again find a positive $\Delta \text{BIC} = 4.26$. In addition, we consider the significance test from Lucy and Sweeney (1971), which asserts that an eccentricity measurement must satisfy $e > 2.45\sigma_e$, where σ_e is the measured uncertainty in eccentricity, in order to be considered significant. Our measured value of $e = 0.01^{+0.03}_{-0.01}$ does not meet the criterion. Therefore, we find the orbit of NGTS-12b to be circular at a statistically significant level, and therefore adopt the parameters derived using the fixed circular orbit for our final system parameters.

For the large bulk of hot Jupiter planets with orbital periods ≤ 4 d, we would expect a circular orbit, due to the quick circularization timescales. For example, using equation 3 from Adams and Laughlin (2006) with a tidal quality factor of $Q_p = 10^6$, we find a tidal circularization timescale of just 375 Myr for a planet of Jupiter radius and mass in a 4 d orbit around a solar mass star. However, at longer orbital periods, such as the 7.53 d orbit of NGTS-12b, the situation is less clear cut; the circular orbit of NGTS-12b is less obvious a priori. Again following Adams and Laughlin (2006) and with $Q_p = 10^6$, we find an orbital circularization timescale for NGTS-12b of $\tau_{\text{circ}} = 3.77 \pm 0.90$ Gyr. This is significantly shorter than the lifetime of the system (9.4 ± 1.5 Gyr), and so tidal circularization alone is enough to explain the circular orbit.

2.3.3 Dilution of the *TESS* transits

As discussed in Section 2.3.2, we fitted a dilution factor, D , for the *TESS* photometry, and found a value of $8.5 \pm 4.7\%$. We expect that the majority of the contaminating flux, F_{cont} , in the *TESS* photometry will be due to the bright ($T = 12.016$ mag) neighbour TIC-157230670. We inspected

the *TESS* Full-Frame Image to determine the point-spread function (PSF) in the region of the camera surrounding NGTS-12 to estimate the contamination from TIC-157230670, as well as other nearby stars.

We model the PSF as a 2D elliptical Gaussian using the (S, D, K) parameterisation PSF model (Pál, 2009). As a part of the Cluster Difference Imaging Photometric Survey (CDIPS), Bouma et al. (2019) calculated (S, D, K) shape parameters for a selection of stars across the *TESS* cameras. We extract shape parameters for the sample of stars with CCD positions closest to NGTS-12. There were relatively few CDIPS targets in *TESS* Sector 10, Camera 2, CCD4. However, since the shape of the PSF depends almost entirely on the *TESS* optics, the shape parameters for a given CCD are stable across the different sectors. As such, we can use data from *TESS* Sector 7, for which Camera 2 CCD 4 has a significantly higher coverage of CDIPS stars, to determine the shape parameters for our model PSF for NGTS-12. We therefore extract shape parameters for NGTS-12 of $S = 1.688 \pm 0.022$, $D = -0.0220 \pm 0.0047$, $K = 0.104 \pm 0.012$.

We use this model PSF to estimate the amount of light from the nearby stars which falls into the photometric aperture used for NGTS-12. We consider all the stars in TICv8 (Stassun et al., 2019) within $1'$ of NGTS-12, as well as the bright neighbour TIC-157230670 (see Figure 2.2). We use the *TESS* magnitude values for each neighbouring star to weight the total flux contained within each star's PSF. This method yields an estimated dilution factor of $D = 6.09 \pm 0.15 \%$, which is consistent with the dilution factor derived from the global model. We are therefore confident that the difference in the transit depths between NGTS and *TESS* is due to blending in the *TESS* photometry, and that our global modeling is correctly accounting for this blending.

This dilution estimation method can be applied to other *TESS* targets where the light curve is extracted from the *TESS* Full-Frame Images. Since we had undiluted photometry from NGTS for NGTS-12, we simply used this as a check to ensure the fitted dilution factor (Section 2.3.2) was a physically reasonable value. However in other cases where no undiluted photometry is available, this method can be used to estimate the degree of dilution in the *TESS* photometry, ensuring an accurate estimation of the planet radius.

2.4 Discussion

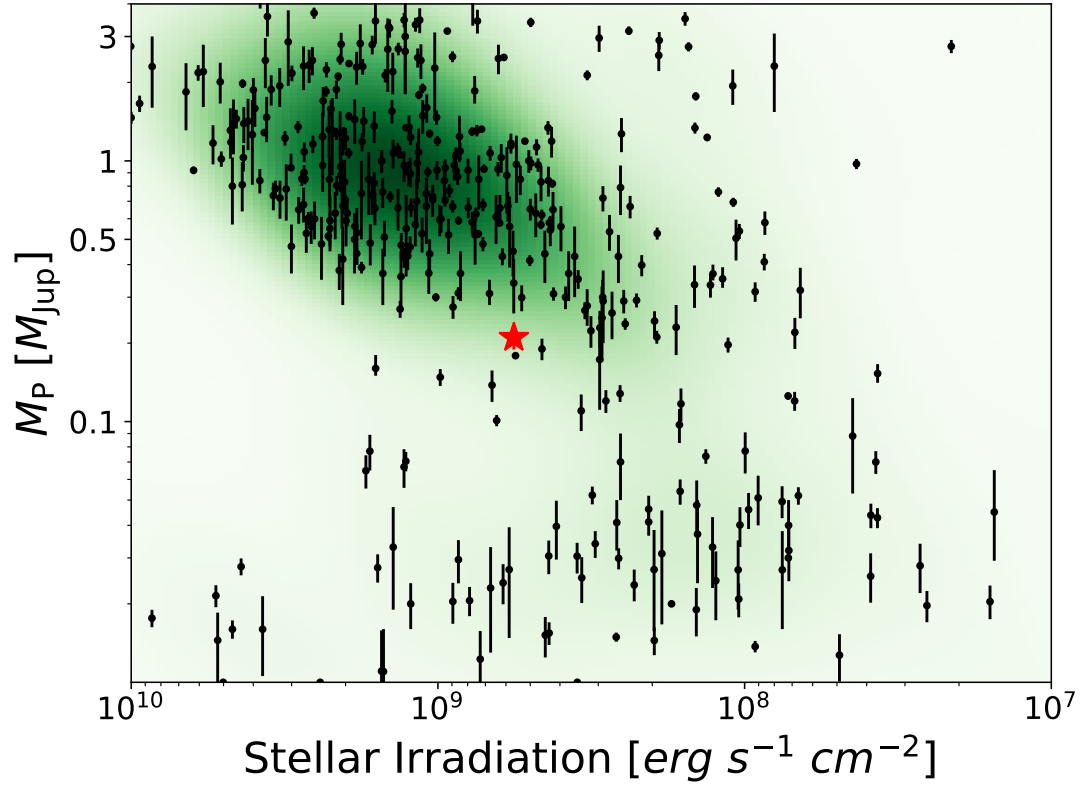


Figure 2.5: Irradiating stellar flux incident on the planet vs planetary mass for a selection of known planets from the NASA Exoplanet Archive with a radius measured to better than 10% and a mass measured to better than 50%. NGTS-12b is plotted with the red star, and the colour shading gives the number density of planets in a given region of irradiation-mass parameter space.

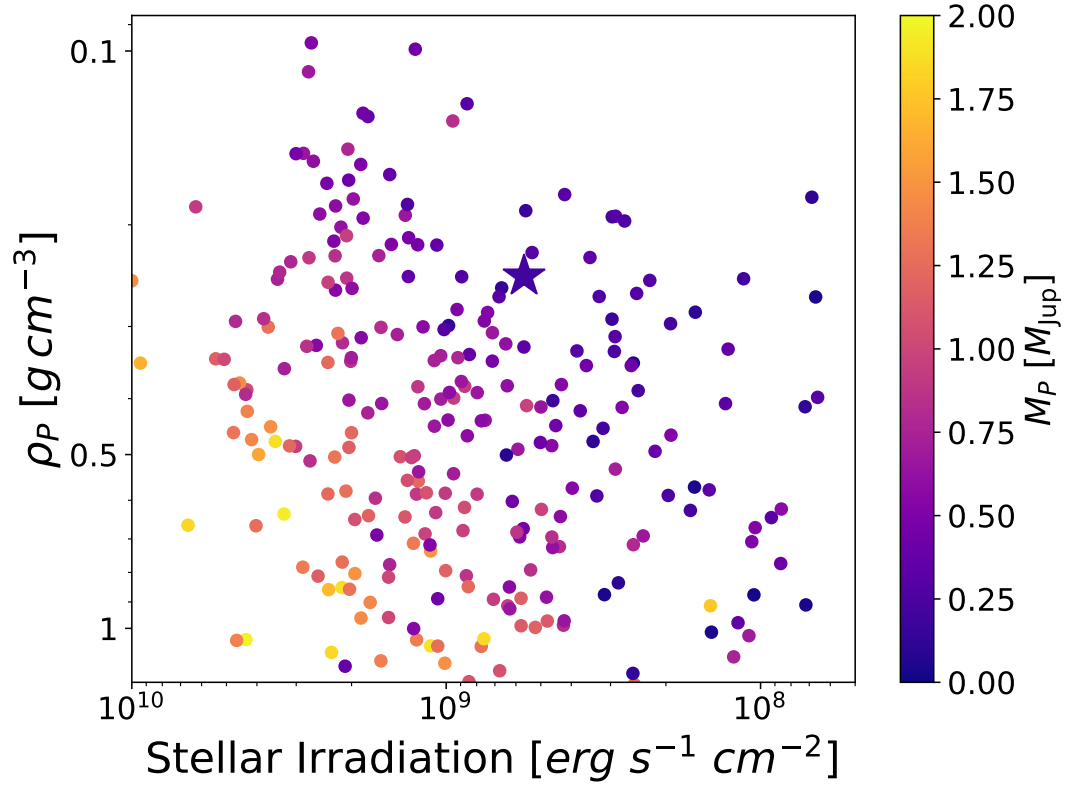


Figure 2.6: Distribution of the densities of known exoplanets against incident stellar flux. The circles are the same sample of planets as Figure 2.5, but with an additional mass constraint of $0.01M_J \leq M_P \leq 2.0M_J$. The star gives the position of NGTS-12b. The colour of the points gives the planetary mass. Note that both axes are inverted, so low density, highly irradiated planets reside at the top left of the plot.

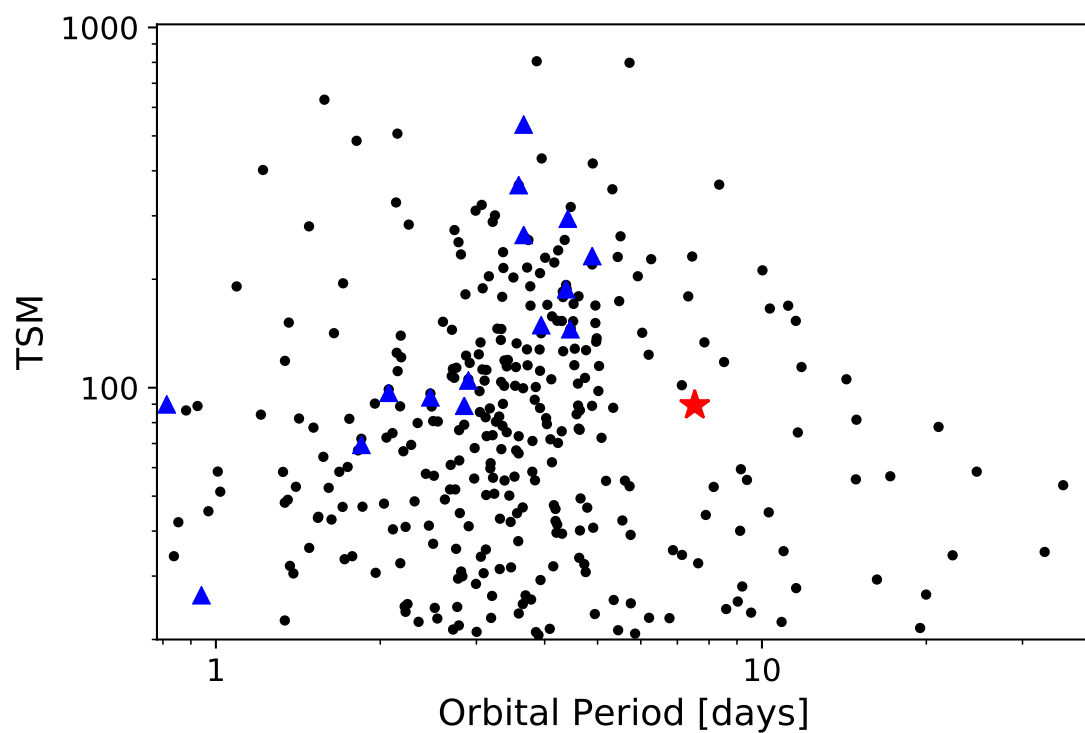


Figure 2.7: Transmission Spectroscopy Metric (TSM) against orbital period for the same sample of planets as Figure 2.5. NGTS-12b is denoted by the red star and the *JWST* community targets (Stevenson et al., 2016; Bean et al., 2018) are highlighted by the blue triangles.

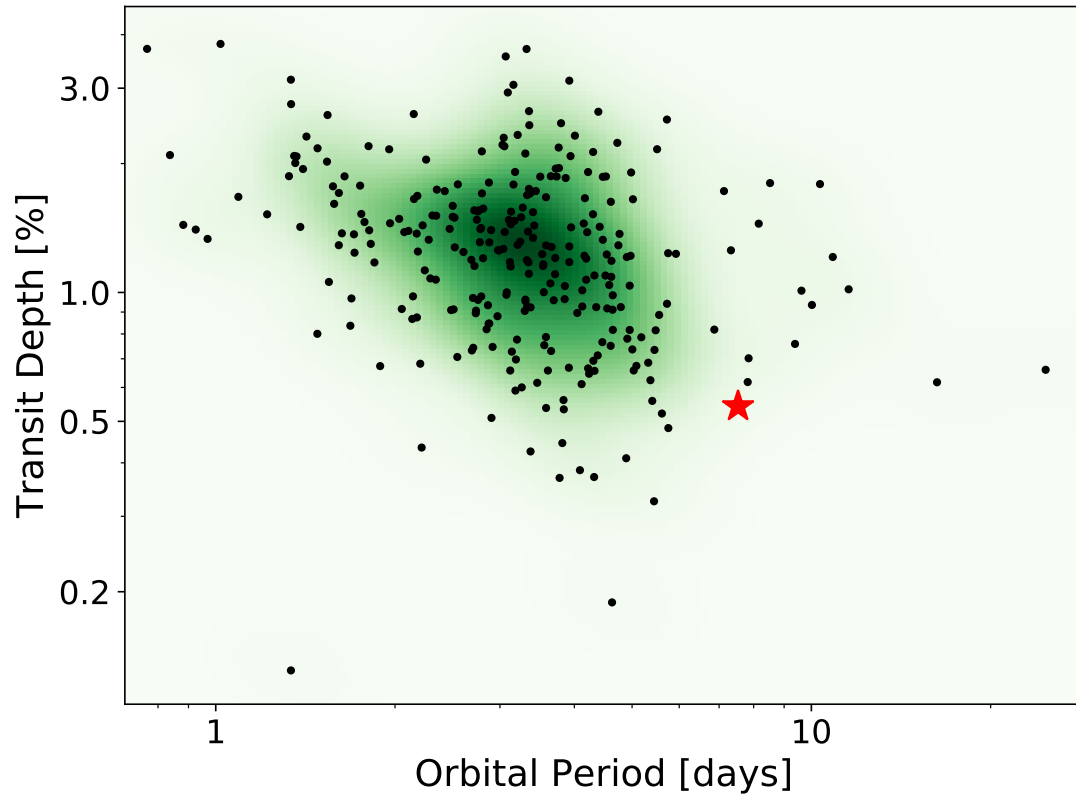


Figure 2.8: Orbital period and transit depth for all planets detected by ground-based transit surveys, with a radius measured to better than 10% and a mass measured to better than 50%. NGTS-12b is again plotted with the red star. The colour shading gives the number density of planets in a given region of parameter space.

Table 2.4: Fitted parameter priors and values for NGTS-12b from modelling detailed in Section 2.3.2.

Parameter	Symbol	Unit	Prior	Value
Time of Transit Centre	T_C	BJD (TDB)	$\mathcal{U}^d (2458572.70, 2458572.90)$	2458572.8549 ± 0.0017
Orbital Period	P	d	$\mathcal{N}^d (7.5328, 0.1)$	7.532806 ± 0.000048
Radius Ratio	(R_P / R_*)		$\mathcal{U} (0., 1.)$	0.0678 ± 0.0012
Impact Parameter	b		$\mathcal{U} (0., R_P / R_*)$	0.20 ± 0.13
Stellar Density	ρ_*	g cm^{-3}	$\mathcal{N} (0.359, 0.039)$	$0.362^{+0.022}_{-0.032}$
Nat. Log. of RV Semi-Amplitude	$\ln(K)$	$\ln (\text{m s}^{-1})$	$\mathcal{N} (3.075, 3.0)$	3.06 ± 0.10
Eccentricity	e		$\beta (0.697, 3.27)^a$	0.0^b
NGTS LDC ^c 1	$U_{1, \text{NGTS}}$		$\mathcal{K}^e (0., 1.)$	$0.30^{+0.22}_{-0.19}$
NGTS LDC ^c 2	$U_{2, \text{NGTS}}$		$\mathcal{K} (0., 1.)$	$0.35^{+0.31}_{-0.37}$
TESS LDC ^c 1	$U_{1, \text{TESS}}$		$\mathcal{K} (0., 1.)$	$0.51^{+0.25}_{-0.27}$
TESS LDC ^c 2	$U_{2, \text{TESS}}$		$\mathcal{K} (0., 1.)$	$0.06^{+0.41}_{-0.31}$
Mean NGTS Flux Baseline	$F_{0, \text{NGTS}}$		$\mathcal{U} (0.998, 1.002)$	1.000168 ± 0.000019
Mean TESS Flux Baseline	$F_{0, \text{TESS}}$		$\mathcal{U} (0.998, 1.002)$	0.999985 ± 0.000026
NGTS Error Term	σ_{NGTS}		$\mathcal{N} (0.002, 0.1)$	0.001996 ± 0.000018
TESS Dilution Factor	D	%	$\mathcal{U} (0., 50.)$	8.5 ± 4.7
Systemic Radial Velocity	γ_{RV}	m s^{-1}	$\mathcal{N} (-12595, 50)$	-12595.6 ± 1.4
FEROS RV Offset	ΔRV_{FEROS}	m s^{-1}	$\mathcal{N} (0., 50)$	-3.0 ± 7.1

a - This is the β distribution for the eccentricity of short period planets from Kipping (2013b)

b - Adopted eccentricity. 95% confidence level upper limit is 0.08

c - LDC = limb darkening coefficient

d - $\mathcal{U} (A, B)$ denotes a uniform prior between A and B and $\mathcal{N} (\mu, \sigma)$ denotes a Gaussian prior with mean μ and standard deviation σ

e - \mathcal{K} denotes the informative quadratic LDC parameterisation from Kipping (2013a)

Table 2.5: Derived parameter priors for NGTS-12b from modelling detailed in Section 2.3.2.

Parameter	Symbol	Unit	Value
Planet Radius	R_P	R_J	1.048 ± 0.032
Planet Mass	M_P	M_J	0.208 ± 0.022
Planet Density	ρ_P	g cm^{-3}	0.223 ± 0.029
Planet Surface Gravity	$\log g_P$	$\log \text{cm s}^{-2}$	$2.670^{+0.049}_{-0.056}$
RV Semi-Amplitude	K	m s^{-1}	21.3 ± 2.1
Scaled Semi-Major Axis	a/R_*		$10.28^{+0.21}_{-0.31}$
Semi-Major Axis	a	au	0.0757 ± 0.0014
Orbital Inclination	i	degrees	88.90 ± 0.76
Transit Duration	T_{14}	hours	5.85 ± 0.073
Incident Stellar Flux	F_{inc}	$\text{erg s}^{-1} \text{cm}^{-2}$	$(5.66 \pm 0.62) \times 10^8$
Equilibrium Temperature ^f	T_{eq}	K	1257 ± 34
Atmospheric Scale Height ^g	H	km	1020^{+150}_{-130}

f - assuming zero albedo

g - assuming atmospheric mean molecular mass is $2.2u$

From the analysis set out in Section 2.3, we find NGTS-12b to be an inflated sub-Saturn mass planet, with a mass and radius of $M_P = 0.208 \pm 0.022 M_J$ and $R_P = 1.048 \pm 0.032 R_J$. This mass and radius gives NGTS-12b a relatively low density of $\rho_P = 0.223 \pm 0.029 \text{ g cm}^{-3}$, and using the method of Southworth et al. (2007) we derive a surface gravity of $\log g_P = 2.670^{+0.049}_{-0.056}$. Based on these parameters, we expect NGTS-12b to have an extended gaseous atmosphere.

We compare NGTS-12b to the population of currently known planets in Figure 2.5. We note that NGTS-12b is at the lower mass edge of the large majority of the currently known hot-Jupiter planet population. In Figure 2.5, the presence of the Neptunian desert (e.g. Mazeh et al., 2016) can be clearly seen, and NGTS-12b lies on the edge of the desert. The desert boundaries found by Mazeh et al. (2016) are not particularly well defined for periods $P > 5$ d, and based on this one might not consider NGTS-12b a true Neptune desert planet based on period alone. The fact that NGTS-12b quite clearly lies on the boundary of the desert when we consider incident flux instead of simply period implies that the stellar parameters must be taken into account when studying the Neptune desert and the physical processes which shape it. This same effect has been investigated previously in more detail by Eigmüller et al. (2019) in relation to NGTS-5b.

Tidal interaction between the star and planet has recently been shown to be a significant source of inflation for sub-Saturn mass planets (Millholland et al., 2020). Despite focusing on planets with $R_P < 8.0 R_\oplus$, Millholland et al. (2020) also noted that tidal inflation could play a role

for larger radius planets (e.g. WASP-107b; Anderson et al., 2017). Baraffe et al. (2008) provide model radii for irradiated planets at a distance of 0.045 au from the Sun. This is a reasonable approximation as the irradiation received by NGTS-12b is equivalent to orbiting at a separation of 0.049 au from the Sun. Assuming a heavy metal fraction of $Z = 0.02$, the Baraffe et al. (2008) tables give a predicted radius for a $50 M_{\oplus}$ planet at an age of 7.95–10.01 Gyr of $1.044\text{--}1.057 R_J$. This prediction agrees well with the derived radius of $1.048 \pm 0.032 R_J$. Therefore, we conclude that the inflation of NGTS-12b is driven by stellar irradiation and tidal effects have very little, if any, influence on R_p . Due to the circular orbit of NGTS-12b this is not surprising, however obliquity tides alone could still have had an impact (Millholland et al., 2020).

We also investigate how the bulk density of a planet, ρ_p , varies with both the stellar irradiation flux incident on it, F_{inc} , as well as the planet’s mass, M_p . From Figure 2.6 we can see a steady decrease in ρ_p with increasing F_{inc} for planets of a similar mass. We also note from Figure 2.6 that NGTS-12b has one of the lowest densities for planets with a similar level of irradiation. It can also be seen that the majority of planets with lower densities than NGTS-12b have both a larger F_{inc} and M_p . We also note that all the planets in the top left region of Figure 2.6 with $F_{\text{inc}} > 10^9 \text{ erg s}^{-1} \text{ cm}^{-2}$ and $\rho_p < 0.2 \rho_J$ have a greater mass than NGTS-12b. This implies that a minimum mass is required to maintain an extended atmosphere under these extreme levels of irradiation. This suggests that the level of irradiation received by NGTS-12b is close to an upper limit of irradiation before significant atmospheric loss occurs.

Given NGTS-12b has a low bulk density ($0.223 \pm 0.029 \text{ g cm}^{-3}$), a relatively high equilibrium temperature ($1257 \pm 34 \text{ K}$) and orbits a fairly bright host star ($T = 11.6 \text{ mag}$), NGTS-12b provides a valuable target for atmospheric characterization through transmission spectroscopy. Kempton et al. (2018) introduced a Transmission Spectroscopy Metric (TSM) for the purposes of identifying good targets for transmission spectroscopic follow-up, based on the expected signal-to-noise of *JWST* observations. In Figure 2.7 we compare the TSM value for NGTS-12b to other transiting planets. We note that NGTS-12b has a reasonably high TSM, especially when compared to planets of similar and longer orbital periods. Therefore, NGTS-12b presents an opportunity to study the atmosphere of a planet on a longer period than the main population of currently known hot Jupiters.

The discovery of NGTS-12b again shows that NGTS is able to find transiting planets that were not detectable to previous ground-based transit surveys. Figure 2.8 shows that NGTS-12b is one of the longest period planets discovered with a ground-based transit survey to date. Only twelve other ground-based transit survey planets have longer orbital periods. Of these, all have deeper transits than NGTS-12b. The placement of NGTS-12b on in Figure 2.8 suggests that the higher photometric precision achieved by NGTS compared to other ground-based transit surveys will allow more planets with longer orbital periods and shallow transits to be found by NGTS

over the coming years.

2.5 Conclusions

We report the discovery of NGTS-12b, a sub-Saturn mass transiting exoplanet with a mass and radius of $0.208 \pm 0.022 M_J$ and $1.048 \pm 0.032 R_J$. The 7.53 d orbital period of NGTS-12b, which is longer than the periods of 95% of the other planets discovered by all ground-based transit surveys, makes it the longest period planet to date discovered by the main NGTS survey. The transits of NGTS-12b are also detected in the *TESS* Full-Frame Images, and the overall precision of the phase-folded *TESS* light curve is similar to that of the NGTS light curve (see Figure 2.4).

With its low density ($0.223 \pm 0.029 \text{ g cm}^{-3}$), and long orbital period (7.53 d), NGTS-12b represents a good chance to study the atmosphere of a planet with a longer period than the bulk population of hot Jupiters. The mass and irradiation of NGTS-12b places it on the boundary of the Neptunian desert in a currently under-sampled region of parameter space. Therefore, NGTS-12b can play an important role in understanding the physical processes shaping this region.

Chapter 3

Simultaneous TESS and NGTS Observations of WASP-166b

Note

This chapter is a reproduction of the paper “*Simultaneous TESS and NGTS transit observations of WASP-166 b*” (Bryant et al., 2020b) published in Monthly Notices of the Royal Astronomical Society in June 2020. All observations and analyses were performed by me, as was the writing of all sections.

Abstract

We observed a transit of WASP-166 b using nine NGTS telescopes simultaneously with *TESS* observations of the same transit. We achieved a photometric precision of 152 ppm-per-30 minutes with the nine NGTS telescopes combined, matching the precision reached by *TESS* for the transit event around this bright ($T = 8.87$ mag) star. The individual NGTS light curve noise is found to be dominated by scintillation noise and appears free from any time-correlated noise or any correlation between telescope systems. We fit the NGTS data for T_C and R_P/R_* . We find T_C to be consistent to within 0.25σ of the result from the *TESS* data, and the difference between the *TESS* and NGTS measured R_P/R_* values is 0.9σ . This experiment shows that multi-telescope NGTS photometry can match the precision of *TESS* for bright stars, and will be a valuable tool in refining the radii and ephemerides for bright *TESS* candidates and planets. The transit timing achieved will also enable NGTS to measure significant transit timing variations in multi-planet systems.

3.1 Introduction

The Transiting Exoplanet Survey Satellite (*TESS*; Ricker et al., 2015) has been hunting for exoplanets transiting bright stars since July 2018. During its two year nominal mission, *TESS* monitored $\approx 80\%$ of the sky, providing light curves at a 2 minute cadence for $> 200,000$ stars and at a 30 minute cadence for the full field-of-view. *TESS* has already made a number of notable discoveries of exoplanets transiting bright stars, including Π Mensae c (Huang et al., 2018; Gandolfi et al., 2018), HD1397 b (Brahm et al., 2019; Nielsen et al., 2019), and the HR858 system (Vanderburg et al., 2019).

As part of this discovery process, ground-based transit photometry is used to improve spatial resolution, verify the transit is achromatic, check for transit timing variations, and improve the precision on transit parameters such as period, phase, and depth (e.g. Collins et al., 2018b). However ground-based photometric observatories struggle to reach the precision of *TESS* for bright stars. The primary obstacle is that precise ground-based time-series photometry requires similar magnitude reference stars to the target star in order to adequately correct for photometric changes caused by the Earth’s atmosphere. However for a $T = 8.87$ mag star the nearest similar magnitude reference star is, on average, separated by 1 degree (Collins et al., 2018b). This is far outside the field-of-view of most photometric facilities (Collins et al., 2018b).

The Next Generation Transit Survey (NGTS; Wheatley et al., 2018) is an exoplanet hunting facility situated at ESO’s Paranal Observatory in Chile. It consists of twelve robotic telescopes, each with a 20 cm diameter and a field-of-view of 8 deg^2 . The wide field-of-view of NGTS places it in a unique position to obtain photometric follow-up from the ground of the brightest exoplanet host stars. One limitation is that the 20 cm telescope apertures do not collect as many photons we would wish for high-precision photometry. We mitigate this limitation with NGTS by observing a target star simultaneously with multiple telescopes. This increases the effective collecting area of the facility, allowing us to obtain a light curve equivalent to a larger aperture telescope while preserving the wide field-of-view.

One of the main sources of photometric noise for NGTS observations of bright stars is scintillation noise. Scintillation noise arises from light passing through regions of turbulence in the Earth’s atmosphere, resulting in changes in intensity (eg. Osborn et al., 2015). Scintillation has been shown to behave as white noise on transit timescales (Föhring et al., 2019). As such, simultaneous observations also reduce the noise present in the light curves due to atmospheric scintillation by a factor \sqrt{N} , where N is the number of telescopes used. This is provided that scintillation noise does not correlate between the telescopes. This is especially important for NGTS observations of bright stars ($I \leq 10$ mag) as in this regime scintillation noise dominates all other noise sources (Wheatley et al., 2018).

An early experiment using multiple NGTS telescopes was the observation of the K2 transiting planet HD 106315 c in 2017 (Smith et al., 2020). This work demonstrated that by using multiple NGTS telescopes we could achieve the photometric precision needed to detect a shallow (0.1%) transit from the ground.

In this chapter we present a study into the photometric precision and noise properties of the NGTS multi-telescope observations for a bright star hosting a transiting planet. WASP-166 is a $V = 9.351$ mag F-type dwarf star which hosts a $0.64 \pm 0.03 R_J$ transiting exoplanet which orbits the star on a period of 5.4435 d (Hellier et al., 2019). A summary of the main properties of WASP-166 are set out in Table 3.1. We were able to observe WASP-166 simultaneously with *TESS*, which provides a unique opportunity to rigorously compare the NGTS ground-based light curve with the *TESS* light curve.

We set out this study in the following manner. In Section 3.2 we outline both the NGTS and the *TESS* observations of WASP-166. In Section 3.3.1 we examine the noise properties of the multi-telescope NGTS photometry. We model the NGTS data and examine the uncertainties on key system parameters in Sections 3.3.2 & 3.3.3. The comparison between the NGTS and *TESS* photometry is set out in Section 3.3.5. Finally, we provide a discussion of our results in Section 3.4.

3.2 Observations

3.2.1 NGTS Photometry

WASP-166 was observed with NGTS on the nights 2019 February 25 and 26. The observations were taken at airmass < 2 and under photometric conditions. Across both nights, nine of the twelve NGTS telescopes were available to be used to simultaneously observe WASP-166. Each telescope used the custom NGTS filter (520 – 890 nm). A total of 40,003 images were taken across the two nights, all with an exposure time of 10 seconds. The NGTS cameras have a readout time of approximately 3 seconds, and therefore the full cadence of these observations was 13 seconds. For all observations, due to the brightness of WASP-166 the telescopes were slightly defocussed, in order to avoid saturation. The NGTS telescope guiding is performed using the DONUTS auto-guiding algorithm (McCormac et al., 2013); this extremely high precision guiding resulted in a mean RMS of the location on the CCD of the target of 0.27 pixels (pixel scale: $4.97''/\text{pix}$) across the two nights.

The reduction is carried out on the raw frames using a custom aperture photometry pipeline which utilises SEP (Bertin and Arnouts, 1996; Barbary, 2016). This pipeline computes the photometry for a set of circular apertures with a range of radii, and the final light curve is

Table 3.1: Stellar Properties for WASP-166

Stellar Parameters	Value	Source
Name	WASP-166	Hellier et al. (2019)
TIC ID	408310006	TIC v8
TOI ID	576	
R.A.	09 ^h 39 ^m 30 ^s 09	2MASS
Dec	−20°58′56″9	2MASS
$\mu_{\text{R.A.}}$ (mas y ^{−1})	−55.082 ± 0.072	<i>Gaia</i> DR2
$\mu_{\text{Dec.}}$ (mas y ^{−1})	10.927 ± 0.069	<i>Gaia</i> DR2
Parallax (mas)	8.7301 ± 0.0448	<i>Gaia</i> DR2
R_* (R _⊙)	1.25 ± 0.06	TIC v8
M_* (M _⊙)	1.14 ± 0.15	TIC v8
<i>TESS</i> (mag)	8.8685 ± 0.0062	TIC v8
<i>Gaia G</i> (mag)	9.257 ± 0.00031	<i>Gaia</i> DR2
<i>V</i> (mag)	9.351 ± 0.002	
<i>B</i> (mag)	9.940 ± 0.034	
<i>J</i> (mag)	8.350 ± 0.021	2MASS
<i>H</i> (mag)	8.135 ± 0.033	2MASS
<i>K</i> (mag)	8.032 ± 0.023	2MASS
<i>W1</i> (mag)	7.999 ± 0.025	WISE
<i>W2</i> (mag)	8.054 ± 0.019	WISE

2MASS (Skrutskie et al., 2006); WISE (Wright et al., 2010);
Gaia DR2 (Gaia Collaboration et al., 2016); TIC v8 (Stassun et al., 2018)

determined by finding the aperture with the minimum RMS scatter. Background subtraction is performed by creating and subtracting a global background map. This background map is created using SEP. After extensive testing we find that bias, dark, and flat-field frame corrections do not improve the precision of the photometry. In some conditions these corrections decrease the precision. Therefore, we do not apply these corrections during the image reduction.

Comparison stars are ranked according to their colour, brightness and position on the image, relative to the target star. This ranking is used to select the best non-saturated non-variable comparison stars. Any comparison stars with a significantly bright *Gaia* neighbour which would contaminate the photometric aperture are automatically discarded. The differential target star flux is computed by dividing the photometric counts from the target star by the total sum of the counts from all the comparison stars.

Despite WASP-166 being a bright star ($T = 8.87$ mag), the wide field-of-view of NGTS allowed us to monitor 23 good quality comparison stars of similar magnitude to WASP-166, more than could be monitored by a 1 m telescope. The 23 comparison stars monitored were the same for each telescope. We combine and analyse these photometric data from each NGTS telescope in Section 3.3.

On the night of 2019 February 25, a transit of WASP-166 b was observed, and we use these data to investigate the precision with which we can measure planetary system parameters with this observing mode. We use the out-of-transit data from the night of 2019 February 26 to investigate the multi-telescope noise properties of NGTS, as it is independent of any transit modeling steps. The nine individual NGTS telescope light curves are displayed in Figure 3.1 and the NGTS photometry is provided in Table 3.2.

3.2.2 *TESS* Photometry

WASP-166 was observed by *TESS* (Ricker et al., 2015) at a cadence of 2 minutes from 2019 February 02 to 2019 February 27 during Sector 8 of the primary *TESS* mission. *TESS* observes over a wavelength range of 600 – 1000 nm. WASP-166 fell on *TESS* Camera 2/CCD 3 and data were reduced by the official SPOC pipeline (Jenkins et al., 2016). We accessed the data through the MAST portal¹ and utilized the PDCSAP_FLUX, which has had any spacecraft systematics removed (see Jenkins et al., 2016, for details). The full *TESS* light curve of WASP-166 spans ≈ 27.4 d and contains four full transits. However for this work we consider only the sections of the light curve which coincide with the NGTS observations; $2458540.51961711 \leq \text{BJD} \leq 2458540.8531236$ for the transit night and $2458541.5199 \leq \text{BJD} \leq 2458541.84915$ for the non-transit night. This allows for a more direct comparison of the light curve and parameter

¹<https://mast.stsci.edu/portal/Mashup/Clients/Mast/Portal.html>

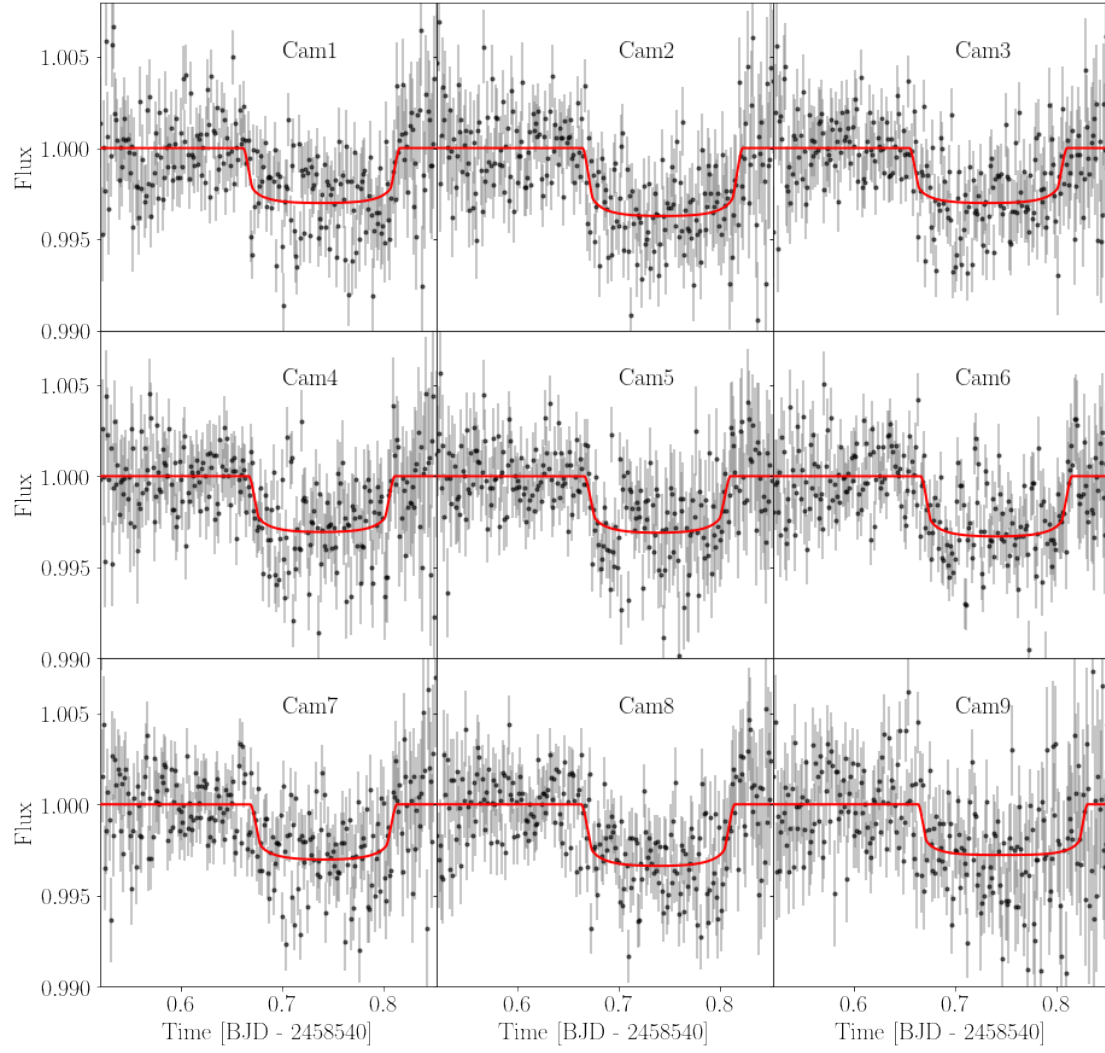


Figure 3.1: The nine individual NGTS telescope light curves for the transit of WASP-166 b on 2019 February 25. The normalised flux data points are all shown binned to 2 minutes. The solid red lines give the individual transit models for each light curves (see Section 3.3 for details).

Table 3.2: Example table of the NGTS photometry of WASP-166. The full table is available with the online journal publication of this study (Bryant et al., 2020b).

BJD (TDB) (-2450000)	Flux	Flux Error	Cam
8540.51964025	0.998963	0.008012	1
8540.51979072	0.999378	0.007995	1
8540.51994118	0.999461	0.007972	1
8540.52009164	0.997650	0.007938	1
8540.52024211	0.997247	0.007918	1
8540.52039257	1.000107	0.007918	1
8540.52054303	0.998085	0.007882	1
8540.52068192	1.015229	0.007980	1
8540.52083238	0.995757	0.007831	1
8540.52098285	0.980196	0.007706	1

precision available from the two datasets.

3.3 Analysis

3.3.1 NGTS Noise Properties

We used our NGTS observations of WASP-166 on the night of 2019 February 26 to investigate noise correlation between NGTS telescopes. We studied three main properties of the noise of the individual NGTS light curves.

Noise properties of the Individual Telescopes

To investigate the noise properties of the individual NGTS telescopes, we computed the RMS precision over a range of timescales, τ , from unbinned cadence (13 seconds) up to 45 minutes. We compare the RMS trend with timescale to that expected from purely white (Gaussian) noise. Our results are plotted in Figure 3.2. We find that the individual NGTS telescopes closely follow the predicted $1/\sqrt{\tau}$ white noise scaling. This suggests that the noise in the NGTS light curves is dominated by Gaussian noise, and that we do not have any significant systematic noise on these timescales. In some telescopes we see deviations from the predicted Gaussian noise scaling, especially at larger τ values. This is a consequence of only having a small number of binned flux data points at large τ values. This result gives us confidence that systematic noise is not a major hindrance to the effectiveness of this multi-telescope observing method.

Flux Correlations between Telescopes

We performed a pair-wise correlation test of all the NGTS light curves of WASP-166 to search for any obvious correlation in the photometric noise between the NGTS telescopes. Since the NGTS telescopes all operate independently, the time-stamps for the nine individual light curves are not perfectly synchronous. We therefore create a set of time-stamps at 13 second intervals, between the start and end of the observations. Each telescope time series was then mapped to these new time-stamps before comparing to the other telescopes. This was done by assigning each flux data point to the new time-stamp which represents the smallest deviation in time from the actual mid-point of the exposure. This allows for a more accurate comparison between the fluxes from the pairs of telescopes.

We find no flux correlation between any pair of telescopes – see Figure 3.3. We also note that the flux distribution for each telescope looks Gaussian. This again gives us confidence that the light curves are free from systematic noise.

Combining Individual Telescope Data

Given individual NGTS light curves show uncorrelated Gaussian noise, by combining the light curves we expect a combined light curve with a RMS scatter, σ_m , given by:

$$\sigma_m = \frac{\sigma_s}{\sqrt{N}}, \quad (3.1)$$

where σ_s is the RMS scatter of a single telescope light curve, and N is the number of telescopes combined.

For each value of N , we calculated σ_m at a timescale of 30 min for each possible telescope combination. We then found the mean of the σ_m for each value of N . The results are set out in Figure 3.4, showing that the calculated σ_m values are very close to the uncorrelated Gaussian-noise expectation of σ_m given by Equation 3.1. The deviation from the expected σ_m for $N = 9$ is just 5 ppm.

Scintillation Noise

As stated in Section 3.1, the noise in NGTS light curves of bright stars ($I \leq 10$ mag) is expected to be dominated by scintillation noise (Wheatley et al., 2018). We tested this by analysing the variation in the flux RMS during the observation and comparing this variation to the predicted light curve noise. We calculated the predicted scintillation noise using the modified Young's

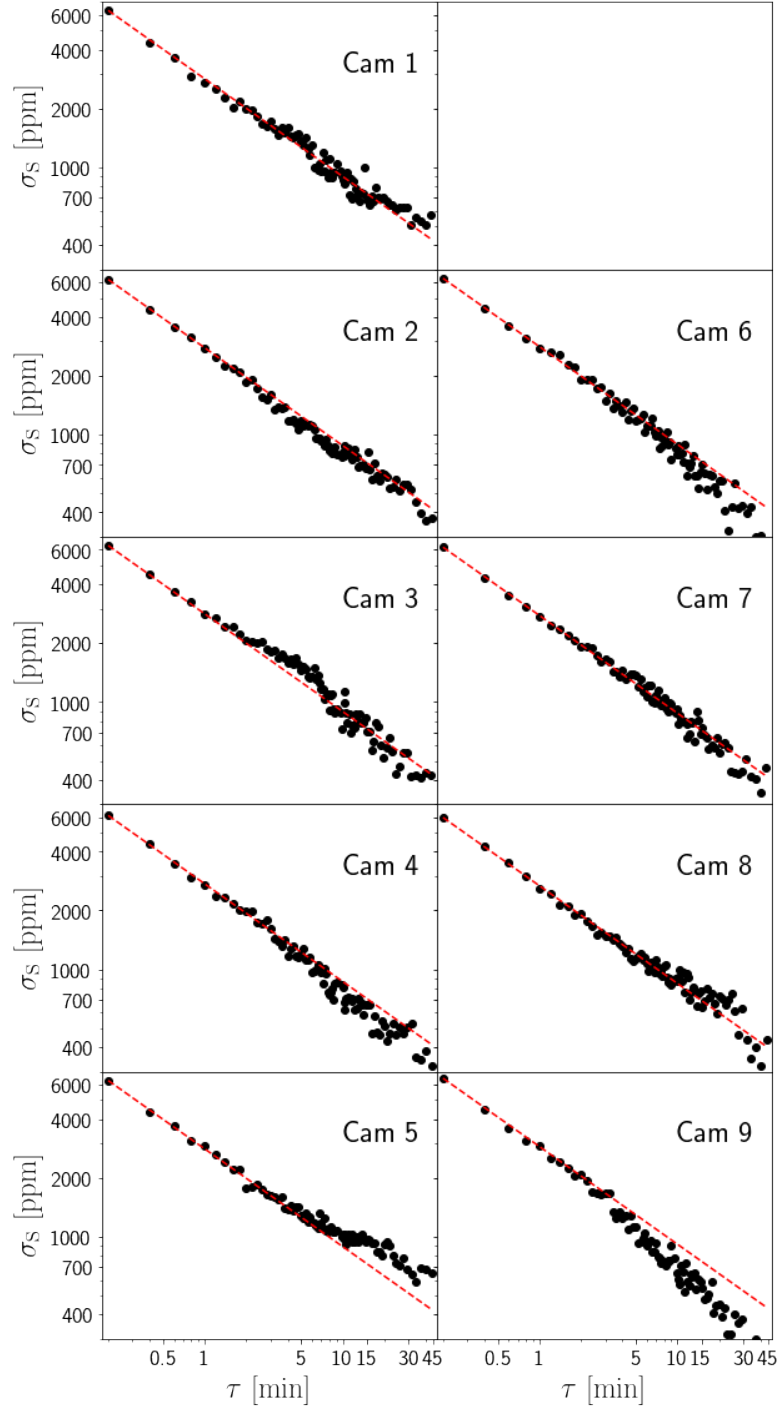


Figure 3.2: Variation of the light curve precision for each individual telescope light curve with the timescale over which the precision is calculated. The red dashed lines give the $1/\sqrt{\tau}$ Poisson noise scaling that would be expected for a pure white noise light curve and are scaled to the first point, which is a timescale of 13 seconds - ie. unbinned data. Each panel gives the results from a single NGTS telescope, with the panel labels giving the ID of this telescope.

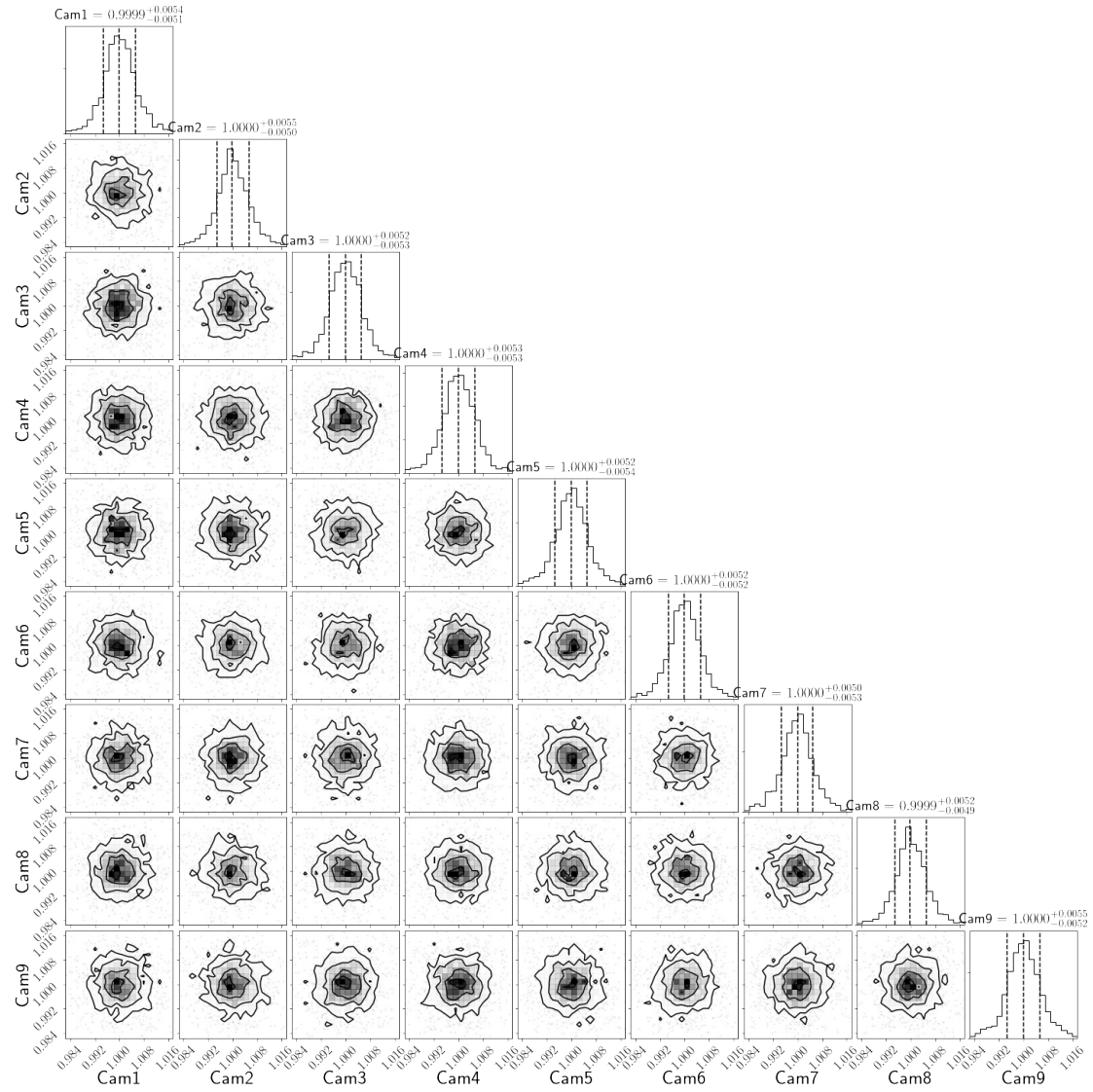


Figure 3.3: Corner plot displaying how the flux from WASP-166 correlates for each possible pair of the nine NGTS telescopes. The headers give the median and 1σ deviations of the flux from each telescope. The plot has been produced using CORNER.PY (Foreman-Mackey, 2016).

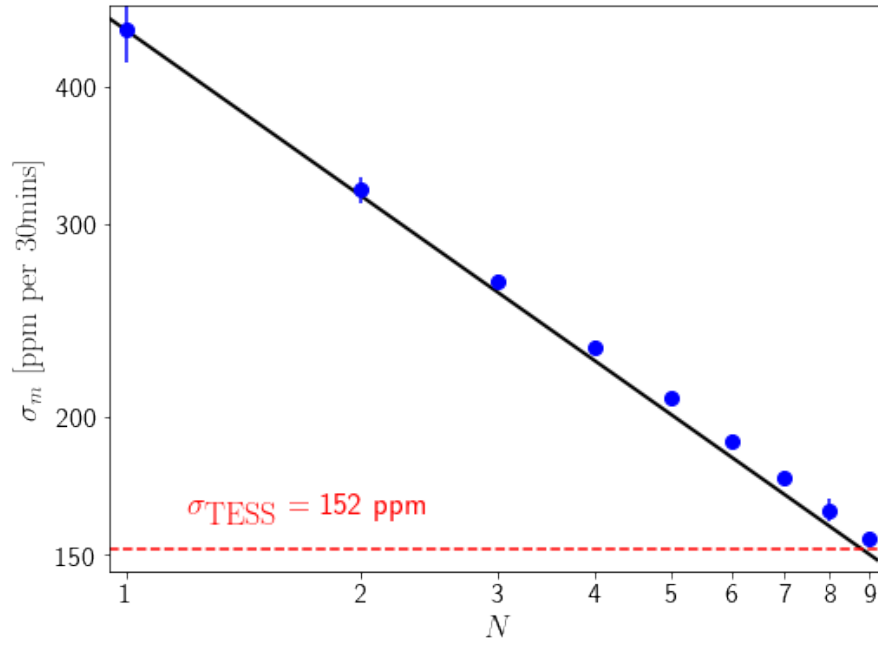


Figure 3.4: 30 minute RMS precision (σ_m) of the NGTS combined light curve for WASP-166 as a function of the number of individual telescope light curves co-added. The blue points give the mean precision for each possible combination of N individual light curves (see the text for details). The errorbars give the standard error on this mean. The solid black line shows the Gaussian $1/\sqrt{N}$ improvement in σ_m for pure white noise, scaled from the $N = 1$ data point. The dashed red line shows the calculated RMS precision of the *TESS* light curve for WASP-166.

approximation

$$\sigma_Y^2 = 10 \times 10^{-6} C_Y^2 D^{-4/3} t^{-1} (\sec z)^3 \exp(-2h_{\text{obs}}/H), \quad (3.2)$$

where D is the diameter of the telescope aperture (m), t is the exposure time used (s), z is the zenith distance, h_{obs} is the altitude of the observatory (2,440 m for Paranal), and H is the scale height of the atmospheric turbulence, which is taken to be 8,000 m (Osborn et al., 2015). C_Y ($\text{m}^{2/3}\text{s}^{1/2}$) is an empirical coefficient and σ_Y is the dimensionless normalised scintillation noise (Young, 1967; Osborn et al., 2015).

At high airmass, differential refraction across the field-of-view will cause the comparison stars to move on the CCD relative to the target star. The slight differences in sensitivity of neighbouring pixels on the CCD will result in this movement causing an increase in the flux RMS at high airmass. Therefore, we expect the scintillation noise model (Equation 3.2) to not perfectly describe the observed light curve noise at high airmass.

We modelled the noise in our data as a combination of scintillation noise and photon noise from both the target star and the sky background. We used only the data with airmass $\sec z < 1.2$ and fit for the coefficient C_Y , finding a value of $C_Y = 1.57 \pm 0.06$. This is in good agreement with the results from Osborn et al. (2015). They find a median value of $C_Y = 1.56$ for Paranal, with 1st and 3rd quartiles of 1.27 and 1.90.

The flux RMS and the noise model are displayed in Figure 3.5, and we see that the noise in the NGTS light curve is dominated by the scintillation noise, as predicted. The variation in this noise during the night is well described by Young’s approximation for low airmass. The predicted deviation of the flux RMS values from the noise model at high airmass can also be clearly seen.

3.3.2 Fitting Individual NGTS Light Curves

In order to determine the transit parameters of WASP-166 b from our NGTS data from the night of 2019 February 25, we simultaneously detrended the individual NGTS telescope light curves with respect to external parameters and fitted each transit using *BATMAN* (Kreidberg, 2015). We tested a number of external parameters for detrending, including airmass, target pixel position, sky background, and time. We found that only detrending with respect to time significantly improved the log likelihood, $\ln \mathcal{L}$, of the final model.

For the *BATMAN* transit model, we used the following free parameters: the time of the transit centre, T_C , the orbital period, P , the planet-to-star radius ratio, R_P/R_* , the impact parameter, b , and the stellar density, ρ_* . We used a quadratic limb-darkening law, and fitted the parametrized coefficients q_1 and q_2 from Kipping (2013a). For these coefficients, we used

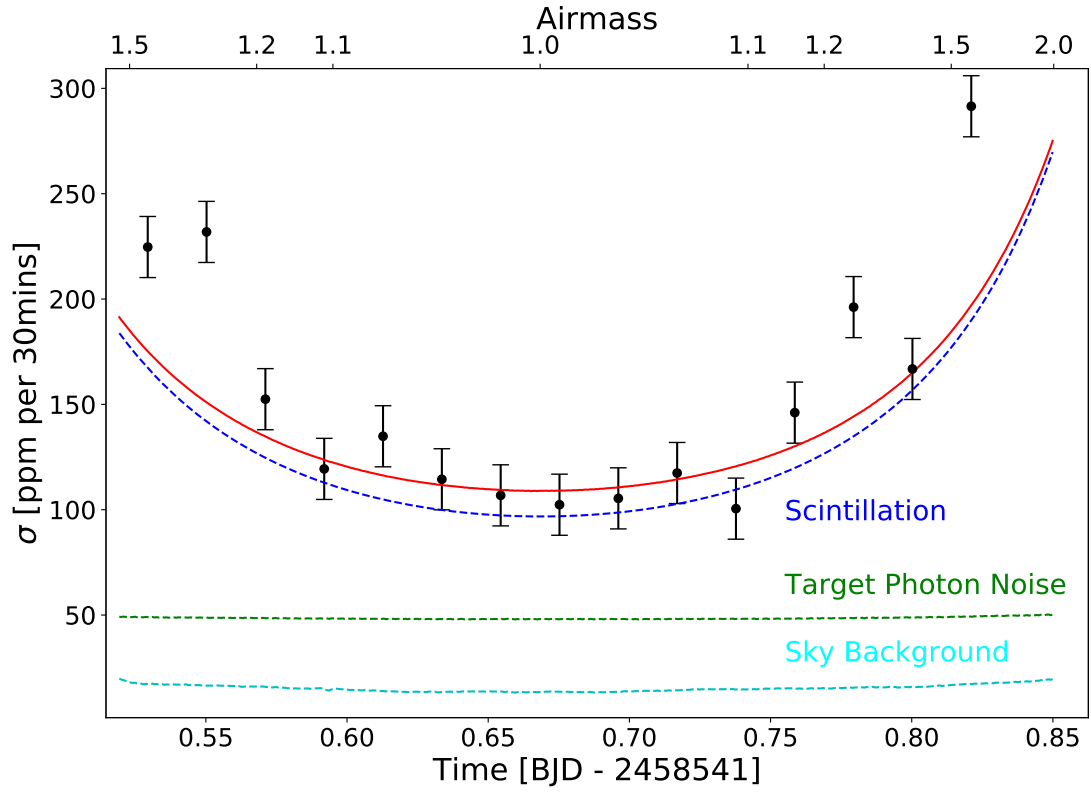


Figure 3.5: Variation of the flux RMS for the combined NGTS light curve. The total noise model (solid red) includes the scintillation noise (blue dashed) and the photon noise from the target star (green dashed) and the sky background (cyan dashed).

uniform priors between 0 and 1, in order to ensure physically realistic limb-darkening profiles (Kipping, 2013a).

As the NGTS data cover just a single transit, they alone do not place any constraints on the period. However, Hellier et al. (2019) were able to very tightly constrain the period due to the very long time baseline afforded to them by the combination of WASP and *TESS* photometry, as well as their precise measurement of the Rossiter-McLaughlin effect for WASP-166. Therefore we place a 1σ Gaussian prior on the period, based on the period and uncertainty reported in Hellier et al. (2019). We also utilise the stellar parameters from version 8 of the TIC (Stassun et al., 2019) to place a Gaussian prior on ρ_* with a mean and standard deviation of $0.58 \pm 0.11 \rho_\odot$. In addition, we impose a uniform prior on R_p/R_* with limits of 0. and 0.25 and a further uniform prior that ensures that $b \geq 0$. Hellier et al. (2019) find a 2σ upper limit of the eccentricity of $e < 0.07$, and so they adopt a circular orbit. Based on this, and the fact that our photometric data provide little information on the eccentricity of the orbit, we also adopt $e = 0$. The modelling was performed using an MCMC sampling method implemented using the *emcee* Ensemble Sampler (Foreman-Mackey et al., 2013). We ran 50 walkers for 15,000 steps as a burn-in process, and then a further 5,000 draws were made to sample the posterior for each chain. The chains were inspected and found to be well mixed. We plot the best fit models for each individual light curve in Figure 3.1.

In analysing these fits, we focus on the two main parameters which can be obtained from a single transit: the planet-to-star radius ratio, R_p/R_* , and the time of the transit centre, T_C . In Figure 3.6, we compare the posterior parameter distributions (PPDs) for these two parameters from the modelling of the nine individual NGTS light curves.

In terms of the individual PPDs, we see good agreement between the obtained parameter values for the two parameters. For R_p/R_* , the PPDs behave as might be expected, with the single telescope PPDs being scattered around the "true" value. The average single telescope uncertainty in R_p/R_* is ± 0.0034 . The weighted mean of the nine R_p/R_* measurements is 0.05245 ± 0.00110 .

For T_C , we again see the expected distribution of single light curve values, but with a couple of outliers. These outliers are present for T_C but not R_p/R_* since the measured value of T_C is dependant upon the measured ingress and egress times. These sections of the light curve are each only 13 minutes long for a transit of WASP-166 b, and so a few out-lying points in these sections of the light curve strongly bias the measured T_C value. On the other hand, as the section of the light curve from which R_p/R_* is measured is ≈ 3.5 hours long, the same number of outlying points will not have a noticeable effect on the measured R_p/R_* value. The average single telescope uncertainty from all nine measurements of T_C is ± 0.00318 d. We find a weighted mean of the nine measurements of $2458540.74035 \pm 0.00088$.

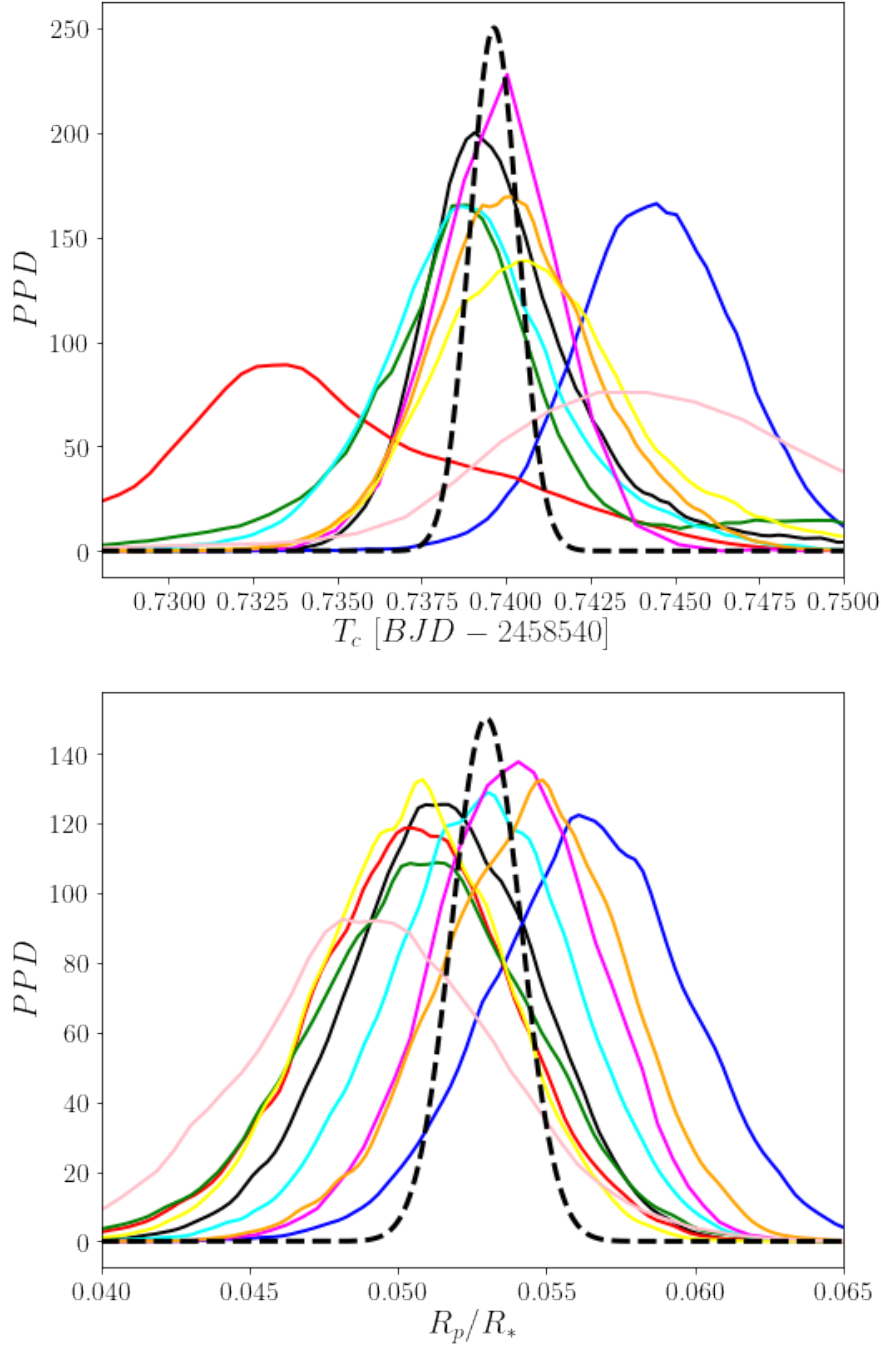


Figure 3.6: Posterior Parameter Distributions (PPDs) for the two main free parameters included in the fits: T_C (top panel) and R_p/R_* (bottom panel). The solid lines give the PPDs for the individual telescopes, with each colour corresponding to the same telescope in each panel. These PPDs are normalised such that the area enclosed is equal to 1. The dashed black curves give the PPDs from the fit to the full combined dataset. These curves are scaled such that the area enclosed is less than 1 for clarity.

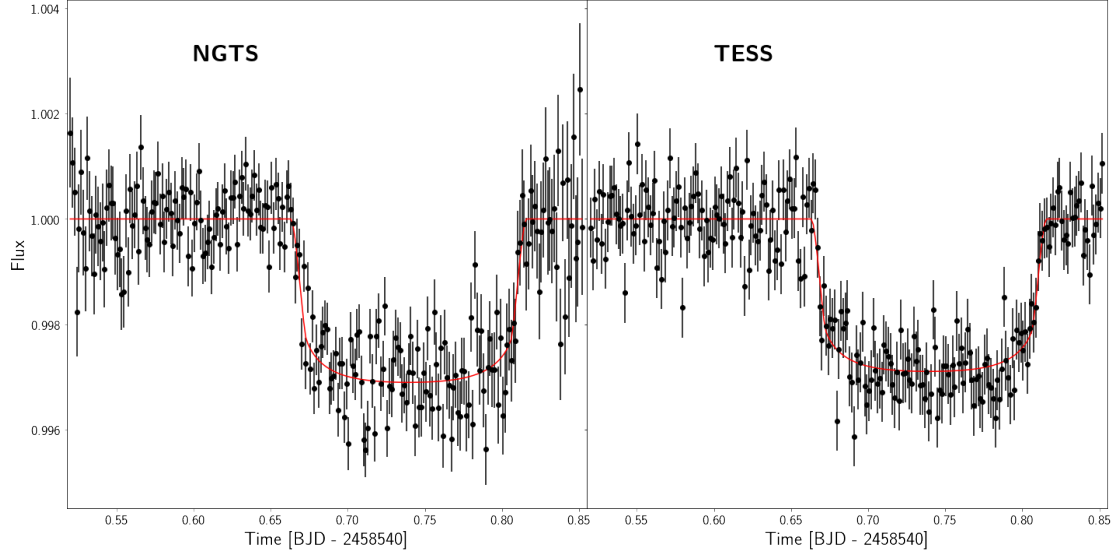


Figure 3.7: Light curves showing the 2019 February 25 transit of WASP-166 b. **Left:** combined light curve obtained with a simultaneous observation using nine NGTS telescopes. The black circles show the data binned to 2 minutes, for visual comparison with the 2 minute cadence *TESS* data. The solid red line gives the best fit transit model from the modelling process (section 3.3.3). **Right:** Black circles show the unbinned 2 minute cadence *TESS* data. The solid red line again gives the transit model from the modelling process (section 3.3.4).

3.3.3 Fitting Combined Light Curve

In addition to fitting each of the individual light curves, we also fitted the combined light curve. For this fitting we also included a constant offset, c , to account for the position of the out-of-transit flux baseline.

The combined NGTS light curve and the resultant transit model from this modelling process are displayed in Figure 3.7. The system parameters obtained are given in Table 3.3, where the parameter values reported are the median values from the posterior distributions, with the corresponding 1σ uncertainties.

We compare this combined light curve fit to the individual light curves fits from Section 3.3.2. The PPD of the combined light curve fit is plotted in Figure 3.6. The average single telescope uncertainty in R_p/R_* is ± 0.0034 , while the uncertainty in R_p/R_* from the combined light curve is ± 0.0012 . Thus we see that the uncertainty in the measured value of R_p/R_* from the combined light curve is reduced by a third, as expected from the $1/\sqrt{N}$ scaling. In addition, the combined light curve uncertainty is comparable to the error on the weighted mean of the nine individual light curve measurements. We also find that the R_p/R_* value derived from the combined light curve is consistent with the nine light curve weighted mean at the 1σ level.

The uncertainty in T_C measured from the combined light curve is ± 0.0007 d, which is a reduction from the average of the individual light curve uncertainties found in Section 3.3.2 (± 0.00318 d) of more than a third. The two individual light curves with the high T_C uncertainties inflate the average single telescope uncertainty. However, the fit to the combined light curve is less affected by the outlying points which result in the higher single telescope uncertainties.

As with R_p/R_* , the T_C value derived from the combined light curve is consistent with the nine light curve weighted mean at the 1σ level. We note that the error on this weighted average is slightly higher than the combined light curve T_C uncertainty. This is again likely a result of the outlying individual T_C measurements having more of an effect on the weighted mean than is had by the outlying data points in these light curves on the combined light curve T_C measurement.

3.3.4 Fitting *TESS* Data

In order to make a direct comparison to the results of modelling the NGTS data, we model the *TESS* data with a process identical to that for the combined NGTS light curve detailed in Section 3.3.3. We select just the portion of the *TESS* data obtained simultaneously with our NGTS data ($2458540.51961711 \leq \text{BJD} \leq 2458540.8531236$). The *TESS* data and the resulting best fit transit model are displayed in Figure 3.7, with the parameter values given in Table 3.3. Comparing the precision of the *TESS* and NGTS data for the transit night, we find RMS values of 545 ppm-per-2 minutes for the *TESS* data and 701 ppm-per-2 minutes for the NGTS data. We also note that the scatter of the NGTS data depends strongly on the airmass of the observations (see Figure 3.5). Considering just the NGTS data with airmass $z < 1.2$, we find an RMS of 579 ppm-per-2 minutes.

3.3.5 NGTS and *TESS* Comparison

The main parameters of interest for this comparison are T_C and R_p/R_* , as they both can be constrained by a single transit. We plot the PPDs for these parameters in Figure 3.8.

We find the two values of T_C from NGTS and *TESS* to be consistent to within 0.25σ of each other. The value of R_p/R_* measured from the *TESS* transit is found to be a lower than the value measured from the NGTS data, with a difference of 0.9σ . The R_p/R_* values from NGTS and *TESS* are formally consistent to 1σ , but we note that a similar modelling of the first transit of WASP-166 b in the *TESS* light curve yields a value of $R_p/R_* = 0.05235 \pm 0.00105$. This value represents a difference from the NGTS value of just 0.4σ . We fitted the limb darkening coefficients during the modelling, therefore any differences in measured R_p/R_* values will not be due to any depth difference caused by the differences between the *TESS* and NGTS pass bands. Hellier et al. (2019) measure a value of $R_p/R_* = 0.0530 \pm 0.0007$, which is consistent with the

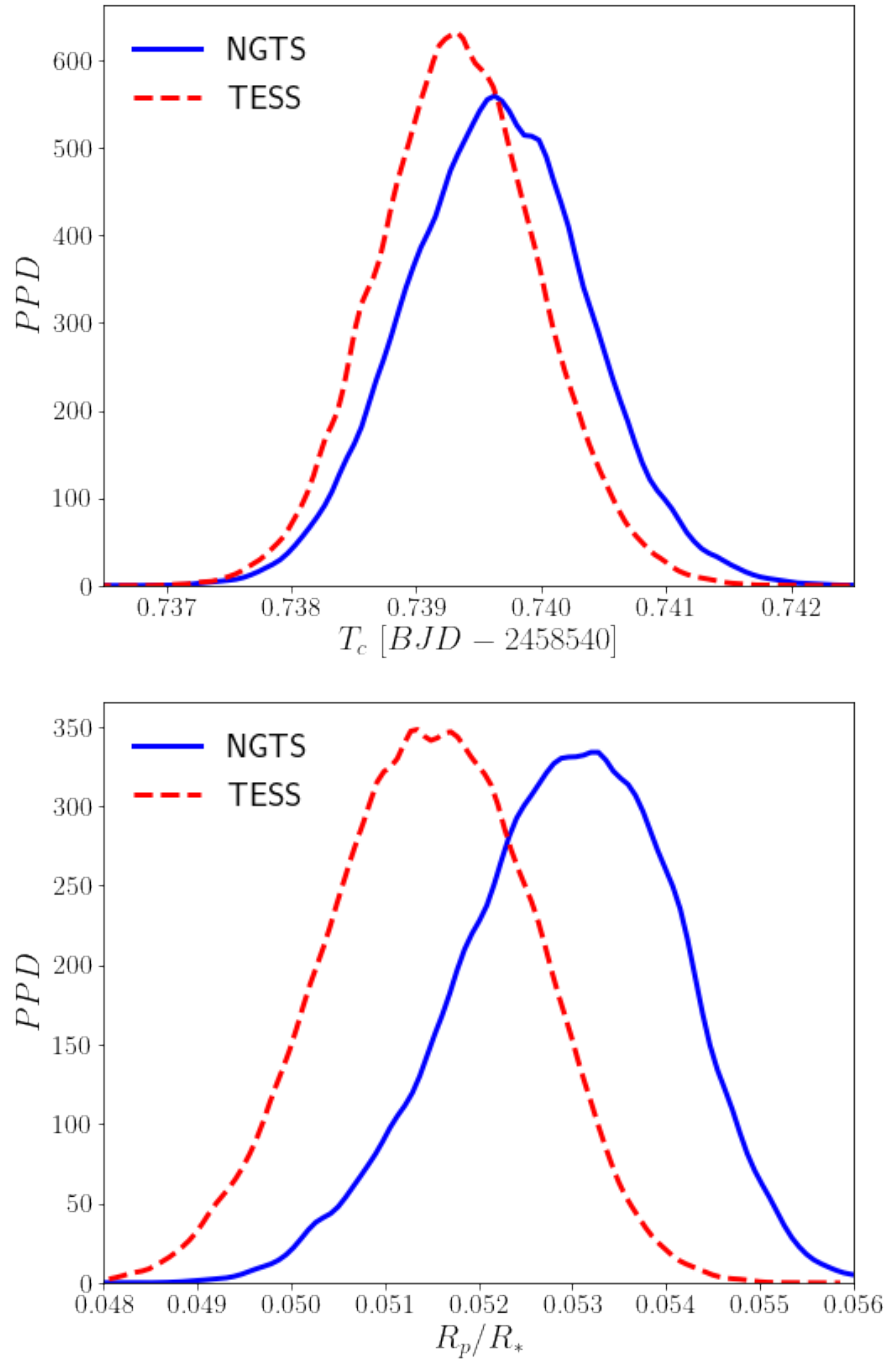


Figure 3.8: Same as Figure 3.6 but comparing the PPDs from the fit to the combined NGTS light curve (solid blue line) and the fit to the *TESS* transit on 2020 February 25 (dashed red line)

value measured from the NGTS transit and the first *TESS* transit, but is discrepant with the value from the *TESS* transit on 2020 February 25.

During Sector 8 of the *TESS* mission, a few days prior to the 2020 February 25 transit, an instrument anomaly caused the heaters to switch on². The resulting temperature increase affected both the camera focal plane scale and the individual CCD mean dark current. It is probable that this resulted in a problem with the systematic error corrections in SPOC pipeline, which could have induced the slightly shallower transit depth observed for this transit.

3.4 Discussion

The NGTS photometric noise for bright stars is dominated by atmospheric scintillation (Wheatley et al., 2018; O’Brien et al., 2022). Scintillation behaves as white noise on the timescales of exoplanet transits (Föhring et al., 2019), and indeed the NGTS light curves in this study confirm this: see Section 3.3.1. We also find that there is no correlation between the photometric noise from individual NGTS telescopes - see Figures 3.3 & 3.4. This indicates that the spacing between the telescopes (approximately 2 m) is of a sufficient size such that the light paths through the atmosphere are separated enough to ensure that they do not result in correlated scintillation noise. The fact that the NGTS telescopes are well spaced is critical for the success of these observations.

For these bright stars, the noise will be dominated by scintillation and photon noise, which will both result in the precision increasing by \sqrt{N} when combining telescopes. However, from Wheatley et al. (2018), CCD readout and sky background become significant noise sources for $I > 13$ mag. This suggests that combining NGTS telescopes would be less advantageous for fainter targets.

We find that we can achieve a precision for transit centre time, T_C , of a single transit of 1 minute for a transit of this bright star. This will allow NGTS multi-telescope observations to measure T_C with a precision of a few minutes for systems of multiple small planets (depth ≈ 1000 ppm), orbiting bright host stars. The *TESS* mission has already revealed many candidate systems of this type, such as TOI-175 (Kostov et al., 2019; Cloutier et al., 2019), TOI-178 (Leleu et al., 2019), and TOI-270 (Günther et al., 2019). These stars are 2 to 3 magnitudes fainter than WASP-166, and so we expect lower photometric precision than we achieved for WASP-166. A lower photometric precision is likely to result in a higher uncertainty on the transit timing (Carter et al., 2008).

We also find in Section 3.3.3 that the measured value of T_C from a single telescope light curve can be biased by outlying data points during ingress or egress. This in turn affects the T_C value that is derived from a weighted mean of the individual T_C measurements. By modelling all

²https://archive.stsci.edu/missions/tess/doc/tess_drn/tess_sector_08_drn10_v02.pdf

the data together as a combined light curve, we find that the measured T_C value and uncertainty is more resistant to these flux outliers.

Observing simultaneously with multiple telescopes also grants some protection against technical faults with individual telescope systems. This is especially of importance for high priority candidates with not many opportunities for observations, such as long period candidates (eg. TOI-222, Lendl et al. (2020); TIC-238855958, Gill et al. (2020c)).

The *TESS* mission has recently been extended for two more years³. As such, the Southern sky will be re-observed by *TESS* between July 2020 and June 2021. *TESS* observes in the anti-Sun direction, and so this extended mission will provide many more opportunities for simultaneous ground and space observations for bright planet hosting stars.

3.5 Conclusion

Our data have shown that the noise in NGTS bright star light curves is dominated by scintillation noise. We have shown that this noise is Gaussian, and is uncorrelated between the telescopes. This allows us to combine simultaneous observations with multiple telescopes to obtain ultra-high precision light curves of individual exoplanet transits. We can combine this technique with the wide field-of-view of the NGTS cameras to achieve some of the highest precisions from the ground for the brightest stars.

We can use this technique to achieve transit timing on order of minutes for planets orbiting bright stars, with transit depths on the order ≈ 1000 s ppm. As a result, this technique will enable NGTS to measure any significant transit timing variations in multi-planet systems with similarly bright host stars. The precise transit ephemerides achievable with this observing method will also allow NGTS to monitor the transit timing variations of short period Jupiter-like planets to search for signs of orbital decay (eg. Baluev et al., 2019; Yee et al., 2020; Patra et al., 2020). In addition to measuring transit timing variations, the precise ephemerides achievable with NGTS multi-telescope observations will also be of use for the scheduling of future transmission spectroscopic measurements, and other characterisation efforts.

Over the next few years, hundreds of rocky planet candidates orbiting bright stars will be detected by *TESS*. The confirmation of these planets and the measurement of their masses will contribute to the *TESS* Level 1 Science goal of measuring the mass of 50 planets with a radius $\leq 4 R_\oplus$. We have demonstrated that NGTS can achieve the same precision as space-based photometry from the ground through simultaneous multi-telescope observations. As such, NGTS will contribute significantly to the confirmation of these planets around bright stars, both

³<https://heasarc.gsfc.nasa.gov/docs/tess/announcement-of-the-tess-extended-mission.html>

Table 3.3: Planetary System properties for WASP-166

Planetary Parameters	Value (NGTS)	Value (TESS)
Fitted Parameters		
T_C (BJD)	$2458540.73965^{+0.00072}_{-0.00073}$	$2458540.73939^{+0.00072}_{-0.00067}$
Orbital Period (d)	5.4435399 ± 0.0000028	$5.4435402^{+0.0000027}_{-0.0000030}$
R_P/R_*	$0.0530^{+0.0011}_{-0.0012}$	$0.0515^{+0.0011}_{-0.0011}$
b	$0.42^{+0.09}_{-0.12}$	$0.40^{+0.09}_{-0.11}$
ρ_* (ρ_\odot)	$0.593^{+0.082}_{-0.080}$	$0.627^{+0.074}_{-0.081}$
q_1	$0.26^{+0.31}_{-0.15}$	$0.33^{+0.30}_{-0.17}$
q_2	$0.16^{+0.31}_{-0.12}$	$0.16^{+0.28}_{-0.12}$
Derived Parameters		
a (R_*)	$11.00^{+0.47}_{-0.51}$	$11.14^{+0.42}_{-0.50}$
a (au)	$0.0647^{+0.0042}_{-0.0041}$	$0.06475^{+0.0041}_{-0.0040}$
i ($^\circ$)	$87.80^{+0.67}_{-0.59}$	$87.95^{+0.62}_{-0.59}$
Fixed Parameters		
e	0.	0.
ω ($^\circ$)	90.	90.

by confirming the transit signal and by measuring the mass by detecting any TTV signals.

Chapter 4

A transit timing variation observed for the long-period extremely low-density exoplanet HIP-41378 f

Note

This chapter is a reproduction of the paper “*A transit timing variation observed for the long-period extremely low-density exoplanet HIP-41378 f*” (Bryant et al., 2021) published in Monthly Notices of the Royal Astronomical Society in June 2021. All the analysis and the majority of the write up was performed by me. External co-author contributions to this paper are in the form of observational data and associated instrument information in Sections 4.2.2, 4.2.3, and 4.2.5.

Abstract

HIP-41378 f is a temperate $9.2 \pm 0.1 R_{\oplus}$ planet with period of 542.08 d and an extremely low density of $0.09 \pm 0.02 \text{ g cm}^{-3}$. It transits the bright star HIP-41378 ($V = 8.93$ mag), making it an exciting target for atmospheric characterization including transmission spectroscopy. HIP-41378 was monitored photometrically between the dates of 2019 November 19 and November 28. We detected a transit of HIP-41378 f with NGTS, just the third transit ever detected for this planet, which confirms the orbital period. This is also the first ground-based detection of a transit of HIP-41378 f. Additional ground-based photometry was also obtained and used to constrain the time of the transit. The transit was measured to occur 1.50 hours earlier than predicted. We use an analytic transit timing variation (TTV) model to show the observed TTV can be explained

by interactions between HIP-41378 e and HIP-41378 f. Using our TTV model, we predict the epochs of future transits of HIP-41378 f, with derived transit centres of $T_{C,4} = 2459355.087^{+0.031}_{-0.022}$ (May 2021) and $T_{C,5} = 2459897.078^{+0.114}_{-0.060}$ (November 2022).

4.1 Introduction

The bright ($V = 8.93$ mag) F-type star HIP-41378 is known to host five transiting planets (Vanderburg et al., 2016), based on photometric data taken during campaign C5 of the K2 mission (Howell et al., 2014). The outermost planet known in the system, HIP-41378 f only transited once during these observations. A second transit of HIP-41378 f was observed during K2 campaign C18 and showed it to have a maximum possible orbital period of 1084.159 d (Becker et al., 2019). Extensive spectroscopic monitoring with HARPS by Santerne et al. (2019) revealed the true period of HIP-41378 f to be 542.08 d - half the possible maximum.

With a mass of $M_p = 12 \pm 3 M_\oplus$ and a radius of $R_p = 9.2 \pm 0.1 R_\oplus$, the low density of HIP-41378 f, combined with its cool temperature, makes it a particularly interesting target for atmospheric characterization. Using the system parameters from Santerne et al. (2019) we calculate a Transmission Spectroscopy Metric (TSM) for HIP-41378 f of 343 (Kempton et al., 2018), which shows HIP-41378 f to be very well suited to transmission spectroscopy follow-up. For these observations, a precise orbital ephemeris is needed. Despite the high quality K2 data, with only two recorded transits there was previously no information regarding any transit timing variations (TTVs) of HIP-41378 f. In a multi-planet system, a planet with a long orbital period such as HIP-41378 f may experience large transit timing variations (TTVs) (eg. Agol et al., 2005; Kawahara and Masuda, 2019). Since HIP-41378 f resides in near 2:1 and 3:2 mean motion resonances with planet e and d respectively, we may expect TTVs on the order of hours to days.

Ground-based photometric observations of the HIP-41378 system are needed to measure any TTVs to place additional constraints on the masses and orbital periods of planets in the HIP-41378 system. Monitoring the TTVs also has the potential to reveal other exoplanets in the system, and additionally will help predict future transit events for atmospheric characterisation. However, for a star with a magnitude of $V = 8.93$ mag, the field-of-view of most ground-based photometric facilities will often not include enough comparison stars of a similar brightness (Collins et al., 2018b). In fact, for HIP-41378, the nearest star with a *Gaia* G magnitude difference of less than 0.5 mag is 17 arcminutes away (Gaia Collaboration, 2018).

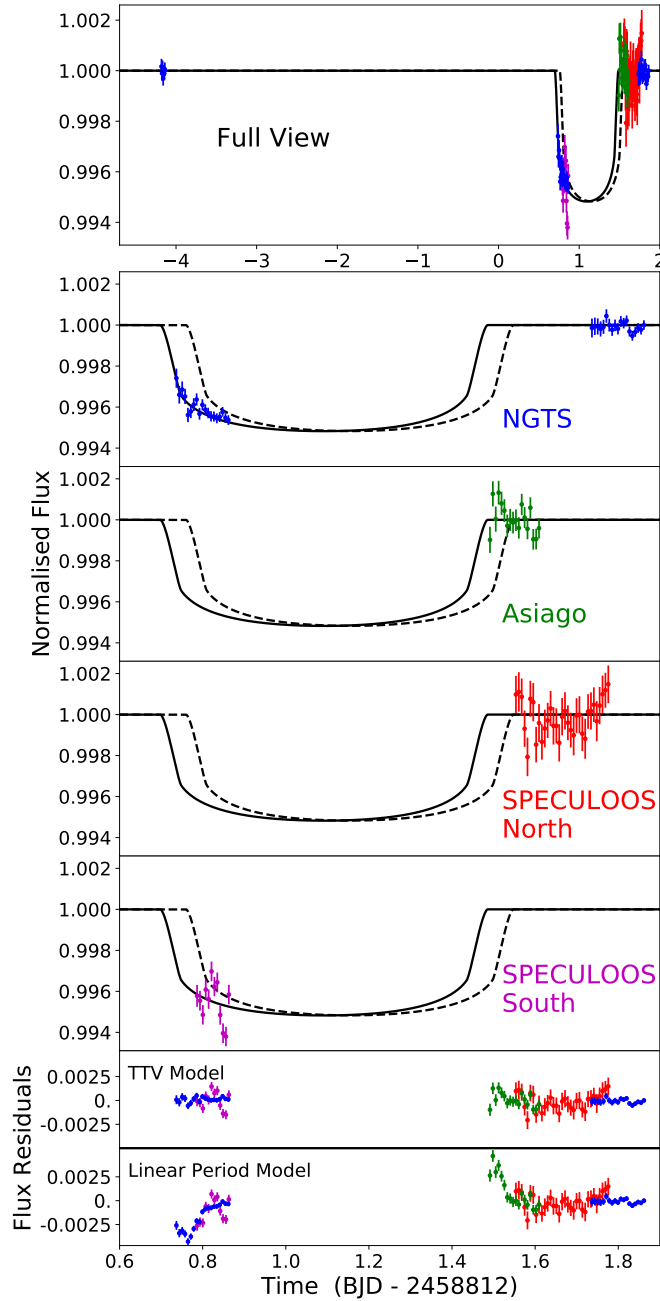


Figure 4.1: Ground-based relative time-series photometry of HIP-41378. All the photometric data included in the analysis are shown in the top panel. The individual datasets are presented in the following panels: NGTS (blue; second panel) showing a zoom in on the transit of HIP-41378 f, Asiago (green; third panel), SNO (red; fourth panel) and SSO (magenta; fifth panel). All data are binned to 10 minutes. The predicted transit model of HIP-41378 f from the K2 and HARPS data is given by the dashed black line, and the model from our sampling process is given by the solid black line. The residuals to the TTV model from our fitting are presented in the sixth panel and the residuals to the predicted linear period model from the two prior transits are presented in the bottom panel. We note that the colours used to denote the individual datasets are consistent across each panel. Note that we plot the detrended NGTS data and the relative flux offsets between the photometry obtained at different facilities were fit as free parameters during the modelling set out in Section 4.3.

4.2 Photometric Observations

4.2.1 NGTS

The Next Generation Transit Survey (NGTS; Wheatley et al., 2018) is a photometric facility situated at ESO’s Paranal Observatory in Chile. It consists of twelve fully-robotic telescopes with 20 cm diameter apertures and wide fields-of-view of 8 square degrees. I have demonstrated that the dominant photometric noise sources in NGTS bright star light curves are Gaussian and uncorrelated between the individual telescopes (see Bryant et al., 2020b, and Chapter 3). Combined with the wide field-of-view, this allows NGTS to use simultaneous observations with multiple telescopes to achieve high precision light curves of bright stars (Smith et al., 2020; Bryant et al., 2020b, , and Chapter 3).

HIP-41378 was observed with NGTS on the nights UT 2019 November 19, 24 and 25. On all nights, HIP-41378 was monitored using eleven NGTS telescopes, each using the custom NGTS filter (520–890 nm) and an exposure time of 10 seconds. Across all nights, a total of 23,841 images were taken. The target was above an altitude of 30° for all the observations, and the observing conditions were good.

The NGTS data were reduced using a custom aperture photometry pipeline, which utilises the SEP Python library (Bertin and Arnouts, 1996; Barbary, 2016). The pipeline uses the *Gaia* DR2 catalogue (Gaia Collaboration et al., 2016; Gaia Collaboration, 2018) to automatically identify comparison stars that are similar in magnitude, colour and CCD position to HIP-41378 (for more details see Chapter 3 and Bryant et al., 2020b). Comparison stars which are shown to display variability or high levels of photometric scatter are excluded from the reduction. The NGTS photometry is plotted in Figure 4.1.

4.2.2 SPECULOOS

HIP-41378 was observed by SPECULOOS (Search for habitable Planets Eclipsing ULtra-cOOl Stars; Burdanov et al., 2018; Gillon, 2018; Delrez et al., 2018; Sebastian et al., 2021). It was observed from the SPECULOOS Southern Observatory (SSO) at Paranal, Chile on UT 2019 November 24 and from the SPECULOOS Northern Observatory (SNO) at the Teide Observatory on Tenerife, Spain on UT 2019 November 25. The SSO observations consists of 342 images obtained using the r' filter, an exposure time of 12 seconds, and a defocus of 300 steps to avoid saturation. SNO obtained 254 images using also the r' filter, with an exposure time of 12 seconds and a defocus of 300 steps. For each night of observation, the automatic SSO Pipeline (Murray et al., 2020) was used to reduce images and extract precise photometry. The SSO Pipeline is built upon the CASUTOOLS software (Irwin et al., 2004) and performs automated differential

photometry to mitigate ground-based systematics, including a correction for time-varying telluric water vapour. The SNO and SSO data are plotted in Figure 4.1.

4.2.3 Asiago Telescope

HIP-41378 was observed on the night UT 2019 November 25 using the 67/92-cm Schmidt telescope based at the Asiago Observatory in northern Italy, operated by the Italian National Institute of Astrophysics (INAF). A total of 301 images were obtained through the Sloan r filter under a good sky quality, using a constant exposure time of 30 seconds and defocusing the camera to minimize pixel-to-pixel systematic errors. The light curve was extracted by using a custom version of the `STARSKY` code, a pipeline to perform high-precision differential photometry originally developed for the TASTE project (Nascimbeni et al., 2011). The unbinned RMS is 2.0 mmag, the scatter being much larger at the beginning of the series due to the much higher airmass (1.97 for the first frame). All the time stamps were converted to the BJD-TDB system (Eastman et al., 2010). The Asiago data, binned over a 10-min time scale (rms: 825 ppm) are plotted in Figure 4.1.

4.2.4 Photometric Transit Detection

The NGTS data show a clear flux decrease which is consistent to the predicted transit depth and near to the predicted transit time. This flux decrease is clearly seen in the top two panels of Figure 4.1. We note that the NGTS photometry is of sufficient precision that an ingress occurring at the time predicted from the K2 and HARPS data would be robustly detected. The SSO and Asiago data are consistent with the change in transit time seen by NGTS, ruling out an on-time ingress and egress respectively. The SNO data rule out a late transit. With photometric coverage on three separate nights surrounding the transit event, we are confident that the flux offset seen in the NGTS data is a real signal. However the relative flux offsets between the data from the different facilities, including the offset of the SSO data, were fit independently as free parameters during the modelling detailed in Section 4.3. The combination of these four datasets gives us confidence that the transit occurred earlier than the prediction from the linear orbital ephemeris derived from the K2 and HARPS data (Santerne et al., 2019). This is the third transit of this planet to be detected and the first from the ground, with the other two being detected from data obtained by the K2 mission. The detection of this transit confirms the mean 542.08 d period predicted for this planet from K2 and HARPS data (Santerne et al., 2019).

4.2.5 Additional Ground Based Photometry

Additional photometry for HIP-41378 was also obtained with various other ground-based facilities: PEST, LCO (CTIO), PROMPT-8 (CTIO), MUSCAT2 at Teide Observatory, Lick Observatory, Hazelwood Observatory, and Phillip’s Academy Observatory. Unfortunately, due to poor observing conditions or a lack of suitable comparison stars, none of the data from these facilities had a photometric precision better than a threshold of 2 ppt-per-10 mins. As such we do not include these datasets in our analysis.

4.3 Analysis

We jointly modelled the photometry from NGTS, Asiago, SSO and SNO in order to determine the time of transit centre for the November 2019 transit, $T_{C,3}$. Note we use the notation $T_{C,N}$ to refer to the time of transit centre for transit epoch N . The first transit of HIP-41378 f in K2 C5 is taken to occur at $T_{C,0}$. We generated a transit light curve template based on the parameters from Vanderburg et al. (2016), and using the period derived by Santerne et al. (2019). We performed an MCMC sampling process to model the ground-based photometric data. The free parameters used in the modelling were $T_{C,3}$, the limb darkening coefficients, the detrending coefficients for the NGTS data, and relative flux offset factors for the other datasets. Note that each NGTS single-telescope light curve was detrended against airmass independently from the other NGTS telescopes, and a single linear trend with time is applied to the entire NGTS multi-telescope light curve. We used a quadratic limb darkening profile, constraining the coefficients based on theoretically derived limb-darkening coefficients for the NGTS filter. The r' filter used for the SSO observations has a large amount of overlap with the wavelength range of the NGTS filter, and so the limb-darkening coefficients derived for the NGTS filter provide a good approximation for the SSO data. The precision of the SSO data also means that including an additional set of limb-darkening coefficients for the SSO data does not have an effect on the derived value of $T_{C,3}$. Therefore, we use the theoretical values of 0.315 ± 0.004 and 0.289 ± 0.001 , which were computed from the Claret and Bloemen (2011) tables, as Gaussian priors for the model for all datasets.

The sampling was performed using the Ensemble Sampler from `emcee` (Foreman-Mackey et al., 2013). We ran 70 chains for 10,000 steps, following a burn-in phase of 2,500 steps. The number of effective samples for each parameter ranged from 600,000 to 800,000. The number of effective samples for $T_{C,3}$ was 698,539.4. From this analysis, we obtained a transit time of $T_{C,3} = 2458813.0913 \pm 0.0046$, which is 1.50 ± 0.11 hours earlier than predicted. The best fit model from this analysis is shown in Figure 4.1 and the derived transit time variation is shown

in Figure 4.2.

4.4 TTV Analysis

Due to its anomalously low density, HIP-41378 f is an attractive target for atmospheric characterisation studies. As such, knowing the precise ephemerides for future transits is of high importance. Therefore, we use analytical TTV formulae from Lithwick et al. (2012) to predict the times of the upcoming transits of HIP-41378 f, in particular the next two transits in May 2021 and Nov 2022.

Of the planets already known in the system, the TTV signal of HIP-41378 f will be most affected by HIP-41378 d and HIP-41378 e. These two planets have masses of $M_d < 4.6M_\oplus$ and $M_e = 12 \pm 5M_\oplus$ (Santerne et al., 2019), and reside near to 2:1 and 3:2 mean motion resonances with HIP-41378 f respectively. The amplitude of the TTVs of HIP-41378 f as a result of its interactions with HIP-41378 d and HIP-41378 e will depend strongly on M_d and M_e respectively. The interactions with HIP-41378 e are likely to dominate the TTV signal of HIP-41378 f since $M_e > M_d$ (Santerne et al., 2019) and thus we consider solely the TTVs due to interactions between HIP-41378 f & e for the rest of this analysis. We note that neither HIP-41378 d nor HIP-41378 e were robustly detected by Santerne et al. (2019) in HARPS radial velocity measurements, and so they are only able to place loose constraints on the masses and periods of these planets. The constraints on the period of HIP-41378 e are derived from a combination of transit analyses and asteroseismic stellar constraints (Santerne et al., 2019; Lund et al., 2019). Future monitoring of the TTVs of HIP-41378 f will allow us to place tighter independent constraints on the masses and periods of HIP-41378 d and HIP-41378 e.

We use the Lithwick et al. (2012) analytic formulae for TTV signals for planets in a near mean motion resonance to obtain the following equations for the amplitude, V , and super-period, P_{ttv} , for the TTV signal of HIP-41378 f as a result of its interactions with HIP-41378 e. These are

$$V = P_f \frac{M_{\text{pl,e}}}{3\pi\Delta M_*} \left(-G + \frac{3}{2\Delta} (F e_e + G e_f) \right), \quad (4.1)$$

$$P_{\text{ttv}} = \frac{P_f}{3|\Delta|}, \quad (4.2)$$

where P_f is the mean linear orbital period of HIP-41378 f, $M_{\text{pl,e}}$ and M_* are the masses of HIP-41378 e and HIP-41378, e_e and e_f are the orbital eccentricities of HIP-41378 e and HIP-41378 f respectively, and F and G are coefficients given in Table 3 of Lithwick et al. (2012). The Δ

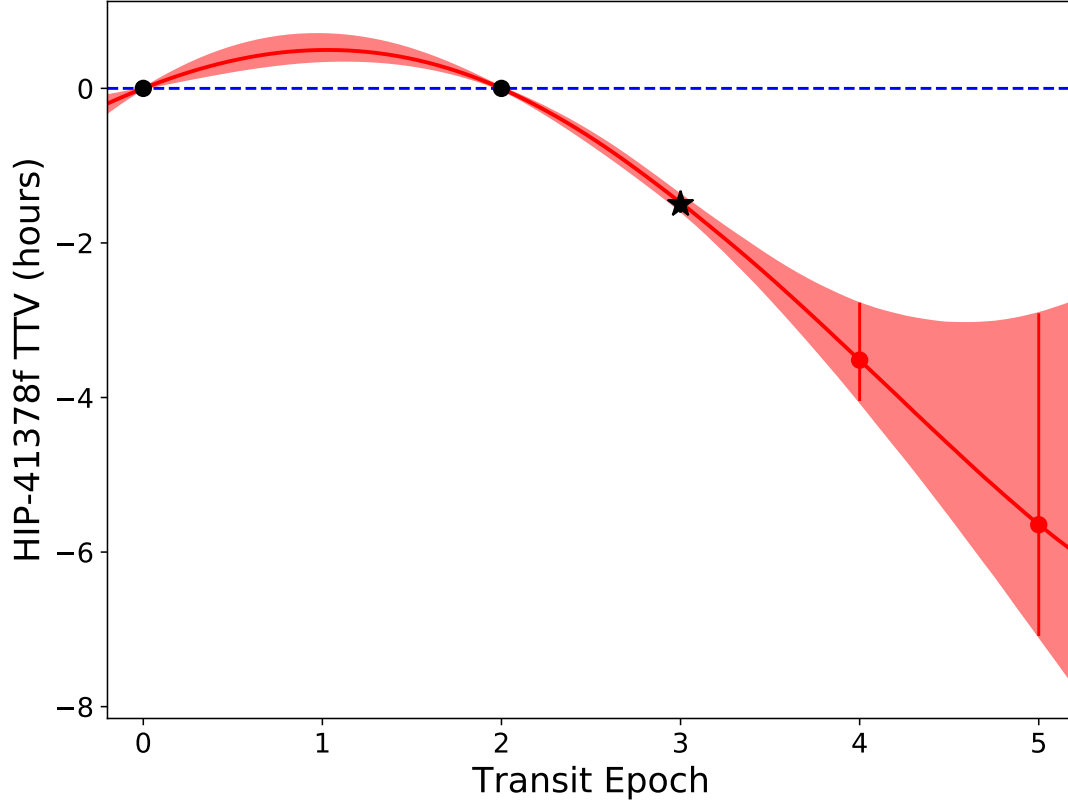


Figure 4.2: Transit times for HIP-41378f. The black points give the T_C values for the two transits of HIP-41378f observed by K2. The black star gives the new $T_{C,3}$ determined in this work. The 1σ errorbars on these values are plotted but are too small to be visible. The red points and errorbars give the predicted transit times for $T_{C,4}$ (May 2021) and $T_{C,5}$ (Nov 2022) and their respective 1σ uncertainties. The solid red line gives the median TTV signal from the TTV analysis (see Section 4.4), and the red shaded area gives the 1σ uncertainty on this signal. The TTV values are relative to the linear ephemeris based on the period from Santerne et al. (2019) of $T_0 = 2457186.91451$ and $P_f = 542.07975$ d, and this linear ephemeris is shown by the blue dashed line.

parameter is the normalized distance to resonance

$$\Delta = \frac{P_f}{P_e} \frac{2}{3} - 1, \quad (4.3)$$

where $P_e = 369 \pm 10$ d is the mean linear orbital period of HIP-41378 e. Using the planetary parameters given in Table 1 of Santerne et al. (2019), we calculate values of $V = 1.3667$ d, and $P_{\text{ttv}} = 8757.577$ d. We note that the expected TTV signal from HIP-41378 e alone is enough to account for the TTVs observed in Section 4.2. Additional planets in the system are not required to explain the observations (nor do the observations rule them out).

With just three transit times, we cannot use TTV modelling to place any constraints on the masses and orbital eccentricities of the planets in the HIP-41378 system. Neither can we robustly refine the period of HIP-41378 e. However, we can combine the analytical TTV signals derived in Lithwick et al. (2012) with our knowledge of HIP-41378 f and e to predict the times of the next transits of HIP-41378 f. We do this using an MCMC sampling method, again using EMCEE Ensemble Sampler. The TTV model we use for this sampling is of the form

$$T_{C,N} = T_0 + P_f N + V \sin \left(\frac{2\pi P_f}{P_{\text{ttv}}} (N + \phi) \right) \quad (4.4)$$

where $T_{C,N}$ is the time of transit centre of the N^{th} transit, T_0 is a reference epoch and N is the the transit epoch, such that $T_0 + P_f N$ is the mean linear ephemeris of HIP-41378 f, and ϕ is the phase shift of the TTV signal. The free parameters in this sampling are T_0 , P_f , ϕ , $M_{\text{pl,e}}$, P_e , e_e and e_f . For the following parameters: $M_{\text{pl,e}}$, P_e , e_e and e_f we impose Gaussian priors using the posterior values from Santerne et al. (2019). In this way, we explore the parameter space of TTV signals which can explain the transit times we observe for HIP-41378 f and are also physically plausible. For the sampling, we run 40 walkers each for 200,000 steps as a burn-in, and then a following 50,000 steps to explore the parameter space. The resultant predicted TTV signal from this sampling is given in Figure 4.2. The median values of the resultant probability distributions for $T_{C,4}$ and $T_{C,5}$, as well as the 68%, 95%, and 99% confidence intervals, are provided in Table 4.1.

4.5 Conclusions

We detected a transit of HIP-41378 f on 2019 November 24 and 25, the first ever ground-based transit detection for this planet, primarily with data obtained using NGTS. As this is just the third ever transit of HIP-41378 f detected, we confirm the 542.08 d orbital period of this planet. This long orbital period makes HIP-41378 f the longest period planet to have a transit detected from the

	$T_{C,4}$ (BJD TDB - 2450000)	$T_{C,5}$ (BJD TDB - 2450000)
Median	9355.087	9897.078
68%	9355.064 - 9355.118	9897.018 - 9897.192
95%	9355.032 - 9355.156	9896.910 - 9897.293
99%	9355.020 - 9355.205	9896.884 - 9897.455

Table 4.1: Confidence intervals for the predictions of $T_{C,4}$ and $T_{C,5}$.

ground. The long transit duration (19 hours) makes detecting transits of HIP-41378 f challenging and makes photometric efforts with increased longitudinal coverage useful for recovering such transits. On the other hand, the fact that many of the observations taken for this particular effort were not able to be used to constrain the transit parameters highlights the value of photometric facilities like NGTS, when it comes to obtaining high precision photometry of bright stars like HIP-41378.

We found the transit to arrive 1.50 hours earlier than predicted from a linear extrapolation of the K2 transits (Vanderburg et al., 2016; Becker et al., 2019) and extensive spectroscopic monitoring (Santerne et al., 2019). Using analytic formulae for TTV signals from Lithwick et al. (2012), we have shown that the TTV observed for HIP-41378 f can be explained solely through the interaction between HIP-41378 e and HIP-41378 f. Therefore, the presence of additional planets in the HIP-41378 system is not required to explain our observations. However our observations do not rule out the presence of additional planets. We predict that the next transit of HIP-41378 e will be centred on BJD 2459355.087 with a 99% confidence interval of 4.4 hours (2021 May 20), and the following transit will occur around BJD 2459897.078 with a 99% confidence interval of 13.7 hours (2022 November 13).

Both P_{ttv} and V depend strongly on the ratio of P_f/P_e . As P_f is well constrained by the available transits of HIP-41378 f, this results in the amplitude and period of the predicted TTV signal depending strongly on the orbital period of HIP-41378 e. The current large uncertainty on P_e combined with the shallow transit depth of just 1.5 mmag mean that detecting another transit of HIP-41378 e, especially with ground-based facilities, will be tough. However, doing so would greatly refine the predictions of the TTV signal of HIP-41378 f. Additionally, detecting the upcoming transits of HIP-41378 f will allow us to greatly refine the ephemeris of HIP-41378 e, due to the constraints that the improved measurements of V and P_{ttv} will place on P_e . The next transit of HIP-41378 e is predicted to have a centre time of $T_C = 2459356 \pm 60$ (UT 2021 May 21). HIP-41378 d is in near 4:3 mean-motion resonance with HIP-41378 e, and so based on our TTV models we expect HIP-41378 d to also experience large TTVs. Therefore, detecting transits of HIP-41378 d will further allow us to refine our TTV models and make better predictions for

upcoming transits of HIP-41378 e. Using the sampling method from Section 4.4, we predict the next transit of HIP-41378 d to have transit mid-point of $T_C = 2459393.13 \pm 0.59$ (2021 June 27).

With six planets in the HIP-41378 system, many of which reside near to mean-motion resonances, there are likely to be lots of interactions between the planets. With only a small number of transit detections for each of the outer three planets, a full dynamical analysis of the system is beyond the scope of this work. However, this robust transit detection of HIP-41378 f by NGTS and the discovery of significant TTVs in the system demonstrates that with future photometric monitoring we will be able to characterise the amplitude and super-period of the TTV signal of HIP-41378 f. This monitoring will enable us to place independent constraints on the masses, orbital periods, and eccentricities of the planets in this remarkable system.

Chapter 5

Revisiting WASP-47 with ESPRESSO and TESS

Note

This chapter is a reproduction of the paper “*Revisiting WASP-47 with ESPRESSO and TESS*” (Bryant and Bayliss, 2022) accepted for publication in The Astronomical Journal in February 2022. All analysis and write up for this paper was performed by me.

Abstract

WASP-47 hosts a remarkable planetary system containing a hot Jupiter (WASP-47 b; $P = 4.159$ d) with an inner super-Earth (WASP-47 e; $P = 0.7896$ d), a close-orbiting outer Neptune (WASP-47 d; $P = 9.031$ d), and a long period giant planet (WASP-47 c; $P = 588.4$ d). We use the new *TESS* photometry to refine the orbital ephemerides of the transiting planets in the system, particularly the hot Jupiter WASP-47 b, for which we find an update equating to a 17.4 minute shift in the transit time. We report new radial velocity measurements from the ESPRESSO spectrograph for WASP-47, which we use to refine the masses of WASP-47 d and WASP-47 e, with a high cadence observing strategy aimed to focus on the super-Earth WASP-47 e. We detect a periodic modulation in the K2 photometry that corresponds to a 32.5 ± 3.9 d stellar rotation, and find further stellar activity signals in our ESPRESSO data consistent with this rotation period. For WASP-47 e we measure a mass of $6.77 \pm 0.57 M_{\oplus}$ and a bulk density of $6.29 \pm 0.60 \text{ g cm}^{-3}$, giving WASP-47 e the second most precisely measured density to date of any super-Earth. The mass and radius of WASP-47 e, combined with the exotic configuration of the planetary system, suggest that the WASP-47 system formed through a mechanism different

to systems with multiple small planets or more typical isolated hot Jupiters.

5.1 Introduction

The formation mechanisms for hot Jupiter planets ($R_p > 0.6 R_J$; $P < 10$ d) remain uncertain, although viable formation pathways have been proposed (Dawson and Johnson, 2018). One possible scenario is that hot Jupiters begin their formation at large orbital distances and then migrate towards the star during formation (eg. Lin et al., 1996; Nelson et al., 2000). This planetary migration could arise from multiple causes, such as interactions between the protoplanet and the circumstellar disk (Papaloizou and Larwood, 2000) or through some form of high eccentricity migration, which can be triggered by planet-planet scattering (Chatterjee et al., 2008) or secular interactions between multiple bodies, including Kozai-Lidov cycles (Kozai, 1962; Lidov, 1962). This high eccentricity migration removes inner planets from the system (Mustill et al., 2015), leaving most hot Jupiter planets isolated and without other planetary companions in close orbits (eg. Steffen et al., 2012). The observational evidence seems to support this model. The vast majority of hot Jupiters do not have close orbiting companions, although many have long-period massive outer companions (eg. Knutson et al., 2014). For the longer period warm Jupiters the situation is different, and warm Jupiter planets are significantly more likely to be accompanied by closely orbiting small planetary companions (Huang et al., 2016). A possible explanation for this is that these warm Jupiters are forming in-situ, as opposed to migrating from outer regions.

Out of the hundreds of hot Jupiters discovered to date, only three have been found to also host small, inner planets: Kepler-730c (Cañas et al., 2019), TOI-1130c (Huang et al., 2020b), and WASP-47 b (Hellier et al., 2012). The 55 Cancri system (Bourrier et al., 2018) is also similar to the WASP-47 system in that it contains a super-Earth with an orbital period shorter than one day (55 Cancri e), and a close-in giant planet (55 Cancri b; 14.6 d). As a result of the brightness of the host star ($V = 5.95$ mag), the 55 Cancri system, and particularly 55 Cancri e, have been very well studied (eg. Demory et al., 2012; Tsiaras et al., 2016; Angelo and Hu, 2017).

Since the configuration of these systems bears more resemblance to the population of warm Jupiters than to hot Jupiters it has been speculated that these systems also formed through an in-situ pathway (Huang et al., 2020b). It is therefore imperative to study these systems in detail to determine if there is any other evidence that they formed through a different pathway to the majority of hot Jupiter systems. In order to do this, we require precise knowledge of the planetary system parameters, especially the planetary masses, densities, and orbital periods.

WASP-47 has been extensively studied since its discovery in 2012. Initially, WASP-47 was shown to host a 4.159 d period transiting hot-Jupiter WASP-47 b (Hellier et al., 2012). Later, an extensive spectroscopic monitoring campaign revealed the presence of the 588.4 d

giant planet WASP-47 c (Neveu-VanMalle et al., 2016). It is not currently known whether or not WASP-47 c transits the star, although Vanderburg et al. (2017) derived a 10% probability that it does transit. This estimate is greater than the geometric probability ($\approx 0.6\%$) and arises from additional dynamical constraints placed by the stability of the inner WASP-47 system on the inclination of WASP-47 c. Most surprisingly, two additional small planets were discovered through photometric monitoring (Becker et al., 2015) with the *Kepler* space telescope during the K2 mission (Howell et al., 2014). WASP-47 d is a Neptune-mass planet exterior to the hot Jupiter, while WASP-47 e is a super-Earth interior to the hot Jupiter. The orbital configuration of the inner region of this remarkable planetary system is shown in Figure 5.1 and we provide key stellar properties in Table 5.1.

Further to these discovery papers, there have been many independent efforts to measure the masses of the planets in the WASP-47 system. Multiple radial velocity monitoring campaigns using the PFS (Dai et al., 2015), HIRES (Sinukoff et al., 2017), and HARPS-N (Vanderburg et al., 2017) spectrographs have been carried out. Dynamical analyses have also been performed to determine the masses of the planets (eg. Almenara et al., 2016; Weiss et al., 2017). These different studies reached slightly differing conclusions about the mass, and therefore the composition, of WASP-47 e.

In addition to the consequences for planetary formation, WASP-47 e represents one of the best cases to study the composition of a super-Earth like planet, thanks to the wealth of data available on the system. Therefore, we seek to shed yet more light on this system.

In this work we use one of the next generation of high precision spectrographs, ESPRESSO, in order to obtain the most precise and accurate measurements of the planet masses and densities, particularly focusing on the super-Earth WASP-47 e.

5.2 Observations

5.2.1 ESPRESSO

ESPRESSO (Echelle SPectrograph for Rocky Exoplanets and Stable Spectroscopic Observations; Pepe et al., 2021) is a new high-resolution, visible spectrograph operating at the Very Large Telescope (VLT) at ESO’s Paranal Observatory in Chile. ESPRESSO can be fed from any of the 8.2 m Unit Telescopes (UTs) and can also be fed simultaneously by all four. The three main exoplanet science objectives of ESPRESSO are to find new Earth-mass planets orbiting in the habitable zone of Sun-like stars, to characterize the atmospheres of exoplanets, and to determine precisely the masses of low-mass transiting exoplanets. ESPRESSO has already been used to confirm *TESS* discoveries, including LP 714-47 b (TOI-442 b; Dreizler et al., 2020), TOI-130 b

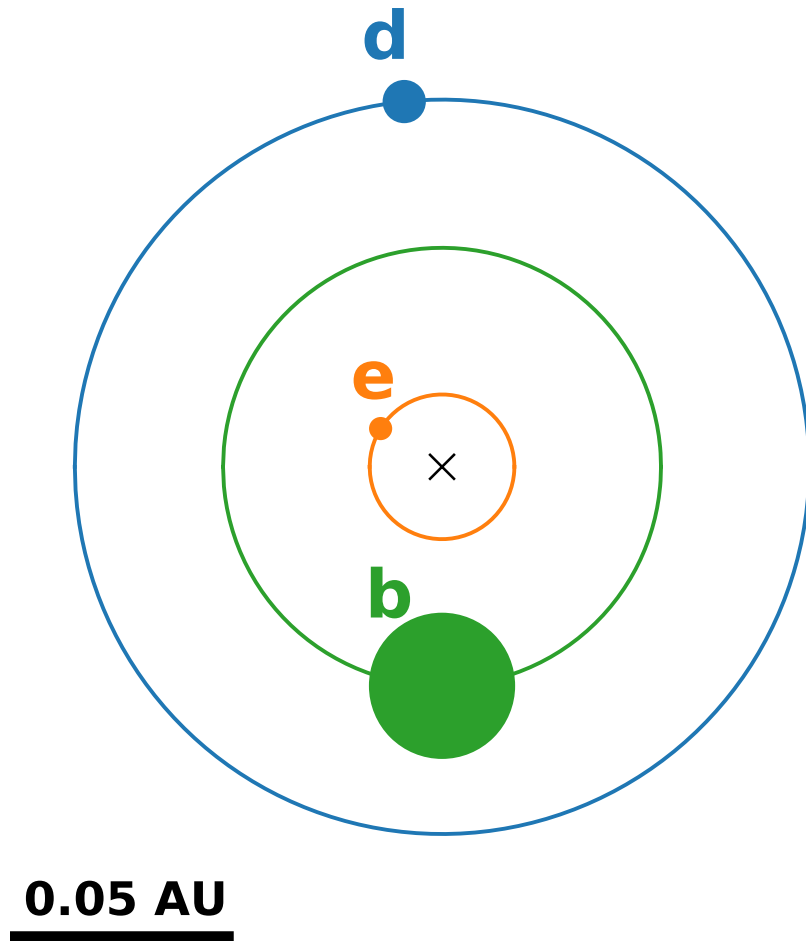


Figure 5.1: Orbital configuration of the inner three planets in the WASP-47 system. The three lines show the orbits of the planets: WASP-47 b (green), WASP-47 d (blue), WASP-47 e (orange). The position of the WASP-47 star is depicted by the black cross. The filled circles give the positions of the planets at 2549449.35 BJD, which is the time of the first transit of WASP-47 b observed by *TESS*. The orbits are orientated such that the observer is viewing from bottom of plot and the planets orbit in the anti-clockwise direction. The relative sizes of the filled circles are proportional to the the relative radii of the planets.

Table 5.1: Key Stellar Properties for WASP-47

Property	Value	Source
TIC	102264230	TICv8
RA (deg)	331.20309414396	<i>Gaia</i> EDR3
Dec (deg)	−12.01907283535	<i>Gaia</i> EDR3
μ_{RA} (mas)	15.074 ± 0.020	<i>Gaia</i> EDR3
μ_{Dec} (mas)	-41.467 ± 0.020	<i>Gaia</i> EDR3
Parallax (mas)	3.7010 ± 0.0201	<i>Gaia</i> EDR3
<i>V</i> (mag)	11.936 ± 0.046	TICv8
<i>B</i> (mag)	12.736 ± 0.024	TICv8
<i>TESS</i> (mag)	11.29 ± 0.0061	TICv8
<i>Gaia G</i> (mag)	11.7817 ± 0.0028	<i>Gaia</i> EDR3
<i>Gaia G_{Bp}</i> (mag)	12.1716 ± 0.0029	<i>Gaia</i> EDR3
<i>Gaia G_{Rp}</i> (mag)	11.2294 ± 0.0038	<i>Gaia</i> EDR3
<i>J</i> (mag)	10.613 ± 0.022	2MASS
<i>H</i> (mag)	10.310 ± 0.022	2MASS
<i>K</i> (mag)	10.192 ± 0.026	2MASS
M_* (M_{\odot})	1.040 ± 0.031	V2017
R_* (R_{\odot})	1.137 ± 0.013	V2017
ρ_* (g cm^{-3})	0.998 ± 0.014	Section 5.3.1
T_{eff} (K)	5552 ± 75	V2017
[Fe/H]	0.38 ± 0.05	V2017
$\log g$ (cgs)	4.3437 ± 0.0063	V2017
TICv8 - Stassun et al. (2019)		
<i>Gaia</i> EDR3 - Gaia Collaboration et al. (2021)		
2MASS - Skrutskie et al. (2006)		
V2017 - Vanderburg et al. (2017)		

(Sozzetti et al., 2021), and the planets in the TOI-178 system (Leleu et al., 2021). ESPRESSO radial velocity measurements have also been used to improve upon the precision of the masses of LHS-1140 b and c (Lillo-Box et al., 2020).

ESPRESSO operates in the wavelength range 380–788 nm, and is designed to achieve a radial velocity precision of 10 cm s^{-1} for bright stars ($V < 8 \text{ mag}$) in order to be capable of detecting Earth-mass planets around solar type stars. This unprecedented radial velocity precision is achieved both by building on and improving the technologies used in the HARPS spectrograph for stability and calibration accuracy but also through the increased light-collecting capacity of the VLT UTs compared to the ESO 3.6 m.

WASP-47 was observed by ESPRESSO between the dates of 2019 August 6 and 30 September (Run ID: 0103.C-0422; PI Bayliss) using an exposure time of 1,250 seconds and with an airmass < 1.5 . We reduced all the spectra using the ESPRESSO reduction pipeline (version 2.2.1) through the ESOReflex workflow environment (Freudling et al., 2013). The signal-to-noise achieved from our observations ranged from 40–60 at $\lambda = 550 \text{ nm}$. The radial velocity CCFs were computed using a G9 mask, and the pipeline automatically extracts diagnostic information on the CCFs, including the FWHM of the CCF. In total, WASP-47 was observed 25 times by ESPRESSO. Two of these observations show anomalous CCF profiles likely caused by cloud coverage or moon contamination, and are not used in the analysis. An additional four observations were identified as having been taken during a transit of WASP-47 b. We also remove these from our analysis so that the Rossiter-McLaughlin signal of WASP-47 b (Sanchis-Ojeda et al., 2015) does not affect our radial velocity model and analysis. This left us with 19 radial velocity measurements from ESPRESSO for our analysis. We run spectral analysis on our co-added ESPRESSO spectra using the ESPRESSO-DAS pipeline. The values we derive for effective temperature and metallicity are consistent with those derived by Vanderburg et al. (2017).

In addition to the ESPRESSO data, we utilize a number of archival radial velocity measurements of WASP-47, which were obtained using the HARPS-N (69 data points with mean a precision of 3.2 m s^{-1} ; Vanderburg et al., 2017), HIRES (43 data points with mean a precision of 2.0 m s^{-1} ; Sinukoff et al., 2017), PFS (26 data points with mean a precision of 3.2 m s^{-1} ; Dai et al., 2015), and CORALIE (52 data points with mean a precision of 12.5 m s^{-1} ; Neveu-VanMalle et al., 2016) spectrographs. We did not perform any additional reduction of these datasets.

5.2.2 K2

As we discuss in Section 5.3, a degree of variability in the radial velocity data indicates relatively strong stellar activity on WASP-47. In order to help understand and account for this activity,

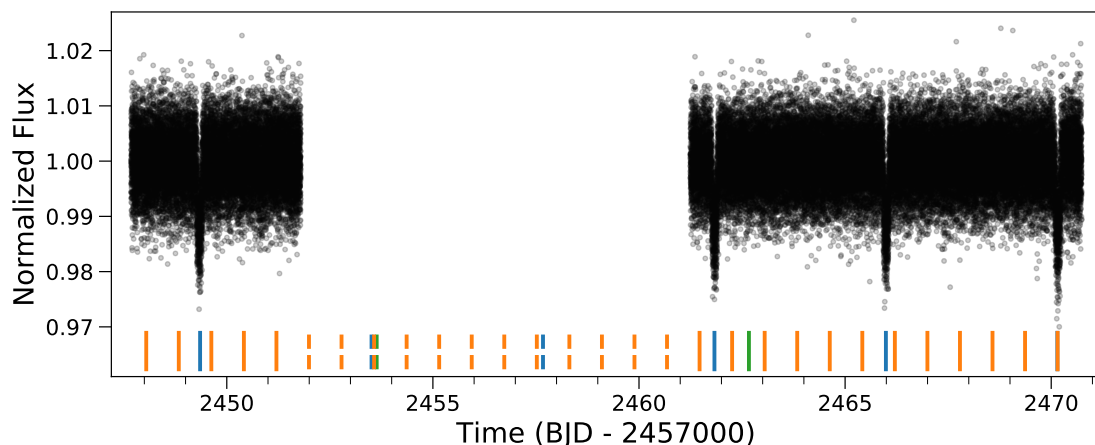


Figure 5.2: *TESS* 20 second cadence PDCSAP_FLUX photometry for WASP-47. The colored bars at the bottom show the positions of the transits of WASP-47 b (blue), WASP-47 d (green), and WASP-47 e (orange), with the dashed bars showing the positions of transits which fall in the large data gap caused by Earth and Moon crossing events and the data download between orbits.

we turned to the high precision time series photometry for WASP-47 from the *Kepler* space telescope (Borucki et al., 2010).

WASP-47 was observed by the *Kepler* space telescope during Campaign 03 of the K2 mission (Howell et al., 2014). WASP-47 was observed continuously for 67 d between the dates of 2014 November 17 and 2015 January 23. WASP-47 was observed in the short cadence mode, and a short cadence light curve was extracted by Becker et al. (2015) using the method of Vanderburg et al. (2015). We accessed this light curve for the transit analysis performed in this work¹.

5.2.3 *TESS*

WASP-47 was observed by the *TESS* mission (Ricker et al., 2015) during Sector 42 between the dates of 2021 August 21 and September 15. WASP-47 fell on camera 1 CCD 4. We utilized the 20 second cadence light curve produced by the SPOC pipeline (Jenkins et al., 2016), which we downloaded from the Mikulski Archive for Space Telescopes (MAST). We use the PDCSAP_FLUX time series in this work, which has had instrumental and blending effects corrected in the light curve (Jenkins et al., 2016).

During both orbits of Sector 42, the Earth crossed the field of view of camera 1, with the Moon also crossing the field of during the first orbit². Due to the significant increases in scattered light in the background during these events, the PDCSAP_FLUX time series spans only 4.11 d

¹The short cadence light curve was accessed from <http://www.cfa.harvard.edu/~avanderb/wasp47sc.csv>

²Data release notes available at https://archive.stsci.edu/missions/tess/doc/tess_drn/tess_sector_42_drn60_v01.pdf.

in the first orbit and 9.48 d in the second, giving a total of around half the nominal 27 d coverage for a given sector. The *TESS* light curve is shown in Figure 5.2.

5.3 Analysis

5.3.1 Transit Analysis

We analysed the *TESS* data, along with the short cadence K2 photometry, in order to refine the planetary parameters of the WASP-47 planets. It is not known if WASP-47 c transits the host star (Neveu-VanMalle et al., 2016). However based on the best ephemeris for WASP-47 c it is not expected to transit during the *TESS* monitoring; the next conjunction of WASP-47 c is predicted to occur just under 60 d after the end of the *TESS* observations. We searched the light curve for evidence of any previously unknown transiting planets. We mask out the transits of WASP-47 b, d, and e, and search for additional transit signals using BLS (Kovács et al., 2002) but we do not find any evidence for a previously unknown transiting planet. Therefore, we consider just WASP-47 b, d, and e in this analysis.

We model the transit light curves of the three planets using BATMAN (Kreidberg, 2015) with the following free parameters: the times of transit centre, T_C , the orbital periods of the planets, P , the planet-to-star radius ratios, R_P/R_* , the orbital inclinations, i , and the stellar density, ρ_* , from which we can compute the scaled semi-major axes, a/R_* . For T_C and P we use wide uniform priors centred on the values derived by Becker et al. (2015). For R_P/R_* and i we use uniform priors between 0 and 1 and between 0° and 90° respectively. For ρ_* we use another wide uniform prior between 0.9 and 1.1, based on the prior knowledge of the stellar parameters from Vanderburg et al. (2017). We use a quadratic limb-darkening law with two independent sets of coefficients for the K2 and *TESS* data. We sampled for these coefficients using the parameterization of Kipping (2013a). For the analysis of WASP-47 b and WASP-47 e we adopted circular orbits based on the findings of Vanderburg et al. (2017) that the tidal circularization timescales for these two planets are significantly shorter than the age of the system. We allow for a non-circular orbit for WASP-47 d and impose a half-Gaussian prior with a width of 0.014 and centred on 0 for e_d . This constraint on the eccentricity of WASP-47 d comes from the dynamical analyses performed independently by Becker et al. (2015) and Weiss et al. (2017). This eccentricity is taken into account when calculating the value of a/R_* from ρ_* for the orbit of WASP-47 d. We explore the parameters using a Monte Carlo Markov Chain (MCMC) analysis using the EMCEE Ensemble Sampler (Foreman-Mackey et al., 2013). A total of 48 walkers were run for a burn in of 3,000 steps followed by a further 10,000 steps per chain to sample the

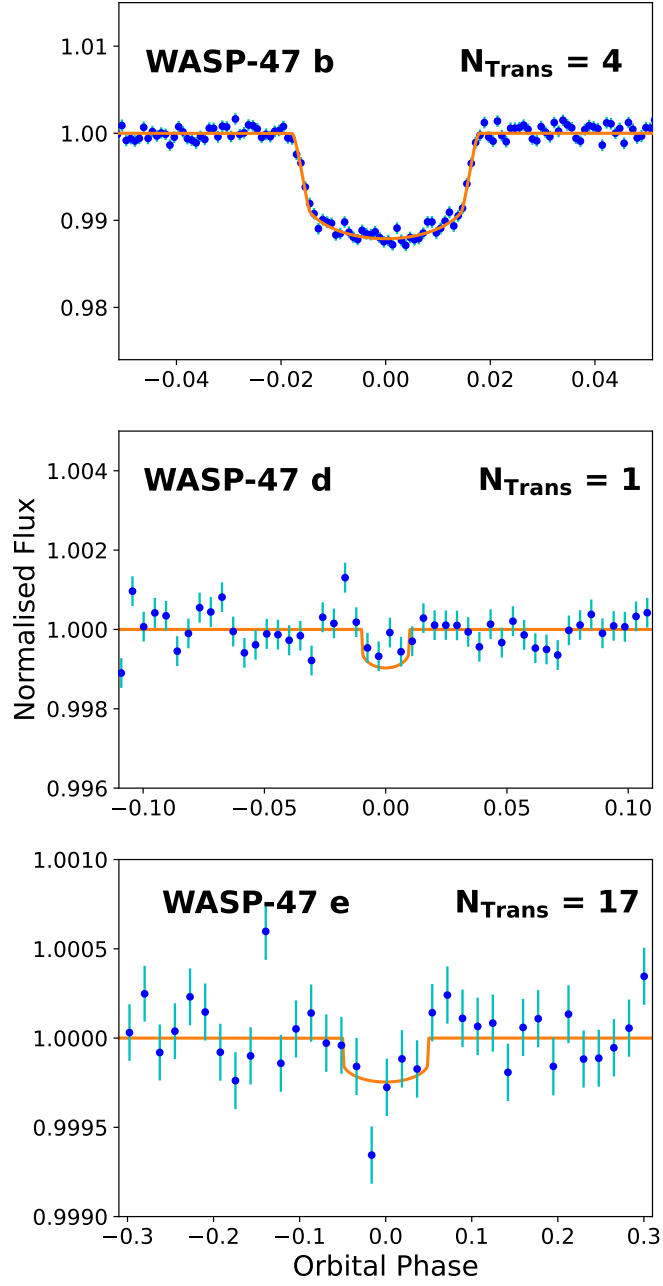


Figure 5.3: Phase-folded *TESS* photometry of WASP-47 zoomed around the transit events for **Top:** WASP-47 b **Middle:** WASP-47 d and **Bottom:** WASP-47 e. For all panels the photometry (blue circles) has had the transit models from the other two planets subtracted and is binned in phase on a time scale of 20 minutes for WASP-47 b and WASP-47 e and 60 minutes for WASP-47 d. The orange lines show the best fit transit models from the modelling in Section 5.3.1.

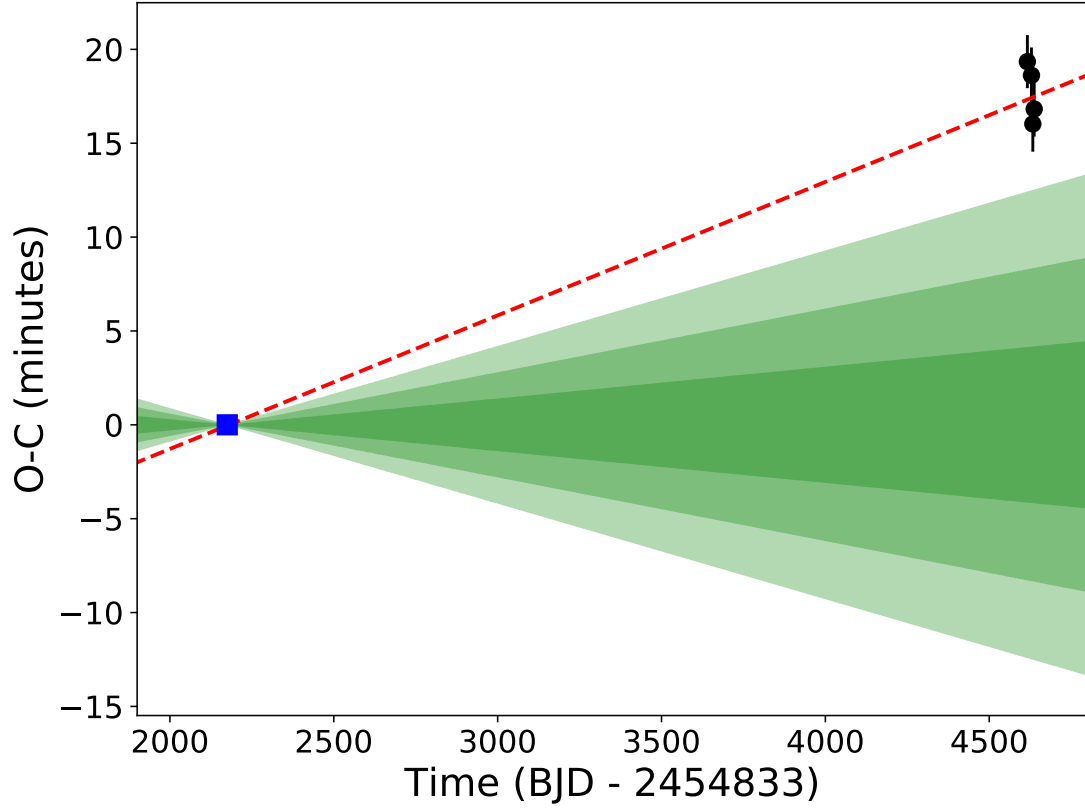


Figure 5.4: Measured transit times for WASP-47 b transit events in the *TESS* data (black circles) compared with the literature ephemeris (blue square and green shaded regions) from Becker et al. (2015). The uncertainties on the *TESS* transit times have had an additional 1 minute added in quadrature to account for the TTVs of WASP-47 b. The shaded green regions give the 1, 2, and 3 σ uncertainties of the predicted ephemeris from Becker et al. (2015). The red dashed line represents the updated ephemeris determined in this work.

posterior distribution. We calculated the autocorrelation lengths, τ , for each parameter and find $\tau \ll N/100$, where N is the chain length, indicating good convergence for all parameters except ω_d which has $\tau = N/26.5$. This is unsurprising, as due to the eccentricity of WASP-47 d being low and consistent with 0 at 2σ , from the transit light curves alone we cannot place strong constraints on ω_d and so do not expect excellent convergence. The transit models recovered from this analysis are plotted in Figure 5.3. The planetary radii we derive are reported in Tables 5.2 and 5.3. From this analysis, we obtain a stellar density of $\rho_* = 0.998 \pm 0.014 \text{ g cm}^{-3}$, which we note is consistent with the current best estimates for the stellar mass and radius (Vanderburg et al., 2017).

Compared to the parameters from just the K2 photometry alone, the inclusion of the *TESS* photometry into the analysis does not provide additional information on the radii of the planets. This is a result of both the reduced time coverage of the *TESS* photometry compared to the K2 (13.59 d vs 67 d) and the significantly reduced photometric precision (3040 ppm-per-minute vs 350 ppm-per-minute). In particular, WASP-47 d transited just once during the available *TESS* photometry (see Figure 5.2), and so the recovery of the transit in the *TESS* data is marginal.

TESS data have provided a useful method for refining the ephemerides for known transiting hot Jupiters by increasing the baseline of transit observations (Shan et al., 2021). We are able to take advantage of this method by increasing the baseline of observations to refine the orbital periods of the WASP-47 planets. For the hot Jupiter WASP-47 b our results yield an orbital period of $4.1591492 \pm 0.0000006 \text{ d}$, which is significantly (4.15σ) longer than the current literature value (Becker et al., 2015) (see Figure 5.4). We also reduce the uncertainty on this period by a factor of seven. WASP-47 b displays transit timing variations with an amplitude on the order of 1 minute (Becker et al., 2015) however these cannot account for the offset in transit times observed, which has a magnitude of 17.4 minutes. For WASP-47 d we find an orbital period of $9.03055 \pm 0.000008 \text{ d}$, which is slightly shorter than the Becker et al. (2015) period, but only differs by just over 1σ . We have reduced the uncertainty on this period by a factor of 2.4. For the super Earth WASP-47 e our measured orbital period of $0.789595 \pm 0.000005 \text{ d}$ agrees with the Becker et al. (2015) results, but again we significantly improve the precision on this measurement by a factor of 3.6.

5.3.2 Radial Velocity Analysis

We modelled our ESPRESSO radial velocity data along with the archival data from HARPS-N, HIRES, and CORALIE using the *EXOPLANET* Python package (Foreman-Mackey et al., 2021). The *EXOPLANET* package allows for robust probabilistic modelling of astronomical time series data using PYMC3. We used *EXOPLANET* to model the multiple radial velocity datasets using the

No U-Turn Sampler Hamiltonian Monte Carlo method.

The free system parameters included in the analysis were the orbital periods of the planets, P_i , the times of conjunction, $T_{C,i}$, and the radial velocity semi-amplitudes, K_i , where i represents the planets b, c, d , and e . For P_i and $T_{C,i}$ we used Gaussian priors taken from the posteriors of the transit analysis. We also fitted for the eccentricities and arguments of periastron of planets c and d , $e_c, e_d, \omega_c, \omega_d$. As with the transit analysis, we fix $e_b = e_e = 0$, and for e_d we imposed a half-Gaussian prior with a width of 0.014 and centred on 0. For e_c we use a uniform prior constraining the eccentricity to be between 0 and 1. For ω_c and ω_d we used uniform priors between -180° and $+180^\circ$. We also include a white noise jitter term, σ , and a systemic radial velocity, γ , for each instrument. For CORALIE, we use independent jitter and systemic velocity terms for the data taken before and after the upgrade in November 2014.

The archival PFS data (Dai et al., 2015) has been excluded from prior analyses on WASP-47 due to the presence of large scatter in the radial velocities and the high risk of contamination from systematic errors (Vanderburg et al., 2017). From our initial modelling, we also find a large jitter term is required for the PFS data. Motivated by this, we investigated the effect had by excluding the PFS data from our analysis. We find that the derived parameter values, specifically K_i , are unaffected by including the PFS data, and that the maximum log-likelihood value obtained during the sampling increases when the PFS data are not included in the analysis. Therefore, we also exclude the PFS data from our analysis.

From this initial modelling, we found a significant jitter term was required for our ESPRESSO data. The value required was $\sigma_{\text{ESP}} = 3.25 \text{ m s}^{-1}$, compared to the median photon-limited uncertainty of 0.55 m s^{-1} for the ESPRESSO radial-velocities. Motivated by this we searched for evidence of periodicity in the residuals to the initial model. This excess scatter in the ESPRESSO radial-velocities suggests the presence of additional noise that we have not accounted for in our model. This additional noise is likely to arise from the stellar activity of WASP-47. We studied the available data for WASP-47 to investigate any evidence for stellar variability.

5.3.3 Stellar Rotation Analysis

Vanderburg et al. (2017) used the HARPS-N spectra to derive a maximum stellar rotational velocity of 2 km s^{-1} based on the line broadening of the stellar absorption lines. This implies a minimum rotation period of $P_{\text{Rot}; \text{min}} = 28.762 \text{ d}$. Independently, Sanchis-Ojeda et al. (2015) derived a value of $v \sin i = 1.8^{+0.24}_{-0.16} \text{ km s}^{-1}$ from their Rossiter-McLaughlin analysis of WASP-47 b. From this measurement we estimate a rotation period of WASP-47 of $P_{\text{Rot}} = 31.96 \pm 4.36 \text{ d}$. These P_{Rot} estimates are assuming WASP-47 is aligned along our line-of-sight. This is a

reasonable assumption given the Rossiter-McLaughlin measurement of a spin aligned orbit for WASP-47 b (Sanchis-Ojeda et al., 2015). These P_{Rot} limits and estimates will be important for properly interpreting our rotation analyses.

Photometric Rotation Analysis

We used the K2 data of WASP-47 to search for photometric signs of stellar activity. Stellar spots are cooler and less bright than the majority of the stellar surface. As the star rotates, these spots rotate into and out of view of the telescope, resulting in a sinusoidal-like variation in the photometric data at the rotation period of the star, or some harmonic of this period. During the production of the K2 short cadence light curve, long term photometric variations were fitted and removed using a spline (Becker et al., 2015). It is these exact variations that we want to study here. Therefore, we use a different long cadence K2 light curve that has been generated using the "self-flat-fielding" method (Vanderburg and Johnson, 2014). This reduction technique significantly improves upon the precision of the raw K2 photometry and in most cases gets to a precision within a factor of two of the photometry delivered by *Kepler* during the nominal mission (Vanderburg and Johnson, 2014). More importantly, this method preserves long term astrophysical variations in the photometry.

We used the orbital parameters from Becker et al. (2015) to remove any data points taken during a transit of any of the three WASP-47 transiting planets. We also excluded the data points during two sharp ramps. These two ramps are related to the settling of the roll of the spacecraft at the start of the campaign and after the change in the roll direction around 50 d into the campaign. We fit quadratic polynomials to the two remaining continuous data chunks in order to remove long-term systematic trends in the data believed to be spacecraft systematics rather than astrophysical in nature. The detrended K2 photometry is shown in Figure 5.5.

We ran a Lomb-Scargle analysis on the remaining out-of-transit photometry. The resultant periodogram is shown in the bottom panel of Figure 5.5. The K2 photometry displays some sign of periodicity on periods which are similar to those present in the ESPRESSO data. However due to the 67 d length of the K2 photometry and the detrending methods applied, this period search becomes less sensitive for longer period signals, especially for signals around half the monitoring length and longer. The significant peak in the K2 periodogram is at a period of 16.26 ± 1.94 d. This period is shorter than the $P_{\text{Rot}, \text{min}}$ limit set by Vanderburg et al. (2017). Periodic signals are expected in photometric time series at the second harmonic of the rotation period (Clarke, 2003). Particularly in cases where there are multiple active regions on the surface of the star. For these scenarios the largest peak in the periodogram can be at half the true rotation period (eg. McQuillan et al., 2013). Therefore, this 16.26 ± 1.94 d signal likely corresponds to

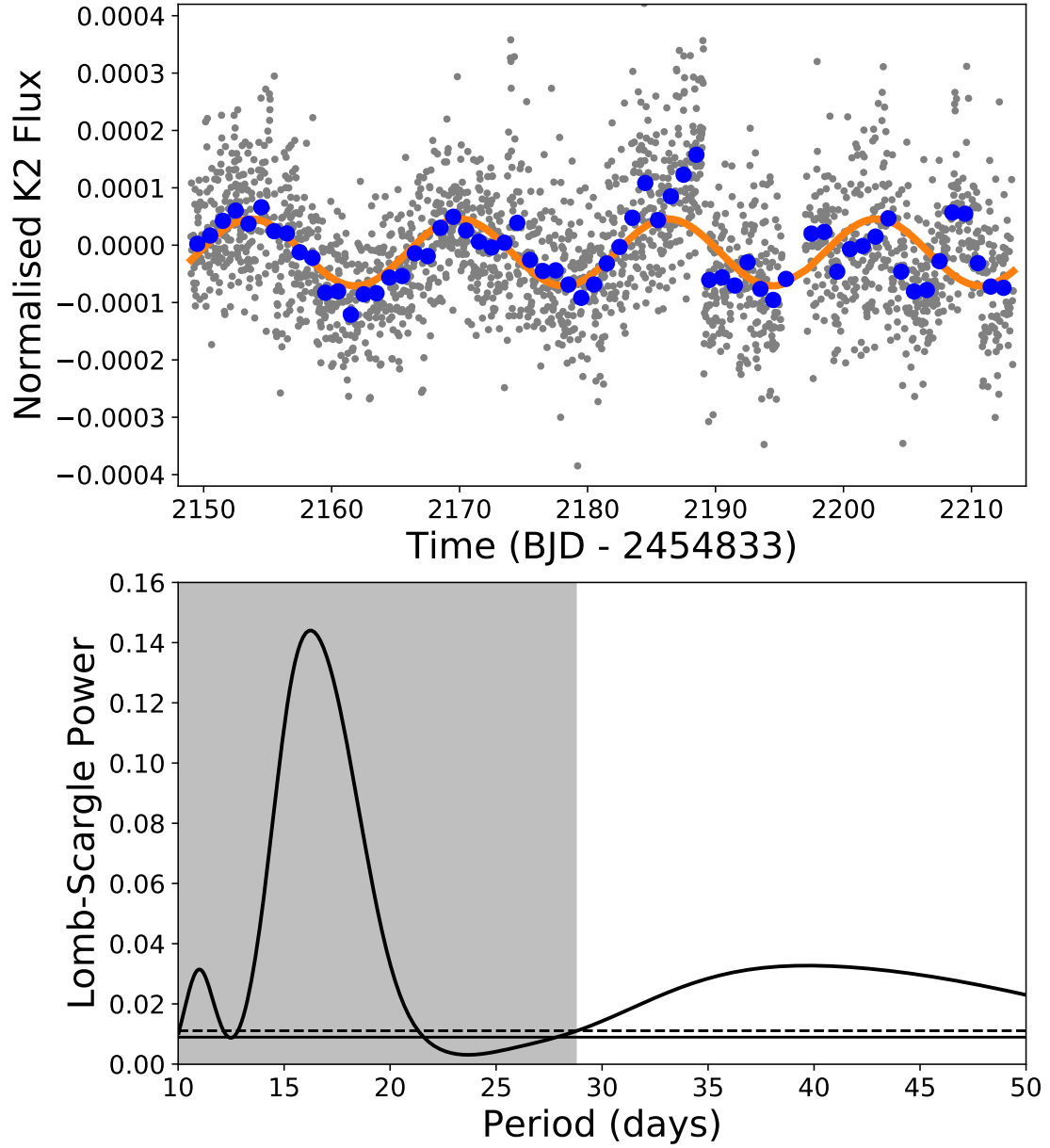


Figure 5.5: **Top:** K2 photometry from campaign 3 for WASP-47 used for the rotation analysis in this work. The grey points show the detrended data (see Section 5.3.3) and the blue points give the data binned to a timescale of 1 d. The orange line shows the most significant Lomb-Scargle period of 16.26 d with an amplitude of 0.1 mmag. **Bottom:** Lomb-Scargle periodogram for the K2 photometry. The shaded area highlights the rotation periods excluded by the minimum $P_{\text{Rot}} = P_{\text{Rot}, \text{min}}$. The significant peak at 16.26 d likely corresponds to half the true rotation period. The horizontal lines give the 0.1% (solid) and 0.01% (dashed) false alarm probabilities.

half the true rotation period of WASP-47, giving a rotation period of $P_{\text{Rot}} = 32.5 \pm 3.9$ d, which is consistent with the prediction from the Sanchis-Ojeda et al. (2015) $v \sin i$ measurement.

We also turn to theoretical predictions for stellar rotation periods to confirm that this value is a physically reasonable rotation period for WASP-47. We use the model from Barnes (2007) which estimates P_{Rot} given the stellar magnitudes in the B and V pass-bands and the age of the star. For WASP-47, we have magnitudes of $V = 11.936$ mag and $B = 12.736$ mag, and by assuming a solar age of 4.5 Gyr we find a predicted rotation period of $P_{\text{Rot; pred}} = 34.96$ d.

We note that Hellier et al. (2012) searched the WASP photometry of WASP-47 for signs of stellar rotation and did not find any significant rotational modulation, placing an upper limit of 0.7 mmag for the amplitude of any such modulation. From the K2 photometry in Figure 5.5, the peak-to-peak amplitude of the modulation is approximately 0.1 mmag, therefore the non-detection of rotational modulation in the WASP photometry is not inconsistent with the K2 detection. Similarly, due to the short time coverage and low precision, the *TESS* data are unable to help constrain the stellar rotation.

Spectroscopic Rotation Analysis

We search for periodic signals in our spectroscopic ESPRESSO data that might provide evidence that the excess scatter seen in the ESPRESSO radial velocities arises as a result of stellar activity. We ran a generalized Lomb-Scargle analysis on the residuals to the model from the fitting in Section 5.3.2, which revealed periodicities at periods of roughly 35 and 18 d, as shown in Figure 5.6. We also searched for periodic signals in the ESPRESSO CCF FWHM measurements, as the FWHM of the CCF has been shown to act as a stellar activity indicator (Boisse et al., 2011; Oshagh et al., 2017). Stellar spots suppress the flux contributions from different sections of the stellar surface to the stellar lines and thus modify the CCF profile. Spots on the limb of the star suppress the wings of the line, resulting in the CCF profile showing a smaller FWHM. Conversely, spots on the centre of the stellar disc affect the centre of the stellar lines, resulting in a wider CCF FWHM (Boisse et al., 2011). Periodic signals with the same periods as those found in the RV residuals were found in the CCF FWHM measurements (see Figure 5.6). Boisse et al. (2011) also find that the stellar activity causes the CCF contrast, the fractional height of the CCF peak, to anti-correlate with the FWHM. We compare the contrast and FWHM for the ESPRESSO CCFs and find an anti-correlation (Pearson $R = -0.34$; see Figure 5.7). This anti-correlation is in line with the predictions and strengthens the confidence that the variations in the CCF FWHM, and by extension the ESPRESSO radial velocity residuals, are a result of stellar activity.

We also used the Ca-II H and K lines in the ESPRESSO spectra to determine values of the activity index $\log R'_{\text{HK}}$. Running a further Lomb-Scargle analysis on this activity indicator

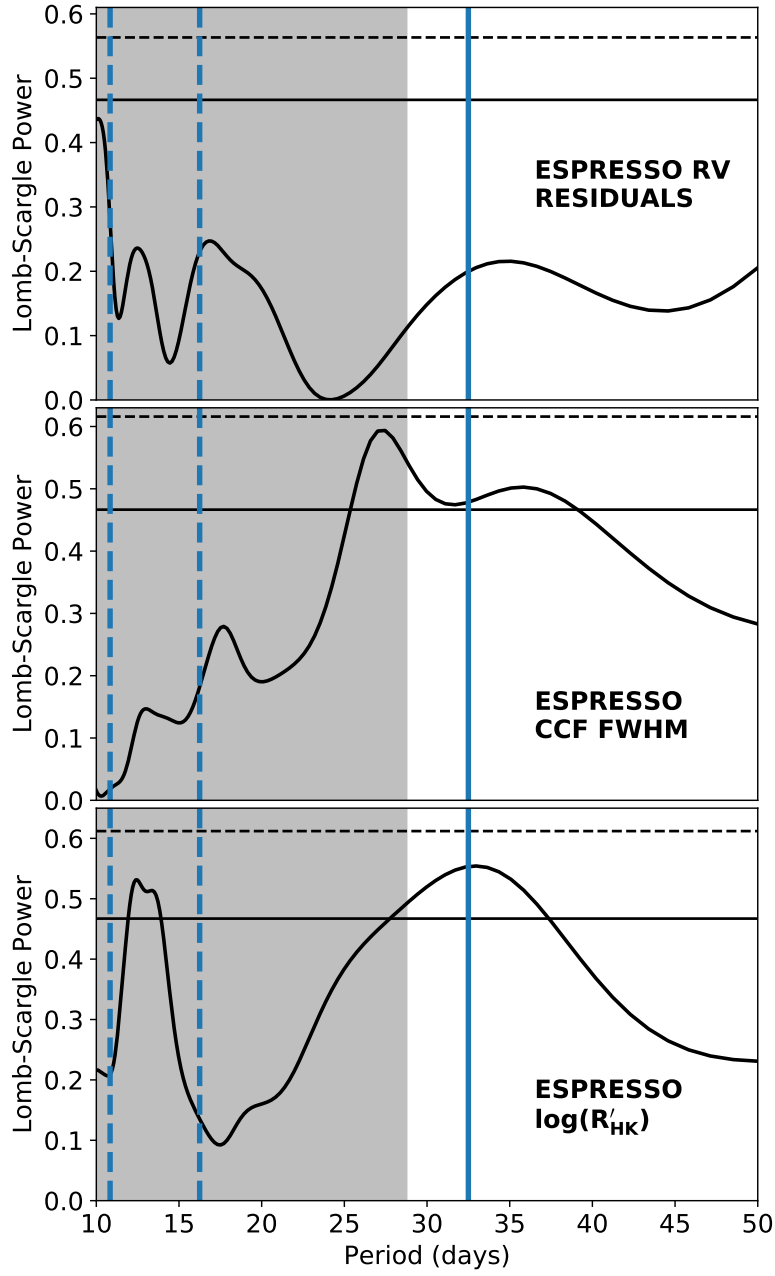


Figure 5.6: Generalized Lomb-Scargle periodograms for: **Top:** ESPRESSO radial velocity residuals to the initial model from Section 5.3.2; **Middle:** the ESPRESSO CCF FWHM measurements; **Bottom:** measurements of $\log R'_{\text{HK}}$ from the ESPRESSO spectra. The solid vertical blue line denotes the rotation period of $P_{\text{Rot}} = 32.5$ d derived from the K2 photometry, with the vertical dashed blue lines marking $P_{\text{Rot}}/2$ and $P_{\text{Rot}}/3$ harmonics. The shaded area highlights stellar rotation periods that are excluded by the calculated minimum rotation period of 28.762 d. The horizontal lines indicate the 1% (dashed) and 10% (solid) false alarm probabilities.

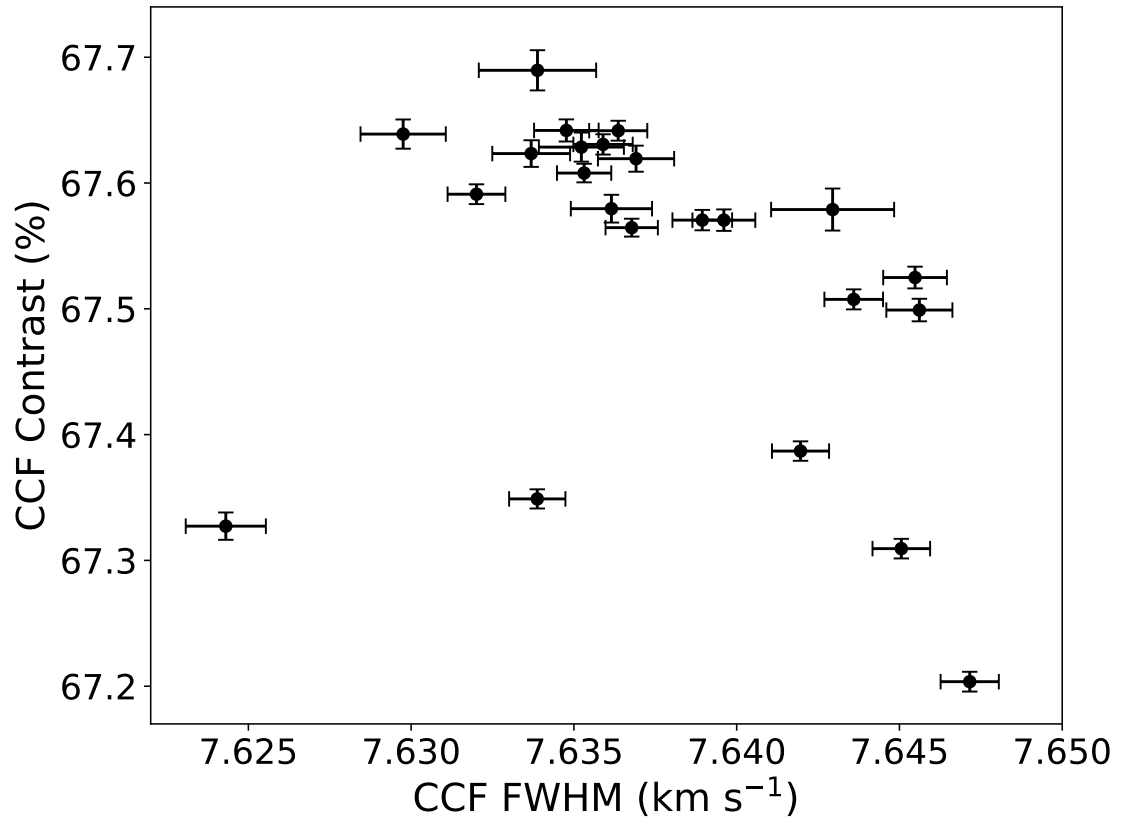


Figure 5.7: The contrast and FWHM values for the ESPRESSO cross-correlation functions for our observations of WASP-47. We see a strong anti-correlation, indicative of spot-induced stellar activity (Boisse et al., 2011).

reveals a periodic signal in the range 30–40 d with a peak around 33 d (Figure 5.6).

5.3.4 Stellar Activity Analysis

We expect the spectroscopic signals from stellar activity to manifest at periods equal to P_{Rot} and at the $P_{\text{Rot}}/2$ and $P_{\text{Rot}}/3$ harmonics (Boisse et al., 2011). From the ESPRESSO radial velocity periodogram (top panel of Figure 5.6), we see a signal close to $P = 35$ d, with harmonics close to $P/2$ and $P/3$. These peaks are also seen in the CCF FWHM periodogram, although an extra peak is seen close to 27 d that is likely due to the moon. The $\log R'_{\text{HK}}$ activity index from the ESPRESSO spectra has a peak in the periodogram at approximately 33 d.

The periodicities detected in the ESPRESSO RV residuals and activity indicators are consistent with the 32.5 ± 3.9 d rotation period derived from the K2 photometry for WASP-47. Based on the continuous coverage and very high precision of the K2 data, we take the K2 P_{Rot} value as the most probable rotation period.

5.3.5 Gaussian Process Analysis

We utilize a Gaussian Process (GP) kernel with a periodicity close to $P_{\text{Rot}} = 32.5$ d in order to accurately model the radial velocity variability due to spot rotation. We use the `celerite2` *rotation term* kernel constructed from two Simple Harmonic Oscillator (SHO) terms at P_{Rot} and $P_{\text{Rot}}/2$, implemented using the `EXOPLANET` (Foreman-Mackey et al., 2021) and `celerite2` (Foreman-Mackey et al., 2017; Foreman-Mackey, 2018) Python packages. A single SHO term is given by

$$\kappa(\tau) = \sigma_{\text{GP}}^2 \exp\left(-\frac{\pi\tau}{QP_{\text{Rot}}}\right) \left[\cos\left(2\pi\eta\frac{\tau}{P_{\text{Rot}}}\right) + \frac{1}{2\eta Q} \sin\left(2\pi\eta\frac{\tau}{P_{\text{Rot}}}\right) \right] \quad (5.1)$$

where $\eta = |1 - (4Q^2)^{-1}|^{1/2}$. The *rotation term* kernel takes as its hyperparameters: the standard deviation of the process, σ_{GP} , which is related to the amplitude of the variability signal, the stellar rotation period, P_{Rot} , the signal quality, Q , the difference in signal quality between the P_{Rot} and $P_{\text{Rot}}/2$ modes, ΔQ , such that $Q_{P_{\text{Rot}}} = Q_{P_{\text{Rot}}/2} + \Delta Q$, and the mix factor between the two modes, f , such that $\sigma_{P_{\text{Rot}}}^2 = f \sigma_{P_{\text{Rot}}/2}^2$. Such a kernel has been designed to be a good model for variability due to stellar rotation and has been used successfully in previous exoplanet high precision radial velocity analysis (eg. Osborn et al., 2021b).

During the analysis, we used the same kernel to fit the radial velocity measurements and the CCF FWHM activity indicators of the ESPRESSO observations. By modelling the variations in CCF FWHM simultaneously with the RVs, we get a better estimate of the impact of the stellar variability on the RV measurements. This allows us to limit any impact on the measured planetary RV signals due to over-fitting of the GP, and so extract better quality mass

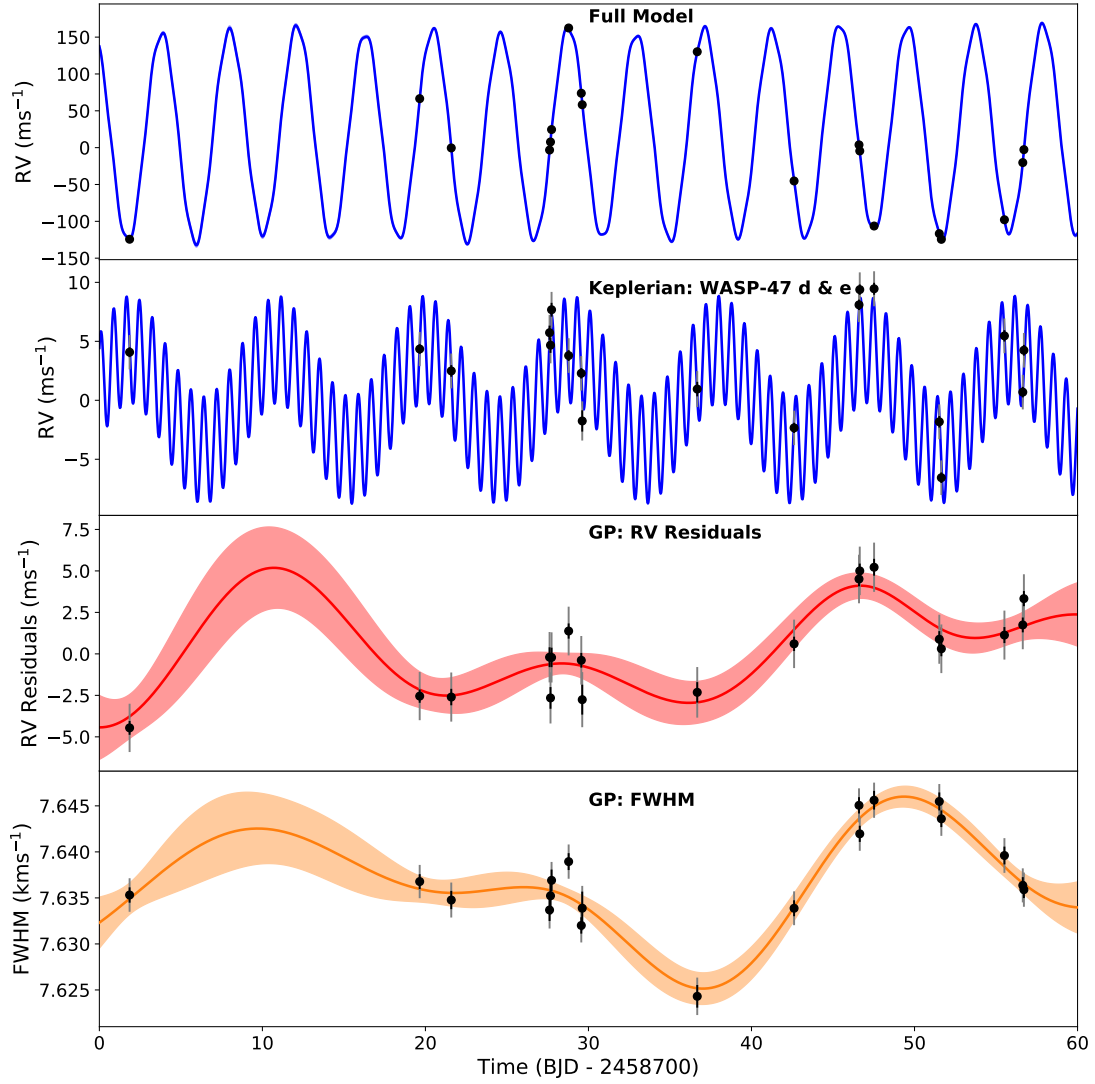


Figure 5.8: ESPRESSO time series data for WASP-47. **Top:** ESPRESSO radial velocity measurements with the systemic velocity γ_{ESP} subtracted. The blue line gives the full Keplerian model for all four planets and the GP. **Second:** ESPRESSO radial velocity measurements with γ_{ESP} , the Keplerian models for WASP-47 b and c, and the GP model subtracted. The blue line gives the two-planet Keplerian model for WASP-47 d and e. **Third:** ESPRESSO radial velocity residuals to the four-planet Keplerian model. The red line gives the GP model and the shaded area provides the 1σ confidence interval of the GP. **Bottom:** FWHM measurements of the ESPRESSO CCFs. The orange line gives the GP model and the shaded area provides the 1σ confidence interval of the GP.

measurements. A similar method was used by Osborn et al. (2021b) to account for the stellar variability of TOI-755.

For this method, during the sampling we use the same P_{Rot} , Q , ΔQ , and f hyperparameters for all datasets and a different σ_{GP} and mean for each activity or radial velocity time series. We use a wide Gaussian prior centred on 35 d for P_{Rot} taken from our Lomb-Scargle analysis. The Q hyperparameter is related to the damping timescale of the SHO modes, which in a physical sense is related to the decay timescale of the stellar spots. As such, we also implement a prior enforcing $Q > \pi$, which in turn ensures the spot decay timescale is longer than P_{Rot} . This requirement comes from our prior knowledge of the lifetimes of active stellar regions (Donahue et al., 1997). Avoiding low values of Q also helps prevent the GP over-fitting the data (Kosiarek and Crossfield, 2020).

To assess the statistical justification of using a GP to account for stellar activity in the radial velocity datasets, we perform a simple model comparison analysis. We calculate and compare the Bayesian Information Criterion (BIC, Schwarz, 1978; Neath and Cavanaugh, 2012) for both sets of models, one with the GP and one without. This statistic assesses whether or not the model fit to the data is sufficiently improved to justify the increased complexity of the new model. When comparing models, the model which produces the lower BIC value is preferred.

We calculate independent BIC values for the ESPRESSO, HARPS-N, and HIRES datasets. We calculate the change in the BIC, ΔBIC , between the models with and without the GP included. We find values for the HARPS-N and HIRES datasets of $\Delta \text{BIC}_{\text{HARPS-N}} = 4.88$ and $\Delta \text{BIC}_{\text{HIRES}} = 8.76$. This indicates that the inclusion of GPs for these two datasets is not justified. For the ESPRESSO radial velocities, we calculate a value of $\Delta \text{BIC}_{\text{ESPRESSO}} = -16.86$. This is strong statistical evidence for the inclusion of a GP to model the stellar activity in the ESPRESSO radial velocities. It is not unexpected that the use of a GP is justified for ESPRESSO and not HARPS-N and HIRES. The larger telescope diameter of the VLT results in the photon-limited uncertainties of the ESPRESSO radial velocities (0.55 m s^{-1}) being a factor of six smaller than those for HARPS-N (3.2 m s^{-1}) and a factor four smaller than HIRES (2.0 m s^{-1}). This increased precision of the data allows for the robust detection of the stellar activity signal. We do not use GPs for the CORALIE data as uncertainty is 12.5 m s^{-1} , which is too large to detect the stellar activity signal seen in the ESPRESSO data.

Table 5.2: Planetary parameters for WASP-47 b and e derived in this work in sections 5.3.1 and 5.3.6.

Parameter	Symbol	Unit	Prior	Value
Planetary parameters				
<i>WASP-47 e</i>				
Time of conjunction	T_C	BJD (TDB)	$\mathcal{N}(2457011.34863, 0.00030)$	$2457011.34862 \pm 0.00030$
Orbital Period	P	d	$\mathcal{N}_{\mathcal{U}}(0.789595, 0.000005, 0., \infty)$	0.7895933 ± 0.0000044
RV Semi-Amplitude	K_e	m s^{-1}	$\mathcal{N}_{\mathcal{U}}(5., 10., 0., \infty)$	4.55 ± 0.37
Radius Ratio	R_e/R_*		$\mathcal{U}(0., 1.0)$	0.01458 ± 0.00013
Planet Mass [†]	M_e	M_{\oplus}		6.77 ± 0.57
Planet Radius [†]	R_e	R_{\oplus}		1.808 ± 0.026
Planet Density [†]	ρ_e	g cm^{-3}		6.29 ± 0.60
<i>WASP-47 b</i>				
Time of conjunction	T_C	BJD (TDB)	$\mathcal{N}(2457007.932103, 0.000019)$	$2457007.932103 \pm 0.000019$
Orbital Period	P	d	$\mathcal{N}_{\mathcal{U}}(4.1591492, 0.0000006, 0., \infty)$	4.1591492 ± 0.0000006
RV Semi-Amplitude	K_b	m s^{-1}	$\mathcal{N}_{\mathcal{U}}(150., 50., 0., \infty)$	140.84 ± 0.40
Radius Ratio	R_b/R_*		$\mathcal{U}(0., 1.0)$	0.10191 ± 0.00022
Planet Mass [†]	M_b	M_{\oplus}		363.6 ± 7.3
Planet Radius [†]	R_b	R_{\oplus}		12.64 ± 0.15
Planet Density [†]	ρ_b	g cm^{-3}		0.989 ± 0.040

Table 5.3: Planetary parameters of WASP-47 c and d derived in this work in sections 5.3.1 and 5.3.6.

Parameter	Symbol	Unit	Prior	Value
Planetary parameters				
<i>WASP-47 d</i>				
Time of conjunction	T_C	BJD (TDB)	$\mathcal{N}(2457006.36955, 0.00035)$	$2457006.36955 \pm 0.00035$
Orbital Period	P	d	$\mathcal{N}_{\mathcal{U}}(9.03055, 0.0002, 0., \infty)$	9.03055 ± 0.00008
RV Semi-Amplitude	K_d	m s^{-1}	$\mathcal{N}_{\mathcal{U}}(5., 10., 0., \infty)$	4.26 ± 0.37
Radius Ratio	R_d/R_*		$\mathcal{U}(0., 1.0)$	0.02876 ± 0.00017
Planet Mass [†]	M_d	M_{\oplus}		14.2 ± 1.3
Planet Radius [†]	R_d	R_{\oplus}		3.567 ± 0.045
Planet Density [†]	ρ_d	g cm^{-3}		1.72 ± 0.17
Orbital Eccentricity	e_d		$\mathcal{N}_{\mathcal{U}}(0., 0.014, 0., 1.)$	$0.010^{+0.011}_{-0.007}$
Argument of Periastron	ω_d	deg	$\mathcal{U}(-180., 180.)$	$16.5^{+84.2}_{-98.6}$
<i>WASP-47 c</i>				
Time of conjunction	T_C	BJD (TDB)	$\mathcal{N}(2457763.4, 20.)$	2457763.1 ± 4.3
Orbital Period	P	d	$\mathcal{N}_{\mathcal{U}}(590, 15., 0., \infty)$	588.8 ± 2.0
RV Semi-Amplitude	K_c	m s^{-1}	$\mathcal{N}_{\mathcal{U}}(30., 15., 0., \infty)$	31.04 ± 0.40
Planet Minimum Mass [†]	$M_c \sin i$	M_{\oplus}		398.9 ± 9.1
Orbital Eccentricity	e_c		$\mathcal{U}(0., 1.)$	0.295 ± 0.016
Argument of Periastron	ω_c	deg	$\mathcal{U}(-180., 180.)$	112.0 ± 4.3

[†] - Parameter derived from fitted parameters

5.3.6 Final Combined Model

We modelled the ESPRESSO, HARPS-N, HIRES, and CORALIE data using our final model built from Keplerian orbits for the four planets along with a GP to account for the stellar variability signals present in the ESPRESSO dataset. The GP was simultaneously fit to the ESPRESSO radial velocities and CCF FWHM measurements, in order to limit the effect of over-fitting the GP to the radial velocities. We perform the sampling using the method detailed in Section 5.3.2. We ran 40 chains for 10,000 steps each, following a burn-in of 4,000 steps for each chain. We calculate the Gelman-Rubin statistic (\hat{R} ; Gelman and Rubin, 1992) for all the chains, and find that all chains have $\hat{R} \lesssim 1.001$ indicating good convergence.

From this analysis we find a radial velocity semi-amplitude for WASP-47 e of $K_e = 4.55 \pm 0.37 \text{ m s}^{-1}$. This value is consistent with the semi-amplitude derived from the initial modelling in Section 5.3.2 of $4.73 \pm 0.39 \text{ m s}^{-1}$, but represents an improvement in the precision of the measurement. This corresponds to an improvement in the mass measurement precision from $M_p = 7.03 \pm 0.59 M_\oplus$ for the initial model to $M_p = 6.77 \pm 0.57 M_\oplus$ for the final model. We also note that the value of P_b derived from this analysis is consistent with the value derived from the transit analysis in Section 5.3.1. The stellar rotation period of WASP-47 derived from this analysis is $P_{\text{Rot}} = 39.4^{+2.2}_{-4.5} \text{ d}$, which again is consistent with the rotation period derived from the K2 photometry.

The ESPRESSO data are plotted in Figure 5.8 and the radial velocity phase folds for all planets and instruments are plotted in Figure 5.9. The parameters derived are given in Tables 5.2, 5.3 and 5.4.

With the inclusion of our ESPRESSO data we have obtained a mass of WASP-47 e of $6.77 \pm 0.57 M_\oplus$. This value is consistent at the 1σ level with the mass determined by Vanderburg et al. (2017), but we have improved on the precision they quote on the mass by 15%. With the improved precision of the ESPRESSO data we have uncovered a clear stellar activity signal, which is consistent with the stellar variability seen in the K2 photometry. This allows us to model the stellar activity using a physically motivated GP informed by our knowledge of the stellar rotation.

Our results also allow us to improve the constraints on the bulk density of WASP-47 e. We derive a density of $\rho_e = 6.29 \pm 0.60 \text{ g cm}^{-3}$, making WASP-47 e the super-Earth with the second most precisely constrained density to date, behind only 55 Cancri e (Bourrier et al., 2018). Our ESPRESSO data also improve the constraint on M_d . We find a mass of $14.2 \pm 1.3 M_\oplus$, which is both consistent with the mass measured by Vanderburg et al. (2017) and a 13% improvement on the precision of the mass measurement. For the hot Jupiter WASP-47 b we improve the precision of the radial velocity semi-amplitude, yet the precision on the mass remains unchanged from

Table 5.4: Additional parameters from the sampling in Section 5.3.6.

Parameter	Unit	Prior	Value
Instrumental Parameters			
γ_{ESP}	m s^{-1}	$\mathcal{U}(-27350., -26850.)$	-27165.95 ± 1.27
γ_{HARPS}	m s^{-1}	$\mathcal{U}(-27350., -26850.)$	-27041.03 ± 0.55
γ_{HIRES}	m s^{-1}	$\mathcal{U}(-250., 250.)$	6.50 ± 0.75
$\gamma_{\text{COR;A}}^{\dagger}$	m s^{-1}	$\mathcal{U}(-27500., -26500.)$	-27081.33 ± 1.89
$\gamma_{\text{COR;B}}^{\dagger}$	m s^{-1}	$\mathcal{U}(-27500., -26500.)$	-27067.57 ± 5.96
γ_{ESPFWHM}	m s^{-1}	$\mathcal{U}(7600., 7700.)$	7635.6 ± 1.0
$\log_{10} \sigma_{\text{ESP}}$	$\log \text{m s}^{-1}$	$\mathcal{U}(-5., 1.)$	0.145 ± 0.214
$\log_{10} \sigma_{\text{HARPS}}$	$\log \text{m s}^{-1}$	$\mathcal{U}(-5., 1.)$	-2.33 ± 1.82
$\log_{10} \sigma_{\text{HIRES}}$	$\log \text{m s}^{-1}$	$\mathcal{U}(-5., 1.)$	0.488 ± 0.069
$\log_{10} \sigma_{\text{COR;A}}^{\dagger}$	$\log \text{m s}^{-1}$	$\mathcal{U}(-7., 2.)$	-2.38 ± 3.03
$\log_{10} \sigma_{\text{COR;B}}^{\dagger}$	$\log \text{m s}^{-1}$	$\mathcal{U}(-7., 2.)$	-2.95 ± 2.75
$\log_{10} \sigma_{\text{ESPFWHM}}$	$\log \text{m s}^{-1}$	$\mathcal{U}(-7., 1.)$	-2.79 ± 0.13
GP Hyperparameters			
P_{Rot}	d	$\mathcal{N}_{\mathcal{U}}(35, 10, 28, \infty)$	$39.4^{+2.2}_{-4.5}$
$\ln Q$		$\mathcal{U}(1.15, 15)$	$2.6^{+5.2}_{-1.1}$
$\ln \Delta Q$		$\mathcal{U}(-7, 10)$	$-0.40^{+6.18}_{-5.04}$
f		$\mathcal{U}(0, 1)$	$0.52^{+0.32}_{-0.31}$
$\sigma_{\text{GP,ESP}}$		$\mathcal{U}(0, 20)$	$4.58^{+3.83}_{-2.44}$
$\sigma_{\text{GP,ESPFWHM}}$		$\mathcal{U}(0, 100)$	$7.04^{+4.18}_{-2.16}$

\dagger - COR;A and COR;B refer to the sets of CORALIE data taken before and after the spectrograph was updated in November 2014

Epoch	Mid-Transit Time (BJD TDB)
587	$2459449.35411 \pm 0.00069$
590	$2459461.83099 \pm 0.00076$
591	$2459465.98832 \pm 0.00076$
592	$2459470.14800 \pm 0.00075$

Table 5.5: Measured *TESS* mid-transit times for WASP-47 b. The epoch is relative to the T_C value given in Table 5.2.

the Vanderburg et al. (2017) measurements. From this, we conclude that the primary limiting factor for improving the constraints on M_b arise from the constraints on the stellar mass, which is currently measured to 3% precision, compared to the 0.3% precision to which we have measured K_b . We do not achieve significant improvement on the measurement of the minimum mass of WASP-47 c. This is unsurprising, as our ESPRESSO radial velocity measurements only cover a small fraction of the orbital period of WASP-47 c ($P_c = 588.4$ d).

5.3.7 Transit Timing Analysis

WASP-47 b and WASP-47 d have already been shown to exhibit significant transit timing variations (TTVs, eg. Becker et al., 2015; Weiss et al., 2017). Due to the low signal-to-noise of the *TESS* transits of these planets, we are unable to strongly constrain the transit centre times for the individual *TESS* transits of WASP-47 d or WASP-47 e. However we can measure the transit times for the hot Jupiter WASP-47 b.

We re-fit each transit of WASP-47 b in the *TESS* data in order to measure the individual T_C values. During this analysis, we fix the transit shape to the model derived in Section 5.3.6. Models from the same analysis used to subtract the transits of WASP-47 d and WASP-47 e from the light curve before fitting. We also perform the same analysis for the WASP-47 b transits in the short cadence K2 data. The transit times measured are plotted in Figure 5.10 and the *TESS* T_C values are provided in Table 5.5. The uncertainty on an individual T_C from the *TESS* data is on the order of 1 minute, which is roughly twice the TTV amplitude seen in the K2 data. The *TESS* transit times display a scatter of a similar magnitude. As such, the T_C measurements are consistent with the TTV predictions from the K2 results (see Figure 5.10). However the detection is marginal, and we cannot know the phase of the signal due to the significant time gap between K2 and *TESS* data.

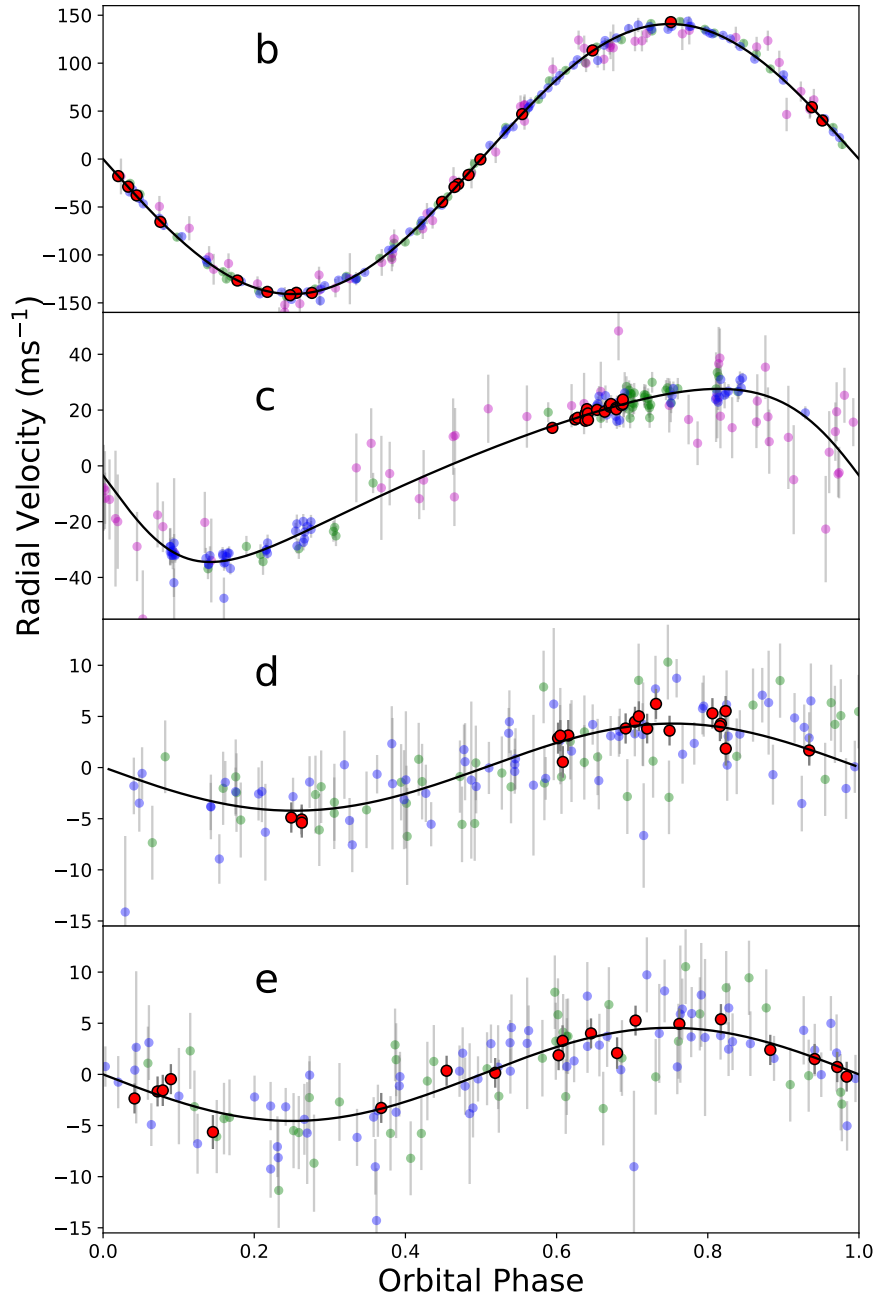


Figure 5.9: Phase-folded RVs with all GPs and systemic velocities removed for WASP-47 b (top), WASP-47 c (second), WASP-47 d (third), and WASP-47 e (bottom). The colours of the data from the various instruments are: ESPRESSO (red); HARPS-N (blue); HIRES (green); CORALIE (magenta). Note we do not plot the CORALIE data for planets d and e as the RMS of the CORALIE data is larger than the semi-amplitudes of these two planets.

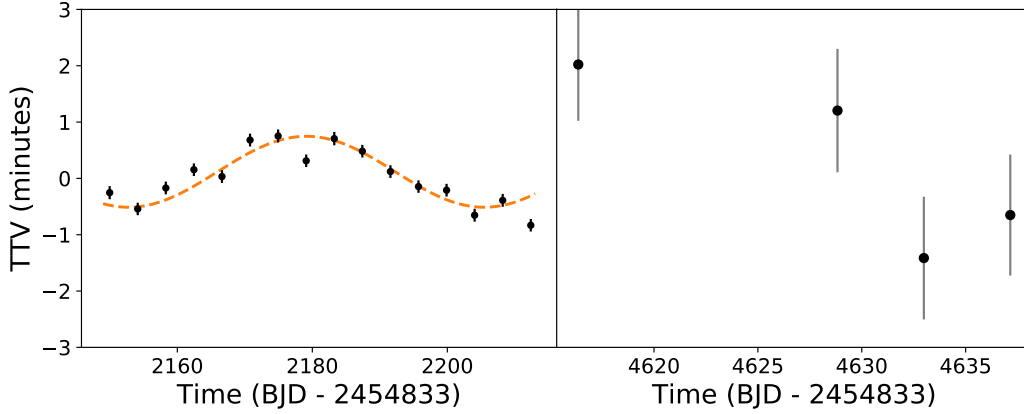


Figure 5.10: Observed TTVs for WASP-47 b for the transits in the **Left:** K2 photometry and **Right:** *TESS* photometry. The orange line gives the TTV model from Becker et al. (2015).

5.4 Discussions

The mass and density we measure for WASP-47 e are consistent at the 1σ level with the results of Vanderburg et al. (2017). Vanderburg et al. (2017) use the planetary composition models of Lopez (2017) to show that their measured parameters of $M_P = 6.83 \pm 0.66 M_\oplus$ and $\rho_P = 6.35 \pm 0.64 \text{ g cm}^{-3}$ are consistent with WASP-47 e having a steam-rich layer surrounding an Earth-like core and mantle. Due to the agreement between these measurements and the values derived in this work, such a composition remains a plausible scenario.

We compare our newly derived parameters for WASP-47 e to the sample of known planets with $M_P < 10 M_\oplus$, $R_P < 2 R_\oplus$ and mass and radius measurement precisions better than 10% (see Figure 5.11). We find that WASP-47 e is similar in mass and radius to 55 Cancri e, and that these two exoplanets are the only ones in the sample which fall onto the 100% MgSiO_3 composition model of Zeng et al. (2019). The WASP-47 and 55 Cancri planetary systems are also the only two to contain close in giant planets: WASP-47 b ($M_P = 1.144 \pm 0.023 M_J$; $P = 4.159 \text{ d}$) and 55 Cancri b ($M_P = 0.804 \pm 0.009 M_J$; $P = 14.6516 \text{ d}$). WASP-47 e has a lower density than K2-141 b and HD-213885 b despite receiving a very similar amount of stellar irradiation (see Figure 5.12). 55 Cancri e receives a similar level of irradiation and has a similar density to WASP-47 e. It is possible that the presence of the close-in giant planet companions to these super-Earths has caused them to have a lower density than other planets with similar levels of stellar irradiation.

Due to the intense stellar irradiation, this reduced density is almost certainly not due to an extended H/He atmosphere because such an atmosphere would have been lost through photo-evaporation (Penz et al., 2008; Sanz-Forcada et al., 2011). One possibility could be the scenario

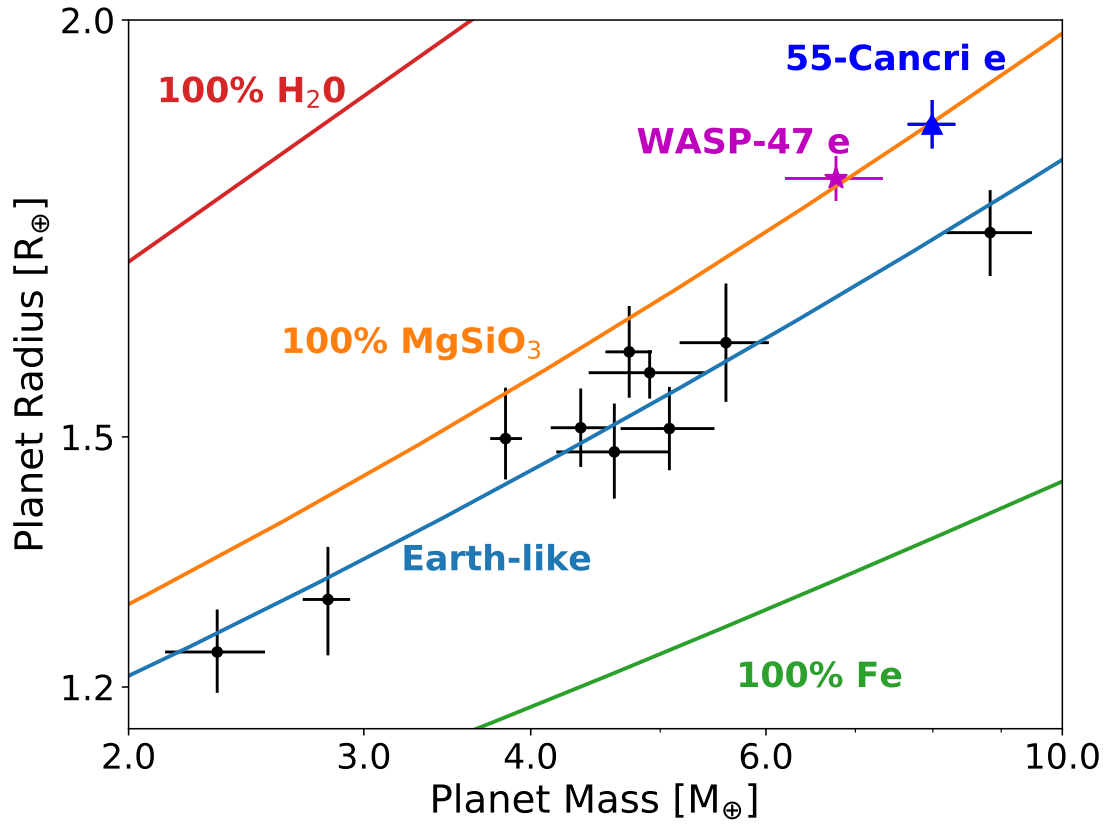


Figure 5.11: Mass-Radius diagram for low-mass exoplanets. The measurements and uncertainties are taken from the NASA exoplanet archive (accessed 2021 May 12). The black points show exoplanets with masses and radii measured to better than 10% precision. WASP-47 e is shown with the magenta star, and 55 Cancr e is plotted with the blue triangle. These two planets now have the most precise density measurements for any known super-Earths. The solid lines give various composition models from Zeng et al. (2016, 2019).

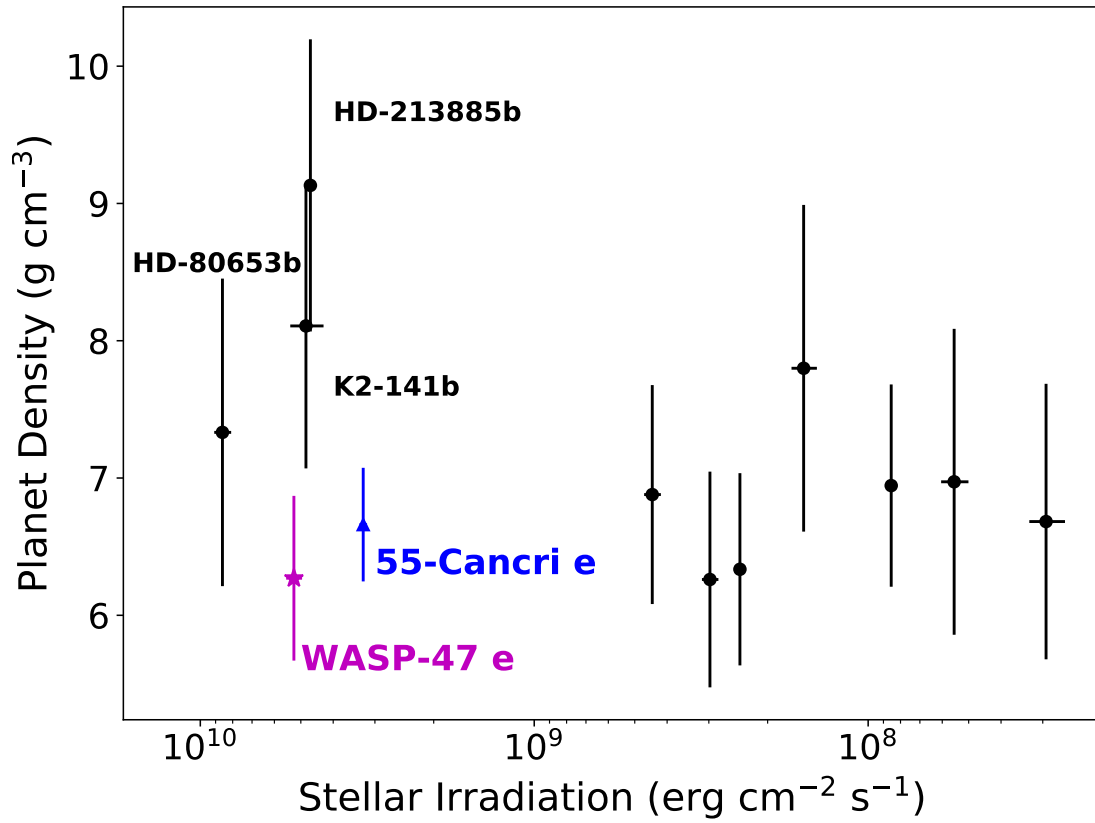


Figure 5.12: The variation of bulk planetary density with stellar irradiation for the sample of planets plotted in Figure 5.11. WASP-47 e is depicted by the magenta star and 55 Cancri e by the blue triangle.

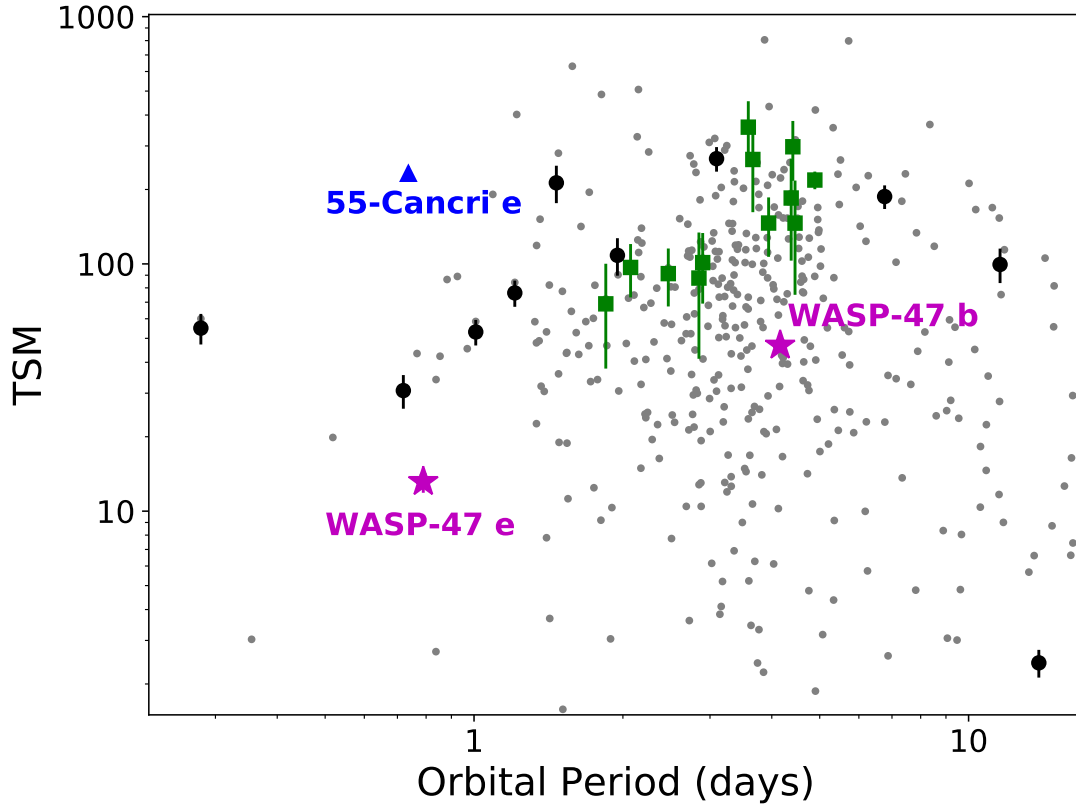


Figure 5.13: Comparison of TSM vs orbital period for various known exoplanets. We plot the sample of planets from the NASA Exoplanet Archive with a radius measured to better than 10% precision and a mass measured to better than 50% precision (grey points), the *JWST* community targets (green squares; Stevenson et al., 2016) and the sample of planets from Figure 5.11 (black points). WASP-47 b and WASP-47 e are depicted by the magenta stars and 55 Cancri e by the blue triangle.

with a steam-rich layer proposed by Vanderburg et al. (2017). Alternatively, Dorn et al. (2019) recently proposed that WASP-47 e and 55 Cancri e could have compositions rich in refractory elements, such as Ca and Al, which condense out of protoplanetary disks at high temperatures. This different elemental make-up was shown to result in planets with densities 10–20% less than a planet of the same R_p but with an Earth-like composition (Dorn et al., 2019) and therefore would explain the lower densities of these two planets, given the irradiation they receive.

Obtaining transmission spectroscopy observations for the three inner WASP-47 planets will provide further clues to unlock the formation history of this system. We use the Transmission Spectroscopy Metric (TSM) from Kempton et al. (2018) to assess the potential for obtaining such observations. The TSM provides near-realistic values of the expected signal-to-noise ratio

obtained from a 10 hour observation sequence with *JWST*. For the inner planets, we calculate values of 13.2 ± 1.3 (WASP-47 e), 46.8 ± 2.3 (WASP-47 b), and 23.4 ± 2.4 (WASP-47 d). While modest compared to other planets with similar orbital parameters due to the relative faintness of WASP-47 ($V = 11.94$ mag) (see Figure 5.13), these values indicate that a significant amount of information on the atmospheric compositions of these planets can be achieved through *JWST* observations. Combined with the precise constraints on the masses of these planets, these atmospheric observations would provide great insight into the composition and possible formation history of the WASP-47 planets.

The potential detection of an atmosphere on 55 Cancri e has been reported from both *HST* (Tsiaras et al., 2016) and Spitzer (Angelo and Hu, 2017) observations. We also note that 55 Cancri e will be observed by *JWST* during its Cycle 1 observations³. Due to the similarities between the two planets and their environments, any revelations about the atmospheric conditions of 55 Cancri e have implications for the likelihood of an atmosphere on WASP-47 e.

WASP-47 e and 55 Cancri e are the only two planets to fall solidly on the 100% MgSiO₃ composition line in Figure 5.11. This different composition of WASP-47 e and 55 Cancri e is possibly the result of these systems forming through a different pathway to the other planets shown. The nature of WASP-47 e orbiting interior to a hot Jupiter also strongly suggests a different planetary formation and evolution mechanism to the large majority of hot Jupiter systems (Huang et al., 2016). The formation of hot Earths and Neptunes interior to hot Jupiters can arise as a result of portions of the protoplanetary disk being shepherded to the inner regions of the planetary system by a giant planet migrating through disk interactions (Fogg and Nelson, 2005, 2007). This disk shepherding prior to the formation of WASP-47 e could provide a high temperature environment amenable to the formation from high temperature condensates (Dorn et al., 2019).

Poon et al. (2021) demonstrated that not only can an in-situ formation mechanism produce planetary systems containing hot Jupiters and inner small planets but also that this formation mechanism does not reproduce the observed population of single hot Jupiters. This again suggests that the WASP-47 planetary system formed through a different mechanism to other hot Jupiter systems. This scenario was also suggested by Huang et al. (2016), who note that the WASP-47 system bears stronger resemblance to the population of warm Jupiter systems, which often have smaller planets interior to the warm Jupiter. It is possible that the WASP-47 and 55 Cancri systems formed through a mechanism similar to warm Jupiter systems, resulting in different bulk compositions for WASP-47 e and 55 Cancri e.

With only two super-Earths with close giant planet companions and precisely measured densities, we do not have a large enough sample size from which to draw significant conclusions.

³*JWST* GO Programs 1952 and 2084.

A larger sample of known planets interior to hot Jupiters would allow us to better identify any trends in the properties of these inner companions. Therefore, further discoveries of small planets interior to hot and warm Jupiters are needed to shed light on how these systems form, and how the compositions of the small planets are sculpted by their formation. There is a possibility that other known hot Jupiters have small planets orbiting interior to them. The majority of known transiting hot Jupiters were discovered by ground based transit surveys, and so the discovery data did not have sufficient photometric precision to detect super-Earth planets. WASP-47 d and WASP-47 e are only known thanks to the K2 data and of the 536 known exoplanets with $P < 10$ d and $M_p > 0.1 M_J$ only 80 have received such high precision monitoring with *Kepler* or K2⁴. It is therefore possible that several of the hot Jupiter host stars that have not been monitored at very high precision also contain inner transiting super-Earths interior to the orbits of their hot Jupiters.

The two stars WASP-47 and 55 Cancri have metallicities of $[Fe/H] = 0.38 \pm 0.05$ (Vanderburg et al., 2017) and $[Fe/H] = 0.35 \pm 0.10$ (Bourrier et al., 2018) respectively. These two stars are significantly more metal rich than the host stars for the other super-Earths in the sample considered in this study (see Figure 5.14). While high metallicities are expected for stars which host close-in giant exoplanets (Fischer and Valenti, 2005), we find that WASP-47 and 55 Cancri have high metallicities even compared to the metallicity distribution for hot-Jupiter host stars. Osborn and Bayliss (2020) investigated this planet-metallicity correlation using a homogeneous sample of 217 hot Jupiter host stars. We find that WASP-47 is more metal rich than 96% of that sample, and 55 Cancri is more metal rich than 94%. It is possible that the high metallicity of the host stars has in some way affected the formation and composition of WASP-47 e and 55 Cancri e. However, we will only be able to confirm this correlation with the discovery of more small planets interior to close-in giant planets.

5.5 Conclusions

We report radial velocity measurements obtained for WASP-47 using the ESPRESSO spectrograph. We combined our new RV measurements with existing data obtained using the HARPS-N, HIRES and CORALIE spectrographs. Our measurements confirm that WASP-47 e is a super-Earth with a mass of $6.77 \pm 0.57 M_\oplus$ and a bulk density of $6.29 \pm 0.60 \text{ g cm}^{-3}$. Using these data, we improve the mass measurement precision for the super-Earth WASP-47 e and the Neptune-sized WASP-47 d by 15% and 13% respectively compared to the previous best measurements (Vanderburg et al., 2017). Our measured bulk density shows that WASP-47 e is similar in density, and likely composition, to 55 Cancri e. WASP-47 e has the second most precisely measured

⁴NASA exoplanet archive, accessed 2022-01-20.

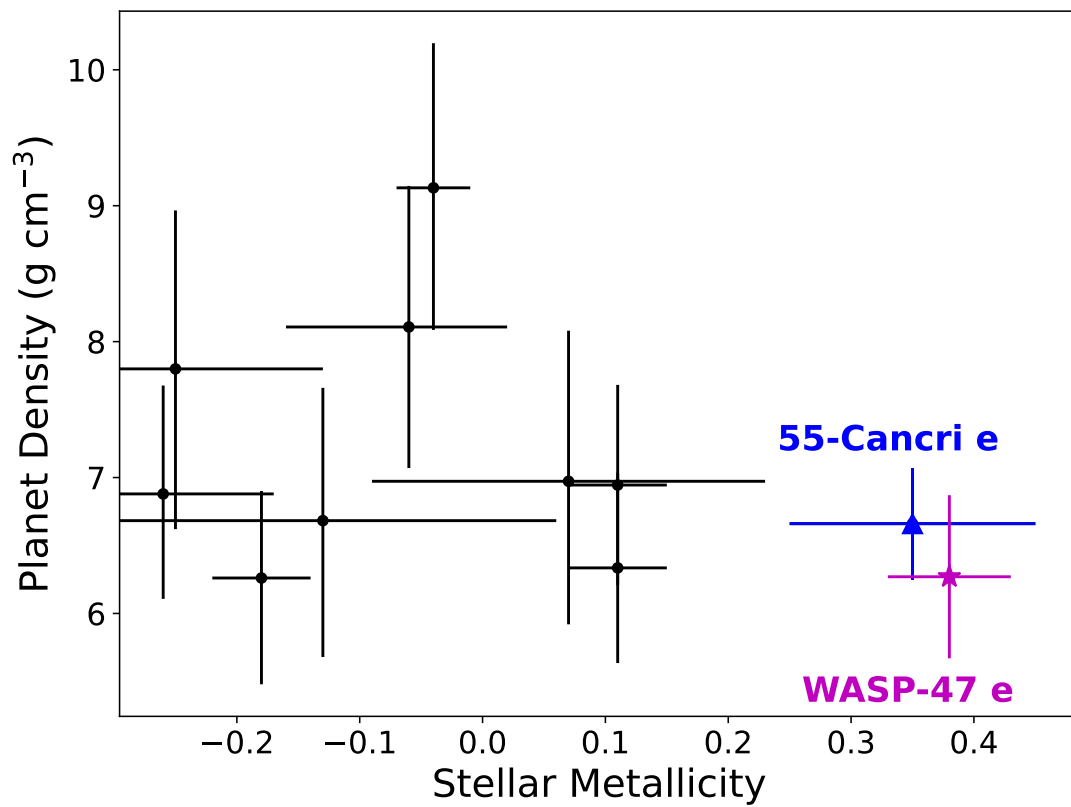


Figure 5.14: Planet bulk density plotted against metallicity of the host star for WASP-47 e, 55 Cancri e, and the sample of super-Earths from Figure 5.11.

density of any super-Earth, only behind 55 Cancri e which orbits a much brighter host star.

We find variability in the K2 photometric data which is indicative of a $P_{\text{Rot}} = 32.5 \pm 3.9$ d rotation period for WASP-47. The improved precision of the ESPRESSO data compared to previous datasets allowed us to identify a stellar activity signal in the ESPRESSO radial velocity residuals and activity indicators with a periodicity consistent with the rotation period derived from K2.

With the inclusion of the *TESS* photometry, we refine the orbital ephemerides of the three inner planets. This refinement is vital for future follow-up observations. As an example, at the start of July 2022 when *JWST* observations should begin, our updated ephemeris predicts the transit of WASP-47 b to occur 20 minutes later than the older ephemeris of Becker et al. (2015). Our updated ephemeris has a 1σ uncertainty of just 0.57 minutes, compared to 4.67 minutes from the older Becker et al. (2015) ephemeris. Similarly for WASP-47 d our new ephemeris predicts the transit to occur 114 minutes earlier, with a reduced 1σ uncertainty of 35 minutes compared to 84 minutes. For WASP-47 e our new ephemeris predicts the transit to occur just 9.73 minutes earlier, but with a reduced 1σ uncertainty of 25 minutes compared to 65 minutes. These refined transit predictions are crucial for properly planning and fully interpreting high value follow-up observations, such as transmission spectroscopy with *JWST*.

Due to the *TESS* photometry having a photometric precision of 3040 ppm-per-minute (c.f. K2 precision of 350 ppm-per-minute), the *TESS* data are unable to improve the constraints on the radii of the transiting planets. For similar reasons the *TESS* data are not sensitive to the stellar variability seen in the K2 data.

Compared to other well characterized super-Earths, WASP-47 e and 55 Cancri e stand out in terms of their low densities given their stellar environments and the presence of a close-orbiting giant planet. It is possible that a different formation mechanism to the majority of hot Jupiters was required to form these systems, and this difference in formation could have resulted in WASP-47 e and 55 Cancri e having different compositions to other super-Earths.

Chapter 6

Transit search for gas giant planets orbiting low-mass stars

Note

This chapter is based on the paper “*Determining the occurrence rates of giant planets orbiting low-mass stars*” which is currently in preparation. All the analysis and writing was performed by me. The only remaining task for this paper is the running of the planet injection-recovery tests.

Abstract

We present a systematic search for transiting giant planets orbiting nearby low-mass stars. Gas giant planets sculpt the formation and evolution of planetary systems and therefore understanding the mechanisms through which giant planets form is crucial. Formation of giant planets around low-mass stars is predicted to be rare by the core-accretion planet formation theory, however currently there is not a robust measurement of the occurrence rate for these systems. In this planet search, we identified fourteen candidate giant planets from a sample of 91,306 low-mass stars using *TESS* 30 minute cadence photometry. With the results of upcoming follow-up spectroscopic observations of our candidates and planet injection-recovery tests we will derive the first precise measurement of the occurrence rate for giant planets with low-mass stellar hosts.

6.1 Introduction

Low-mass stars dominate the Galactic stellar population. An estimated 70% of stars in our Galaxy are K7V or later, equating to masses of $\leq 0.65 M_{\odot}$ (Chabrier and Baraffe, 2000). These low mass stars offer some key advantages for the discovery of exoplanets. For radial velocity monitoring, the semi-amplitude of the exoplanet signal scales as $M_*^{-\frac{2}{3}}$. For the detection of transiting exoplanets, the advantage is even more significant, with the transit depth scaling with R_*^{-2} . This makes the detection of super-Earth and sub-Neptune planets much easier around low-mass stars. In addition, the reduced luminosity of low-mass stars means that the habitable zones can be on the order of a few tens of days (eg. Dressing and Charbonneau, 2015).

For these reasons a number of exoplanet surveys have focused on low-mass host stars. Transit surveys such as NGTS (Wheatley et al., 2018), *TESS* (Ricker et al., 2015), TRAPPIST (Gillon et al., 2011), and SPECULOOS (Delrez et al., 2018) all operate in red optical wavelengths to allow for better photometric precision for low-mass stars. The SPECULOOS project in particular is performing a targeted search of nearby late M-dwarfs for transiting exoplanets (eg. Gillon, 2018; Sebastian et al., 2021). Radial velocity surveys are also focusing on low-mass stars, such as the HARPS M-dwarf survey (Bonfils et al., 2013) and the VLT+UVES M-dwarf planet search (Zechmeister et al., 2009). Specialised high resolution near-IR spectrographs are also being used to monitor low mass stars, such as CARMENES (Quirrenbach et al., 2014), SPIROU (Thibault et al., 2012), NIRPS (Bouchy et al., 2017), and IRD (Tamura et al., 2012).

However, low-mass stars do pose some significant challenges to observers, the most important being the low luminosity of these objects. The luminosity, L , of stars increases with stellar mass, M_* . For stars in the mass range $0.38 M_{\odot} < M_* \leq 1.05 M_{\odot}$ this follows the approximate relation $L \propto M_*^{4.8}$ (Eker et al., 2015). This faintness reduces the signal-to-noise ratio achieved for observations, making it more difficult to obtain the observational precision required for exoplanet detection. Moreover, these low-mass stars often display high levels of magnetic stellar activity (West et al., 2008). This magnetic activity can manifest itself as active regions on the stellar surface, which lead to variability in photometric or radial velocity time series. These high amplitude stellar variability signals can often hide exoplanet transits or Keplerian radial velocity signals.

Since the detection of 51-Pegasi b (Mayor and Queloz, 1995) revealed the existence of giant planets on short orbits ($P \lesssim 10$ d), known as hot Jupiters, the prevalence of these planets has been a question of great interest to the community. As such, there have been numerous studies that have focused on measuring the occurrence rate of these planets. Different planet formation mechanisms should leave signatures in the occurrence rates of the different populations of planets (eg. Emsenhuber et al., 2021a,b; Schlecker et al., 2021). For example, it has been

demonstrated that hot Jupiter planets are found predominantly around high metallicity host stars (Fischer and Valenti, 2005; Osborn and Bayliss, 2020), which has been interpreted as evidence that giant planets largely form through the core-accretion mechanism.

Early radial velocity surveys gave indications that approximately 1% of stars hosted a hot Jupiter. Using radial velocities of FGK-type stars from the HIRES spectrometer at the Keck I telescope, Cumming et al. (2008) derived an occurrence rate of $1.5 \pm 0.6\%$ for planets with $M_P \sin i \geq 0.3 M_J$ and $P < 11.5$ d. A few years later, Mayor et al. (2011) derived an occurrence rate of $0.89 \pm 0.36\%$ for planets with $M_P \sin i \geq 50 M_\oplus$ and $P < 11$ d using data from the HARPS spectrograph.

Ground-based transit surveys found results indicating lower frequencies for close in giant planets. From the OGLE transit survey, Gould et al. (2006) derived occurrence rates for planets with $1.0 R_J \leq R_P \leq 1.25 R_J$ of $0.31^{+0.45}_{-0.18}\%$ for $3 < P < 5$ d and $0.14^{+0.17}_{-0.07}\%$ for $1 < P < 3$ d, at 90% confidence. Through the superLupus survey, observing with the ANU 40 inch telescope at Siding Spring Observatory, Bayliss and Sackett (2011) derived a frequency of $0.10^{+0.27}_{-0.08}\%$ for giant planets with $1 \leq P \leq 10$ d. The discrepancy between the results from radial velocity and transit surveys likely arises from observational biases in radial velocity surveys.

Over the past two decades, the number of known exoplanets has exploded, particularly as a result of the *Kepler* mission (Borucki et al., 2010), resulting in huge advances in our knowledge of hot Jupiter occurrence rates. Using early *Kepler* results, Howard et al. (2012) derived a frequency of $0.4 \pm 0.1\%$ for planets with $R_P \geq 8 R_\oplus$ and $P < 10$ d. Improving upon the estimates of the rate of false positives in the *Kepler* data, Fressin et al. (2013) refined the *Kepler* occurrence rate estimate to $0.43 \pm 0.05\%$ for planets with $6 R_\oplus \leq R_P \leq 22 R_\oplus$ and $0.8 \leq P \leq 10$ d. With early results from the *TESS* mission, Zhou et al. (2019) derived occurrence rates for planets with $0.9 \leq P \leq 10$ d and $0.8 R_J \leq R_P \leq 2.5 R_J$ of $0.41 \pm 0.10\%$ but found no significant variation of the hot Jupiter frequency with stellar mass from for A, F, G dwarf stars. Zhou et al. (2019) measured occurrences for each spectral type of $0.71 \pm 0.31\%$ (G), $0.43 \pm 0.15\%$ (F), and $0.26 \pm 0.11\%$ (A). While the values measured for each successive spectral type do show a decreasing trend, the uncertainties are such that this trend is not statistically significant.

Despite providing a deep insight into the occurrence rates of planets around FGK stars, *Kepler* has not been able to strongly constrain the occurrence rate of giant planets orbiting low-mass stars. *Kepler* monitored far fewer M-dwarfs than FGK stars, however numerous super-Earth discoveries around M-dwarfs allowed for the occurrence rates of small radii planets to be determined (Dressing and Charbonneau, 2015). Unfortunately the low number of M-dwarfs monitored by *Kepler* lead to very few discoveries of the intrinsically rarer gas giant planets.

Since *Kepler* further attempts have been made to measure this value, but they have not yielded conclusive results. The Pan Planets survey (Obermeier et al., 2016) placed upper limits

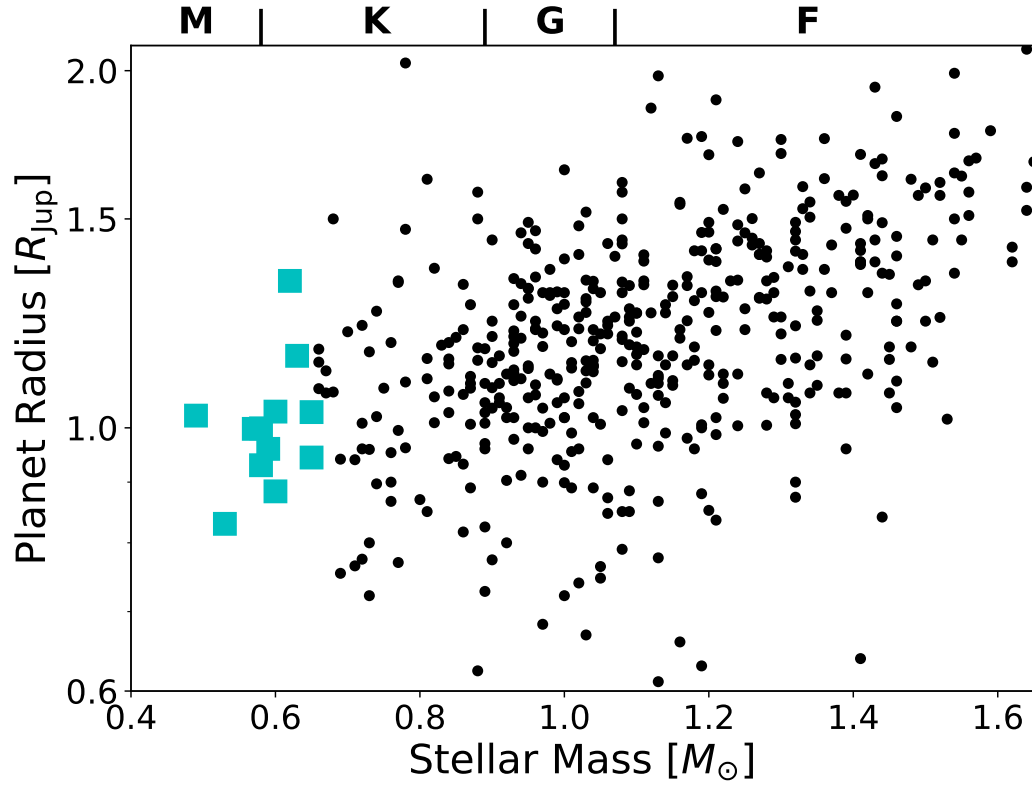


Figure 6.1: Known transiting exoplanets as a function of the mass of the host star (data accessed from the NASA Exoplanet Archive on 2022 March 27). The sample shown is made up of planets with masses between 0.1 and $13 M_{\text{J}}$ and radii larger than $0.6 R_{\text{J}}$. The blue squares show the twelve giant planets with masses less than $0.65 M_{\odot}$.

on the occurrence rates, but could not determine if the occurrence rate differed significantly to the frequency of giant planets orbiting solar type stars. More recently, Sabotta et al. (2021) attempted to derive planet occurrence rates around M-dwarfs using data from CARMENES. This study suffers from a lack of stars monitored and did not detect any giant planets with $P \leq 10$ d. Therefore, they could only place an upper limit on giant planet frequency orbiting low-mass stars.

Determining the frequency of giant planets around low-mass stars will act as a key test for planet formation theories. It has been shown that giant planets form less readily through core accretion around low-mass stars than Sun-like stars (Laughlin et al., 2004; Ida and Lin, 2005). Theoretical population synthesis models from Burn et al. (2021) also predict a decrease in giant planet frequency across the stellar mass range $0.3 - 0.7 M_{\odot}$ from a level similar to FGK stars down to no giant planets at the lower stellar mass end. Recent discoveries of hot Jupiter planets orbiting M-dwarfs (eg. Hartman et al., 2015; Bayliss et al., 2018; Bakos et al., 2020) have shown that it is possible for these systems to form. Despite these recent discoveries, there are still very few known hot Jupiters transiting low-mass stars. From the 485 gas giant exoplanets known to date, only twelve orbit a star with a stellar mass less than $0.65 M_{\odot}$ ¹ (see Figure 6.1). Moreover, the true impact of these discoveries on our knowledge of planet formation cannot be determined without a robust measurement of the occurrence rate of these systems.

In this chapter we present a systematic search for transiting gas giant planets ($R_p \geq 0.6 R_J$) orbiting nearby ($d \leq 100$ pc), low-mass stars in the *TESS* 30 minute cadence light curves (Caldwell et al., 2020). We detail our sample selection in Section 6.2. Our planet search is described in Section 6.3 and the light curve vetting and transit fitting of our candidates are detailed in Sections 6.4 and 6.5. We present the giant planet candidates we discover in Section 6.7 and present some early spectroscopic follow-up of our candidates in Section 6.8. Finally, we present the future pathways for this project in Section 6.9.

6.2 Low-Mass Star Sample

We use the 30 minute cadence light curves produced from the *TESS* Full-Frame-Images (FFIs) by the *TESS*-SPOC team (Caldwell et al., 2020), which we access from the Mikulski Archive for Space Telescopes (MAST) as a High Level Science Product². These light curves are selected as they provide a high quality reduction and a light curve data product that is largely free of instrumental systematics. In addition, the target selection criteria used by the *TESS*-SPOC team prioritises low-mass stars such as those we are targeting in this study. The full-sky coverage of the *TESS* mission combined with this low-mass star selection provides us with high-quality

¹Data accessed from NASA Exoplanet Archive on 2022 March 27.

²*TESS*-SPOC light curves accessed as a bulk download from <https://archive.stsci.edu/hlsp/teess-poc>

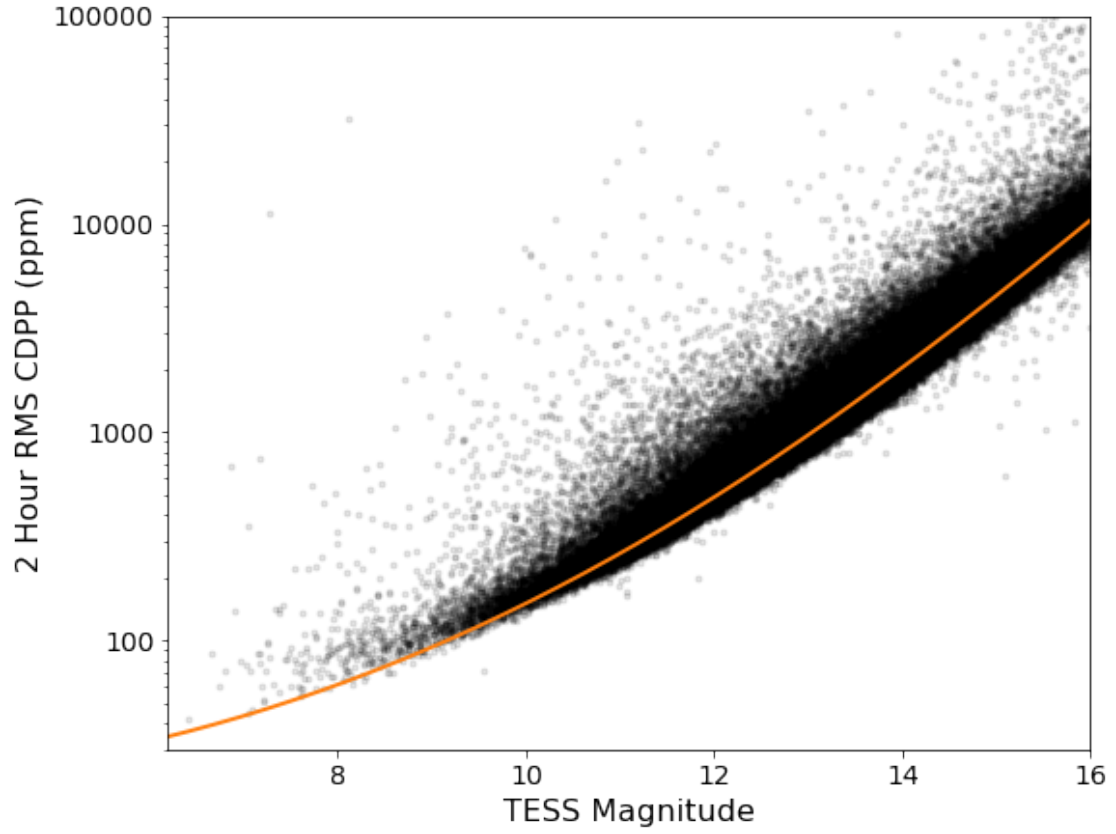


Figure 6.2: The 2 hour CDPP photometric precision measurements for the 91,306 stars in our low-mass star sample, as a function of the apparent magnitude in the *TESS* band. The orange line shows the 10th percentile measurement for all Primary Mission 2 minute cadence targets from Kunitomo et al. (2022).

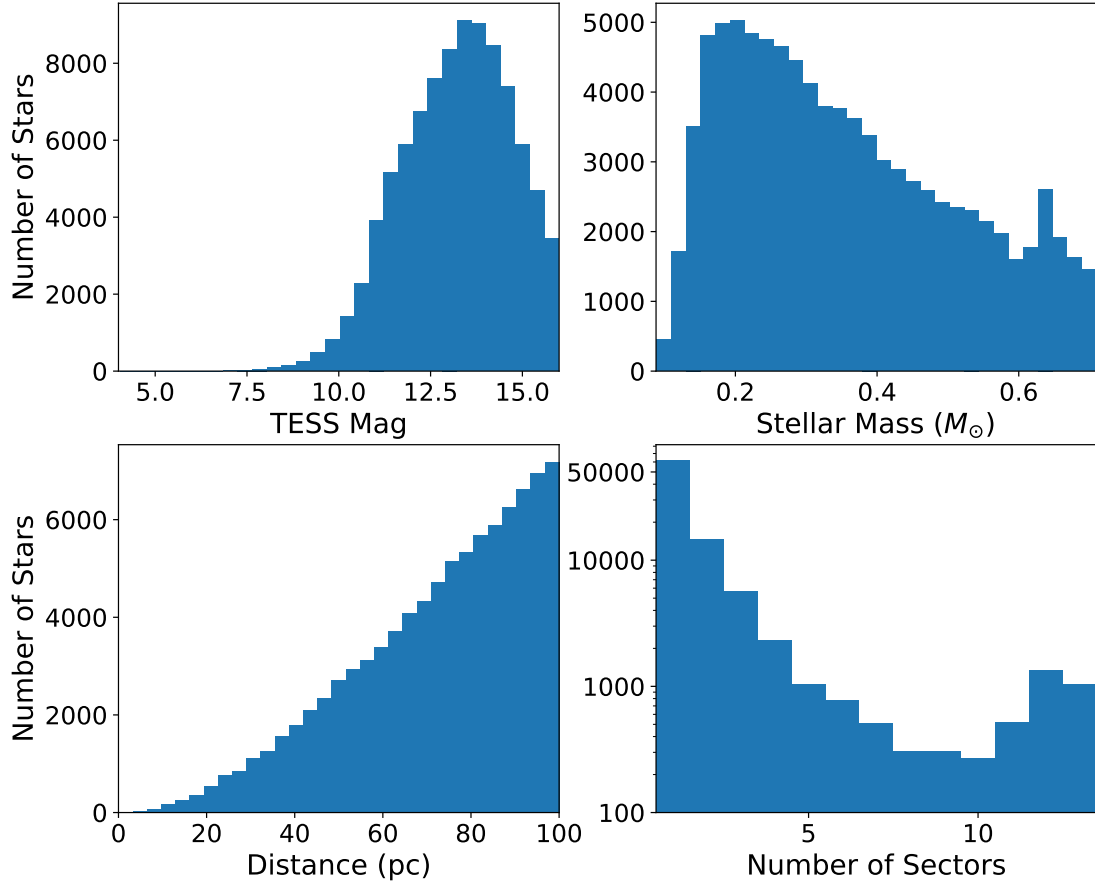


Figure 6.3: Histograms displaying the apparent magnitude (in the *TESS* bandpass), stellar mass, and distances for the 91,306 stars in our low-mass star sample. We also show the number of *TESS* sectors for which a *TESS*-SPOC 30 minute cadence light curve exists for each object, plotting this histogram on a log scale.

photometric light curves for 91,306 low-mass stars for this study. The red-sensitive design of the instrument enables *TESS* to achieve high precision photometry for M and K spectral type stars (see Figure 6.2). This precision allows giant planet transit events of low-mass stars to be readily detected around stars as faint as $T = 16$ mag. Therefore, in this work we seek to use these *TESS* data to place the best constraints to date on the occurrence of giant planets orbiting low-mass stars.

To select a statistical sample of low-mass stars, we used the *TESS* Input Catalog version 8 (TICv8; Stassun et al., 2019). The *Gaia* DR2 parameters are incorporated into TICv8 allowing for low-mass stars to be more reliably identified and our sample to be free of giant stars. We select stars for our sample which meet the following criteria:

1. $T_{\text{eff}} \leq 4500$ K,
2. $R_* \leq 0.75 R_{\odot}$,
3. $d \leq 100$ pc, and
4. $T \leq 16$ mag,

where T_{eff} is the effective temperature of the star, R_* is the stellar radius, d is the distance of the star from the Sun, and T is the stellar apparent magnitude in the *TESS* filter. The distance cut is imposed as the *TESS*-SPOC target selection process uses the same selection cut. By using the same volume limited sample we increase the completeness of our search. These cuts result in a sample which spans spectral types from late-M to late-K dwarf stars. Our low-mass star sample spans a range of stellar masses from ≈ 0.1 to $0.7 M_{\odot}$ (see Figure 6.3), covering the full range of stellar masses over which giant planet frequency is predicted to decrease (Burn et al., 2021). Cross-matching our full sample with the target lists for the *TESS*-SPOC 30 minute cadence FFI light curves yields 91,306 stars with a light curve.

Our all-sky *TESS* low-mass star samples are displayed in Figures 6.2, 6.3, and 6.4. From the histogram in Figure 6.4 we see that the majority of the stars in our sample have the spectral type M2 to M4. This clustering arises from the apparent magnitude and distance criteria, as well as the distribution of stars across the sky. The left-hand side of the spectral type distribution follows the mass function for stars and is a result of us using a volume limited sample and later spectral type stars being more common in the Galaxy (Chabrier and Baraffe, 2000). The turnover and decrease in numbers to very late spectral types is a result of the magnitude limit of our sample ($T \leq 16$ mag) and the very low luminosity of M5 and later spectral types stars. This is the same effect that causes the stellar mass distribution in Figure 6.3.

The apparent magnitude distribution of our sample peaks around $T = 13$ mag. With a magnitude limited sample, we would expect this distribution to continue to rise until the

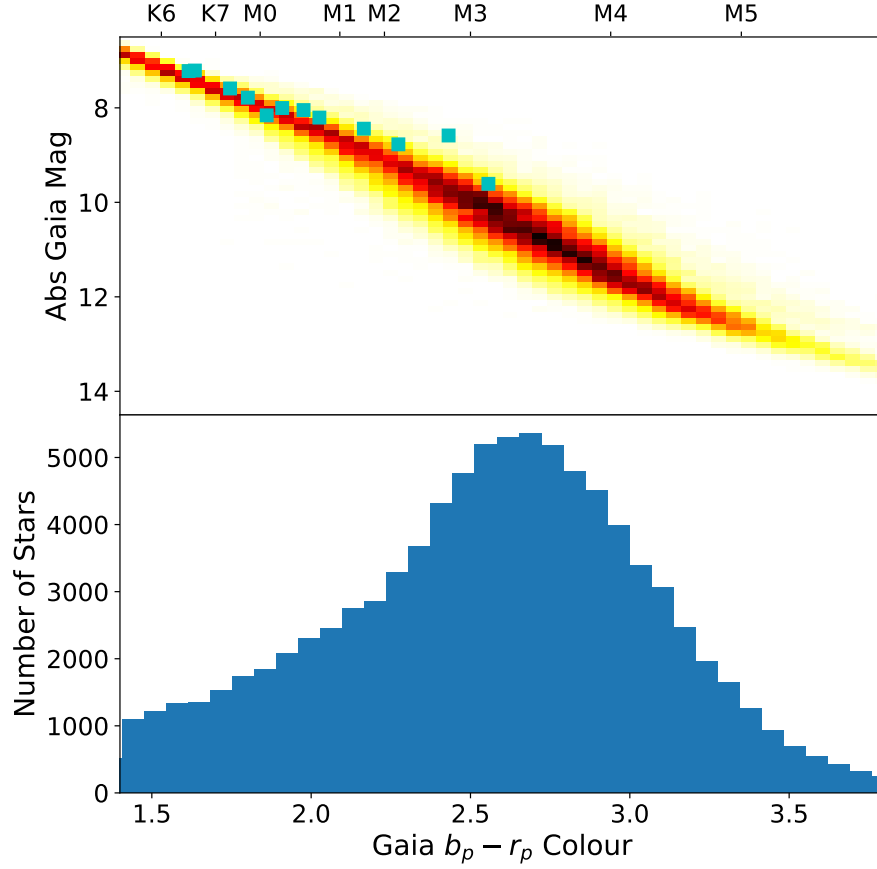


Figure 6.4: **Top:** *Gaia* colour-magnitude diagram showing the 91,306 low-mass stars in our sample (density heat map). Also shown are the twelve known transiting gas giant planets (blue squares). **Bottom:** Histogram showing the *Gaia* colour distribution of the sample.

magnitude limit. The turnover arises as a result of the distance limit imposed on our sample. Early M-dwarf stars with apparent magnitudes of $T \gtrsim 13.5$ mag have distances > 100 pc. The distribution of the number of observing sectors for each star arises from the *TESS* observing strategy (see Figure 1.21). As can be seen from the *TESS* observations footprint, the majority of stars receive one or two sectors of coverage. Moreover, due to the overlapping of sectors in the continuous viewing zones surrounding the Ecliptic poles, a larger fraction of stars receive ≥ 11 sectors of coverage than receive between 6 and 10 sectors of observations.

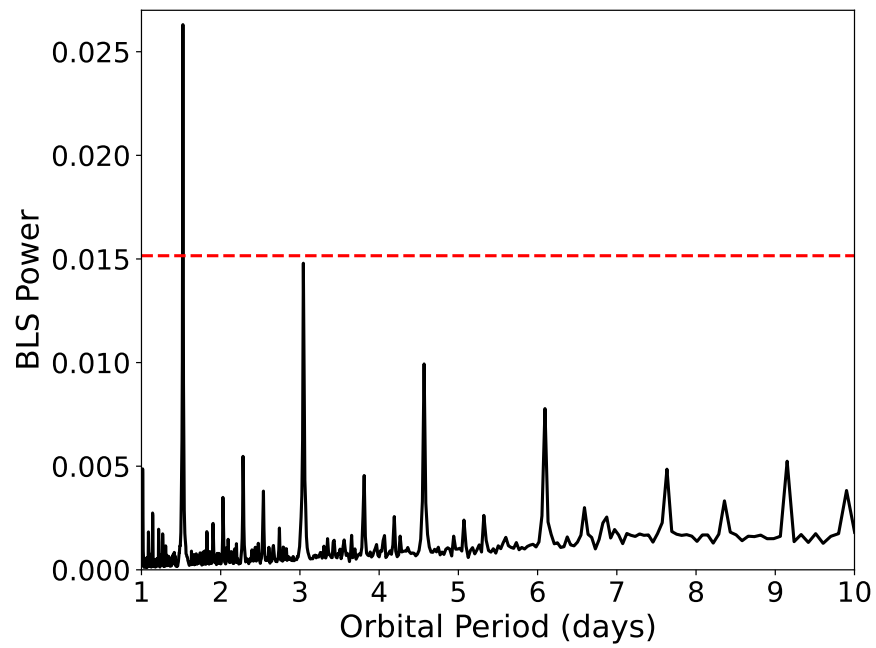


Figure 6.5: The BLS periodogram of TIC-335590096 plotted as an example. The red dashed line shows the level of the $SDE = 8$ threshold for this candidate, and the detected period of 1.523 d is clearly visible.

6.3 Transit Search

Using the TESS-SPOC 30 minute cadence light curves, we firstly exclude any data points with a quality flag $q > 0$. These flags highlight any observations which are adversely affected by cosmic rays and scattered light, among others. For this analysis we use the PDC_SAP flux time series, which has been largely corrected for instrumental systematics but for which real stellar variability has been preserved. To remove stellar variability prior to the planet search we smooth the light curves using a cubic spline. The spline we use has nodes every 45 data points, approximately 1 d. This node spacing is long enough to preserve the transits produced by our target systems, which have durations $\ll 1$ d.

We then search through the TESS-SPOC light curves for periodic planet candidate transit signals using the Box-fitting Least Squares algorithm (BLS; Kovács et al., 2002). We use the `ASTROPY` implementation of the algorithm³. We searched for signals with periods between 1 and 10 d and durations between 0.03 and 0.3 d, using a frequency spacing factor of 20. The frequency grid spacing, δf , for each light curve is then computed using the equation

$$\delta f = 20 \frac{0.03}{(\max t - \min t)^2}, \quad (6.1)$$

where t represents the time values of the light curve. This frequency grid spacing was chosen so as to optimise computational efficiency, while still allowing for the robust detection of the shallowest signals on the longest periods considered in this study. We identify objects with a Signal Detection Efficiency (SDE) ≥ 8 and a transit signal-to-noise (SNR) of greater than 8 as good transiting planet candidates. We plot an example BLS periodogram in Figure 6.5.

6.4 False Positive Identification

Along with planet candidates, our BLS detections also included a large number of false positives. These can be either real astrophysical false positive scenarios, such as eclipsing binaries or variable stars, or spurious detections. We performed a number of vetting checks to identify these false positive detections and exclude them from our candidate list. Previous transit searches have used similar criteria to identify false positives (eg. Montalto et al., 2020). These checks and the number of false positives identified by each are outlined in the following section.

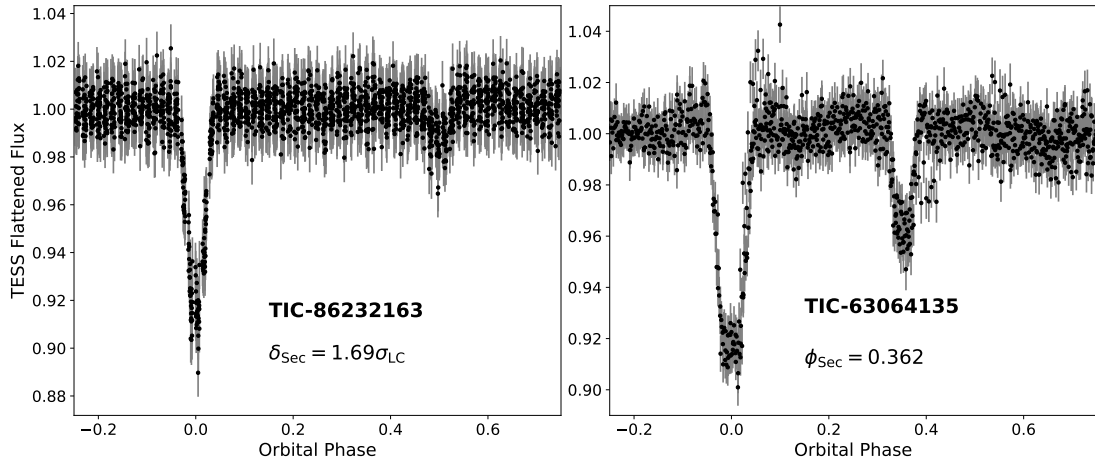


Figure 6.6: Two examples of objects identified as eclipsing binaries through the presence of a secondary eclipse. We plot the spline-smoothed PDC_SAP light curves phase folded on the best BLS period. TIC-86232163 ($P = 1.44$ d) shows an eclipsing binary with a secondary eclipse at phase 0.5 with a depth of $1.69\sigma_{\text{LC}}$. TIC-63064135 ($P = 3.99$ d) is an eccentric eclipsing binary with a secondary eclipse at phase 0.362.

6.4.1 Secondary Eclipse Events

One of the main astrophysical false positive cases for transiting planet searches are eclipsing binary stars (eg. Almenara et al., 2009; Santerne et al., 2012). The main signature of an eclipsing binary is the presence of a secondary eclipse. For a circular orbit this eclipse is present at phase 0.5, however for an eccentric orbit this is not always the case. To search for secondary eclipse events, we determine the median flux level inside a window of width equal to the width of the BLS model between phases 0.2 and 0.8. While designed to look for eclipsing binaries, this check also identifies a large number of variable stars. We compare the median flux level inside the window to the median overall out-of-transit flux baseline, and identify stars where this flux difference is greater than 1.5 times the mean RMS scatter of the light curve, σ_{LC} , as eclipsing binaries or variable stars. A total of 684 objects are identified as false positives by this check, and examples of these objects are displayed in Figure 6.6.

6.4.2 Odd-Even Depth Differences

Eclipsing binaries in circular and eccentric orbits can also result in BLS detections with a difference in depth between the odd and even transit events. This occurs when the BLS algorithm folds the light on half the true period of the binary, resulting in the primary and secondary eclipses

³Docs can be found at <https://docs.astropy.org/en/stable/timeseries/bls.html>

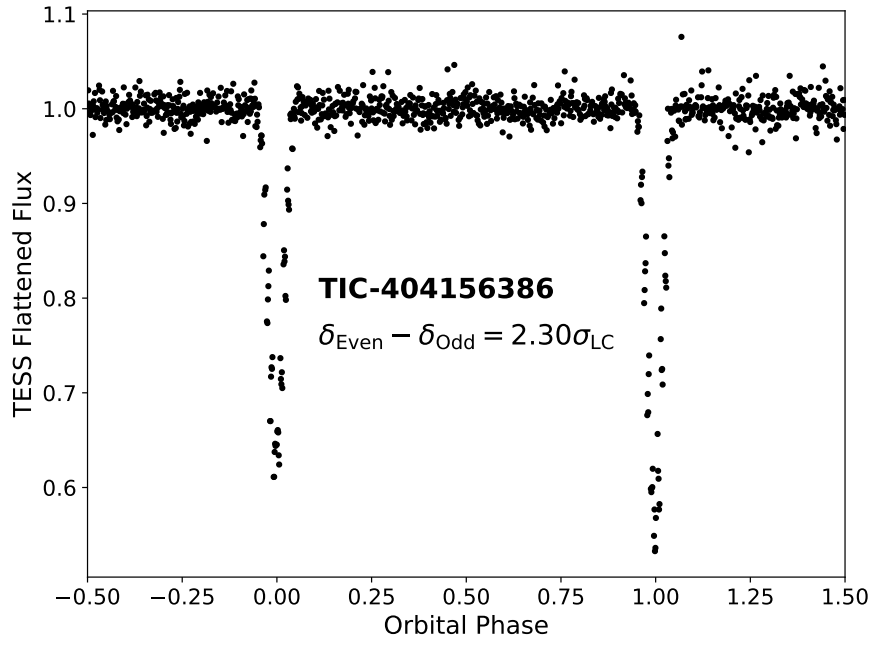


Figure 6.7: Example of an object identified as an eclipsing binary through the presence of an odd-even depth difference. We plot the spline-smoothed PDC_SAP light curves phase folded on a period of $P = 2.34$ d, which is twice the best BLS period of $P = 1.17$ d. Here the even transits are $2.3\sigma_{\text{LC}}$ deeper than the odd transits.

both falling at phase 0. To check for such cases we compare the depth of the odd transits with the depth of the even. The transit depths were again determined by comparing the median in-transit flux level to the median overall out-of-transit flux baseline. Any objects with an odd-even depth difference greater than $2.0 \sigma_{\text{LC}}$ are identified as likely eclipsing binaries. A total of 62 objects are identified as likely eclipsing binaries by this check and an example of one of these objects is displayed in Figure 6.7. Note that in the pipeline these checks are performed sequentially in the order they are presented here, so any objects identified as false positives by the secondary eclipse check are not included in the numbers of objects identified by this check and the following checks.

6.4.3 Sector Depth Differences

In some cases, the depth of the transit events is observed to be different in different sectors, but constant in a given sector. We identified this to be as a result of differing levels of contamination from a nearby eclipsing binary. For different sectors the positions of neighbouring stars relative to a target star will change due to the rotation of the *TESS* spacecraft. Moreover, in different sectors a given star will fall in a different location in the camera field-of-view and so will have a differently shaped PSF. The pixel mask used by the TESS-SPOC pipeline to extract photometry also varies from sector to sector. The result of these effects is that the level of contamination from neighbouring stars into the target pixel aperture is different for different sectors. The TESS-SPOC pipeline computes this dilution value and corrects the target light curve for it, so the depths of transits on the target stars should be unaffected by this. However, if one of these neighbouring stars is itself an eclipsing binary then in sectors in which it contributes more light to the target aperture the eclipse event seen in the light curve will be deeper.

To identify any clear nearby eclipsing binary cases, we compared the depths of the transit events between subsequent sectors, for those objects which were observed in more than one sector. Any object in which a depth difference between sectors of greater than $1.5 \sigma_{\text{LC}}$ was identified as a nearby eclipsing binary. A total of 169 objects are identified as likely nearby eclipsing binaries by this method and an example of such an object is shown in Figure 6.8.

6.4.4 Transit Phased Variability

In addition to secondary eclipses and eclipse depth differences, many eclipsing binaries show out-of-transit variability in phase with the eclipses. This variability can arise from a number of effects, including ellipsoidal modulation of reflection from the an orbiting body (Faigler and Mazeh, 2011). While these effects do occur for close orbiting planets, the amplitude of the resulting variability is much larger for eclipsing binaries.

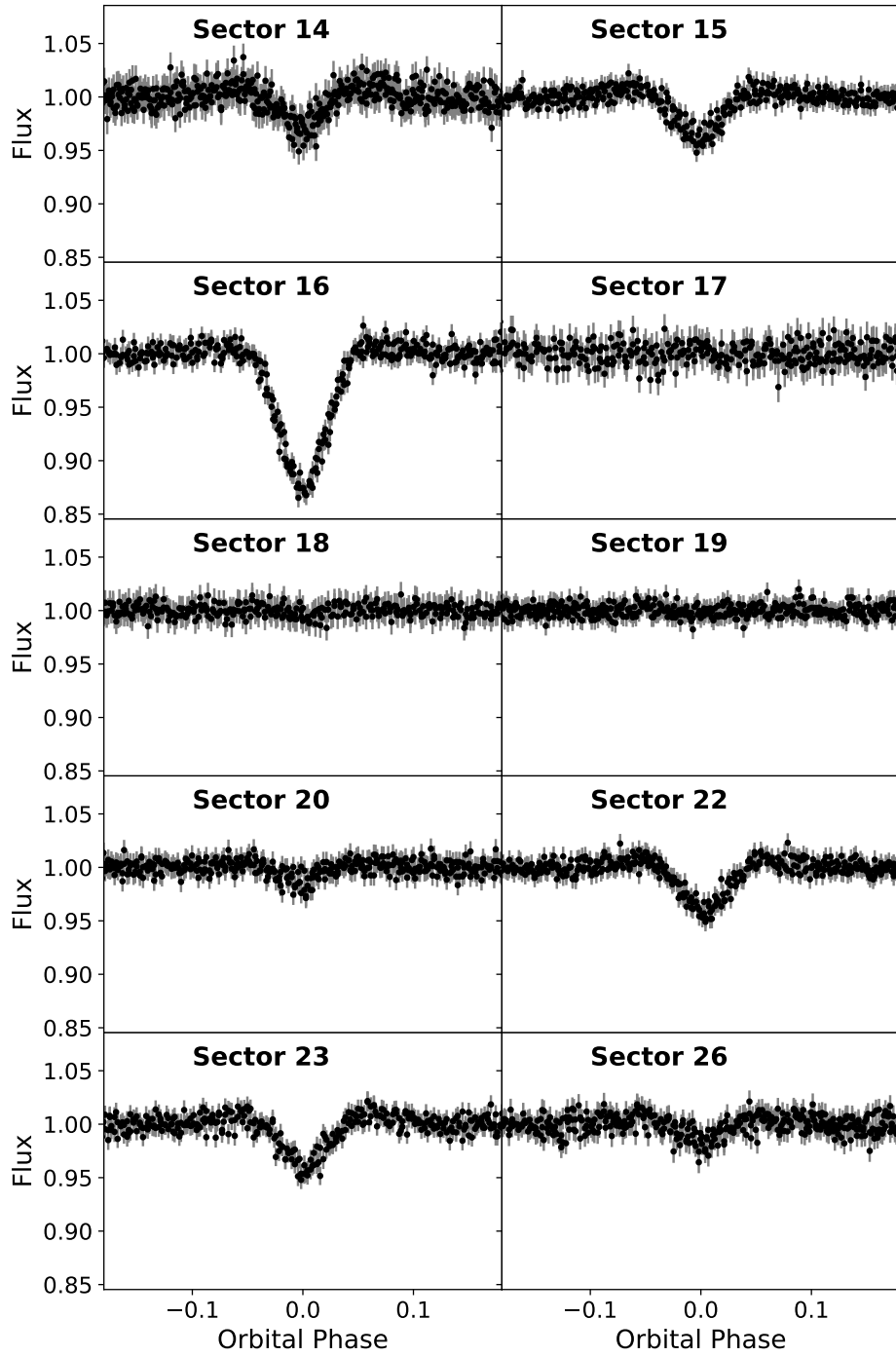


Figure 6.8: Individual sector light curves for TIC-233684011, which was identified as a nearby eclipsing binary through the difference in eclipse depth observed for different sectors. We plot the spline-smoothed PDC_SAP light curves phase folded on the best BLS period of $P = 3.64$ d.

We search for these variability signals in the pre-flattened light curves as we expect them to be removed by our pre-transit search spline flattening. We use the harmonic model presented by Montalto et al. (2020)

$$f_{\text{Harmonic}} = A \cos\left(\frac{2\pi t}{P}\right) + B \sin\left(\frac{2\pi t}{P}\right) + C \quad (6.2)$$

and fit for the coefficients A, B, C for each light curve. We then compare the quality of this harmonic fit to a simple flat line fit by computing the value

$$R_{\text{Harmonic}}^2 = 1 - \frac{\sum_{i=1}^N (f_i - f_{\text{Harmonic},i})^2}{\sum_{i=1}^N (f_i - C)^2}. \quad (6.3)$$

The better the harmonic fit is to the data, the closer to 1 this value becomes. As with the secondary eclipse check (Section 6.4.1) this check finds purely variable stars, as well as eclipsing binaries. We identify any object with $R_{\text{Harmonic}}^2 > 0.5$ as an eclipsing binary or a variable star, and in total identify 254 false positives using this method. An example is shown in Figure 6.9.

6.4.5 Lomb-Scargle Analysis

Besides eclipsing binary stars, the other major astrophysical contaminant in our BLS detections are variable stars. This stellar variability arises from two main mechanisms. The first is the combination of active regions on the stellar surface and the rotation of the star. These active regions are either regions which are less luminous than the majority of the stellar surface, which are called spots, or more luminous, known as faculae. These spots and faculae rotate into and out of view as the star rotates, resulting in a fluctuation in the observed brightness of the star (Boisse et al., 2012). Periodic variability in the brightness of stars can also arise from the radial oscillation of the outer layers of the star, known as stellar pulsations (Cox, 1980). Multiple types of pulsating stars are found, including δ -Scuti (eg. Rodríguez and Breger, 2001) and RR-Lyrae (eg. Simon and Teays, 1982), and can exhibit variability with an amplitude on the order of a magnitude.

As a first check for clear signs of variability we run a Generalised Lomb-Scargle (Lomb, 1976; Scargle, 1982) analysis on the light curve, after masking out the flux data points which are detected as “in-transit” by BLS. Any star with a normalised Lomb-Scargle power of greater than 0.3 is identified as a variable star and excluded from our candidate list. A total of 210 objects are identified as variable stars using this test, and an example is shown in Figure 6.9.

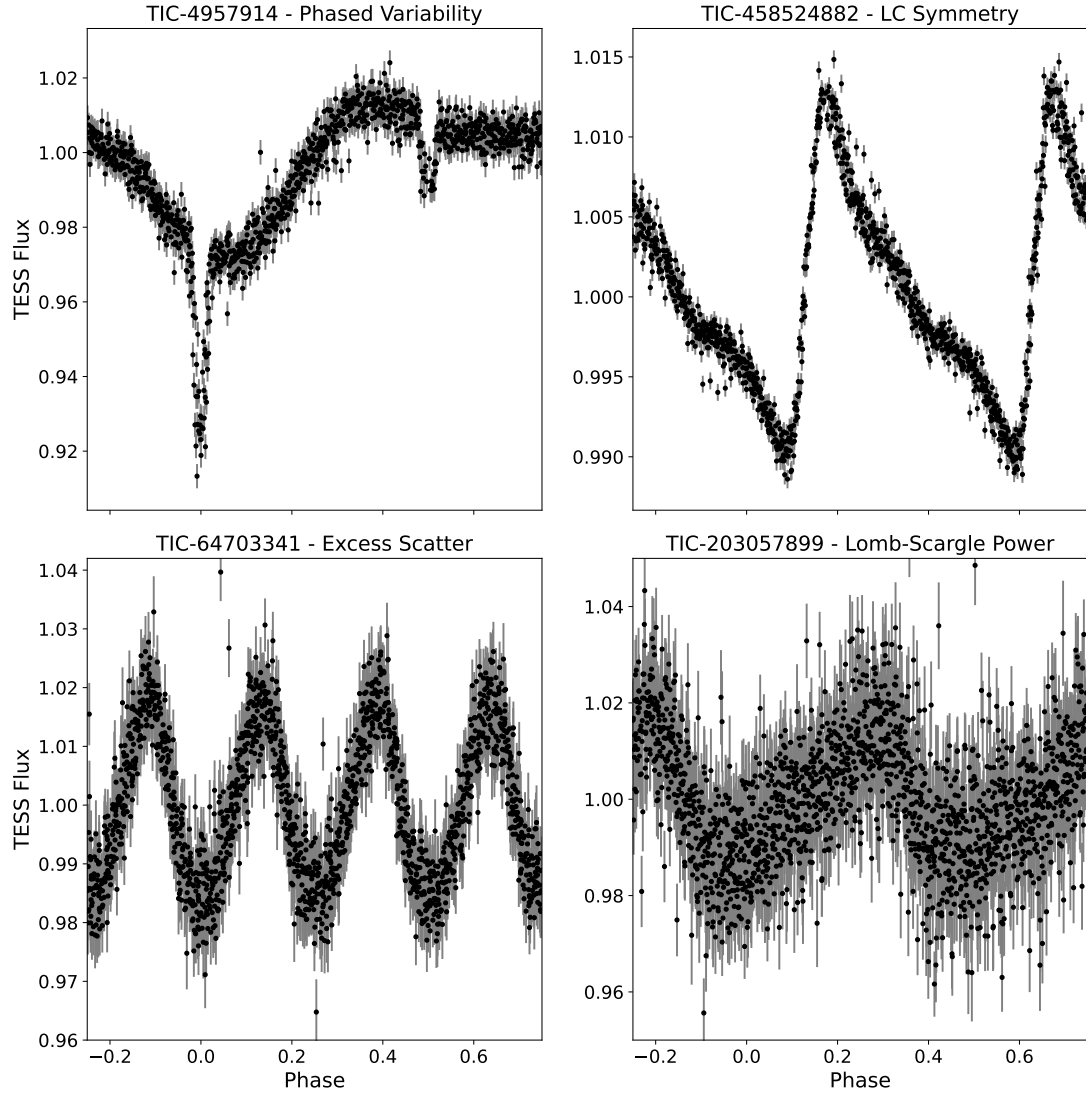


Figure 6.9: Examples of false positives identified by the variability analysis checks detailed in Sections 6.4.4 to 6.4.7. The titles of each panel gives the object plotted as well as the vetting check that identified the object as a false positive. Note that for TIC-4957914 the pre-flattened light curve is plotted, but for the rest the spline smoothing has been applied. All objects are phase folded using the BLS period.

6.4.6 Light curve symmetry

The phase-folded light curve of an exoplanet transit will be symmetric around phase of zero. Variable star light curves which trigger BLS will often not share this symmetry. As such, by determining the symmetry of the folded light curve we can identify variable stars. We calculate the mean point-to-point scatter of the folded light curve in two configurations. The first is a standard fold running from phase -0.5 to 0.5. The second runs from phase 0.0 to 0.5, where we have taken the absolute value of negative phases. We calculate the ratio of these two values and identify any objects with a ratio greater than 1.5 as variable stars. A total of 15 objects are identified as variable stars using this analysis, and an example is shown in Figure 6.9.

6.4.7 Excess standard deviation scatter metric

A further way to identify stellar variability is to compare the RMS scatter of the phase-folded light curve to the root-mean-square of the point-to-point scatter. For a transiting planet light curve, the out-of-transit section of the light curve will be close to flat and dominated by Gaussian noise. Therefore, these two values will differ by a factor of $\sqrt{2}$, with the raw RMS being the smaller of the two. For a variable star, the RMS scatter will be significantly larger than the point-to-point scatter, as the RMS will be dominated by the variability. Therefore, we calculate following metric

$$\sigma_{\text{excess}} = \frac{1}{\sigma_{\text{LC}}\sqrt{2}} \sqrt{\frac{\sum_1^N (f_i - f_{i-1})^2}{N}} \quad (6.4)$$

and identify any star with $\sigma_{\text{excess}} \leq 0.75$ as a variable star. A total of 358 objects are identified as variable stars through this analysis, and an example is shown in Figure 6.9.

6.4.8 Depth metric

As well as astrophysical false positives, our BLS sample also contains a few spurious detections. The most common of these spurious detections are those which are driven by the presence of a small number of outlying points. These outliers can be produced by sharp changes in the scattered light on the camera, or from a decrease in the quality of the spacecraft pointing. To identify these signals, we calculate the median flux level of the “in-transit” data points of the BLS event and compare this value to the reported BLS depth. The BLS depth is determined by a fit to the data, and so is biased to larger values by the outlying points. For real transit events, these two values will be comparable, however for spurious detections being driven by a few outlying points the BLS depth will be significantly larger than the median flux level. We calculate the ratio of the median flux level to the BLS depth and exclude any object with this ratio less than

Parameter	Prior
Transit centre time, T_C	$\mathcal{U}(T_{C, \text{BLS}} - 0.1 P_{\text{BLS}}; T_{C, \text{BLS}} + 0.1 P_{\text{BLS}})$
Orbital Period, P	$\mathcal{U}(0.95 P_{\text{BLS}}; 1.05 P_{\text{BLS}})$
Planet-to-star radius ratio, R_p/R_*	$\mathcal{U}(0; 1)$
Scaled semi-major axis, a/R_*	$\mathcal{U}(1.1; \infty)$
Orbital inclination, i	$\mathcal{U}(0^\circ; 90^\circ)$
Limb-darkening parameter, q_1	$\mathcal{U}(0; 1)$
Limb-darkening parameter, q_2	$\mathcal{U}(0; 1)$
Constant flux offset, f_0	$\mathcal{U}(-0.05; 0.05)$

Table 6.1: Priors used for each free parameter in the transit fitting detailed in Section 6.5. Note $\mathcal{U}(A; B)$ denotes a uniform prior with lower bound A and upper bound B.

0.5 as a spurious event. A total of 154 objects are identified as likely spurious events using this method.

6.5 Transit Fitting and Planet Candidates

Having identified and rejected the false positives, we then fit the transit events for the remaining candidates. We use the `emcee` package (Foreman-Mackey et al., 2013) to perform a Markov Chain Monte Carlo (MCMC) analysis.

The free parameters we use in our analysis are: a reference mid-transit time, T_C , the planetary orbital period, P , the planet-to-star radius ratio, R_p/R_* , the scaled semi-major axis, a/R_* , and the orbital inclination, i . We also fit for a free flux baseline offset, f_0 , which is defined such that the out-of-transit flux is equal to $1 + f_0$. We use a quadratic limb-darkening law and for the limb-darkening coefficients we fit for the q_1, q_2 parameters from the parameterisation of Kipping (2013a). This parameterisation ensures a physically realistic limb-darkening model for the star. The priors used for each parameter are provided in Table 6.1. These priors are selected to ensure that we fit physically realistic transit models to each light curve but also that we do not bias the results in any other way.

For each object, 24 independent chains were each sampled for 7,500 steps, following a burn-in phase of 2,500 steps. This resulted in posterior distributions of 180,000 samples for each candidates. We use these posterior distributions from our transit MCMC analysis to assess the likely planetary nature of our candidates.

We use the R_p/R_* posterior and the host star radius from the TIC to determine a posterior distribution for R_p . Similarly, we use the posteriors for P and a/R_* along with Kepler's 3rd law to determine a posterior distribution for the stellar density, ρ_* . We note that these ρ_* values are calculated assuming a circular orbit. With these distributions in R_p and ρ_* we then determine what fraction of the posterior falls in what we refer to as the "giant planet regime", which we define with the following parameter ranges: $0.6 R_J \leq R_p \leq 2.0 R_J$ and $1.5 \text{ g cm}^{-3} \leq \rho_* \leq 200 \text{ g cm}^{-3}$. We then select any object with this fraction $\geq 50\%$ as a giant planet candidate. From this transit analysis, we identified a sample of fourteen candidate gas giant exoplanets.

6.6 Blend Scenario Checks

Due to the large pixel scale of *TESS* ($21''/\text{pix}$), we must ensure that the transit signals we observe are not due to a nearby star blending into the target aperture. Using the Target Pixel Files (TPFs) from the *TESS*-SPOC pipeline it is possible to inspect each candidate to search for clear signs of a blend scenario. We download the TPFs for each candidate using the *LIGHTKURVE* Python software (Lightkurve Collaboration et al., 2018). We then perform two tests to search for evidence of the source of the signal being a neighbouring star and not the target.

The first of these involves generating light curves using different aperture sizes. We compare three different aperture sizes. The first is the aperture used by the *TESS*-SPOC pipeline. The second is a small aperture of just the single pixel at the location of the target star, and the third is a large 5×5 pixel aperture also centred at the target star location. By comparing the depths of these three light curves, we can reveal blend scenarios. These blend scenarios will in general be cases where a larger aperture results in a deeper transit, signifying that the signal is arising from a nearby star that is only partially within the target aperture, but more fully within the larger aperture. If all three light curves have equal depths then it is unlikely the signal arises from a nearby star. Similarly, a shallower transit for the larger aperture also points towards the signal arising from the target star. This is because the result of increasing the aperture size here is simply the inclusion of an increased amount of dilution, and so the signal being on any of the nearby stars is unlikely. The second test we performed is to generate light curves for each individual pixel in a 7×7 pixel grid centred on the target star location. With these light curves we can investigate whether the transit signals are clustered around the target star, or are offset.

From these tests, none of our candidates displayed clear signs of being from a neighbour-

ing star. This is not unexpected, as the TESS-SPOC sample selection requires the stars to suffer $\leq 50\%$ dilution, and so the light curves will be dominated by light from the target. In addition, such nearby blend scenarios for objects with multi-sector coverage are identified by the vetting checks (see Section 6.4.3).

6.7 Giant Planet Candidates

From the full planet search we have identified a final selection of fourteen giant planet candidates. The numbers of objects from our sample at each step of the planet search pipeline are summarised in Figure 6.10. We provide details on the host stars of our candidates in Tables 6.2 and 6.3. The planetary parameters derived for our candidates in Section 6.5 are provided in Tables 6.4 and 6.5 and we display the transit events for each candidate in Figure 6.11. The majority of our candidates have clean transit light curves and appear good quality planet candidates. The exception is TIC-422986512 that has a light curve that indicates that the true nature of this candidate is probably a slightly eccentric eclipsing binary system.

We also compare our sample of candidates to the known transiting gas giant planets with low-mass stellar hosts in Figures 6.12 and 6.13. From these two figures, it is evident that our search has extended the population of known transiting gas planets to lower stellar mass hosts than ever before. From the colour-magnitude diagram in Figure 6.13, we can see that some of our targets appear raised above the bulk population. Such an effect could be indicative of these objects being binary stars, with the additional star resulting in the objects appearing much brighter than would be expected for a single star of the same spectral type. However, we also note that one of the known giant planets, HATS-74A b (Jordán et al., 2022), also sits raised above the line. This system consists of a low-mass star that hosts a transiting giant planet, as well as a bound stellar companion on a wide orbit. Such wide stellar companions have been found to be common for hot Jupiter host stars (Knutson et al., 2014; Ngo et al., 2016). As such, we cannot exclude these objects as giant planet candidates simply based on their position on the colour-magnitude diagram.

In order to derive fully complete and robust occurrence rates, we require follow-up observations and confirmations of our candidates. Two of our candidates have already been independently confirmed as transiting brown dwarfs – TIC-67646988 (TOI-1779 b/LP 261-75 b; Irwin et al., 2018) and TIC-236387002 (TOI-2119 b; Cañas et al., 2022; Carmichael et al., 2022). A further three of our candidates are *TESS* Objects of Interest (TOIs) and so they already have received photometric or high-resolution imaging follow-up observations through the *TESS* Follow-up Observing Program (TFOP; Collins et al., 2018a). We provide details of the follow-up observations available for our candidates in Table 6.6.

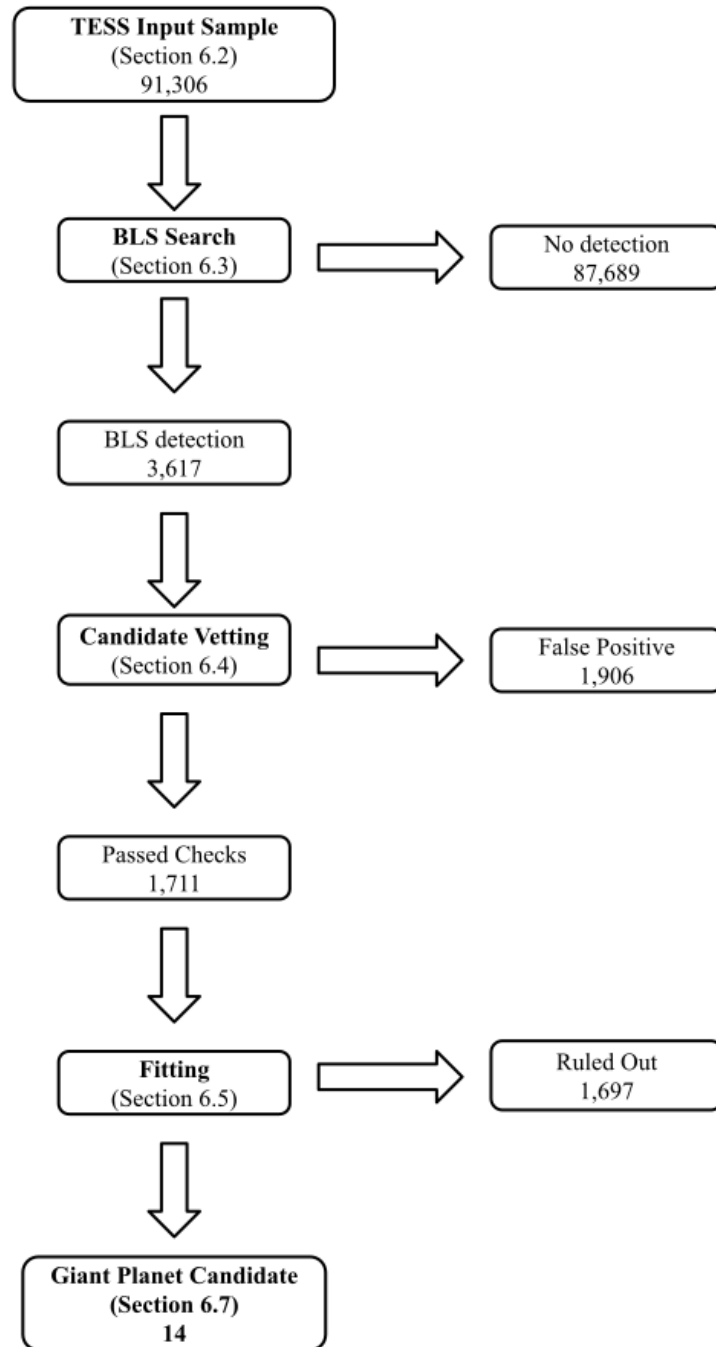


Figure 6.10: Flow chart of the steps of the planet search pipeline. The numbers indicate the number of stars from our sample for each step.

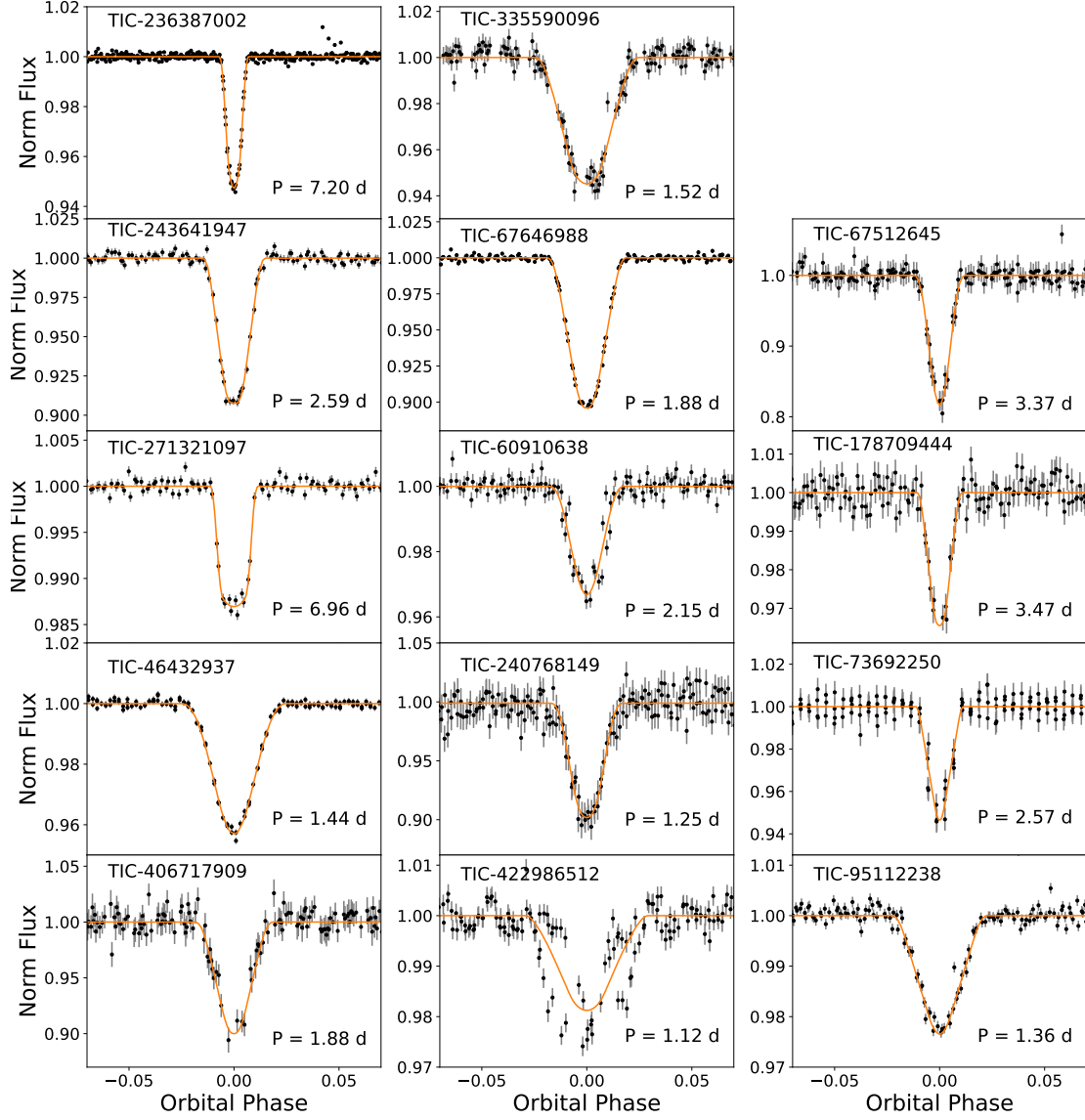


Figure 6.11: Light curves for the fourteen giant planet candidates phase folded using the ephemerides from the fitting detailed in Section 6.5 and zoomed in to show the transit features. The orange lines show the models from this fitting which give the best fit. The periods given for each object are from the same analysis.

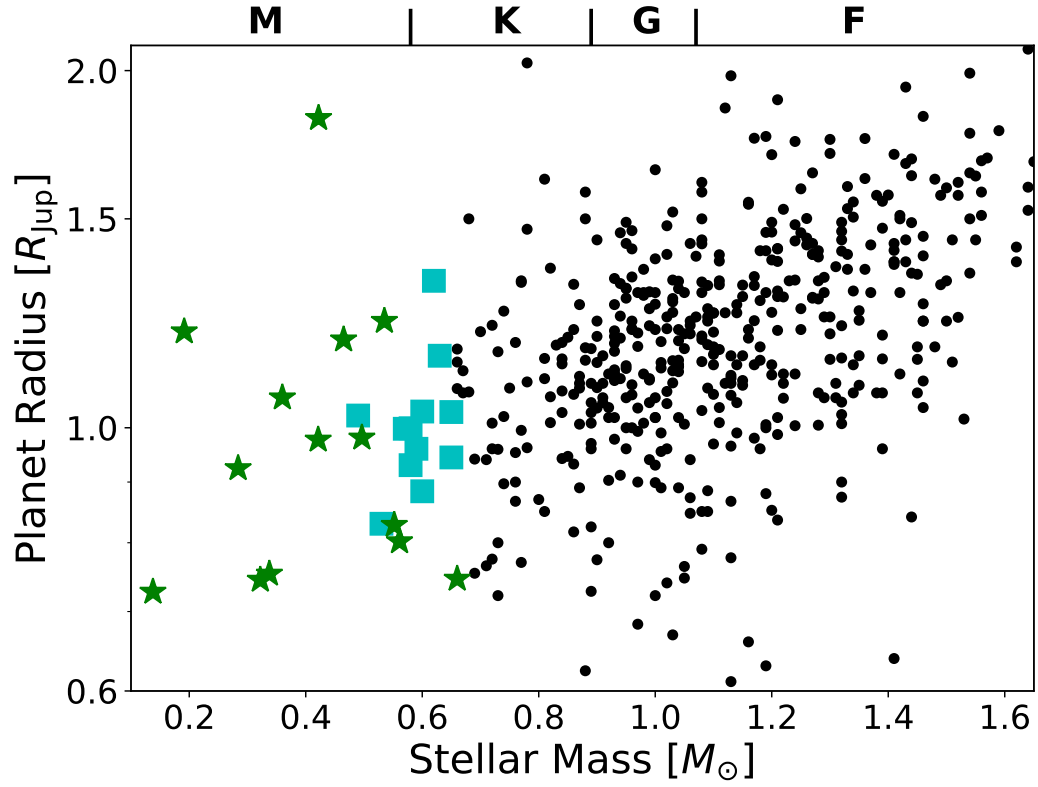


Figure 6.12: Radii of our giant planet candidates compared to the known transiting exoplanets plotted in Figure 6.1 as a function of the mass of the host star. The green stars show the fourteen gas giant planet candidates discovered in this study. For these candidates the R_{P} values plotted are the 50th percentile values from the fitting detailed in Section 6.5 and given in Tables 6.4 and 6.5. As with Figure 6.1 the blue squares show the twelve giant planets with masses less than 0.65 M_{\odot} .

	TIC-236387002	TIC-335590096	TIC-243641947	TIC-67646988
<i>TESS</i> (mag)	10.3978 ± 0.0074	13.7726 ± 0.0079	13.2486 ± 0.0078	12.4368 ± 0.0074
<i>Gaia G</i> (mag)	11.4732 ± 0.0013	15.1091 ± 0.0013	14.4858 ± 0.0007	13.833 ± 0.0008
<i>Gaia G_{Bp}</i> (mag)	12.6478 ± 0.0028	16.7462 ± 0.0062	15.9209 ± 0.0023	15.6355 ± 0.0078
<i>Gaia G_{Rp}</i> (mag)	10.434 ± 0.0016	13.8593 ± 0.0035	13.3138 ± 0.0032	12.5406 ± 0.0019
<i>J</i> (mag)	8.976 ± 0.019	12.056 ± 0.022	11.706 ± 0.025	10.577 ± 0.021
<i>H</i> (mag)	8.393 ± 0.033	11.431 ± 0.026	11.099 ± 0.024	9.96 ± 0.019
<i>K</i> (mag)	8.139 ± 0.021	11.175 ± 0.026	10.819 ± 0.021	9.69 ± 0.019
	TIC-67512645	TIC-271321097	TIC-60910638	TIC-178709444
<i>TESS</i> (mag)	14.9046 ± 0.0078	10.9295 ± 0.0060	13.0687 ± 0.0077	13.6615 ± 0.0073
<i>Gaia G</i> (mag)	16.3092 ± 0.0012	11.6926 ± 0.0005	14.3144 ± 0.0011	14.9535 ± 0.0005
<i>Gaia G_{Bp}</i> (mag)	18.1135 ± 0.0234	12.4418 ± 0.0013	15.7465 ± 0.0077	16.5039 ± 0.0031
<i>Gaia G_{Rp}</i> (mag)	15.0078 ± 0.0026	10.8725 ± 0.0008	13.1344 ± 0.0028	13.7388 ± 0.0014
<i>J</i> (mag)	13.169 ± 0.023	9.884 ± 0.024	11.487 ± 0.02	11.999 ± 0.026
<i>H</i> (mag)	12.486 ± 0.022	9.249 ± 0.028	10.894 ± 0.023	11.348 ± 0.028
<i>K</i> (mag)	12.207 ± 0.021	9.115 ± 0.024	10.654 ± 0.014	11.084 ± 0.027
	TIC-46432937	TIC-240768149	TIC-73692250	
<i>TESS</i> (mag)	12.3718 ± 0.0074	15.0523 ± 0.0523	13.9856 ± 0.0077	
<i>Gaia G</i> (mag)	13.433 ± 0.0004	16.5535 ± 0.0089	15.3646 ± 0.0009	
<i>Gaia G_{Bp}</i> (mag)	14.5196 ± 0.0025	18.7107 ± 0.0289	17.1267 ± 0.0057	
<i>Gaia G_{Rp}</i> (mag)	12.3996 ± 0.0015	15.1879 ± 0.0051	14.0843 ± 0.0028	
<i>J</i> (mag)	11.011 ± 0.022	13.184 ± 0.029	12.239 ± 0.025	
<i>H</i> (mag)	10.427 ± 0.023	12.686 ± 0.027	11.681 ± 0.025	
<i>K</i> (mag)	10.195 ± 0.02	12.343 ± 0.027	11.409 ± 0.02	
	TIC-406717909	TIC-422986512	TIC-95112238	
<i>TESS</i> (mag)	13.5451 ± 0.0080	12.5539 ± 0.0073	12.2745 ± 0.0073	
<i>Gaia G</i> (mag)	14.8626 ± 0.0009	13.7783 ± 0.0004	13.5155 ± 0.0006	
<i>Gaia G_{Bp}</i> (mag)	16.454 ± 0.0063	15.1806 ± 0.0014	14.9506 ± 0.0022	
<i>Gaia G_{Rp}</i> (mag)	13.6273 ± 0.0037	12.6162 ± 0.0011	12.3406 ± 0.0012	
<i>J</i> (mag)	11.897 ± 0.021	10.953 ± 0.022	10.657 ± 0.021	
<i>H</i> (mag)	11.3 ± 0.027	10.362 ± 0.03	10.063 ± 0.024	
<i>K</i> (mag)	11.079 ± 0.023	10.106 ± 0.026	9.807 ± 0.02	

Table 6.2: Stellar Magnitudes for our giant planet candidates. The values are from TICv8 (Stassun et al., 2019), *GAIA* DR2 (Gaia Collaboration, 2018), and 2MASS (Skrutskie et al., 2006).

	TIC-236387002	TIC-335590096	TIC-243641947	TIC-67646988
RA (deg)	244.4300231	183.5647447	207.4749061	147.768528
Dec (deg)	26.3041816	−13.17481731	−46.06623829	35.968556
Parallax (mas)	31.818 ± 0.043	12.450 ± 0.099	13.707 ± 0.099	29.45 ± 0.14
Distance (pc)	31.429 ± 0.043	80.32 ± 0.64	72.96 ± 0.53	33.93 ± 0.16
R_* (R_\odot)	0.498 ± 0.015	0.353 ± 0.011	0.372 ± 0.011	0.3064 ± 0.0092
M_* (M_\odot)	0.496 ± 0.020	0.338 ± 0.021	0.360 ± 0.020	0.284 ± 0.020
T_{eff} (K)	3606 ± 157	3237 ± 157	3375 ± 157	3138 ± 157
log g	4.7389 ± 0.0081	4.87111 ± 0.00054	4.8525 ± 0.0018	4.9187 ± 0.0049
	TIC-67512645	TIC-271321097	TIC-60910638	TIC-178709444
RA (deg)	173.4697891	233.0476509	5.689521944	166.0757629
Dec (deg)	12.45099531	−64.14559325	22.94559776	−47.82139085
Parallax (mas)	13.52 ± 0.0968	12.534 ± 0.030	10.909 ± 0.073	10.129 ± 0.044
Distance (pc)	73.96 ± 0.53	79.78 ± 0.19	91.67 ± 0.62	98.72 ± 0.43
R_* (R_\odot)	0.2221 ± 0.0068	0.711 ± 0.063	0.467 ± 0.014	0.427 ± 0.013
M_* (M_\odot)	0.191 ± 0.020	0.66 ± 0.077	0.465 ± 0.020	0.421 ± 0.021
T_{eff} (K)	3133 ± 157	4223 ± 122.65	3373 ± 157	3296 ± 157
log g	5.027 ± 0.019	4.55 ± 0.10	4.7660 ± 0.0068	4.8023 ± 0.0053
	TIC-46432937	TIC-240768149	TIC-73692250	
RA (deg)	83.86903906	340.2155188	40.0813749354698	
Dec (deg)	−14.59734983	−17.13941279	35.4105323079258	
Parallax (mas)	11.016 ± 0.025	17.78 ± 0.12	11.749 ± 0.087	
Distance (pc)	90.77 ± 0.21	56.24 ± 0.37	85.11 ± 0.63	
R_* (R_\odot)	0.539 ± 0.016	0.1671 ± 0.0052	0.339 ± 0.010	
M_* (M_\odot)	0.535 ± 0.020	0.138 ± 0.020	0.322 ± 0.020	
T_{eff} (K)	3673 ± 157	2957 ± 157	3163 ± 157	
log g	4.7037 ± 0.0093	5.131 ± 0.037	4.8847 ± 0.0011	
	TIC-406717909	TIC-422986512	TIC-95112238	
RA (deg)	309.47724827762	238.080336223333	90.4837848985143	
Dec (deg)	19.5764691725682	20.3751118729141	−16.8166146303267	
Parallax (mas)	10.122 ± 0.046	10.630 ± 0.056	12.543 ± 0.045	
Distance (pc)	98.79 ± 0.45	94.07 ± 0.49	79.72 ± 0.29	
R_* (R_\odot)	0.428 ± 0.013	0.568 ± 0.017	0.557 ± 0.017	
M_* (M_\odot)	0.422 ± 0.020	0.561 ± 0.020	0.552 ± 0.020	
T_{eff} (K)	3266 ± 157	3398 ± 157	3374 ± 157	
log g	4.8014 ± 0.0052	4.679 ± 0.010	4.6878 ± 0.0098	

Table 6.3: Stellar parameters for the host stars of our giant planet candidates. The parameters have been taken from the TICv8 (Stassun et al., 2019).

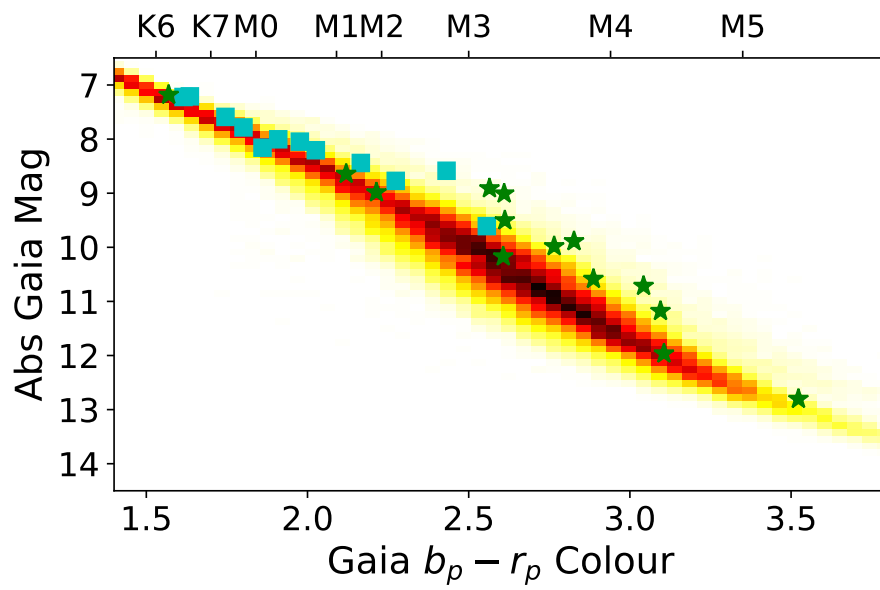


Figure 6.13: Comparison of our fourteen giant planet candidates (green stars) to the *Gaia* colour-magnitude distribution of the 91,306 low-mass stars in our sample (density heat map). Again the twelve known transiting gas giant planets are shown as the blue squares.

	TIC-236387002	TIC-335590096	TIC-243641947	TIC-67646988
T_C (BJD - 2457000)	1958.678208 \pm 0.000103	1571.796564 \pm 0.000600	1603.695065 \pm 0.000329	1871.022577 \pm 0.000113
Period (d)	7.200888 \pm 0.000025	1.522751 \pm 0.000067	2.592472 \pm 0.000076	1.881690 \pm 0.000014
R_P (R_J)	0.981 $^{+0.012}_{-0.016}$	0.753 $^{+0.053}_{-0.041}$	1.060 $^{+0.023}_{-0.030}$	0.924 $^{+0.020}_{-0.026}$
R_P/R_*	0.2023 $^{+0.0025}_{-0.0032}$	0.219 $^{+0.015}_{-0.012}$	0.2927 $^{+0.0063}_{-0.0084}$	0.3100 $^{+0.0066}_{-0.0088}$
ρ_* (g cm $^{-3}$)	14.42 $^{+0.77}_{-1.06}$	8.5 $^{+2.9}_{-3.6}$	17.1 $^{+1.8}_{-2.1}$	19.7 $^{+1.6}_{-1.8}$
a/R_*	34.07 $^{+0.60}_{-0.86}$	10.1 $^{+1.1}_{-1.7}$	18.25 $^{+0.61}_{-0.78}$	15.44 $^{+0.40}_{-0.49}$
i (deg)	89.78 $^{+0.15}_{-0.22}$	88.0 $^{+1.4}_{-2.4}$	89.46 $^{+0.38}_{-0.47}$	89.52 $^{+0.33}_{-0.45}$
	TIC-67512645	TIC-271321097	TIC-60910638	TIC-178709444
T_C (BJD - 2457000)	1901.057646 \pm 0.000840	1634.154933 \pm 0.000873	1764.926059 \pm 0.000775	1572.678652 \pm 0.001255
Period (d)	3.370791 \pm 0.000207	6.955704 \pm 0.000594	2.149810 \pm 0.000117	3.471730 \pm 0.000332
R_P (R_J)	1.21 $^{+0.68}_{-0.33}$	0.746 $^{+0.026}_{-0.024}$	1.19 $^{+1.78}_{-0.42}$	0.98 $^{+1.86}_{-0.27}$
R_P/R_*	0.56 $^{+0.31}_{-0.15}$	0.1078 $^{+0.0038}_{-0.0034}$	0.261 $^{+0.392}_{-0.092}$	0.235 $^{+0.447}_{-0.066}$
ρ_* (g cm $^{-3}$)	20.9 $^{+5.1}_{-4.3}$	1.89 $^{+0.43}_{-0.66}$	5.5 $^{+9.2}_{-1.3}$	8.0 $^{+11.8}_{-2.7}$
a/R_*	23.2 $^{+1.8}_{-1.7}$	16.9 $^{+1.2}_{-2.3}$	11.05 $^{+4.33}_{-0.98}$	17.2 $^{+6.1}_{-2.2}$
i (deg)	87.89 $^{+1.26}_{-0.74}$	88.71 $^{+0.86}_{-1.11}$	84.8 $^{+3.8}_{-2.3}$	86.8 $^{+2.4}_{-1.9}$

Table 6.4: Planetary parameters for eight of our giant planet sample derived from the transit fitting in Section 6.5. The quoted values are the 50th percentiles of the posterior distributions, and the uncertainties are defined by the 16th and 84th percentiles and represent the 1 σ uncertainty.

	TIC-46432937	TIC-240768149	TIC-73692250
T_C (BJD - 2457000)	1468.630229 ± 0.000224	1354.340052 ± 0.001205	1791.488263 ± 0.001093
Period (d)	1.440456 ± 0.000024	1.248069 ± 0.000107	2.572964 ± 0.000212
R_P (R_J)	$1.23^{+0.44}_{-0.29}$	$0.73^{+0.58}_{-0.28}$	$0.744^{+1.021}_{-0.054}$
R_P/R_*	$0.235^{+0.085}_{-0.056}$	$0.45^{+0.36}_{-0.17}$	$0.226^{+0.309}_{-0.016}$
ρ_* (g cm^{-3})	$5.73^{+4.57}_{-0.71}$	$50.1^{+49.8}_{-26.5}$	$26.6^{+17.2}_{-13.3}$
a/R_*	$8.56^{+1.85}_{-0.37}$	$16.0^{+4.2}_{-3.6}$	$21.0^{+3.8}_{-4.3}$
i (deg)	$84.6^{+3.4}_{-1.4}$	$86.7^{+2.3}_{-2.0}$	$88.68^{+0.96}_{-2.71}$
	TIC-406717909	TIC-422986512	TIC-95112238
T_C (BJD - 2457000)	1684.513599 ± 0.001141	$1956.623066 \pm .000858$	1468.539386 ± 0.000413
Period (d)	1.877182 ± 0.000157	1.115786 ± 0.000063	1.362079 ± 0.000048
R_P (R_J)	$1.82^{+1.53}_{-0.58}$	$0.80^{+0.70}_{-0.12}$	$0.828^{+2.587}_{-0.058}$
R_P/R_*	$0.44^{+0.37}_{-0.14}$	$0.145^{+0.127}_{-0.022}$	$0.153^{+0.477}_{-0.011}$
ρ_* (g cm^{-3})	$13.6^{+5.4}_{-3.4}$	$3.4^{+7.0}_{-1.5}$	$10.1^{+8.6}_{-6.1}$
a/R_*	$13.6^{+1.6}_{-1.2}$	$6.1^{+2.7}_{-1.1}$	$10.0^{+2.3}_{-2.6}$
i (deg)	$86.1^{+2.6}_{-1.6}$	$82.5^{+5.9}_{-4.6}$	$86.1^{+2.3}_{-7.0}$

Table 6.5: Planetary parameters for the remaining six giant planet candidates derived from the transit fitting in Section 6.5. The quoted values are the 50th percentiles of the posterior distributions, and the uncertainties are defined by the 16th and 84th percentiles and represent the 1σ uncertainty.

TIC	Photometry	Speckle Imaging	Radial Velocites	Comments
236387002	MuSCAT2 (Full) LCO-McDonald (Full) KeplerCam (Partial)	SOAR SAI	TRES Habitable Planet Finder APOGEE-2N	Known transiting brown dwarf TOI-2119 b Cañas et al. (2022) Carmichael et al. (2022)
335590096	ExTrA (Partial)	NO	NO	TOI-4860
243641947	MEarth (Full)	NO	ESPRESSO	TOI-3235. RVs consistent with a giant planet
67646988	MEarth	RoboAO	TRES	Known brown dwarf TOI-1779b/LP 261-75 b Discovered by MEarth survey (Irwin et al., 2018)
67512645	NO	NO	ESPRESSO	RVs consistent with a giant planet
271321097	NO	NO	NO	
60910638	NO	NO	NO	
178709444	LCO-Siding Spring (Full)	Gemini	ESPRESSO	TOI-762. Preliminary orbit consistent with giant planet
46432937	NO	NO	NO	
240768149	NO	NO	NO	
73692250	NO	NO	NO	
406717909	NO	NO	NO	
422986512	NO	NO	NO	
95112238	NO	NO	NO	

Table 6.6: Summary of currently available follow-up observations for the fourteen giant planet candidates from my search.

6.8 ESPRESSO Radial Velocity Monitoring

As is demonstrated by the two confirmed transiting brown dwarfs in our candidate sample, the only way to be fully confident that our candidates are truly exoplanets is to measure their masses. The ESPRESSO spectrograph has been successfully used to confirm similar systems (eg. HATS-71 b; Bakos et al., 2020).

We have a program that is currently underway to obtain mass measurements for our candidates using the ESPRESSO spectrograph (Pepe et al., 2021) on the VLT. We have been reducing the ESPRESSO data throughout the program using the publicly available pipeline, which runs in the ESOReflex environment (Freudling et al., 2013). As these observations are not yet complete, we do not have full results for all our objects. We do have spectroscopic orbits for some of our candidates, which we present in Figure 6.14. This radial velocity monitoring will continue over the next year in order to measure the masses of all of our candidates.

The radial velocity fitting analysis for these candidates was performed using the DACE platform (Díaz et al., 2014). For this analysis, the planet orbits were fixed as circular and the orbital ephemerides were initially fixed at the photometric values. For TIC-67512645 and TIC-178709444 this resulted in good fits to the data. For TIC-243641947 we had to refit for the period when modelling the radial velocities in order to achieve a good fit to the data. We derived a period of $P = 2.592593 \pm 0.000003$ d from this analysis, which is consistent with the photometric period within 2σ . A full joint analysis will be required to derive the true period of this planet.

6.9 Injection and Recovery Tests

Simply identifying and confirming these candidates is not enough to be able to determine the frequency of these systems. In order complete this study and derive occurrence rates for gas giant planets orbiting low-mass stars, we must determine the detection efficiency of our planet search pipeline. To do this, we will perform planet injection-recovery tests. These methods have been used to great success to test the detection efficiencies of transiting planet searches, including for the *Kepler* pipeline in Christiansen et al. (2020). We have not yet performed the injection-recovery analysis for our search. These tests will be performed contemporaneously to the follow-up observations over the next few months. Briefly, for these tests we will simulate *TESS* 30 minute cadence transiting planet light curves, which we will then pass through our planet search pipelines. With these results we will be able to quantify what fraction of real transiting planets we expect to have recovered with our search, and what fraction we are likely to have missed. We provide a brief outline of our plans for this analysis in the following section.

In order to accurately replicate the noise properties and observing windows for the light

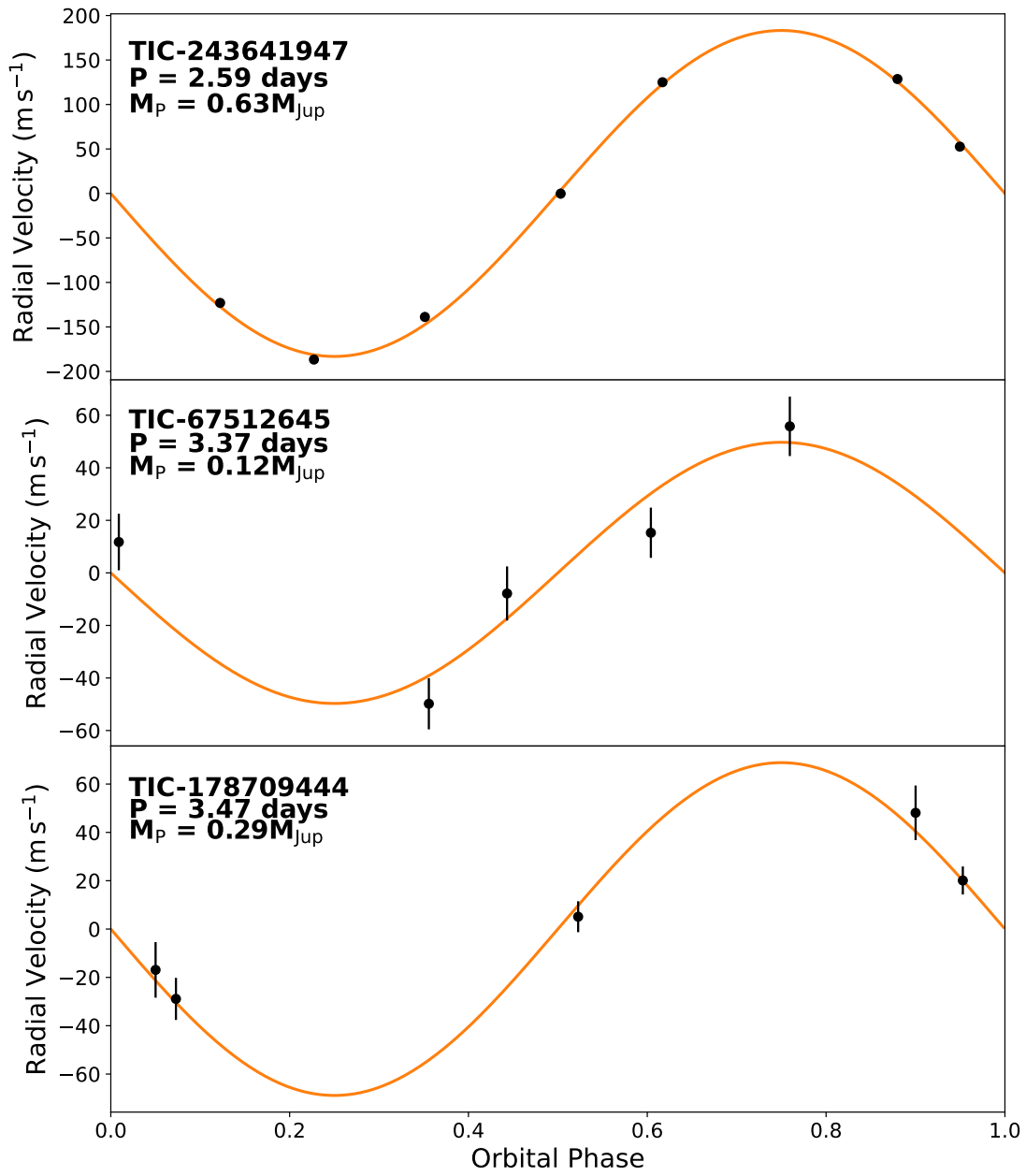


Figure 6.14: Phase folded ESPRESSO radial velocities obtained to date for our giant planet candidates. The orange lines are the results of preliminary fits to the data, and the masses on each panel come from the results of these fits.

curves we will use real TESS-SPOC 30 minute light curves. We will exclude any star which we confidently identified as hosting a transiting planet or being an eclipsing binary system from this analysis. However, any star with a significant BLS detection that was subsequently confidently identified as being due to a variable star or a spurious outlier will be included in these injection tests. Stars that have light curves displaying large systematics or high amplitude variability are likely to be among those most likely to hide transiting giant planet signals. We therefore leave them in our analysis, in order to better estimate the detection efficiency of our search.

We will then simulate the transiting planet signals. For each star we will test transit signals for a range of trial periods. These periods will be spaced evenly every 0.25 d between our search range of 1 and 10 d. For each period, we will also test a range of transit phases, trialling transiting signals with reference transit times spread across one full orbital period in steps of 2 hours. This 2 hour time step is representative of the transit duration of our candidates, and should ensure we cover all phase possibilities for each trial period. For each combination of period and phase, we will simulate 20 different transiting planets. Each of these planets will have a randomly selected radius and orbital inclination. The planet radius will be drawn from a Gaussian distribution which is informed by the distribution of radii of our candidates as well as the known transiting gas giants with low-mass hosts. The orbital inclinations will similarly be drawn from a distribution which arises from the geometry of a randomly aligned orbital plane.

This randomness of the inclinations allows us to account for non-transiting planets in our simulations. This is important given we are interested in deriving the true population of all gas giants with low-mass hosts, not simply those that transit. The first step of our recovery tests will therefore be to assess whether or not a given simulated planet does indeed transit the star. To do this, we require a semi-major axis, a , for each planet, which we will calculate using the stellar mass, M_* , from the TIC and Kepler’s Third Law

$$a^3 = \frac{GM_*P^2}{4\pi^2}, \quad (6.5)$$

where P is the planet orbital period and G is the gravitational constant. We will also assume circular orbits for all simulated planets. Any planet which is shown to be non-transiting we will record as missed by the pipeline. Any planet which does transit will then be passed through the full planet search pipeline.

With the results of these tests we will have a complete picture of the detection efficiency of our planet search pipeline across the full parameter space considered in this study. We will also be able to accurately account for the effect of the *TESS* observing pattern and a realistic sample of highly variable stars through the use of real *TESS* light curves for this study.

6.10 Conclusions and Future Outlook

We have presented a systematic search through *TESS* 30 minute cadence light curves for transiting gas giant planets orbiting low-mass stars. These systems are predicted to be rare by planet formation theory, and so the aim of this search is to derive a robust occurrence rate for these systems for the first time. We have presented our planet search and candidate vetting pipeline, using which we identified fourteen giant planet candidates from an initial sample of 91,306 low-mass stars. Of these candidates, two are a previously known transiting brown dwarfs (Irwin et al., 2018; Cañas et al., 2022; Carmichael et al., 2022) and spectroscopic observations are underway and planned to uncover the nature of the remaining twelve candidates. Our candidate giant planets have stellar hosts which are in general lower mass than the hosts of the twelve such known planets (see Figure 6.4). Therefore, if confirmed as planets, this study will also extend our knowledge of known transiting giant planets to lower stellar masses than ever before.

We will be performing planet injection-and recovery tests to quantify the detection efficiency of our pipeline. Through the combination of these simulations and the results of the follow-up of our candidates, this study will provide for the first time robust occurrence rates for close-in giant planets orbiting low-mass stars.

Chapter 7

Conclusions

7.1 The role of ground-based photometry in the *TESS* Era

TESS has largely superseded ground-based transit surveys, such as NGTS, in the detection of new exoplanets. Despite this, NGTS can still make important contributions to the study of transiting exoplanets. By inspecting the ways through which *TESS* and NGTS contribute to my research, we get an insight into how such facilities can work together in a complementary manner. Throughout this thesis I have presented different studies of transiting exoplanets that use both the ground-based NGTS facility or the space-based *TESS* telescope. These studies involve both the detection of exoplanets (NGTS-12 b in Chapter 2) and the improvement of our knowledge and understanding of previously known systems (eg. the HIP-41378 system in Chapter 4).

Archival photometric datasets from ground-based facilities have already played a significant role in fully exploiting data from the space-based *TESS* mission. For example, long-baseline light curves from WASP have been used to constrain the rotation periods of *TESS* exoplanet host stars (eg., Osborn et al., 2021a; Kossakowski et al., 2021; Hawthorn et al., 2022). Existing ground-based photometry can also be used to aid the detection of long-period exoplanets. These long-period planets often exhibit just one or two transits in the available *TESS* data. Archival ground-based photometry can be searched for additional transits to help derive the period of the planet (eg., Yao et al., 2019; Gill et al., 2020c).

7.1.1 NGTS Wide-Field Transit Observations

Wide-field transit surveys provide the current dominant route to the detection of new exoplanets. Using data from NGTS I lead the discovery of NGTS-12 b, a sub-Saturn mass exoplanet in a 7.53 d orbit (Bryant et al., 2020a). Residing near the so-called Neptunian desert (see Mazeh et al., 2016), NGTS-12 b provides an interesting case study of the atmospheric processes which

have sculpted this desert.

The discovery of NGTS-12 b was made using a ground-based blind transit search. However, now *TESS* is providing high precision continuous coverage for nearly all stars in the sky from space, the role of ground-based transit surveys is limited. This is evidenced by the main surveys of facilities such as WASP, HATNet, and HATSouth coming to an end. There is still space for niche searches from the ground, such as a current program being performed with NGTS surveying open stellar clusters, where the stellar crowding is too high for the $21''/\text{pix}$ pixel-scale of *TESS* (Gillen et al., 2020). For the most part however, ground-based exoplanet photometry is now much better focused on follow-up observations. These follow-up observations are vital for prioritising further, more expensive, ground and space-based follow-up with instruments including the VLT or *JWST*. In this remit, there is a key role that NGTS will play over the coming years.

7.1.2 NGTS Multi-Telescope Observations

I presented a novel ground-based photometric observing method in which multiple NGTS telescopes are used to simultaneously observe the same source (see Chapter 3 and Bryant et al., 2020b). This method and the high-precision photometry it delivers has laid the groundwork for NGTS to operate over the coming years as *TESS* continues to survey the sky.

The wide field-of-view of the NGTS cameras provides access to a large number of comparison stars even for stars up to a brightness of $I \approx 8$ mag. NGTS thus largely avoids the correlated noise which plagues bright star light curves from larger ground-based facilities where insufficient comparison stars are available. Combined with the multi-telescope method, this places NGTS as one of a very small handful of facilities in the world capable of recovering shallow transits ($\delta \approx 1000$ ppm) on bright ($I \leq 10$ mag) host stars. These transit events are produced by the priority candidates of the *TESS* mission – small ($\leq 4.0 R_{\oplus}$) planets amenable to radial velocity follow-up. Already this method has been used to contribute to some of the most exciting *TESS* exoplanet discoveries, such as the very dense planet TOI-849 b that resides within the Neptunian Desert (Armstrong et al., 2020) and the remarkable TOI-178 system that consists of at least six exoplanets locked in a resonant dance (Leleu et al., 2021). In total, NGTS has contributed multi-telescope transit light curves to the discovery of fourteen transiting exoplanets (see Table 7.1), and will continue to contribute substantially to the discovery of exoplanets over the coming years.

In addition to aiding the confirmation of new exoplanets, these observations are also being used for the characterisation of exoplanet systems through the monitoring of transit timing variations. One long-term NGTS project focuses on the transit times of a sample of short period

Planet	Transit Coverage	Ref
LTT-9779 b	Full transit	Jenkins et al. (2020)
HIP-65A b	Two full transits	Nielsen et al. (2020)
TOI-849 b	Two full transits	Armstrong et al. (2020)
TOI-481 b	Partial egress	Brahm et al. (2020)
NGTS-14A b	Partial ingress	Smith et al. (2021)
TOI-561 c	Full transit	Weiss et al. (2021)
TOI-178 g	Full transit	Leleu et al. (2021)
TOI-201 b	Partial ingress	Hobson et al. (2021)
TOI-431 d	Partial ingress	Osborn et al. (2021a)
TOI-1064 c	Partial egress	Wilson et al. (2022)
TOI-560 b	Full transit	Barragán et al. (2022)
TOI-836 c	Full transit	Hawthorn et al. (2022)
TOI-778 b	Partial egress	Clarke et al. (2022)
TOI-620 b	Two full transits	Reefe et al. (2022)

Table 7.1: Summary of the NGTS follow-up light curves contributed to published exoplanet discoveries.

hot Jupiters. This project is searching for signs of period decay due to tidal interactions between the planet and star, such as those observed in the WASP-4 system (eg. Southworth et al., 2019; Baluev et al., 2020; Turner et al., 2022). NGTS also monitors the transits of planets in multi-planet systems. One such system currently being studied is the two planet TOI-1130 system (Huang et al., 2020b). The TTVs in this system were revealed through large offsets in the transit times between data from Years 1 and 3 of *TESS*, however the *TESS* data did not cover sufficient baseline to fully map out the TTV signals.

These and other transit timing variation studies into exoplanet systems will continue over the coming years with NGTS. They also highlight one of the advantages of ground-based photometric facilities being the long-term observation base lines they provide. Particularly for studying the tidal decay of hot Jupiters where transit timings spanning at least ten years are required.

7.1.3 The long-period planet HIP-41378 f

A particularly exciting NGTS result was the detection of a transit of the 542 d period planet HIP-41378 f (Chapter 4 and Bryant et al., 2021). Not only did we detect the transit, but we also detected the transit as arriving 1.5 hours earlier than predicted, signalling the presence of TTVs in the system. Using knowledge of the other planets in the system, I was able to predict the times of the following transits of HIP-41378 f. Recent observations with the Hubble Space Telescope

confirmed the transit timing variation detected with NGTS and my prediction for the upcoming transit times (Alam et al., 2022).

Over the coming years, continued observations of the transits of HIP-41378 f, and potentially also other planets in the system, can and will be performed with NGTS. Through these observations, the TTV signals of the planets can be monitored. This will provide a new route through which to study the planets in the HIP-41378 system, both in terms of their masses and orbits. This could be especially useful for HIP-41378 e. Just one transit of this planet has been observed to date, and its orbital period has been largely constrained through asteroseismic constraints on the stellar density and the constraints on the orbital eccentricity for the stability of the system (Santerne et al., 2019). However, the amplitude and period of the TTV signal of HIP-41378 f also depend on the period of HIP-41378 e. Monitoring the transit times of HIP-41378 f will therefore improve our knowledge of the orbit of HIP-41378 e and improve our chances of detecting a second transit of this planet.

The success of HIP-41378 highlights the scheduling flexibility of ground-based facilities as a further benefit over current space-based facilities. The *TESS* observation schedule is set approximately one year in advance of the observations, and is defined according to the overall survey. This limits its ability to be able to observe transits of long period exoplanets. Conversely, the observing schedules of NGTS and other ground-based facilities are much more flexible, and can be altered to focus on particularly interesting transits, such as those from long-period exoplanets, with just a few days notice. Work using NGTS is being undertaken which further exploits this advantage to recover additional transits of long-period exoplanets which only displayed one or two transits in the available *TESS* data. Detecting these additional transits allows for the true period of the planet to become known, and allows for better characterisation of the planet (Cooke et al., 2018; Gill et al., 2020a; Cooke et al., 2021).

7.1.4 Future Outlook

Looking to the future, one of the major upcoming missions for transiting exoplanet observations is the ESA *PLATO* mission (Rauer et al., 2014). This mission will also utilise multi-telescope observations, and so the lessons we learnt from NGTS multi-telescope observations may be important for maximising the output from *PLATO* observations. In terms of the science output of *PLATO*, one of the main aims of the mission is to search for Earth-like planets orbiting within the Habitable Zone around Sun-like stars. These planets will by their nature have long orbital periods. In order to obtain independent confirmations of these transits, it is likely that the observation scheduling flexibility afforded by ground-based facilities, as was utilised in my study of HIP-41378 f, will be required.

Earth-sized planets around solar type stars will have transit depths on the order of 100 ppm, and so are out of reach of the NGTS facility. However, from the current tests with NGTS observations, the limit on the precision that can be achieved is the number of telescopes available. It is possible that eventually a noise floor will be reached that cannot be surpassed, however it is evident that the current twelve NGTS telescopes do not reach this noise floor. An array of tens of small telescopes, each with the same wide field-of-view as NGTS, could very possibly enable transits with depths as shallow as a few 100 ppm for host stars with magnitudes $V \leq 9$ mag to be robustly detected from the ground. As with other ground-based telescopes being planned and built with larger and larger mirrors, it is possible that another avenue for future ground-based photometric facilities is an array of more and more small telescopes. Such an array could play a crucial role, along with *PLATO*, in discovering the first Earth twin. Recently, such an array concept was proposed as a means of providing high precision observations with very wide fields-of-view (the Argus array; see Law et al., 2021).

TESS with its all-sky coverage, uninterrupted space-based observations, and excellent precision for bright stars ($V \leq 11$ mag) is currently unparalleled for discovering new exoplanets. The exquisite precision and longer monitoring timescales of *PLATO* are likely to see it surpass *TESS* in this position. The exoplanets discovered by these space telescopes will be some of the best targets for new and upcoming facilities, such as *JWST*. A future, larger telescope array could play a similar role for *PLATO* planet candidates. The flexible scheduling capabilities afforded to NGTS, or a future larger array, allow it to play a major role in the study of the longest period transiting exoplanets, which could be crucial for the upcoming *PLATO* mission. In a world of transiting exoplanet discovery and study which is very quickly becoming dominated by space-based telescopes, NGTS and other ground-based photometric facilities still have a vital role to play.

7.2 Exoplanet Populations

With more than 5,000 known exoplanets there is now a much larger focus on what can be learnt from the ensemble of discovered exoplanets. In particular, how do the frequency and planetary parameters vary for different stellar masses and ages? What can these different exoplanet populations tell us about how planets form and evolve? What role does the class and evolution of the star play?

7.2.1 WASP-47

The WASP-47 system is remarkable as it contains a hot Jupiter with two close orbiting small planets – an exterior Neptune and an inner super Earth. Such a configuration of planets is particularly interesting from the perspective of planetary formation and migration. The results I presented in Chapter 5 (Bryant and Bayliss, 2022) improve our knowledge of the masses of these three planets, and will be useful for fully understanding how this system formed and evolved.

Similarities can be seen between the two exoplanets WASP-47 e and 55 Cancri e, both in terms of the sizes of the planets and their orbital configurations and neighbours. One hypothesis is that these two exoplanets may have formed through a different mechanism to other low-mass planets, and represent the beginning of a new population with slightly different compositions to other low-mass exoplanets and close-orbiting giant planet companions. With WASP-47 e and 55 Cancri e as the only two members of this potential new population with measured masses, it is too early to draw significant conclusions. The Kepler-730 (Cañas et al., 2019) and TOI-1130 (Huang et al., 2020b) systems do contain a hot Jupiter with an inner companion, however neither of these low-mass companions currently has a confirmed mass. Future work to uncover more such systems and to measure the masses of the small companions is required to investigate whether trends in mass and radius, similar to WASP-47 e and 55 Cancri e, continue for other such systems.

A recent study searched through the *TESS* data for WASP-47 like systems (Hord et al., 2021), but it yielded no new candidate companions to hot Jupiters. This indicates that these systems are rare. However, the signal-to-noise of the WASP-47 e transits in the *TESS* data is low (see Figure 5.3) and so it is possible that more such planets are hiding in the noise of the *TESS* light curves. Moreover, Huang et al. (2020b) suggested that these systems of hot Jupiters with inner companions might represent the low period end of the population of warm Jupiters with small inner companions, which are much more numerous. Systematic studies into these warm Jupiter systems may also reveal trends in the masses and bulk compositions of the inner companions.

7.2.2 Giant planets orbiting low-mass stars

The exoplanet population I have studied in great detail is the population of close-in giant planets orbiting low-mass stars. Exploiting the all-sky coverage and red sensitivity of *TESS*, I performed a systematic transit search for giant planets in a sample of 91,306 low-mass stars within 100 pc of the Earth. This search produced fourteen giant planet candidates. These planet candidates will form the basis of deriving a robust occurrence rate for giant planets orbiting low-mass stars for the first time. These results will be of great importance for fully understanding how giant

planets form.

From my planet search, I have identified fourteen high quality giant planet candidates. Of these two have been independently confirmed as brown dwarfs (TOI-2119 b; (Cañas et al., 2022; Carmichael et al., 2022) and TOI-1779 b (Irwin et al., 2018)) and a further three have confirmed planetary natures through ESPRESSO observations (TIC-243641947 b, TIC-67512645 b and TIC-178709444 b). With a stellar mass of just $0.191 M_{\odot}$, TIC-67512645 is the lowest mass star to date discovered to host a transiting giant planet. I plan to obtain spectroscopic orbits for the remaining candidates over the next year, thus completing my giant planet sample.

Work still remains to derive the occurrence rate for these systems from this study. This work will take the form of planet injection-and-recovery tests. Through these tests I will be able to robustly estimate the efficiency of my planet detection pipeline, allowing me to estimate the true number of giant planets orbiting low-mass stellar hosts. The occurrence rates I derive will then be compared with the known occurrence rates for close in giant planets orbiting Sun-like stars derived from the *Kepler* mission. This comparison will allow us to investigate how giant planet formation mechanisms differ across a range of stellar masses.

7.2.3 Future Outlook

While the primary aim of the *TESS* mission is to find individual exoplanets amenable to further study, my planet search highlights a further use of *TESS* observations in the study of planetary populations. The systematic all-sky coverage and public availability of the Full-Frame-Images are two key aspects of this. A number of sets of high quality light curves have also been produced and made available to the public, which will be of great use in these studies. These light curve sets include the *TESS*-SPOC light curves (Caldwell et al., 2020), which I used in my research for low-mass stars, and also the Quick Look Pipeline (QLP; Huang et al., 2020a) that has and continues to produce light curves for all objects in the *TESS* field-of-view with magnitudes $T \leq 13.5$ mag. Tools and software also exist for generating light curves quickly and effectively for other stellar samples (eg., *LIGHTKURVE*; Lightkurve Collaboration et al., 2018).

Over the coming years, I plan to extend my current low-mass star search across more *TESS* sectors than currently studied, including the recent *TESS* observations of the ecliptic plane. Increasing the size of the total low-mass star sample will allow me to achieve an even better occurrence rate estimate. I also plan to perform a similar study for a sample of evolved sub-giant stars. These stars were similarly not studied by *Kepler*, and through deriving a robust occurrence rate for giant planets orbiting these stars it may be possible to study the effect that stellar evolution has on planetary systems.

Future missions can also play an important role in achieving a full census of planetary

systems. In terms of transiting planets, *PLATO* will also monitor large numbers of stars with exquisite precision for multi-year observing baselines (Nascimbeni et al., 2022). There is the possibility to utilise *PLATO* data for further exoplanet population studies. In addition, future astrometric data releases from the *Gaia* mission are predicted to yield the discoveries of ≥ 1000 giant planets on wide orbits around nearby low-mass stars (Perryman et al., 2014). By exploiting the results from these and other missions, planetary population studies can be extended to smaller planets and longer periods than currently statistically accessible with the *TESS* Full-Frame-Image data. Direct imaging surveys using the MIRI instrument on *JWST* will yield detections of giant planets orbiting primarily young, low-mass stars (Rieke et al., 2015). Combined with studies of main sequence and evolved stars, we will begin to be able to build a full picture of the birth, evolution, and even death of giant planets.

7.3 The Future of Exoplanet Discovery

Over the next decade, the transit and radial velocity methods are likely to continue to dominate the discovery of exoplanets. *TESS* will continue to survey the whole sky, finding rocky exoplanets around bright stars. The *PLATO* mission (Rauer et al., 2014), set to launch in 2026, will also yield the discoveries of small transiting exoplanets on wide orbits. During the same time frame, a number of other methods will begin to contribute larger numbers of exoplanet discoveries. Future data releases from the *Gaia* mission will contain astrometric data capable of the detection of massive Jupiter-like planets on wide orbits (Perryman et al., 2014).

Upcoming missions, including the Nancy Grace Roman Space Telescope (originally named *WFIRST*; Spergel et al., 2015) and the ESA *Euclid* mission (Amiaux et al., 2012), will significantly increase the number of exoplanets discovered by microlensing. *Roman* is predicted to discover $\approx 1,400$ exoplanets on wide orbits, with ≈ 200 of these being low mass ($\leq 3 M_{\oplus}$) (Penny et al., 2019). The proposed Exoplanet *Euclid* Legacy Survey (ExELS; Penny et al., 2013) predicts that *Euclid* will yield the detection of a few hundred cold exoplanets, including ≈ 50 with masses $\leq 1 M_{\oplus}$. It has also been estimated that both these missions will be able to detect free floating planets (Penny et al., 2013; Johnson et al., 2020), provided there is a sufficiently large population of them. These observations will be able to place constraints on the population size of free floating planets.

The upcoming European Extremely Large Telescope (E-ELT) will have the capability to directly image Jupiter-mass planets on orbits of a few au (Houll   et al., 2021) and even smaller planets ($R_p \leq 4 R_{\oplus}$) around the nearest stars (Bowens et al., 2021). A dedicated direct imaging instrument would extend the reach of the ELT down to temperate Earth-sized exoplanets (Kasper et al., 2021). *JWST* will be able to directly image sub-Jupiter mass exoplanets on orbits

$\gtrsim 30$ au and even exoplanets as low-mass as $0.1 M_J$ on orbits wider than 100 au. *JWST* will also bring great advances in the study of exoplanet atmospheres through transmission spectroscopy, in particular making the atmospheres of sub-Neptune and super-Earth exoplanets available for study (Beichman et al., 2014).

The combination of these techniques and missions over the next decade will lead to the discovery and characterisation of exoplanets in populations and parameter spaces inaccessible for study with current facilities. This will lead us to a much greater understanding of the planetary systems in our Universe.

Bibliography

- Adams F.C. and Laughlin G., 2006. *ApJ*, 649(2):1004–1009.
- Agol E. et al., 2005. *MNRAS*, 359(2):567–579.
- Alam M.K. et al., 2022. *ApJ*, 927(1):L5.
- Almenara J.M. et al., 2009. *A&A*, 506(1):337–341.
- Almenara J.M. et al., 2016. *A&A*, 595:L5.
- Amiaux J. et al., 2012. In M.C. Clampin, G.G. Fazio, H.A. MacEwen, and J. Oschmann Jacobus M., editors, *Space Telescopes and Instrumentation 2012: Optical, Infrared, and Millimeter Wave*, volume 8442 of *Society of Photo-Optical Instrumentation Engineers (SPIE) Conference Series*, 84420Z.
- Anderson D.R. et al., 2017. *A&A*, 604:A110.
- Andrews S.M. et al., 2018. *ApJ*, 869(2):L41.
- Angelo I. and Hu R., 2017. *AJ*, 154(6):232.
- Armstrong D.J., Gamper J., and Damoulas T., 2021. *MNRAS*, 504(4):5327–5344.
- Armstrong D.J. et al., 2020. *Nature*, 583(7814):39–42.
- Baglin A. et al., 2006. In M. Fridlund, A. Baglin, J. Lochard, and L. Conroy, editors, *The CoRoT Mission Pre-Launch Status - Stellar Seismology and Planet Finding*, volume 1306 of *ESA Special Publication*, 33.
- Bakos G. et al., 2004. *PASP*, 116(817):266–277.
- Bakos G.Á., 2018. In H.J. Deeg and J.A. Belmonte, editors, *Handbook of Exoplanets*, 111.
- Bakos G.Á. et al., 2013. *PASP*, 125(924):154.

- Bakos G.Á. et al., 2020. *AJ*, 159(6):267.
- Baluev R.V. et al., 2019. *MNRAS*, 490(1):1294–1312.
- Baluev R.V. et al., 2020. *MNRAS*, 496(1):L11–L15.
- Baraffe I., Chabrier G., and Barman T., 2008. *A&A*, 482(1):315–332.
- Barbary K., 2016. *JOSS*, 1(6):58.
- Barnes S.A., 2007. *ApJ*, 669(2):1167–1189.
- Barragán O. et al., 2022. *MNRAS*. ISSN 0035-8711. Stac638.
- Barros S.C.C. et al., 2015. *MNRAS*, 454(4):4267–4276.
- Batalha N.M. et al., 2010. *ApJ*, 713(2):L109–L114.
- Bayliss D. et al., 2018. *MNRAS*, 475(4):4467–4475.
- Bayliss D.D.R. and Sackett P.D., 2011. *ApJ*, 743(2):103.
- Bean J.L. et al., 2018. *PASP*, 130(993):114402.
- Becker J.C. et al., 2015. *ApJ*, 812(2):L18.
- Becker J.C. et al., 2019. *AJ*, 157(1):19.
- Beichman C. et al., 2014. *PASP*, 126(946):1134.
- Benedict G.F. et al., 2002. *ApJ*, 581(2):L115–L118.
- Benedict G.F. et al., 2006. *AJ*, 132(5):2206–2218.
- Bertin E. and Arnouts S., 1996. *A&AS*, 117:393–404.
- Boisse I., Bonfils X., and Santos N.C., 2012. *A&A*, 545:A109.
- Boisse I. et al., 2011. *A&A*, 528:A4.
- Bond I.A. et al., 2004. *ApJ*, 606(2):L155–L158.
- Bonfils X. et al., 2013. *A&A*, 549:A109.
- Borucki W.J. et al., 2010. *Science*, 327(5968):977.
- Bouchy F. et al., 2004. *A&A*, 421:L13–L16.

- Bouchy F. et al., 2017. *The Messenger*, 169:21–27.
- Bouma L.G. et al., 2019. *ApJS*, 245(1):13.
- Bourrier V. et al., 2018. *A&A*, 619:A1.
- Bowens R. et al., 2021. *A&A*, 653:A8.
- Bowler B.P., 2016. *PASP*, 128(968):102001.
- Brahm R., Jordán A., and Espinoza N., 2017. *PASP*, 129:034002.
- Brahm R. et al., 2019. *AJ*, 158(1):45.
- Brahm R. et al., 2020. *AJ*, 160(5):235.
- Bryant E.M. and Bayliss D., 2022. *AJ*, 163(5):197.
- Bryant E.M. et al., 2020a. *MNRAS*, 499(3):3139–3148.
- Bryant E.M. et al., 2020b. *MNRAS*, 494(4):5872–5881.
- Bryant E.M. et al., 2021. *MNRAS*, 504(1):L45–L50.
- Burdanov A. et al., 2018. In H.J. Deeg and J.A. Belmonte, editors, *Handbook of Exoplanets*, 130. Springer.
- Burn R. et al., 2021. *A&A*, 656:A72.
- Cañas C.I. et al., 2019. *ApJ*, 870(2):L17.
- Cañas C.I. et al., 2022. *AJ*, 163(2):89.
- Caldwell D.A. et al., 2020. *RNAAS*, 4(11):201.
- Carmichael T.W. et al., 2022. *arXiv e-prints*, arXiv:2202.08842.
- Carter J.A. et al., 2008. *ApJ*, 689(1):499–512.
- Chabrier G. and Baraffe I., 2000. *ARA&A*, 38:337–377.
- Charbonneau D. et al., 2000. *ApJ*, 529(1):L45–L48.
- Chatterjee S. et al., 2008. *ApJ*, 686(1):580–602.
- Chaushev A. et al., 2019. *MNRAS*, 488(4):5232–5250.

- Chauvin G. et al., 2004. *A&A*, 425:L29–L32.
- Choi J. et al., 2016. *ApJ*, 823(2):102. ISSN 1538-4357.
- Christiansen J.L. et al., 2020. *AJ*, 160(4):159.
- Claret A. and Bloemen S., 2011. *A&A*, 529:A75.
- Clarke D., 2003. *A&A*, 407:1029–1037.
- Clarke J. et al., 2022. *AJ* – *submitted*.
- Cloutier R. et al., 2019. *A&A*, 629:A111.
- Collins K. et al., 2018a. volume 231 of *American Astronomical Society Meeting Abstracts*, 439.08.
- Collins K.A. et al., 2018b. *AJ*, 156(5):234.
- Colón K.D., Ford E.B., and Morehead R.C., 2012. *MNRAS*, 426(1):342–353.
- Cooke B.F., Pollacco D., and Bayliss D., 2019. *A&A*, 631:A83.
- Cooke B.F. et al., 2018. *A&A*, 619:A175.
- Cooke B.F. et al., 2020. *AJ*, 159(6):255.
- Cooke B.F. et al., 2021. *MNRAS*, 500(4):5088–5097.
- Cox J.P., 1980. *Theory of stellar pulsation*. Princeton Series in Astrophysics. Princeton University Press.
- Crass J. et al., 2021. *arXiv e-prints*, arXiv:2107.14291.
- Cumming A. et al., 2008. *PASP*, 120(867):531.
- Curiel S. et al., 2020. *AJ*, 160(3):97.
- da Silva R. et al., 2006. *A&A*, 446(2):717–722.
- Dai F. et al., 2015. *ApJ*, 813(1):L9.
- Davenhall A.C., Privett G.J., and Taylor M.B., 2001. *Starlink Cookbook*, 5.
- Dawson R.I. and Johnson J.A., 2018. *ARA&A*, 56:175–221.

- Delrez L. et al., 2018. In H.K. Marshall and J. Spyromilio, editors, *Ground-based and Airborne Telescopes VII*, volume 10700 of *Society of Photo-Optical Instrumentation Engineers (SPIE) Conference Series*, 107001I.
- Demory B.O. et al., 2012. *ApJ*, 751(2):L28.
- Díaz R.F. et al., 2014. *MNRAS*, 441(2):983–1004.
- Dipierro G. et al., 2015. *MNRAS*, 453(1):L73–L77.
- Donahue R.A., Dobson A.K., and Baliunas S.L., 1997. *Sol. Phys.*, 171(1):191–209.
- Dorn C. et al., 2019. *MNRAS*, 484(1):712–727.
- Dotter A., 2016. *ApJS*, 222(1):8.
- Dreizler S. et al., 2020. *A&A*, 644:A127.
- Dressing C.D. and Charbonneau D., 2015. *ApJ*, 807(1):45.
- Eastman J., Siverd R., and Gaudi B.S., 2010. *PASP*, 122(894):935.
- Eigmüller P. et al., 2019. *A&A*, 625:A142.
- Einstein A., 1936. *Science*, 84(2188):506–507.
- Eker Z. et al., 2015. *AJ*, 149(4):131.
- Emsenhuber A. et al., 2021a. *A&A*, 656:A69.
- Emsenhuber A. et al., 2021b. *A&A*, 656:A70.
- Espinoza N. and Jordán A., 2015. *MNRAS*, 450(2):1879–1899. ISSN 0035-8711.
- Faigler S. and Mazeh T., 2011. *MNRAS*, 415(4):3921–3928.
- Fischer D.A. and Valenti J., 2005. *ApJ*, 622(2):1102–1117.
- Fogg M.J. and Nelson R.P., 2005. *A&A*, 441(2):791–806.
- Fogg M.J. and Nelson R.P., 2007. *A&A*, 472(3):1003–1015.
- Föhring D. et al., 2019. *MNRAS*, 489(4):5098–5108.
- Foreman-Mackey D., 2016. *JOSS*, 24.

- Foreman-Mackey D., 2018. *RNAAS*, 2(1):31.
- Foreman-Mackey D. et al., 2013. *PASP*, 125(925):306.
- Foreman-Mackey D. et al., 2017. *AJ*, 154:220.
- Foreman-Mackey D. et al., 2021. *JOSS*, 6(62):3285.
- Fressin F. et al., 2013. *ApJ*, 766(2):81.
- Freudling W. et al., 2013. *A&A*, 559:A96.
- Fulton B.J. et al., 2013. *ApJ*, 772(2):80.
- Gaia Collaboration, 2018. *A&A*, 616:A1.
- Gaia Collaboration et al., 2016. *A&A*, 595:A2.
- Gaia Collaboration et al., 2021. *A&A*, 649:A1.
- Galle J.G., 1846. *MNRAS*, 7:153.
- Gandolfi D. et al., 2018. *A&A*, 619:L10.
- Gaudi B.S. et al., 2008. *Science*, 319(5865):927.
- Gelman A. and Rubin D.B., 1992. *Statistical Science*, 7:457–472.
- Gilbert E.A. et al., 2020. *AJ*, 160(3):116.
- Gill S., Maxted P.F.L., and Smalley B., 2018. *A&A*, 612:A111.
- Gill S. et al., 2020a. *MNRAS*, 495(3):2713–2719.
- Gill S. et al., 2020b. *ApJ*, 898(1):L11.
- Gill S. et al., 2020c. *MNRAS*, 491(2):1548–1553.
- Gillen E. et al., 2020. *MNRAS*, 492(1):1008–1024.
- Gillon M., 2018. *Nature Astronomy*, 2:344–344.
- Gillon M. et al., 2011. volume 11 of *European Physical Journal Web of Conferences*, 06002.
- Gould A. et al., 2006. *Acta Astron.*, 56:1–50.
- Günther M.N. et al., 2019. *Nature Astronomy*, 420.

- Haffert S.Y. et al., 2019. *Nature Astronomy*, 3:749–754.
- Hartman J.D. et al., 2015. *AJ*, 149(5):166.
- Hawthorn F. et al., 2022. *MNRAS* – *submitted*.
- Hébrard G. et al., 2020. *A&A*, 640:A32.
- Hellier C. et al., 2012. *MNRAS*, 426(1):739–750.
- Hellier C. et al., 2019. *MNRAS*, 488(3):3067–3075.
- Henden A. and Munari U., 2014. *Contributions of the Astronomical Observatory Skalnaté Pleso*, 43:518–522.
- Henry G.W. et al., 2000. *ApJ*, 529(1):L41–L44.
- Hobson M.J. et al., 2021. *AJ*, 161(5):235.
- Holman M.J. et al., 2010. *Science*, 330(6000):51.
- Hord B.J. et al., 2021. *AJ*, 162(6):263.
- Houllé M. et al., 2021. *A&A*, 652:A67.
- Howard A.W. et al., 2012. *ApJS*, 201(2):15.
- Howell S.B. et al., 2014. *PASP*, 126(938):398.
- Hsu D.C. et al., 2019. *AJ*, 158(3):109.
- Huang C., Wu Y., and Triaud A.H.M.J., 2016. *ApJ*, 825(2):98.
- Huang C.X. et al., 2018. *ApJ*, 868(2):L39.
- Huang C.X. et al., 2020a. *RNAAS*, 4(11):204.
- Huang C.X. et al., 2020b. *ApJ*, 892(1):L7.
- Ida S. and Lin D.N.C., 2005. *ApJ*, 626(2):1045–1060.
- Irwin J.M. et al., 2018. *AJ*, 156(4):140.
- Irwin M.J. et al., 2004. In *Optimizing Scientific Return for Astronomy through Information Technologies*, volume 5493, 411 – 422. SPIE.

- Jenkins J.M. et al., 2016. In G. Chiozzi and J.C. Guzman, editors, *Software and Cyberinfrastructure for Astronomy IV*, volume 9913 of *Society of Photo-Optical Instrumentation Engineers (SPIE) Conference Series*, 99133E.
- Jenkins J.S. et al., 2020. *Nature Astronomy*, 4:1148–1157.
- Johnson J.A. et al., 2010. *PASP*, 122(894):905.
- Johnson S.A. et al., 2020. *AJ*, 160(3):123.
- Jordán A. et al., 2022. *AJ*, 163(3):125.
- Kasper M. et al., 2021. *The Messenger*, 182:38–43.
- Kasting J.F., Whitmire D.P., and Reynolds R.T., 1993. *Icarus*, 101(1):108–128.
- Kaufer A. et al., 1999. *The Messenger*, 95:8–12.
- Kawahara H. and Masuda K., 2019. *AJ*, 157(6):218.
- Kaye L. et al., 2022. *MNRAS*, 510(4):5464–5485.
- Kempton E.M.R. et al., 2018. *PASP*, 130(993):114401.
- Keppler M. et al., 2018. *A&A*, 617:A44.
- Kipping D.M., 2013a. *MNRAS*, 435(3):2152–2160. ISSN 0035-8711.
- Kipping D.M., 2013b. *MNRAS*, 434:L51–L55.
- Kipping D.M., 2014. *MNRAS*, 444(3):2263–2269.
- Knutson H.A. et al., 2007. *ApJ*, 655(1):564–575.
- Knutson H.A. et al., 2014. *ApJ*, 785(2):126.
- Konacki M. et al., 2003. *Nature*, 421(6922):507–509.
- Kosiarek M.R. and Crossfield I.J.M., 2020. *AJ*, 159(6):271.
- Kossakowski D. et al., 2021. *A&A*, 656:A124.
- Kostov V.B. et al., 2019. *AJ*, 158(1):32.
- Kovács G., Zucker S., and Mazeh T., 2002. *A&A*, 391:369–377.

- Kozai Y., 1962. *AJ*, 67:591–598.
- Kreidberg L., 2015. *PASP*, 127(957):1161.
- Kunimoto M. et al., 2022. *arXiv e-prints*, arXiv:2202.03656.
- Lagrange A.M., 2014. *Philosophical Transactions of the Royal Society of London Series A*, 372(2014):20130090–20130090.
- Laughlin G., Bodenheimer P., and Adams F.C., 2004. *ApJ*, 612(1):L73–L76.
- Law N. et al., 2021. volume 53 of *American Astronomical Society Meeting Abstracts*, 235.02.
- Lecavelier des Etangs A. and Lissauer J.J., 2022. *New Astronomy Reviews*, 94:101641. ISSN 1387-6473.
- Leleu A. et al., 2019. *A&A*, 624:A46.
- Leleu A. et al., 2021. *A&A*, 649:A26.
- Lendl M. et al., 2020. *MNRAS*, 492(2):1761–1769.
- Lidov M.L., 1962. *Planet. Space Sci.*, 9(10):719–759.
- Lightkurve Collaboration et al., 2018. Lightkurve: Kepler and TESS time series analysis in Python. Astrophysics Source Code Library.
- Lillo-Box J. et al., 2020. *A&A*, 642:A121.
- Lin D.N.C., Bodenheimer P., and Richardson D.C., 1996. *Nature*, 380(6575):606–607.
- Lithwick Y., Xie J., and Wu Y., 2012. *ApJ*, 761(2):122.
- Llop-Sayson J. et al., 2021. *AJ*, 162(5):181.
- Lomb N.R., 1976. *Ap&SS*, 39:447–462.
- Lopez E.D., 2017. *MNRAS*, 472(1):245–253.
- Lovis C. and Fischer D., 2010. In S. Seager, editor, *Exoplanets*, 27–53. University of Arizona Press.
- Lucy L.B. and Sweeney M.A., 1971. *AJ*, 76:544–556.
- Luger R. et al., 2019. *AJ*, 157:64.

- Lund M.N. et al., 2019. *AJ*, 158(6):248.
- Marois C. et al., 2008. *Science*, 322(5906):1348.
- Marois C. et al., 2010. *Nature*, 468(7327):1080–1083.
- Mayor M. and Queloz D., 1995. *Nature*, 378(6555):355–359.
- Mayor M. et al., 2003. *The Messenger*, 114:20–24.
- Mayor M. et al., 2011. *arXiv e-prints*, arXiv:1109.2497.
- Mazeh T., Holczer T., and Faigler S., 2016. *A&A*, 589:A75.
- McCormac J. et al., 2013. *PASP*, 125(927):548.
- McQuillan A., Aigrain S., and Mazeh T., 2013. *MNRAS*, 432(2):1203–1216.
- Millholland S., Petigura E., and Batygin K., 2020. *ApJ*, 897(1):7.
- Montalto M. et al., 2020. *MNRAS*, 498(2):1726–1749.
- Morton T.D., 2015. *isochrones: Stellar model grid package*.
- Morton T.D. et al., 2016. *ApJ*, 822(2):86.
- Murray C.A. et al., 2020. *MNRAS*, 495(2):2446–2457.
- Mustill A.J., Davies M.B., and Johansen A., 2015. *ApJ*, 808(1):14.
- Nascimbeni V. et al., 2011. *A&A*, 527:A85.
- Nascimbeni V. et al., 2022. *A&A*, 658:A31.
- Neath A.A. and Cavanaugh J.E., 2012. *WIREs Computational Statistics*, 4(2):199–203.
- Nelson R.P. et al., 2000. *MNRAS*, 318(1):18–36.
- Neveu-VanMalle M. et al., 2016. *A&A*, 586:A93.
- Ngo H. et al., 2016. *ApJ*, 827(1):8.
- Nielsen L.D. et al., 2019. *A&A*, 623:A100.
- Nielsen L.D. et al., 2020. *A&A*, 639:A76.
- Obermeier C. et al., 2016. *A&A*, 587:A49.

- O’Brien S.M. et al., 2022. *MNRAS*, 509(4):6111–6118.
- O’Donovan F.T. et al., 2006. *ApJ*, 644(2):1237–1245.
- Osborn A. and Bayliss D., 2020. *MNRAS*, 491(3):4481–4487.
- Osborn A. et al., 2021a. *MNRAS*, 507(2):2782–2803.
- Osborn H.P. et al., 2021b. *MNRAS*, 502(4):4842–4857.
- Osborn J. et al., 2015. *MNRAS*, 452(2):1707–1716.
- Oshagh M. et al., 2017. *A&A*, 606:A107.
- Paczynski B., 1996. *ARA&A*, 34:419–460.
- Pál A., 2009. *Tools for discovering and characterizing extrasolar planets*. Ph.D. thesis, Department of Astronomy, Eötvös Loránd University.
- Papaloizou J.C.B. and Larwood J.D., 2000. *MNRAS*, 315(4):823–833.
- Parviainen H. and Aigrain S., 2015. *MNRAS*, 453(4):3821–3826.
- Pasachoff J.M. and Olson R.J.M., 2011. volume 217 of *American Astronomical Society Meeting Abstracts*, 111.01.
- Patra K.C. et al., 2020. *AJ*, 159(4):150.
- Pearson K.A., 2019. *AJ*, 158(6):243.
- Penny M.T. et al., 2013. *MNRAS*, 434(1):2–22.
- Penny M.T. et al., 2019. *ApJS*, 241(1):3.
- Penz T., Micela G., and Lammer H., 2008. *A&A*, 477(1):309–314.
- Pepe F. et al., 2021. *A&A*, 645:A96.
- Pepper J. et al., 2007. *PASP*, 119(858):923–935.
- Perryman M., 2018. *The Exoplanet Handbook*. Cambridge University Press.
- Perryman M. et al., 2014. *ApJ*, 797(1):14.
- Petigura E.A. et al., 2018. *AJ*, 156(3):89.

- Piaulet C. et al., 2021. *AJ*, 161(2):70.
- Pinte C. et al., 2019. *Nature Astronomy*, 3:1109–1114.
- Pollacco D.L. et al., 2006. *PASP*, 118(848):1407–1418.
- Poon S.T.S., Nelson R.P., and Coleman G.A.L., 2021. *MNRAS*, 505(2):2500–2516.
- Queloz D. et al., 2001. *The Messenger*, 105:1–7.
- Quirrenbach A., 2010. In S. Seager, editor, *Exoplanets*, 157–174. University of Arizona Press.
- Quirrenbach A. et al., 2014. In S.K. Ramsay, I.S. McLean, and H. Takami, editors, *Ground-based and Airborne Instrumentation for Astronomy V*, volume 9147 of *Society of Photo-Optical Instrumentation Engineers (SPIE) Conference Series*, 91471F.
- Rauer H. et al., 2014. *Experimental Astronomy*, 38(1-2):249–330.
- Reefe M. et al., 2022. *AJ* – *submitted*.
- Ricker G.R. et al., 2015. *JATIS*, 1(1):014003.
- Rieke G.H. et al., 2015. *PASP*, 127(953):584.
- Rodríguez E. and Breger M., 2001. *A&A*, 366:178–196.
- Rodríguez J.E. et al., 2020. *AJ*, 160(3):117.
- Rowe J.F. et al., 2014. *ApJ*, 784(1):45.
- Rubenzahl R.A. et al., 2021. *AJ*, 161(3):119.
- Sabotta S. et al., 2021. *A&A*, 653:A114.
- Sachs A., 1974. *Philosophical Transactions of the Royal Society of London. Series A, Mathematical and Physical*, 276.
- Sahlmann J. et al., 2013. *A&A*, 556:A133.
- Salvatier J., Wiecki T.V., and Fonnesbeck C., 2016. *PeerJ Computer Science*, 2:e55.
- Sanchis-Ojeda R. et al., 2015. *ApJ*, 812(1):L11.
- Santerne A. et al., 2012. *A&A*, 545:A76.
- Santerne A. et al., 2019. *arXiv e-prints*, arXiv:1911.07355.

- Sanz-Forcada J. et al., 2011. *A&A*, 532:A6.
- Sarkis P. et al., 2018. *AJ*, 156(5):216.
- Scargle J.D., 1982. *ApJ*, 263:835–853.
- Schlecker M. et al., 2021. *A&A*, 656:A73.
- Schneider P., Ehlers J., and Falco E.E., 1992. *Gravitational Lenses*.
- Schwarz G., 1978. *Annals of Statistics*, 6(2):461–464.
- Sebastian D. et al., 2021. *A&A*, 645:A100.
- Shan S.S. et al., 2021. *arXiv e-prints*, arXiv:2111.06678.
- Simon N.R. and Teays T.J., 1982. *ApJ*, 261:586–594.
- Sinukoff E. et al., 2017. *AJ*, 153(2):70.
- Skrutskie M.F. et al., 2006. *AJ*, 131(2):1163–1183.
- Smith A.M.S. et al., 2020. *Astronomische Nachrichten*, 341(3):273–282.
- Smith A.M.S. et al., 2021. *A&A*, 646:A183.
- Southworth J., Wheatley P.J., and Sams G., 2007. *MNRAS*, 379(1):L11–L15.
- Southworth J. et al., 2019. *MNRAS*, 490(3):4230–4236.
- Sozzetti A. et al., 2021. *A&A*, 648:A75.
- Spergel D. et al., 2015. *arXiv e-prints*, arXiv:1503.03757.
- Stassun K.G. et al., 2018. *AJ*, 156:102.
- Stassun K.G. et al., 2019. *AJ*, 158(4):138.
- Steffen J.H. et al., 2012. *Proceedings of the National Academy of Science*, 109(21):7982–7987.
- Stevenson K.B. et al., 2016. *PASP*, 128(967):094401.
- Struve O., 1952. *The Observatory*, 72:199–200.
- Tamura M. et al., 2012. In I.S. McLean, S.K. Ramsay, and H. Takami, editors, *Ground-based and Airborne Instrumentation for Astronomy IV*, volume 8446 of *Society of Photo-Optical Instrumentation Engineers (SPIE) Conference Series*, 84461T.

- Tamuz O., Mazeh T., and Zucker S., 2005. *MNRAS*, 356:1466–1470.
- Thibault S. et al., 2012. In I.S. McLean, S.K. Ramsay, and H. Takami, editors, *Ground-based and Airborne Instrumentation for Astronomy IV*, volume 8446 of *Society of Photo-Optical Instrumentation Engineers (SPIE) Conference Series*, 844630.
- Tsiaras A. et al., 2016. *ApJ*, 820(2):99.
- Turner J.D. et al., 2022. *AJ*, 163(6):281.
- Udalski A. et al., 1992. *Acta Astron.*, 42:253–284.
- Vanderburg A. and Johnson J.A., 2014. *PASP*, 126(944):948.
- Vanderburg A. et al., 2015. 800(1):59.
- Vanderburg A. et al., 2016. *ApJ*, 827(1):L10.
- Vanderburg A. et al., 2017. *AJ*, 154(6):237.
- Vanderburg A. et al., 2019. *ApJ*, 881(1):L19.
- Weiss L.M. et al., 2017. *AJ*, 153(6):265.
- Weiss L.M. et al., 2021. *AJ*, 161(2):56.
- West A.A. et al., 2008. *AJ*, 135(3):785–795.
- West R.G. et al., 2019. *MNRAS*, 486(4):5094–5103.
- Wheatley P.J. et al., 2018. *MNRAS*, 475(4):4476–4493.
- Wilson J. et al., 2020. *MNRAS*, 497(4):5155–5170.
- Wilson T.G. et al., 2022. *MNRAS*, 511(1):1043–1071.
- Winn J.N., 2010. *arXiv e-prints*, arXiv:1001.2010.
- Winn J.N. et al., 2010. *ApJ*, 718(1):575–582.
- Wolszczan A. and Frail D.A., 1992. *Nature*, 355(6356):145–147.
- Wright E.L. et al., 2010. *AJ*, 140:1868–1881.
- Yao X. et al., 2019. *AJ*, 157(1):37.

- Yee J.C. et al., 2021. *AJ*, 162(5):180.
- Yee S.W., Petigura E.A., and von Braun K., 2017. *ApJ*, 836(1):77.
- Yee S.W. et al., 2018. *AJ*, 155(6):255.
- Yee S.W. et al., 2020. American Astronomical Society Meeting Abstracts, 456.02.
- Young A.T., 1967. *AJ*, 72:747.
- Zechmeister M., Kürster M., and Endl M., 2009. *A&A*, 505(2):859–871.
- Zeng L., Sasselov D.D., and Jacobsen S.B., 2016. *ApJ*, 819(2):127.
- Zeng L. et al., 2019. *Proceedings of the National Academy of Science*, 116(20):9723–9728.
- Zhou G. et al., 2019. *AJ*, 158(4):141.